TECHNISCHE UNIVERSITÄT MÜNCHEN
LEHRSTUHL FÜR AERODYNAMIK UND STRÖMUNGSMECHANIK

Active Flow Control of Delta Wing Leading-Edge Vortices

Anja Kölzsch

Vollständiger Abdruck der von der promotionsführenden Einrichtung Fakultät für Maschinenwesen der Technischen Universität München zur Erlangung des akademischen Grades eines

Doktor-Ingenieurs (Dr.-Ing.)

genehmigten Dissertation.

Vorsitzende/-r:	Prof. Dr.-Ing. Florian Holzapfel
Prüfende/-r der Dissertation:	1. apl. Prof. Dr.-Ing. Christian W. M. Breitsamter
	2. Prof. Dr.-Ing. Mirko Hornung

Die Dissertation wurde am 11.04.2017 bei der Technischen Universität München eingereicht und durch die promotionsführende Einrichtung Fakultät für Maschinenwesen am 06.11.2017 angenommen.

Anja Kölzsch: *Active Flow Control of Delta Wing Leading-Edge Vortices*,
Dissertation, Technische Universität München

E-MAIL:
anja.koelzsch@mytum.de

Abstract

Delta wing aerodynamics at low Mach numbers are characterized by a complex three-dimensional system of vortices and instabilities, that highly depend on the wing geometry and the free-stream conditions. In this thesis, frequency-dependent forcing is experimentally investigated on a generic delta wing configuration at low Mach numbers. The objective is to find flow control set-ups that enhance the aerodynamic characteristics in standard flight situations and high-lift maneuvers. Especially the increase of the lift coefficient in different flight regimes, the increase of the maximum angle of attack and the retardation of vortex bursting are of main interest.

For this purpose, two flow control methods are implemented on a wind tunnel model with generic delta wing geometry. On the one hand, a pulsed blowing system is investigated, that allows for the insertion of pulsed air jets from slots integrated on the upper side of the leading edge. On the other hand, miniature leading-edge flaps are explored, that perform harmonic oscillations around the wing's mid-plane. The components and functionality of the flow control devices, as well as their integration into the wind tunnel models, are elaborately described in this thesis.

The experiments are conducted for three different angle-of-attack regimes, namely pre-stall, stall and post-stall. The obtained experimental data comprise flow visualizations, force measurements, surface pressure measurements, hot-wire measurements and flow field mapping by Stereo-Particle Image Velocimetry.
The study is composed of three consecutive parts: firstly, a comprehensive aerodynamic analysis of the flow phenomena on the basic configuration is carried out for the different flow regimes, elaborating the integral force and moment coefficients as well as the velocity and surface pressure field. Special emphasis is put on the governing flow structures and the flow-inherent instabilities.
Secondly, an extensive parameter study is performed for both pulsed blowing and the miniature leading edge flaps. Relevant actuation parameters are examined including the pulse or flap frequency, the number and the location of active actuation segments as well as the jet velocity and the duty cycle in the case of pulsed blowing. Thereby, mainly the impact on the integral force and moment coefficients is evaluated.
The most promising flow control parameter sets determined in the parameter study are then investigated in-depth for both flow control devices in the third part of the experimental study. The relevant test cases are studied by the unsteady and time-averaged experimental results for the velocity and the surface pressure distribution. Compared to the respective baseline flow field, they offer detailed insight into the effects of the frequency-dependent forcing. Finally, the most potential flow control parameter sets and their effects are summarized and the possibilities and limits of the applied flow control methods are shown.

Danksagung

Diese Arbeit ist in den Jahren 2010 bis 2016 während meiner Tätigkeit am Lehrstuhl für Aerodynamik und Strömungsmechanik der Technischen Universtät München entstanden. Auf diesem Weg bin ich sehr vielen Menschen begegnet, die mich unterstützt und zum Erfolg der Arbeit beigetragen haben. Ihnen allen möchte ich an dieser Stelle meinen herzlichen Dank aussprechen.

Der grösste Dank gilt meinem Betreuer und Doktorvater, Herrn Prof. Dr.-Ing. Christian W. M. Breitsamter. Mit seiner Gruppe für Flugzeugaerodynamik und der entsprechenden Ausstattung für experimentelle und numerische Untersuchungen hat er sehr gute Rahmenbedingungen für ein effizientes Arbeiten geschaffen und den wissenschaftlichen Austausch auf nationaler und internationaler Ebene ermöglicht. Seine Tür stand immer offen für fachliche Diskussionen und mit seiner Expertise und seinem persönlichen Interesse an der Deltaflügelaerodynamik war er ein wunderbarer Ansprechpartner und Impulsgeber.
Einen großen Dank möchte ich Herrn Prof. Dr.-Ing. Mirko Hornung aussprechen, der die Aufgabe des zweiten Prüfers meiner Dissertation übernommen hat. Für die Übernahme des Vorsitzes der Prüfungskommission danke ich Herrn Prof. Dr.-Ing. Florian Holzapfel herzlich.

Allen Kollegen am Lehrstuhl bin ich für die angenehme, freundschaftliche Zusammenarbeit in einem sehr internationalen Umfeld, die gemeinsamen fachlichen Diskussionen und die Unterstützung dankbar. Zuallererst möchte ich den Kollegen aus der Werkstatt des Lehrstuhls danken, denn ohne sie wäre der Betrieb der Windkanäle und die Fertigung der Modelle undenkbar gewesen. Herrn Dipl.-Phys. Roman Ress danke ich für seinen Rat zur Windkanalmesstechnik und Herrn Hans-Gerhard Frimberger für die Unterstützung von Elektroniker-Seite, sozusagen als 'gute Seele des Windkanals'. Ebenso gilt mein Dank Herrn Dr.-Ing. Andreas Hövelmann für seine Starthilfe bei den PIV-Messungen. Ihr habt sehr zum Gelingen der Windkanalexperimente beigetragen!

Für den fachlichen Austausch bedanke ich mich besonders bei Dr.-Ing. Nicolas Thouault, Dr. Kentaro Kato, Dipl.-Ing. Maximilian Winter, Dipl.-Ing. Andrej Buzica, Julie Piquee und Antonio DiGiovanni. Ich danke auch allen Studenten, die in Form von Studien- und Abschlussarbeiten sowie HiWi-Tätigkeiten die Konzeption der Windkanalmodelle und die Durchführung der Experimente im Windkanal tatkräftig unterstützt haben.
Viel Motivation habe ich neben der wissenschaftlichen Arbeit aus den gemeinsamen sportlichen Aktivitäten mit Chris, Stefan, Matze, Susi und Margit geschöpft - schön, dass ich diese Zeit mit Euch teilen durfte!

Schließlich danke ich meiner Familie, meinen Eltern und Großeltern, für die Unterstützung während meiner gesamten Ausbildung. Meinem Partner Mark danke ich für die vielen fachlichen Gespräche, sein Verständnis und seine Liebe.

Contents

List of Figures

List of Tables

Nomenclature

Latin letters:

b	wing span	m
C_D	drag coefficient	-
C_L	lift coefficient	-
C_l	rolling moment coefficient	-
C_m	pitch moment coefficient	-
C_N	normal force coefficient	-
C_n	yaw moment coefficient	-
C_μ	momentum coefficient	-
c_p	pressure coefficient	-
c_r	root chord	m
d	wing thickness	m
E	voltage	V
E_o	laser output	J
f	frequency	Hz
f_A	subharmonic frequency of shear layer instability	Hz
f_B	frequency related to quasi-periodic fluctuations of vortex breakdown location	Hz
f_{dom}	frequency of the helical mode instability	Hz
f_{lp}	low pass filter frequency	Hz
f_{pulse}	pulse frequency	Hz
f_s	sampling rate	Hz
f_S	frequency of shear layer instability	Hz
F	surface area	m^2
F^+	reduced actuation frequency	-
h	slot length	m
	total pressure	Pa
k	reduced frequency	-
	circulation	m^2/s
l_μ	wing mean aerodynamic chord	m
$\dot{m}$	mass flow	kg/s
M	Mach number	-
N	number of samples	-
p	static pressure	Pa
p_{valve}	pressure in front of the closed valve	Pa

q	dynamic pressure	Pa
r	radius	m
R	universal gas constant	-
Re_{mac}	Reynolds number based on mean aerodynamic chord	-
$s_{(l)}$	(local) semi wing span	m
$S^N_{C_p}$	normalized power spectral density of the pressure coefficient	-
$S_{u'}$	power spectral density of the axial velocity fluctuations	m^2/s
S_{axis}	swirl parameter	-
S^*	critical swirl level	-
t	slot width	m
	time	s
T	temperature	$°C$
Tu	turbulence level	-
u, v, w	axial, lateral and vertical velocity in wind-tunnel fixed system	m/s
u_{rms}, v_{rms}, w_{rms}	rms values of u', v', w'	m/s
U	velocity	m/s
U_{jet}	jet velocity	m/s

Greek symbols:

α	angle of attack	°
δ	flap deflection angle	°
γ	helix angle	°
γ_0	eigenvalue	-
Γ	circulation	m^2/s
Λ	aspect ratio	-
ω_x	axial vorticity	1/s
ϕ	leading edge sweep	°
ψ	stream function	m^2/s
ρ	density	kg/m^3
θ	azimuth angle	°

Superscripts:

$()^N$	normalized
$()'$	fluctuating quantity
$\hat{()}$	maximum value (amplitude)

Subscripts:

$()_c$	viscous core
$()_{corr}$	temperature-corrected
$()_{dom}$	dominant
$()_{LE}$ or $()_{le}$	leading edge
$()_{ref}$	reference
$()_N$	normal to the leading edge
$()_o$	outer
$()_\infty$	freestream conditions

Abbreviations:

CFD	Computational Fluid Dynamics
DBD	Dielectric Barrier Discharge
HWA	hot-wire anemometry
LEX	leading-edge vortex
LP	low-pass
PID	Proportional/Integral/Derivative
PIV	Particle Image Velocimetry
PSD	power spectral density
PVT	Position/Velocity/Time
rms	root mean square
TKE	turbulent kinetic energy
$VFE-2$	Vortex Flow Experiment 2

1. Introduction

Delta wing configurations are characterized by low to moderate aspect ratios and high leading edge sweep. Their name is derived from the fourth Greek uppercase letter Δ, as the planform shape of a delta wing resembles it. The sweep of a delta wing leading edge varies with the application but normally falls in the range between $\phi = 40°$ and $70°$. The wing thickness compared to wing span and root chord is relatively small on delta wing geometries. Delta wings are mostly applied for supersonic flight and for aircraft which need to have high maneuverability. They are mainly applied for fighter aircraft (see Fig. 1.1a) and bombers, but were also used for transport aircraft such as the Concorde (see Fig. 1.1b) and the Tupolev Tu 144.

1.1. Motivation

In contrast to high-aspect ratio wings, the flow around delta wings is highly three-dimensional due to their high sweep. Under subsonic flow conditions, the flow pattern is governed by a leading edge vortex system on the lee-side of the wing, which develops at moderate angles of attack. A nonlinear increase in lift is a special feature of delta wings in this flight regime. It is generated by the vortex system and leads to an additional lift portion which is called vortex lift component. Additionally, delta wings are characterized by a considerably higher stall angle compared to high aspect ratio aircraft configurations. Apart from the above mentioned advantages of delta wing configurations, there are also some drawbacks related to the aerodynamics of delta wings. At relatively low speeds,

(a) Italian Eurofighter Typhoon [1]

(b) Concorde [2]

Figure 1.1.: Examples of delta wing aircraft

which occur during take-off and landing or flight maneuvers, a very high incidence is necessary to reach a sufficiently high level of lift. At this flight regime, the drag coefficient is relatively high compared to other wing configurations and it has to be compensated by higher thrust.
Another even more severe drawback is the occurrence of a phenomenon called vortex breakdown, which is accompanied by strong flow fluctuations and leads to a loss in lift. Vortex breakdown begins at the rear part of the wing and propagates upstream. When it has reached the apex, it comes to the collapse of the vortex system and a significant, abrupt change of the aerodynamic forces. In practice, the breakdown-induced fluctuations can cause structural vibrations such as fin buffeting. It can even lead to unmaneuverability or damage of the configuration. The same holds for the area of the abrupt lift decrease after the collapse of the vortex system, which must be avoided under all circumstances.

Novel control effectors aim at extending the high angle-of-attack envelope and reducing the dynamic loads on delta wing configurations. These goals are by far not trivial to achieve, as the vortex systems on delta wings are complex systems with a plenty of unsteady effects and flow instabilities, that interact with each other and highly depend on the free-stream conditions. Particular mention deserves the phenomenon of vortex breakdown, that constitutes a fundamental problem of fluid mechanics, but is not fully understood yet. It governs the delta wing vortex system over a wide angle-of-attack range and causes several flow instabilities. Therefore, a downstream-shift of vortex breakdown and an attenuation of the accompanying fluctuations in the flow are an important issue for novel control effectors.

In the following, a literature study on state-of-the-art flow control methods for delta wing configurations is carried out. Finally, the contribution and the scope of this work are defined.

1.2. State of the art

Flow control is the "attempt to alter the character or disposition of a flow field favorably that is of concern" [18]. In the case of the application to delta wings at low-speed flow conditions, flow control techniques aim at improving the performance of such configurations as well as the stability at the borders of their flight envelope. One can distinguish between active and passive methods for the manipulation of leading-edge vortex structures. While passive methods don't require an auxiliary power supply, active methods are characterized by a necessary energy expenditure [18]. There is a wide range of flow control methods for delta wing configurations. The most important mechanisms were reviewed by Gursul [28] and Mitchell [59]. Their articles form the basis for this subsection, but are supplemented by further findings on aspects of delta wing flow control.

In Table 1.1, an overview of the most important flow control methods applied to delta wing configurations is given. These methods will be explained in more detail in the

following. Thereby, the main focus is on the actuation by control surfaces varying the local angle of attack at the separation line, called leading edge flaps, and on the actuation by blowing and/or suction.

Table 1.1.: Delta wing flow control methods

Classification	**Flow control device**	**Specification**
Passive methods	Additional fixed components for the creation of multiple vortex systems	Double delta wings
		Strakes
		Canards
	Elastic wings	
	Modifications to leading edge geometry	Varying nose radius/leading edge bluntness
		Varying leading edge contour
Active methods	Control surfaces	Varying angle of attack at separation line
		Varying leading edge sweep
		Integrated in the apex
	Continuous/periodic blowing and/or suction	In the leading edge region
		Along/near-the-core blowing
		Trailing edge blowing
	Plasma actuators	

1.2.1. Passive flow control methods

All methods that change the delta wing geometry or the wing structure in order to improve the flow properties, but are not characterized by an energy expenditure, are assigned to passive flow control methods. A disadvantage of these passive methods is, that they are permanently installed on the configuration and can therefore cause undesired effects and phenomena at different flow regimes [28].

1.2.1.1. Creation of multiple-vortex systems

The installation of delta wing forebodies (e.g. at double delta wings [78] and tandem delta wings know as chinard configuration [52]), and the installation of strakes or canards [33], [61] are examples for the creation of multiple-vortex systems. The forebodies generate additional upstream vortices, which interact with the vortex system of the main wing. These additional vortices energize the flow and delay the vortex breakdown on the main wing [28], as shown in Fig. 1.2.

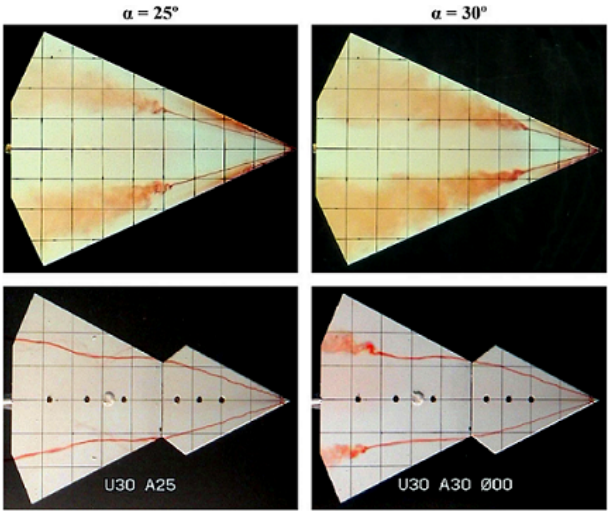

Figure 1.2.: Formation and breakdown of leading edge vortices for a 65°/65° tandem delta wing [52]

1.2.1.2. Flexible delta wings

The idea of flexible delta wings is another passive method applicable to nonslender geometries ($\phi = 35 - 55°$). In Ref. [77], the lift enhancement and the stall delay is studied in comparison to a rigid wing of the similar geometry. The consciously generated interaction of structural oscillations of the flexible wing with the shear layer supports the reattachment of the flow (see Fig. 1.3) and therefore leads to a significant lift enhancement in the post-stall regime. Nevertheless, additional self-excited dynamic loads are induced on the wing structure and therefore, this method is not really applicable in practice.

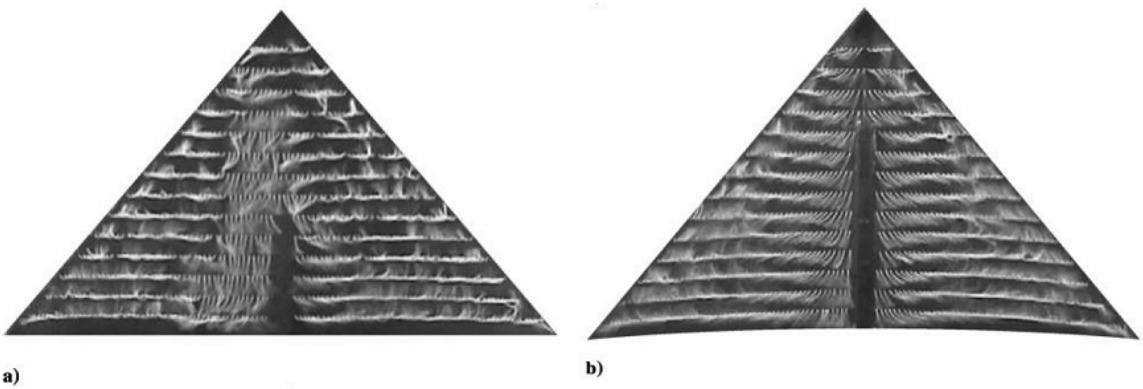

Figure 1.3.: Flexible nonslender deltawing: Tuft visualizations showing surface flow patterns at $\alpha = 27°$ for the a) rigid wing and b) flexible wing. [77]

1.2.1.3. Modifications to the leading-edge geometry

The flow properties of a delta wing can also be influenced by the variation of the leading-edge geometry. Here, the leading edge nose radius is an important influencing factor. For a sharp leading edge with $r_{le}/l_{\mu} = 0$, the primary separation line is fixed to the location of the leading edge. On the contrary, for a blunt leading edge, the separation line varies with the angle of attack and the free-stream Reynolds number. Therefore, a significant effect of the leading-edge bluntness can be observed on the onset and the progression of leading edge vortices [49].

1.2.2. Active flow control methods

Active methods for flow control can basically be divided into three major groups: control surfaces, continuous or periodic blowing and/or suction, and plasma actuators. In addition, the effect of heating a delta wing surface was studied in [54]. The focus of this study was to improve the understanding of re-entry effects for the space shuttle. Since the results showed that heating leads to an increase in drag and does not positively affect the lift and pitching moment, this method is not applied for flow control on modern fighter aircraft.

1.2.2.1. Steady and unsteady excitation

Active flow control can be classified into steady and unsteady methods. Both periodic blowing and the oscillation of flaps with a small deflection angle are more effective than their quasi-static counterparts [28]. On the basis of the actuation frequency f, the non-dimensional frequency F^+ is defined by

$$F^+ = \frac{f c_r}{U_\infty}, \tag{1.1}$$

and is utilized to classify the unsteady methods into low-frequency ($F^+ \approx 0.1$) and high-frequency ($F^+ \approx 1$) excitation [28]. While low-frequency types can influence the burst behaviour via variation of the axial pressure gradient, the high-frequency types aim at a manipulation of vortex-related instabilities.

1.2.2.2. Control surfaces

Control surfaces for delta wing flow control comprise leading-edge flaps to adapt the angle of attack at the separation line [44], [10], [11], [12], flaps to adapt the leading-edge sweep [27], and flaps integrated at the apex of the wing [36].

Leading-edge flaps. Leading-edge flaps alter the structure of leading-edge vortices and change the location of vortex breakdown [27]. They lead to a reduction of drag and to an improvement of the lift-to-drag ratio, if they are deflected downwards [44].

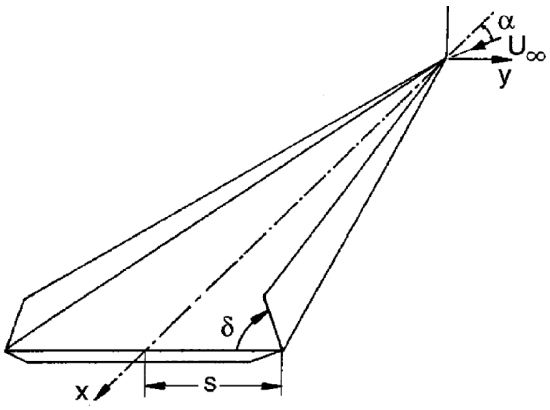

(a) Leading-edge flaps [12]

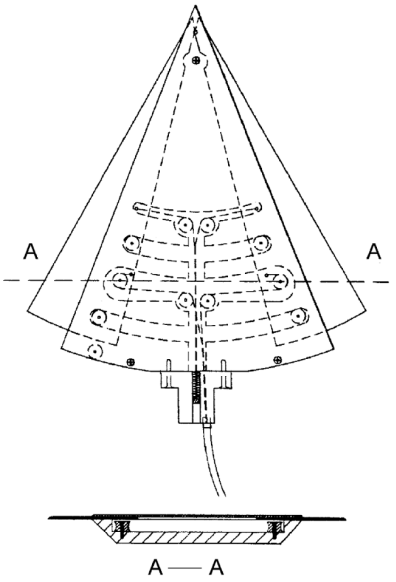

(b) Variable wing sweep [27]

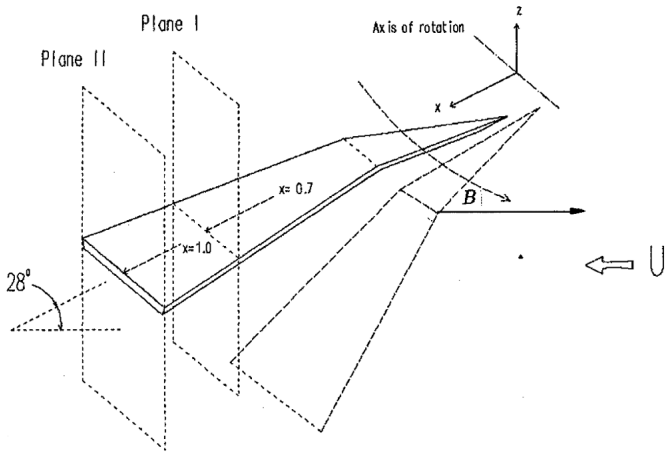

(c) Drooping apex flap [36]

Figure 1.4.: Various control surfaces

For upward deflected leading edge flaps, an increase in lift as well as in drag is observed [44]. Deng and Gursul investigated the effects of stationary [10] and oscillating [11], [12] upwards deflected leading edge flaps (Gurney flaps, see Fig. 1.4a) on the vortex system and the vortex breakdown on a 70° swept delta wing at $Re_{c_r} = 5 \times 10^5$. Their results for an angle of attack $\alpha = 30°$ showed a dynamic response in form of a downward shift of the

breakdown location. They observed that the breakdown location may move upstream and downstream compared to the quasi-steady case, dependent on the amplitude of flap oscillations and the angle of attack. In contrast to the quasi-steady case, the variation of breakdown location reveals hysteresis loops for the oscillating flaps.

Variable sweep. Gursul et al. used a variable leading-edge extension to vary the wing sweep angle of a delta wing model from $\phi = 60°$ to $\phi = 70°$ [27], see Fig. 1.4b. Experiments were conducted at $Re_{c_r} = 1.9 \times 10^5$. Their results showed that the vortex breakdown location can be controlled by varying the leading-edge sweep on the basis of a feedback control loop using pressure fluctuations as input signal.

Apex flaps. The effect of an apex flap (see Fig. 1.4c) was tested by Klute et al. for both fixed and dynamically pitching delta wing models with 75° sweep angle at $Re_{c_r} \approx 2.9 \times 10^5$ [36]. They found that a drooping apex flap delays the appearance of vortex breakdown over the wing by 8 degrees compared to the corresponding value of the unmodified wing.

1.2.2.3. Pneumatic devices

In the field of flow control by pneumatic devices, several methods were investigated. Namely, these are continuous or periodic blowing and/or suction in the leading-edge region [20], [22], [55], [69], [73], [74], [79], [81], [83], concentrated tangential blowing in the apex region [28], along- or near-the-core blowing [25], [79] and unsteady trailing edge blowing [34]. For the description and assessment of the unsteady blowing effectiveness, the moment coefficient is defined as follows:

$$C_\mu = 2 \left(\frac{< U_{jet} >}{U_\infty} \right)^2 \frac{A_{slot(s)}}{A_w}. \tag{1.2}$$

Leading edge blowing and suction. Gursul distinguishes between blowing in outward direction, upward direction with and without a Coanda surface, and suction at the leading edge [28]. These methods have different effects on the swirl level of the vortex. Blowing in outward direction leads to the formation of strong jet vortices merging with the leading-edge vortex [28]. Celik et al. [8] and Hong et al. [31] studied lateral blowing on a 60° delta wing through blowing slots along the leading edge symmetrically and asymmetrically for $Re_{c_r} = 3.25 \times 10^5$ and $Re_{c_r} = 5 \times 10^5$. They found that depending on the angle of attack and the jet strength the leading-edge vortex is strengthened by the vorticity from the blowing jet feeds and their direct jet momentum. This leads to an increase in vortical lift at small angles of attack. For symmetrical blowing, the normal force is augmented, whereas for asymmetrical blowing, a rolling moment is produced. Besides, partial slot blowing from small aspect-ratio slot is of higher efficiency compared with full slot blowing.

Margalit et al. [55] applied periodic excitation by segmented piezoelectric fluidic actuators to a 60-deg sweptback delta wing in the stall and post-stall regime. Unsteady blowing at five leading edge slots in the outward direction was studied at root chord Reynolds numbers $Re_{c_r} = 1.5{\times}10^5$ to $Re_{c_r} = 3.5{\times}10^5$. Three different excitation modes (sinusoidal, amplitude modulation and burst mode signals) at reduced frequencies ranging from $\mathcal{O}(1)$ to $\mathcal{O}(10)$ were applied. The best results in the sense of an increase in the normal force were gained for amplitude modulation and pulsed blowing. Optimal results were found for the momentum coefficients $C_\mu = 0.03\%$ for pulsed blowing and $C_\mu = 0.4\%$ for blowing with amplitude modulation. The actuation at reduced frequencies $F^+ \approx 1 - 2$ was found to be most effective and lead to a significant increase in lift in the post-stall regime ($\alpha > \alpha_{max}$). This is the consequence of a reformation of the flow field from a separated shear layer emanating from the stalled leading edge in the baseline case to a rolled-up shear layer forming a burst leading edge vortex in the case with active flow control.

Williams et al. [81] investigated pulsed blowing with a 50° swept delta wing at a Reynolds number $Re_{c_r} = 2 \times 10^5$ in the post-stall region. The direction of the most successful type of blowing was inclined between the outward and the upward direction. In this work, the generation of a vortex was observed, if the shear layer emanating from the leading edge was exposed to pulsed blowing at frequencies in the range of $F^+ \approx 1.5$. Pressure measurements showed the greatest enhancement in the suction force for the momentum coefficient $C_\mu = 0.01\%$. Another finding of this study is, that once the shear layer has reattached along the whole wing, a further increase of the momentum coefficient does not improve the pressure distribution on the wing's upper surface in the sense of a suction force. Nevertheless, the minimum required momentum coefficient increases as the angle of attack is increased.

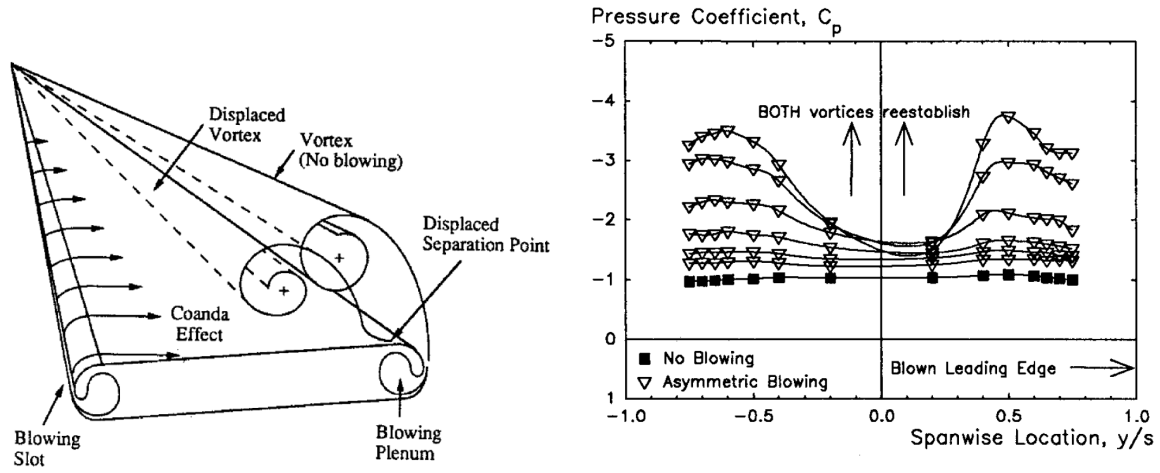

(a) Configuration

(b) One-sided coanda-blowing leads to reestablishment of vortices in the post-stall regime

Figure 1.5.: Tangential blowing with the Coanda effect [23]

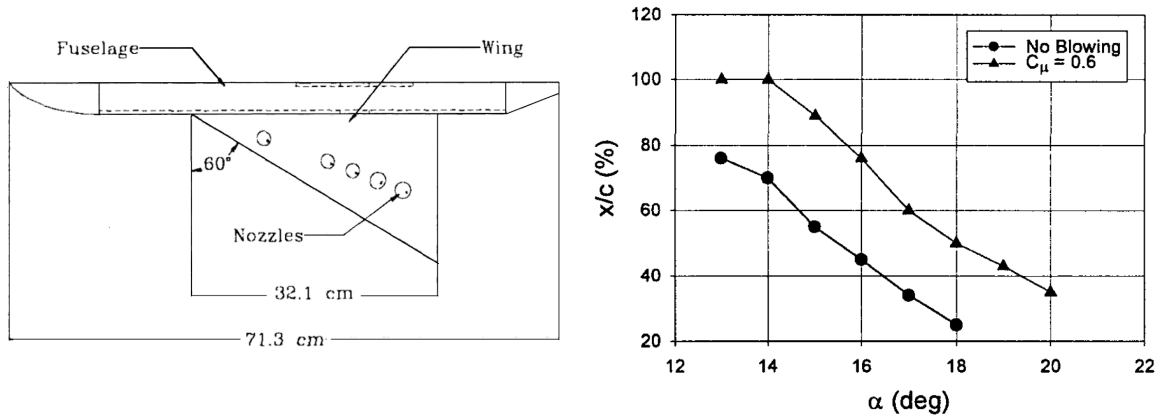

(a) Configuration for near-core blowing

(b) Results: breakdown location for the baseline and controlled cases

Figure 1.6.: Near-core blowing [25]

Blowing with a Coanda surface (see Fig. 1.5) has only a small effect on the normal force at low to moderate angles of attack, but for high angles of attack in the post-stall region, a lift enhancement due to the flow reattachment of the energized shear layer is observed [23], [83]. McCormick and Gursul studied the effects of suction near the separation point on a delta wing with a wing sweep of $\phi = 70°$ for Reynolds numbers $Re_{c_r} = 4 \times 10^5$ to 5×10^4 [56]. As a result, the orientation of the shear layer as well as the location and the structure of the primary vortex was modified. The vortex breakdown location was shifted downstream by a decrease of the circulation.

Along- or near-core blowing. Visser [79] and Guillot [25] conducted experiments to study blowing at locations in the vicinity of the vortex core. Visser investigated the effect of a jet on the aerodynamic characteristics of a 70° wing sweep configuration at $Re_{c_r} = 1.6 \times 10^5$ to 2.5×10^5 at the angles of attack $\alpha = 30°$ and $\alpha = 35°$. He found that the optimum position of the jet is in the leading edge region, aligned parallel to the leading edge. The effect of the jet shows that the swirl angle in the outer region of the vortex is decreased leading to a delay of vortex breakdown [79]. On a delta wing configuration of 60° wing sweep and at a root chord Reynolds number $Re_{c_r} = 2.6 \times 10^5$, Guillot showed that near-core blowing (see Fig. 1.6) leads to an acceleration of the vortex core velocity, a stabilization of the vortex and a shift of the vortex breakdown location towards the trailing edge [25].

Trailing-edge blowing. Trailing-edge jets have been studied for example by Helin [30], Jiang [34], Mitchell [60] and Phillips [65]. They change the external pressure gradient and can therefore cause a delay of vortex breakdown, even in the presence of a vertical fin [28], [65]. One example is shown in Fig. 1.7, where trailing edge blowing was investigated in a water tunnel with a 75° swept delta wing at $Re_{c_r} = 3.5 \times 10^4$ [65]. The results

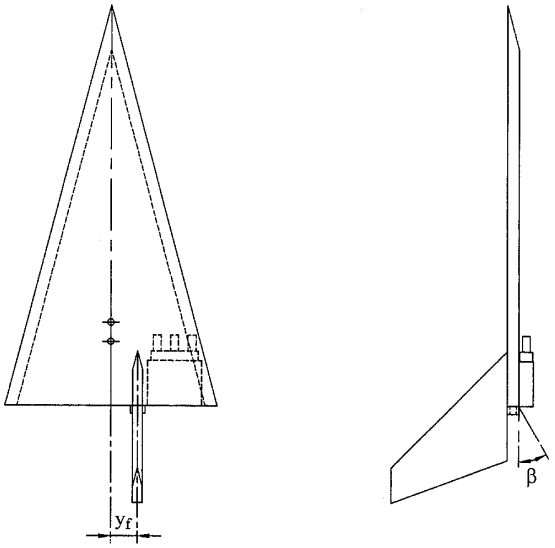

(a) Experimental configuration with definition of the fin location y_f and the jet deflection angle β

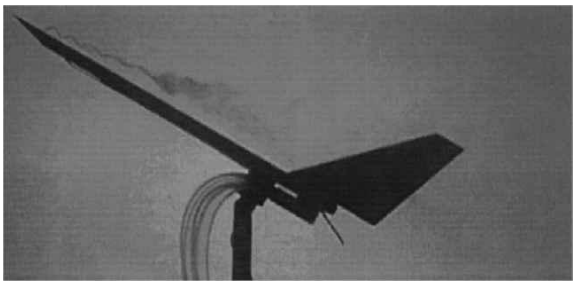

(b) Flow visualization for $U_{jet}/U_\infty = 0$, $y_f/s = 0.2$, $\alpha = 30°$

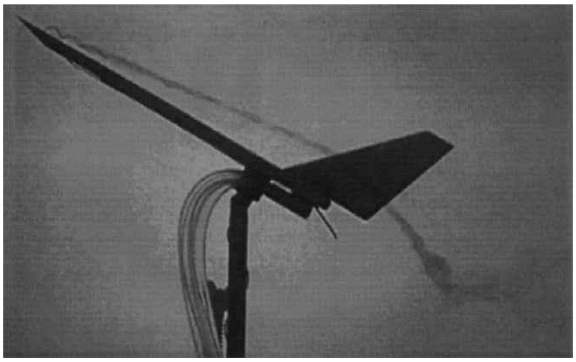

(c) Flow visualization for $U_{jet}/U_\infty = 8.9$ ($C_\mu = 0.708$), $y_f/s = 0.2$, $\alpha = 30°$, and $\beta = 30°$

Figure 1.7.: Example for trailing-edge blowing [65]

showed, that the vortex breakdown can be delayed into the wake and up to 60% of the root chord length by increasing the momentum coefficient of the jet. Highest effectiveness was observed for deflected jets with deflection angles $\beta = 30°$ and $\beta = 45°$. Furthermore, in some cases the authors showed that it is possible to shift the buffeting envelope up to $\Delta\alpha = 12°$. Nevertheless, the effectiveness of this flow control technique highly depends on the wing sweep angle: trailing edge blowing is very effective for high wing sweep angles, but much less for nonslender delta wings [28].

Effectiveness of the different methods. Gursul et al. compared the effectiveness of various methods applying blowing/suction to delta wings, see Fig. 1.8 [28]. Their conclusion is, that along-the-core blowing shows to be most effective in delaying the vortex breakdown location $\Delta x_{bd}/c_r$, second is leading-edge suction and blowing, followed by trailing-edge blowing.

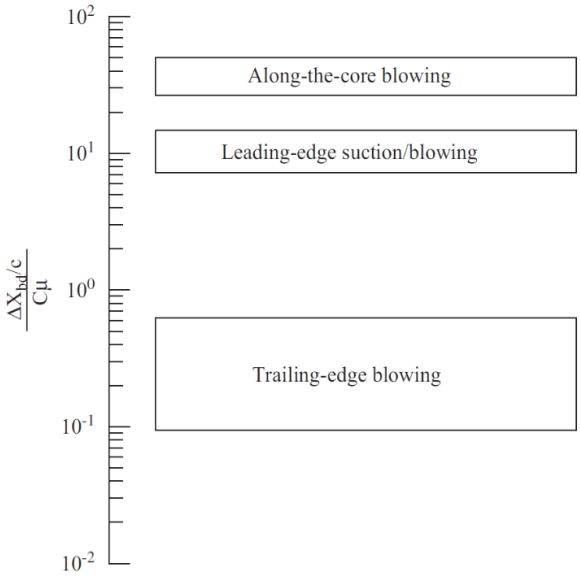

Figure 1.8.: Comparison of effectiveness for different blowing/suction methods [28]

1.2.2.4. Plasma actuators

Greenblatt et al. [21] studied the effect of Dielectric Barrier Discharge (DBD) plasma actuators employed at the leading edge of a delta wing, see Fig. 1.9. Similar to periodic blowing, the installed DBD plasma actuators induce a jet. In this case, it is directed inboard from the leading edge. The actuators are driven in pulse modulation mode with a reduced frequency $F^+ = 1$. They are therefore analogue to a nonzero-mass-flux pulsed jet with a steady and an unsteady component of the momentum coefficient. The advantage of these actuators is that they can be applied very flexibly with regard to their orientation and location.

The experiments were carried out at free-stream conditions of $Re_{c_r} = 2.0 \times 10^5$ to $Re_{c_r} = 7.5 \times 10^5$ on a semispan delta-wing model with a wing sweep $\phi = 60°$. The wing geometry was relatively thin ($t/c_r = 1\%$). Most of the experiments were conducted at a relatively large angle of attack in the poststall regime ($\alpha = 36°$). In a frequency and duty cycle scan, optimum conditions $F^+ \approx 1$ and $DC = 10\%$ were found. The results showed that a large vortex can be generated above the wing surface by pulsed actuation at reduced frequencies in the order of unity. Furthermore, an increase in $C_{L,max}$ of approximately 10% and a drag reduction was observed.

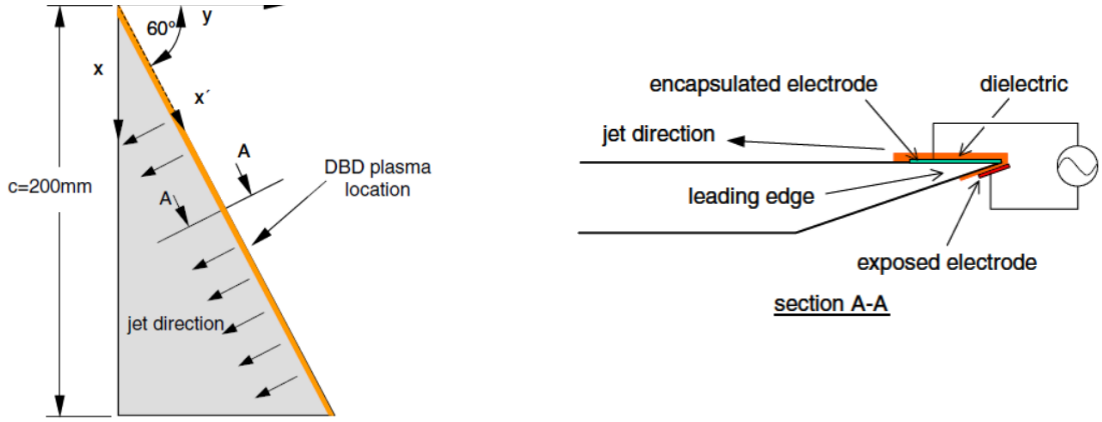

(a) Top view (b) Actuator layout

Figure 1.9.: Delta wing model with DBD plasma actuators [21]

1.3. Research objectives and methodology of the study

Research objectives. The main objective of this work is to study flow control methods on a delta wing configuration and to thereby identify possibilities to influence the delta wing aerodynamics positively in terms of the flow characteristics, aerodynamic loads and the flight envelope at specific angles of attack in the subsonic flight regime. In detail, the following issues are highly desirable:

- an increase in lift as well as an increase of the maximum angle of attack,
- the control of the reattachment line of the primary vortices,
- the retardation of vortex breakdown over the wing to higher angles of attack as well as a downstream-shift of the vortex-breakdown location over the wing,
- the stabilization of the vortex and the reduction of the (pressure) fluctuations which are caused by vortex breakdown and can lead to fin buffeting and severe damage of an aircraft configuration,
- an attenuation of the lift decrease in the post-stall regime and
- the promotion of desired as well as the suppression of undesired aerodynamic moments to improve controllability.

Methodology. In this work, two active unsteady flow control methods for the low speed regime are investigated elaborately on a generic delta wing configuration with

sharp leading edge. These are geometrically segmented oscillating leading edge flaps and segmented pulsed blowing in the leading edge region, cf. Fig. 1.10.

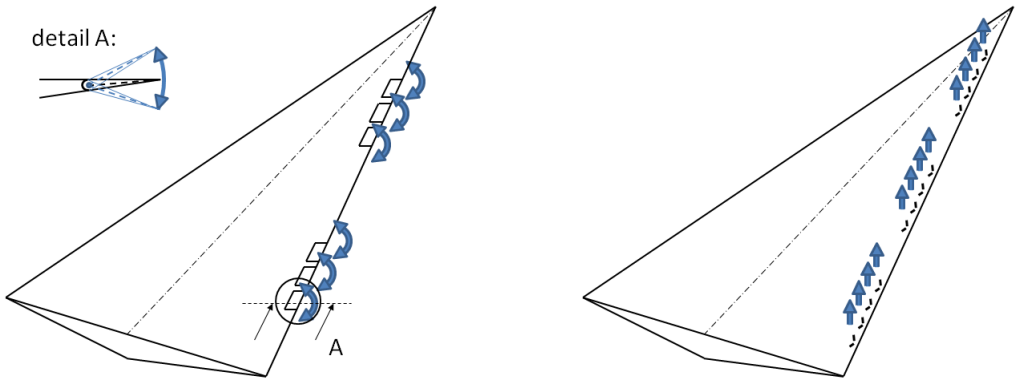

(a) Leading-edge flaps (b) Pulsed leading-edge blowing

Figure 1.10.: Flow control devices

As the flow control devices are integrated along the leading edge, the setup enables a specific manipulation of the primary vortex shear layer by frequency-dependent forcing. Moreover, steady and unsteady forcing can be compared on the same delta wing configuration.

The approach is as follows:

- As a starting point, the flow field without actuation (referred to as 'baseline case' in the following) is recorded by force, velocity and pressure measurements in the pre-stall, stall and post-stall regime.
- The results are analyzed with special regards to the characteristics of the velocity and pressure spectra, because valuable information about the flow-inherent instabilities can be deduced from the spectral analysis.
- On this basis, a parameter study for the two flow control methods is carried out, varying the different control parameters. From the results of this parameter study, three representative test cases are derived, which are then investigated and analyzed in more detail by extensive measurements.

Thanks to this approach, the most effective control parameters in the pre-stall, stall and the post-stall regime can be identified and the understanding of the underlying fluid-physical processes will be improved.

1.4. Outline

In chapter 2, a short description of the aerodynamics of slender stationary delta wings is given, with a focus on vortex systems at low-speed flow conditions and the phenomenon of vortex breakdown.

The experimental set-up for the flow measurements is described in chapter 3. It comprises a detailed depection of the wind tunnel models, their geometry and production as well as the explanation of the integrated actuator techniques. Moreover, the test conditions are described in this chapter. This part includes a short presentation of the wind tunnel facilities and the applied measurement techniques.

Subsequently, in chapter 4, the flow physics of the basic configuration are presented for different angles of attack in the pre-stall, stall and post-stall regime. The analysis contains results of the aerodynamic load, surface pressure and velocity measurements and special emphasis is given on the spectral analysis of the flow-field quantities. The knowledge of the basic flow field presented in this chapter forms the basis for the choice of the actuation parameters for active flow control.

In chapter 5, the experimental results for active pulsed blowing along the leading edge are discussed for different test cases and compared to the respective baseline cases. Thereby, the effectiveness of the actuation parameters can be evaluated. A synthesis of the results is given at the end of the chapter. The same approach is applied in chapter 6, in which the effect of the oscillating miniature leading edge flaps is studied for different angles of attack.

As conclusion, all steps outlined in this thesis and the most important results are summarized in chapter 7. This comprises the comparison of the two applied flow control methods and their results as well as concrete recommendations for the optimal actuation parameters in the three studied angle-of-attack regimes. Finally, a recommendation for the continuation of the presented work in the context of delta wing flow control is given.

2. Fundamentals of delta wing aerodynamics

On the one hand, the character of delta wing flow is affected by the geometric parameters wing sweep ϕ, aspect ratio Λ, relative wing thickness t/c_r, relative leading edge or nose radius r_{le}/l_μ and also the trailing edge geometry. On the other hand, the free-stream conditions Mach number M, Reynolds number Re, angle of attack α and sideslip angle β have an important impact on delta wing aerodynamics. A review of the influence of all these parameters is given by Lee and Ho in [46]. Besides the wing sweep, the angle of attack and the Mach number are the dominating variables that govern the flow over delta wings. Their dependencies will be shown in the following.

2.1. Classification as a function of Mach number and angle of attack

Stanbrook and Squire [75] showed for flat delta wings with high sweep that the flow is mainly governed by the angle of attack α_N and the Mach number M_N perpendicular to the leading edge, see Fig. 2.1a. These parameters are defined as follows:

$$\alpha_N = \arctan \frac{\tan \alpha}{\cos \phi} \tag{2.1}$$

$$M_N = M_\infty \cos \phi \sqrt{1 + \sin^2 \alpha \tan^2 \phi} \tag{2.2}$$

This work has been further expanded by Miller and Woods [58], who distinguished between six different regimes of attached- and separated-flow conditions for the lee-side flow of a flat delta wing, see Fig. 2.1b. These are: a separation bubble with no shock (1), a classical vortex system (2) and a vortex with shock (3) for subsonic perpendicular Mach numbers M_N and a separation bubble with shock (4), shock-induced separation (5) and a shock with separation (6) for supersonic M_N. Since the focus of this thesis is on low Mach number delta wing flows, the regime with a classical vortex system (2) is of most interest and is described in more detail in the following.

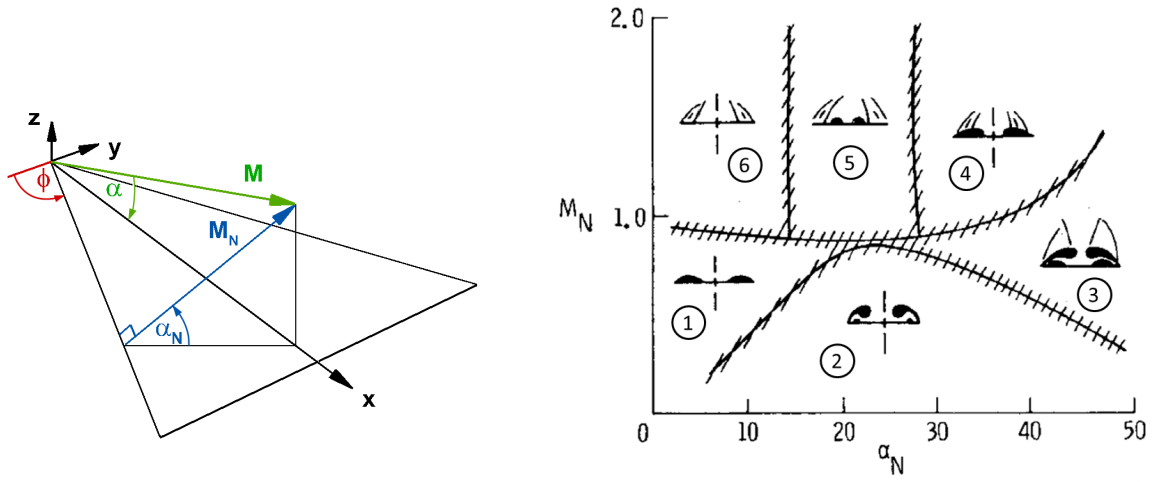

(a) Definition of α_N and M_N

(b) Classification of flow regimes [84]

Figure 2.1.: Flat delta wing leeside flow characteristics

2.2. Leading edge vortex systems

Development with respect to angle of attack and wing sweep. Fig. 2.2a shows the development of a leading edge vortex system as function of the angle of attack α and the leading edge sweep ϕ for planar wings of thickness $\delta/c_r \approx 4\%$ with high wing sweep and sharp leading edge at low Mach numbers. For wings with sharp leading edge, the flow is separating at the leading edge already at low angles of attack. This separation starts at the rear part of the wing and is propagating towards the apex as the angle of attack is increased (1).

The separated shear layer is rolling up on the wing's lee-side to form a system of two (primary) counter-rotating leading edge vortices. When the separation has reached the apex of the wing, one refers to a fully-developed leading edge vortex (2), see also Fig. 2.2b. The vortices induce additional velocities, which cause additional negative pressures on the suction side of the wing and lead to a nonlinear increase in lift compared to attached flow. Another consequence is a high maximum angle of attack.

As the shear layer is rolling up like a spiral, fluid is transported to the inside of the vortex. It is forming a rotational core, whose diameter is at the order of $(\nu x/U_\infty)^{1/2}$, see also Fig. 2.2c. In the inner part of the vortex, there is a small region of $d << (\nu x/U_\infty)^{1/2}$, where viscous effects dominate. It is called viscous core and the fluid's rotation around the vortex center can be described as a rigid-body rotation in this region. It is characterized by high gradients of the circumferential velocity components in the vortex center. The primary vortices cause positive pressure gradients on the wing surface between the suction peak under the primary vortex axis and the higher pressure at the location of the leading edge. Thereby, a pair of secondary vortices which is located under the primary leading edge vortices and further outboard than the primary vortices' cores is induced. The

sense of rotation of the secondary vortices is contrary to the one of the primary vortices (Fig. 2.2b).

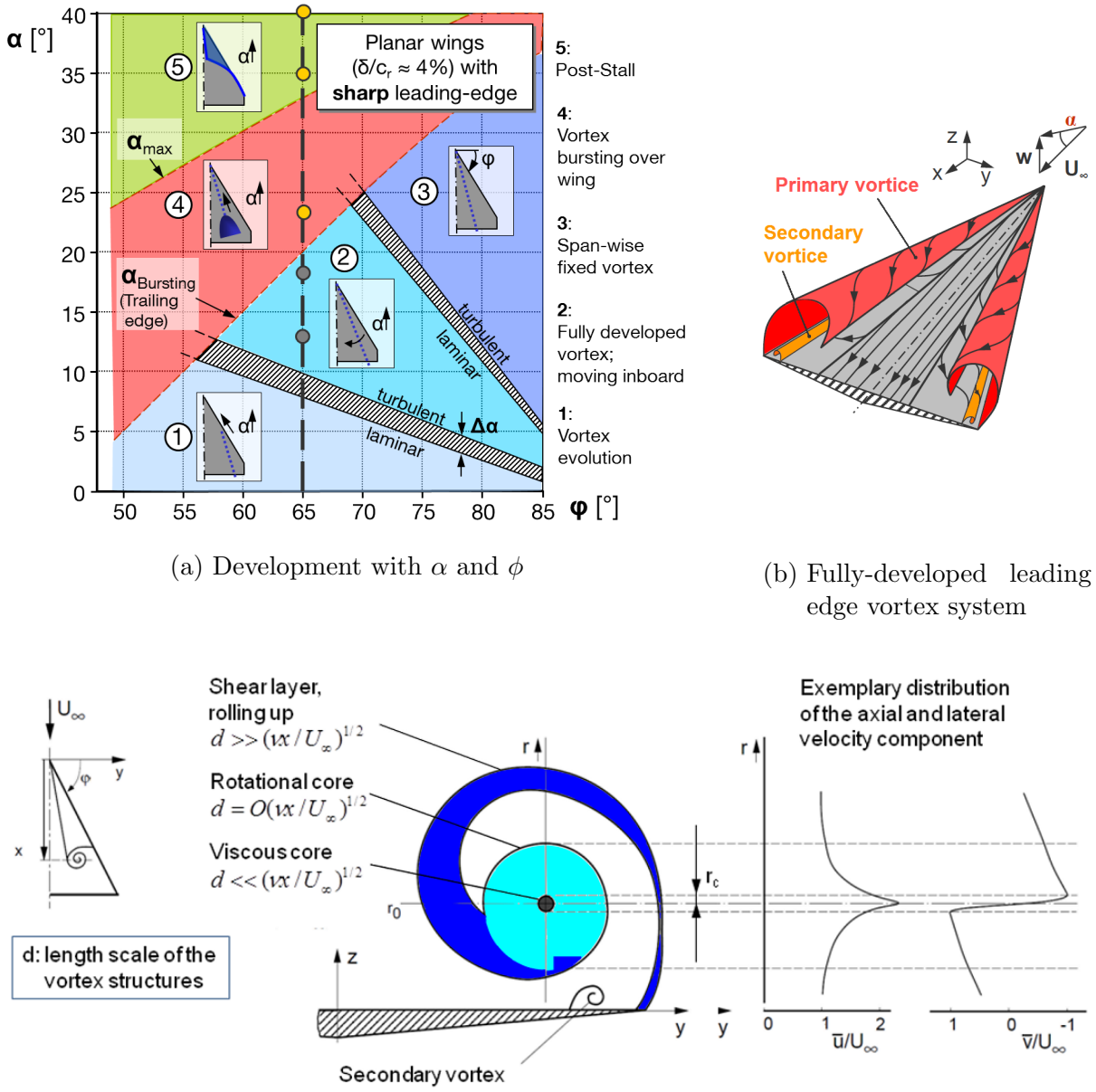

(a) Development with α and ϕ

(b) Fully-developed leading edge vortex system

(c) Primary vortex structure

Figure 2.2.: Low speed delta wing aerodynamics, cf. [76] and [7]

With increasing angle of attack and for a sufficiently high wing sweep, the cross-sectional area taken by the vortex is expanding and its center is therefore moving further inboard.

When the vortices cannot expand anymore due to the presence of their counterpart on the other wing side, the vortex is span-wise fixed (3) and its axis is moving vertically away from the wing surface.

As a result of high circumferential velocities, high radial pressure gradients as well as low total pressures at the location of the vortex axis, the vortex reaches a critical state at very high angles of attack, which is called vortex bursting (4). This phenomenon was first observed by Werlé [80] in the year 1954. The strongly increasing adverse axial pressure gradient at the trailing edge then causes the reformation of the vortex core profiles from axially accelerated to decelerated flow in conjunction with a strong radial expansion of the vortex core and the generation of large-scale fluctuations. This process starts at the wing's trailing edge and moves towards the apex as the angle of attack is further increased. When vortex bursting is approaching the apex region, the maximum angle of attack α_{max} is reached.

The regime of even higher angles of attack is called post-stall regime (5), which is characterized by a decrease in lift because the shear layer emanating from the leading edge is not rolling up to form a leading edge vortex over the wing any more, but is transported downstream without inducing additional velocities on the wing surface.

Unsteady aspects. The flow structures in the vortex system over delta wings are of an unsteady character over a broad range of scales and include non-linear interaction between each other. The main unsteady elements in delta wing flow which were reviewed by Gursul [26] are:

- Shear layer instabilities (Kelvin-Helmholtz instability (K-H)): If the Reynolds number is sufficiently high, the shear layer is separating from the leading edge and rolls up periodically to form discrete vortical substructures, which are fed into the primary vortices, see Fig. 2.3c.

- Vortex wandering: In the absence of vortex breakdown, large velocity fluctuations are observed in the vortex core upstream the breakdown location. The maximum rms swirl velocities are very high and can reach half of the time-averaged swirl velocity. The vortex core displacements correlate with the present Kelvin-Helmholtz instability [29] and are explained by a Biot-Savart induction of the small-scale vortices on the primary vortex [26].

- Helical mode instability of vortex breakdown: At Reynolds numbers and ratios of vortex-induced to free-stream velocities, that are typical for aerodynamic applications, the vortex bursting is of a spiral type. The core flow of the burst vortex is characterized by an instability type referred to as helical mode instability, see Fig. 2.3a and Fig. 2.3d.

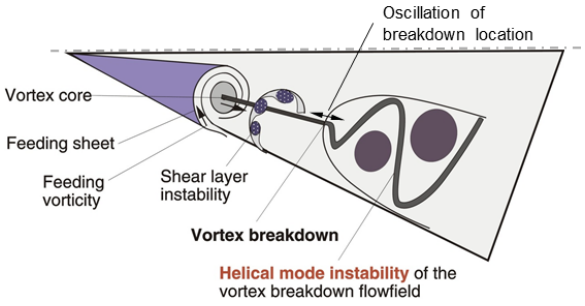

(a) Schematic vortex structure and flow instabilities [7]

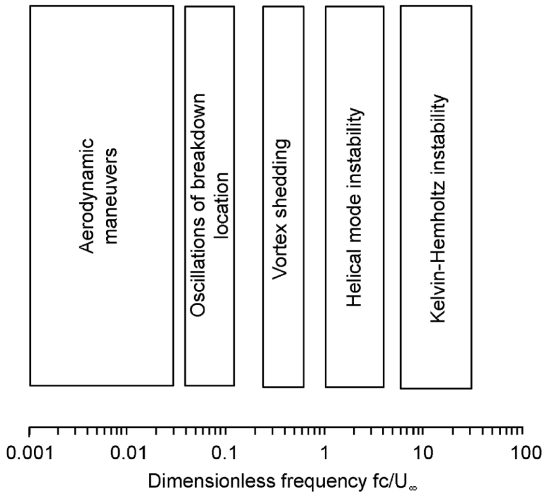

(b) Spectrum of unsteady flow phenomena [57]

(c) Flow visualization at $Re_{c_r} = 2.3 \times 10^5$ showing discrete vortical structures in the shear layer [48]

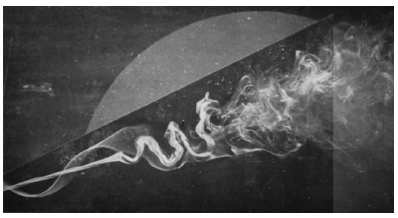

(d) Spiral vortex bursting [45]

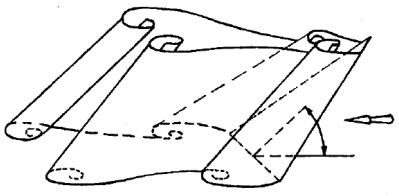

(e) Symmetric vortex shedding at very high angles of attack [68]

Figure 2.3.: Unsteady flow phenomena over delta wings

- Oscillations of the breakdown location: The vortex breakdown location shows an unsteady behavior as it is fluctuating in the direction of the vortex axis (see Fig. 2.3a). This motion is anti-symmetric on the two halves of a delta wing. The dominant frequency of the oscillation is significantly lower than that of the helical mode instability. The inversely phased oscillation of the breakdown points on the two wing sides may induce an undesired periodic rolling moment [13].

- Vortex shedding: This phenomenon is observed at very large angles of attack, when the vortex breakdown location has reached the apex of the wing. Vortices are shed periodically from the leading edge, in a symmetric mode for incidences $\alpha \approx 35°$ to $70°$, see Fig. 2.3e [67], [68], [26].

A spectrum of the main unsteady phenomena related to delta wing aerodynamics is shown in Fig. 2.3b. Further unsteady effects mentioned in this graph are related to very low frequency ranges and occur during aerodynamic maneuvers, such as pitching delta wings or wing rock motion.

2.3. Vortex breakdown

Criteria leading to vortex breakdown. The prerequisite for the formation of a stationary vortex is the balance between the convection of vorticity along the axis of the vortex core and the vorticity generation at the boundary layer of the leading edge [46]. This underlines the importance of the axial convection along the core to maintain a stationary vortex. It is initiated by the component of the free-stream in the direction parallel to the vortex axis and can be reflected either by the helix angle γ between the perpendicular and axial velocity components along the vortex axis:

$$\gamma = tan^{-1}\left[\frac{V_\theta}{V_{x(axis)}}\right], \tag{2.3}$$

or by the so-called swirl level or swirl parameter $S_{(axis)}$. It is defined as the quotient of the outer circulation Γ_o and the product of the radius of the viscous core r_c and the axial velocity in the vortex core $V_{x(axis)}$ [13]:

$$S_{(axis)} = \frac{\Gamma_o}{r_c \overline{V}_{x(axis)}}. \tag{2.4}$$

A vortex with a swirl level lower than the critical swirl level S^* is called supercritical and develops steadily and slowly until it dissipates due to viscous effects. If the swirl level reaches the critical value ($S_{(axis)} \geq S^*$), vortex breakdown will occur and a jump to a subcritical state including a transition to a different flow character will take place [13]. On the basis of different experiments, the value of the critical swirl level was estimated to be $S^* \approx 1.37$ [13]. Furthermore, vortex breakdown is observed if the local helix angle γ approaches a value of $50°$. The second important parameter for the occurrence of vortex

breakdown is represented by the adverse pressure gradient ΔC_p outside the vortex core. An increase in the adverse pressure gradient will reduce the axial convection and can therefore also lead to the unstable state of vortex bursting. Both parameters, the swirl level and the adverse pressure gradient, are strong functions of the geometric parameters sweep angle and incidence, as far as delta wings are concerned [26].

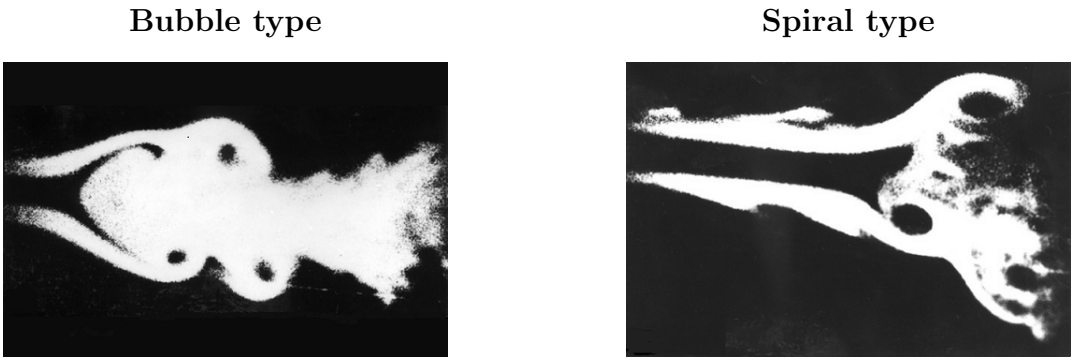

(a) Smoke visualization by Payne et al. [64], $\phi = 76°$, $\alpha = 40°$

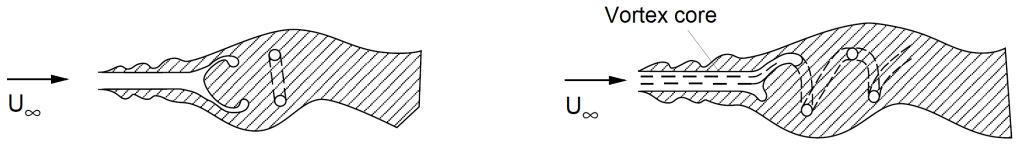

(b) Profile of the vortex core flow [6]

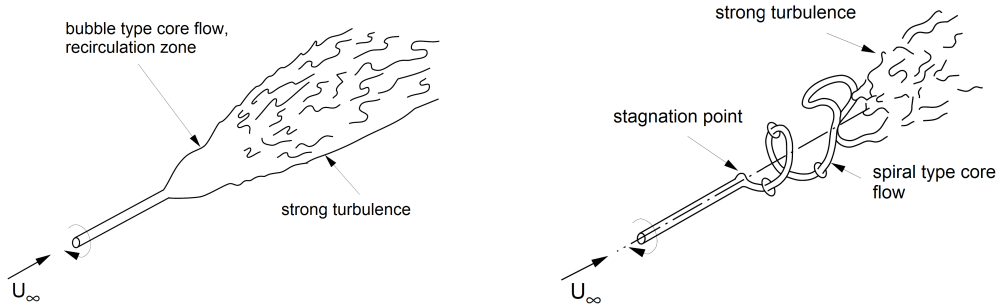

(c) Schematics of the vortex core flow development [6]

Figure 2.4.: Bubble and spiral type breakdown

Types of vortex breakdown. Although this point is discussed controversially, two main different types of vortex breakdown exist: the bubble and the spiral type of breakdown, the latter being more common in delta wing aerodynamics [26]. Examples of these two types of breakdown are shown in Fig. 2.4. In the case of the bubble type of breakdown (see Fig. 2.4a), the core flow "seems to expand around an oval-shaped recirculation

zone" [62], and then seems to be shed downstream in the form of vortex rings. In the case of spiral type breakdown shown in Fig. 2.4b, this recirculation zone is not observed. A stagnation of the axial core flow can be observed, but this time it forms a spiral which is constant for a certain number of rotations and will finally result in a flow of high turbulence [6].

Theories of explanation There are several theories trying to explain the mechanism of vortex breakdown, which can be found in literature and are summarized in different review articles [4], [47], [14], [13]. They can all be assigned to one of the four following classes:

1. the quasi-cylindrical approach (analogy to boundary layer separation),
2. the solution of the axisymmetric Navier-Stokes equations,
3. wave propagation or the concept of the critical state and
4. hydrodynamic instabilities.

3. Experimental setup

Experimental investigations have been performed to analyze the effect of two different flow control devices on the flow properties of a semi span delta wing model. In this chapter, the setup for the experimental studies is presented. First, the wind tunnel models with their geometry and the integrated actuators for flow control are described in detail. Then, the wind tunnel facilities and the applied measurement techniques are specified. These comprise force and surface pressure measurements as well as flow field measurements by hot wire anemometry and Stereo Particle Image Velocimetry.

3.1. Windtunnel models with flow control devices

Two half delta wing models, one equipped with a pulsed blowing system and the other with an oscillating leading edge flap system, were built. The properties and the setup of the basic wing geometry are described in the first part of this section. Subsequently, the setup of the two flow control devices integrated along the model's leading edge and their functionality are described.

3.1.1. Basic configuration

Both wind tunnel models are based on the same geometry and dimensions like the configuration used in the International Vortex Flow Experiment 2 (VFE-2), [9]. Within the VFE-2 project, an extensive experimental and numerical database on the flow around a generic delta wing configuration was gathered, see for example [32], [51], [16], [17]. It covers the cases of the partly developed, fully developed and the burst leading-edge vortex depending on the type of primary separation and the angle of attack. In particular, the data contains information on the development of the boundary layer and on the spectral distributions of the turbulent fluctuations in the flow.

VFE-2 geometry. The VFE-2 wing geometry is characterized by a wing sweep $\phi = 65°$, a relative thickness $t/c_r = 3.4$ % and an aspect ratio $\Lambda = 1.865$ and is based on the NASA NTF configuration (see Fig. 3.1). It has no twist or camber and consists of a flat central portion, exchangeable leading edge sections, a trailing edge and a model sting. Four different leading edge versions were studied in the VFE-2 project, one sharp leading edge with $r_{le}/l_\mu = 0$ and three versions with different nose radii $r_{le}/l_\mu = 0.0005, 0.0015$, and 0.0030.

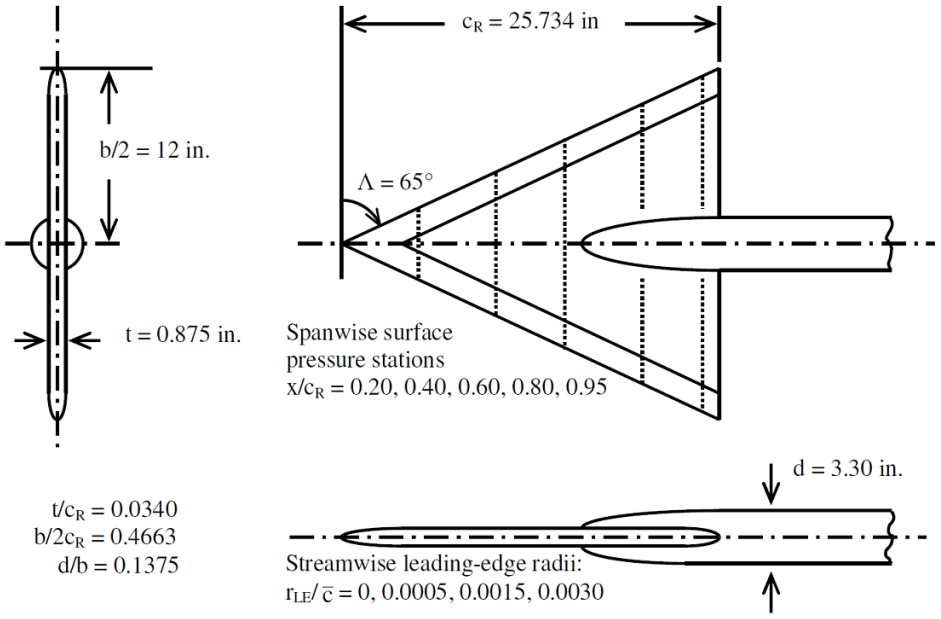

Figure 3.1.: VFE-2 configuration: NASA NTF delta wing [9]

Half models. The wind tunnel models studied in this work were built as half delta wing models. This had the advantage that only one leading edge per flow control method had to be built and to be equipped with the actuators. Furthermore, the blockage ratio in the wind tunnels is reduced due to the smaller wing surface at the same root chord. One disadvantage of the half wing models is that interactions of the two primary vortices, which normally appear on a full delta wing configuration, cannot be investigated. Comparative measurements were carried out to ensure that the measurement results from the half wing models are comparable to those of a full wing configuration (see chapters 4.1 and 4.2).

Both half wing models have a root chord $c_r = 0.98\ m$, a wing semi span $s = 0.457\ m$ and a thickness $t = 0.033\ m$ (see Table 3.1). The leading edge contour is sharp ($r_{le}/l_\mu = 0$). The models consist of two flat aluminum plates of 4 mm thickness in the central portion, a leading edge made of glass fiber composites, as well as a trailing edge made of plastics. The leading edges were produced in a counterpart mould construction. The trailing edge is milled from the solid. Between the two flat plates, a cross joint is screwed to determine the distance between the two plates and to structurally stabilize the model, see Fig. 3.3b and Fig. 3.8b. The vertical part of the cross juts out of the bottom of the model and is used for the connection to the underfloor balance in the wind tunnel. Each half wing model is equipped with a péniche of 55 mm height (Fig. 3.2) to elevate it out of the floor boundary layer, minimizing the corresponding interference effects. The technical devices for flow manipulation are integrated in the leading-edges. Their description is to follow in the next two subsections.

Table 3.1.: Main dimensions of the half delta wing models

Parameter	Abbreviation	Value
wing sweep	ϕ	65°
root chord	c_r	0.98 m
mean aerodynamic chord	l_μ	0.653 m
half wing span	s	0.457 m
wing thickness	t	0.033 m
nose radius	r_{le}/l_μ	0 (sharp leading edge)
wing area	F	0.448 m^2
wing aspect ratio	λ	1.865

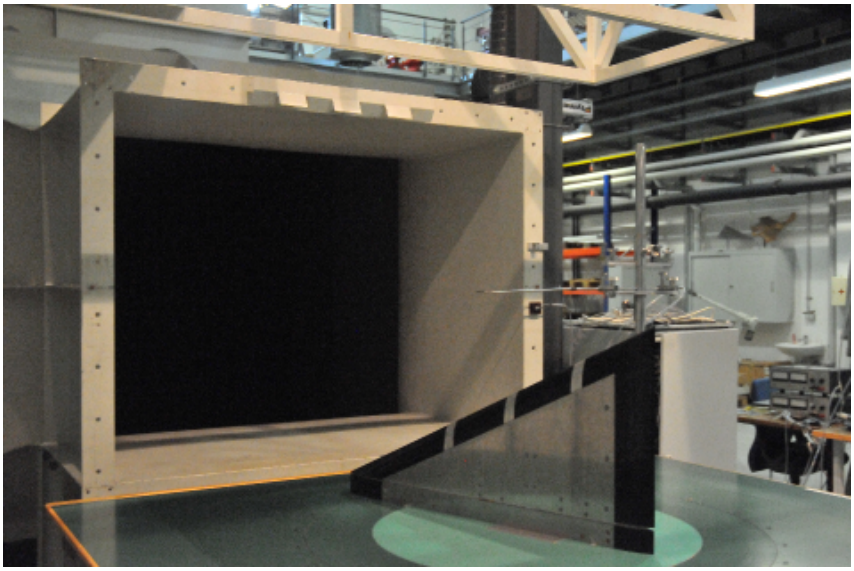

Figure 3.2.: Half delta wing model in Wind Tunnel B of Technische Universität München

3.1.2. Pulsed blowing system

The wind tunnel model for pulsed blowing is shown in the form of a technical drawing and a photo of the model's interior in Fig. 3.3. The installed blowing system consists of three leading-edge slot sections which comprise a total of twelve slot pairs regularly distributed in sections at chord-wise positions $x/c_r = 0.2 - 0.4$, $x/c_r = 0.4 - 0.6$ and $x/c_r = 0.6 - 0.8$ along the leading edge. The slot size is $t = 2\ mm \times h = 10\ mm$. The

slots are arranged oblique, at an angle of 45° to the leading edge, and each slot pair forms an orthogonal angle (see Fig. 3.3a, detail A). Pulsed jets are brought into the flow on the suction side of the delta wing through the slots. The pulsed jets are generated by solenoid valves, that are pressurized by the institute's pressure line.

In the following, the production and assembly of the leading edge, the components of the integrated actuator system and the profile of the pulsed jets are described in more detail.

3.1.2.1. Assembly of the leading edge

Both leading edges were fabricated in a composite mold construction and consist of one upper and one lower laminated shell. The shells are agglutinated at the sharp outer edge. The leading edges are laminated with a black-colored face sheet of epoxy resin, one thin layer of glass fabric (25 g/m^2) and three layers of heavy glass fabric (390 g/m^2). Each layer is soaked by the black epoxy resin for a better opacity. The wall thickness is approximately 2 mm. At chord-wise positions $x/c_r = 0.2$, 0.4, 0.6, 0.8 and 0.95, 30 mm wide block-outs are integrated on the upper side of the leading edges. They are designated for the insertion of pressure measurement insets. The leading edges are connected to the two inner flat plates of the wing models via fixing ridges.

The 12 slot pairs and the corresponding pre-chambers were cast by a stamp (Fig. 3.4a). On the inner side, the chambers are bounded by aluminum plates. Fig. 3.4b shows a section of four magnetic valves, which are connected to four pre-chambers in the leading edge. The finished design depicted in Fig. 3.4c features four fixing ridges. Three of them were integrated during the lamination process of the leading edge and the fourth, made of green plastics, was sticked to the leading edge in hindsight.

3.1.2.2. Actuator system

The compressed-air for the generation of the jets is provided by the Institute's pressure line supply. In total, three pressure supplies are used. The compressed air is regulated by three parallel pressure reducers, see Fig. 3.5. A connected tube system branches out from the three pressure reducers to 12 tubes which merge into 12 electromagnetic valves. The valves generate the jet pulse and can switch between an opened and a closed state at a frequency of up to 1000 Hz. This pulse frequency is controlled by a LabVIEW programme sending a digital bit pattern from a controller card (DT9836) to the valves' controller modules. Each of the six controller modules is transferring the control signal to two respective valves. The pulse frequency can be controlled and varied for all 12 valves. Via synchronization of the 12 channels, the pulse phasing between the different valves can be adjusted. After the valves, the pulse jets are led into 12 pre-chambers redirecting the flow to the slot pairs on the upper side of the leading edge, where the pulsed flow exits the model on the suction side of the wing. The cables and the tubes are integrated inside the wing model and are led into the model through two holes in the upper plate of the wind tunnel balance and the péniche, see Fig. 3.3b.

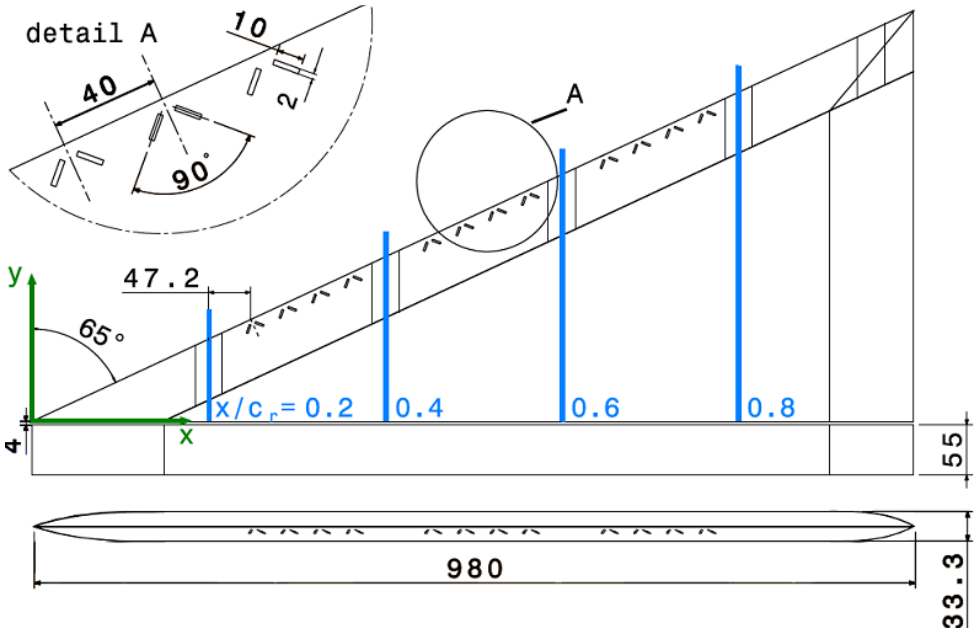

(a) Technical drawing

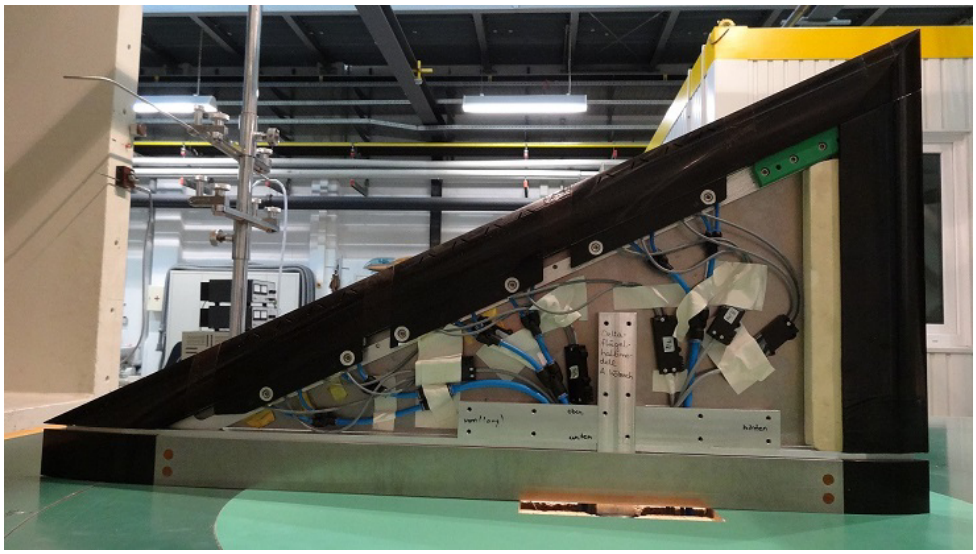

(b) Interior of the wing

Figure 3.3.: Delta wing model for pulsed blowing

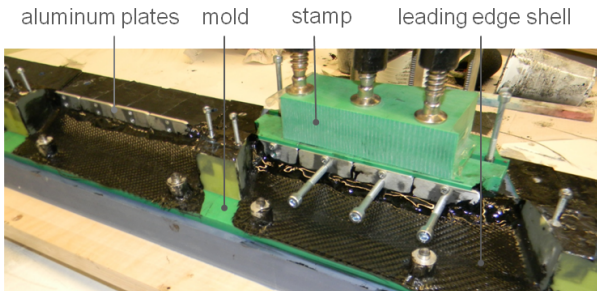

(a) Lamination of the leading edge shell and cast of the pre-chambers

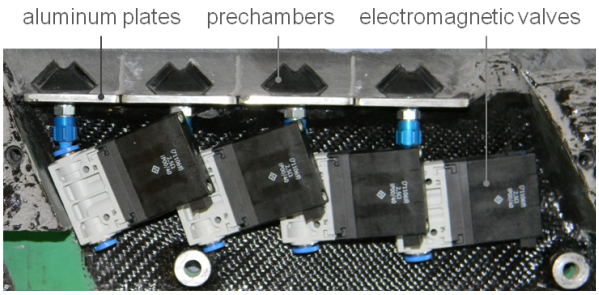

(b) Connection of the magnetic valves to the pre-chambers

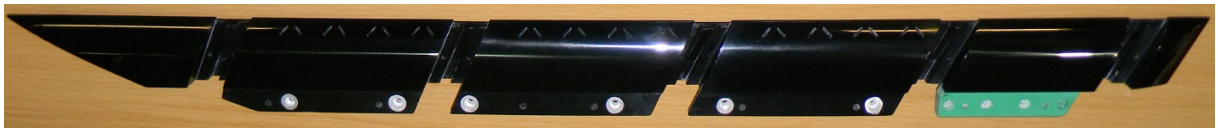

(c) Top view

Figure 3.4.: Leading edge for pulsed blowing [15]

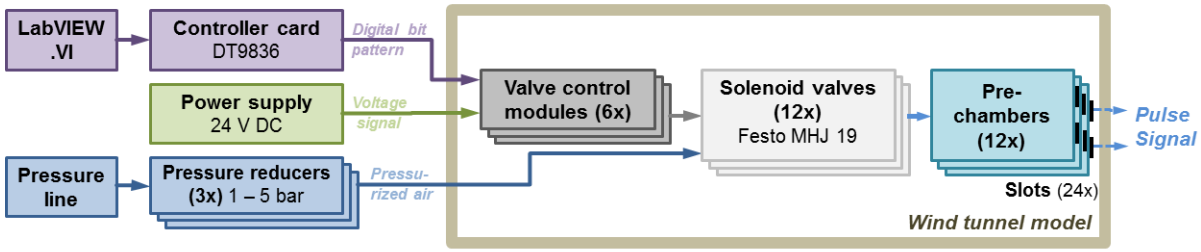

Figure 3.5.: Generation of the pulsed blowing signal

3.1.2.3. Pulsed blowing profile

The jet velocity signal is of square form (see Fig. 3.7a) and the direction of the jet flow is approximately orthogonal to the wing surface. The signal is characterized by the pulse frequency f_{pulse}, which corresponds to the reciprocal of the cycle duration $f_{pulse} = 1/T$, the jet velocity during the pulse period U_{jet}, and the duty cycle DC corresponding to the time ratio of the opened state of the valve to the cycle duration.

The parameters f_{pulse} and DC are set in the LabVIEW program and converted into a digital bit pattern that is sent to the magnetic valves. The maximum inaccuracy of the pulse frequency is less than 5 %. Additionally, the phasing of the pulse signals can be set in the program and varied for the different slot pairs. The jet velocity during the pulse phase can only be manipulated indirectly. It mainly depends on the total pressure in front of the valves (in a closed state). This pressure is controlled by the pressure reducers. As

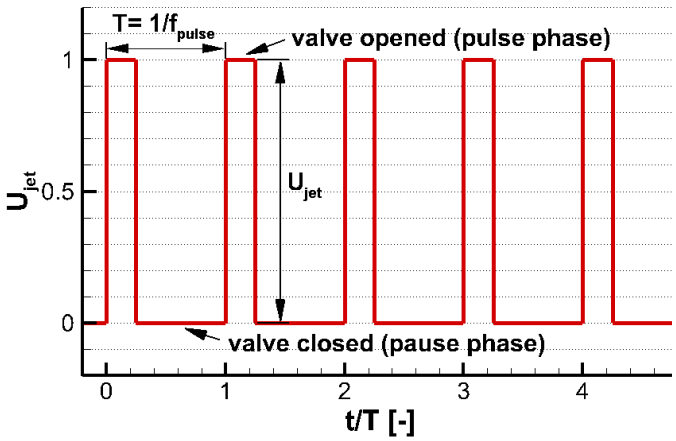

Figure 3.6.: Idealized pulse signal and terminology

the three blowing sections have individual pressure supplies and pressure reducers, the jet velocity can be varied individually for each section. Nevertheless, the jet velocity is also a function of the pulse frequency and the duty cycle.

The time series in Fig. 3.7b and Fig. 3.7c show two examples of the jet velocities measured by hot-wire anemometry 6 mm vertically above the slot in the jet's core region at pulse frequencies $f_{pulse} = 8\ Hz$ and $52\ Hz$ and a duty cycle of $DC = 25\ \%$ (see Fig. 3.7a). The average value of the velocity flank is $U_{jet} \approx 55\ m/s$. The pulse frequency can be verified by a spectral analysis of the jet velocity signal (see 3.2.3.1), which confirms the chosen frequencies (see Fig. 3.7d for $f_{pulse} = 52\ Hz$).

A calibration is conducted to determine the average jet velocity during the pulse phase for different combinations of the pressure p_{valve}, the pulse frequency f_{pulse} and the duty cycle DC. Fig. 3.7e shows the jet velocity U_{jet} measured for different pulse frequencies and pressures p_{valve} at a duty cycle $DC = 25\%$.

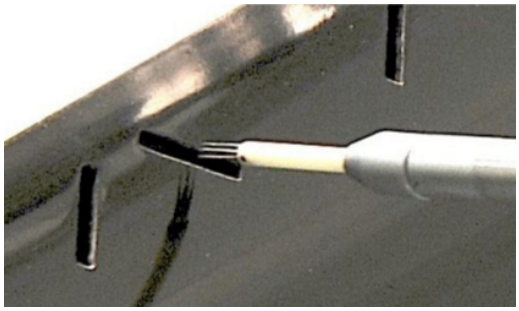

(a) Measurement of the pulsed blowing signal by hot-wire anemometry

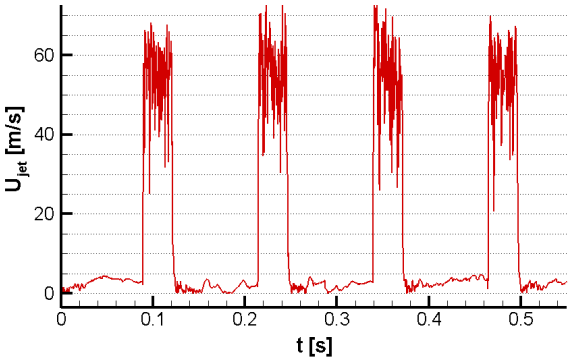

(b) Time series of jet velocity U_{jet}, 6 mm above the slot for $f_{pulse} = 8\ Hz$, $DC = 25\%$, $p_{valve} = 4\ bar$

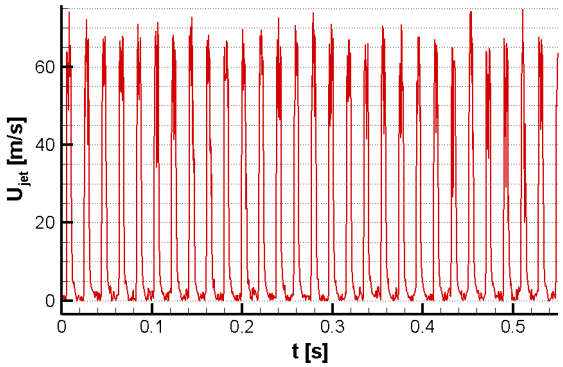

(c) Time series of jet velocity U_{jet}, 6 mm above the slot for $f_{pulse} = 52\ Hz$, $DC = 25\%$, $p_{valve} = 4\ bar$

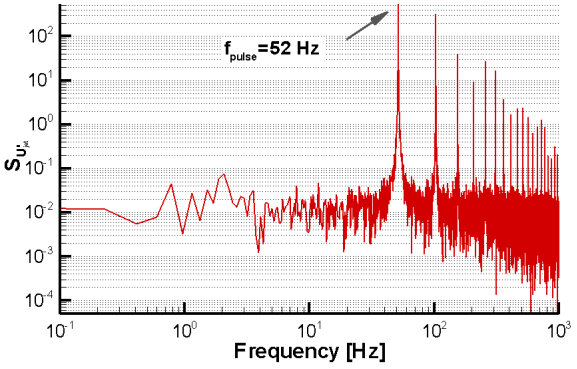

(d) Power spectral density of jet velocity for $f_{pulse} = 52\ Hz$, $DC = 25\%$, $p_{valve} = 4\ bar$

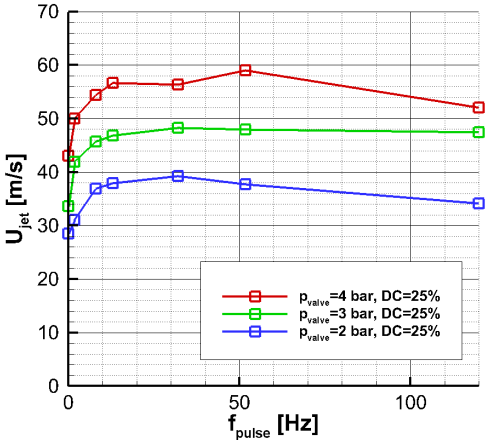

(e) Mean jet velocity during the pulse phase

Figure 3.7.: Pulsed blowing signal [38]

3.1.3. Oscillating leading-edge flap system

The second wind tunnel model is equipped with two flap groups consisting of three miniature leading-edge flaps each. They are located at chord-wise positions between $x/c_r = 0.2 - 0.4$ and $x/c_r = 0.6 - 0.8$, respectively (Fig. 3.8a). The external geometry and the general set-up of this model corresponds to the configuration with integrated pulsed blowing devices. The flaps are 30 mm wide and 15 mm long and their contour corresponds to the contour of the leading edge. Mechanically powered by linear motors, they can execute harmonic movements at different frequencies and amplitudes [71].

In analogy to the last subsection, the assembly of the leading edge as well as the actuator technique and the generated flap movement signal are presented in the following paragraphs.

3.1.3.1. Assembly of the leading edge

Leading edge. A CAD model of the leading edge with miniature flaps is shown in Fig. 3.9a. The laminated leading edge shell is fixed to the inner flat plates of the delta wing model by three metal ridges (see also Fig. 3.9b). Orthogonally to the sharp edge, the leading edge has six cut-outs for the insertion of the miniature flaps, see detail A. At the inner side behind the cut-outs, supporting points for the axle bearing of the miniature flaps are provided. The miniature linear motors are fixed to the leading edge by brackets.

Miniature flaps. The demands on the miniature flaps are very high: they have to reflect the outer geometry of the VFE-2 leading edge geometry with a high surface quality, they should have a low weight to minimize the moment of inertia around the rotary axis, and be of sufficient rigidity. To meet all these requirements, the miniature flaps are fabricated in a hand lay-up process. The flap (see Fig. 3.10a) is made in a shell construction with a $\pm 45°$ ply of carbon fiber reinforced plastic (TeXtreme®) as outer layer (1) and a Rohacell® support material (4). A carbon roving (3) is included in the nose to stabilize the leading edge. The side wall ribs (2) are made of glass fiber reinforced plastics, which also provide bearing positions for two pins: one at the center plane of the flap for its bearing in the leading edge and the other for the connection to the linear motor.

Flap kinematics. The components of the flap kinematics are shown in Fig. 3.11. A swivel head (2) is screwed to the shaft of the linear motor (1). It is connected to the leading edge flap via an adapter (3). The flap (5) itself is pivot-mounted on a pin (4) 15 mm behind the leading edge in the middle plane of the wing. This is the rotary axis of the flap.

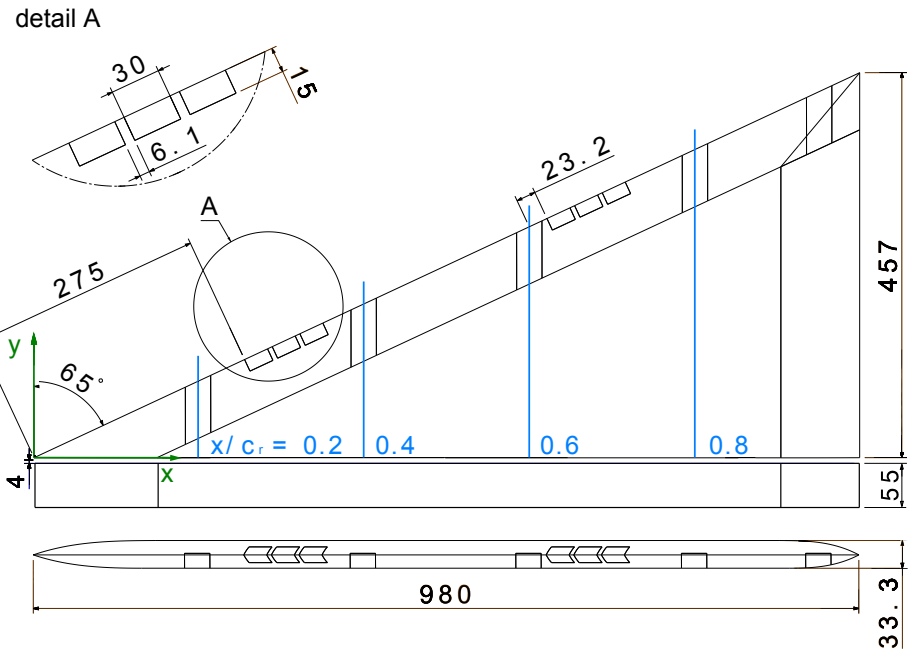

(a) Technical drawing

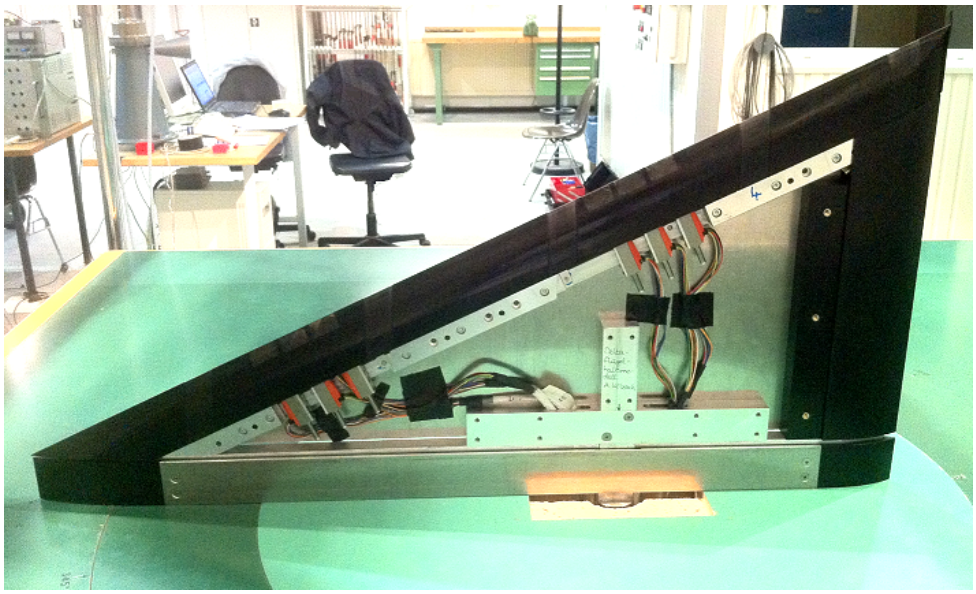

(b) Interior of the wing [63]

Figure 3.8.: Delta wing model with miniature flaps

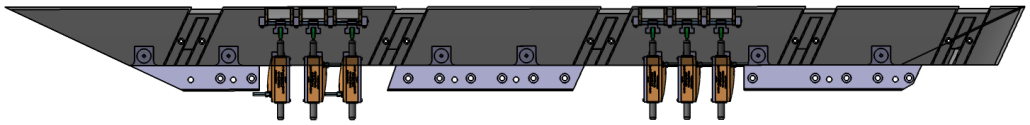

(a) CAD model

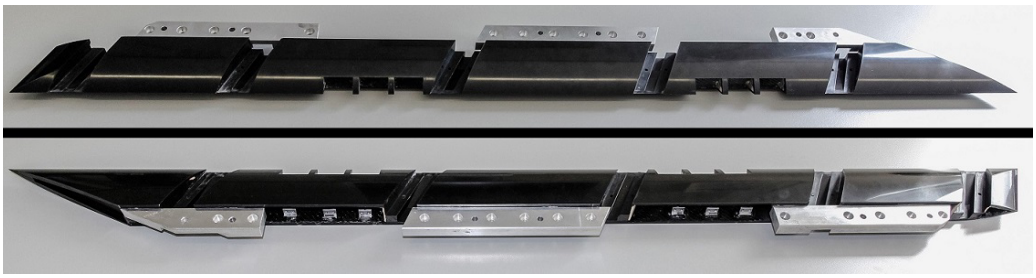

(b) Front and rear view of the laminated leading edge

Figure 3.9.: Leading edge with miniature flaps [82]

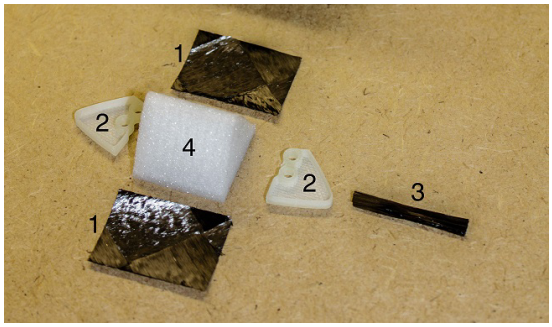

(a) Parts for the hand lay-up

(b) Assembly

Figure 3.10.: Miniature leading edge flaps [82]

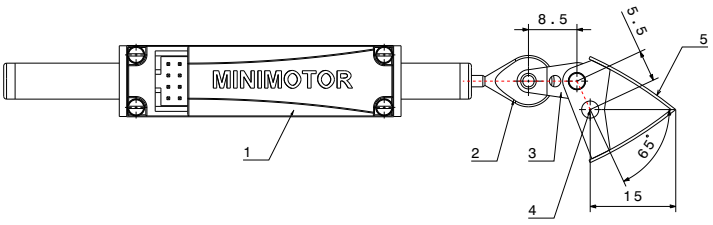

Figure 3.11.: Kinematics of the flap element cf. [35]

3.1.3.2. Actuator system

The flap actuation is realized with six digital PID controllers (SimplIQ by Elmo MC), which drive the leading edge flaps via linear motors of type Faulhaber QUICKSHAFT® LM1247, see Fig. 3.12. The flaps can execute oscillatory motions at a certain amplitude and frequency. The synchronized actuation of the flaps is realized via integration of the Elmo control units to a CAN network system. Thereby, the SimplIQ control units act as CAN slaves, which are linearly arranged in a CAN Bus that is mastered by a superior controller, a Gold Maestro by Elmo MC.

While the kinematic elements and the linear motors are integrated in the half delta wing model, the CAN system including the SimplIQ controllers, the Gold Maestro and their power supplies is positioned outside of the wind tunnel test section. The power supply and the control signal for the linear motors are provided by cables connecting the SimplIQ controllers to the motors. The cables are led into the model through two holes in the upper plate of the wind tunnel balance and the péniche, see Fig. 3.8b.

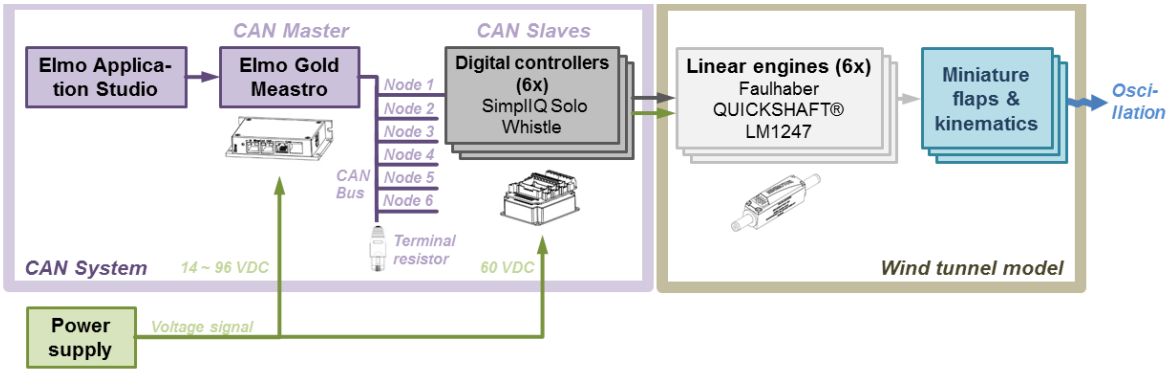

Figure 3.12.: Generation of the oscillating flap signal

The CAN system is controlled by a software called Elmo Application Studio (EAS). Here, the master and the slaves of the CAN system are liaised and the control parameters of the SimplIQ controllers are set.

3.1.3.3. Oscillatory flap movement

The flap movement generated by the CAN System and the linear motors is an approximately harmonic oscillation about the center plane of the wing. The movement is generated by a Position/Velocity/Time (PVT) table, which prescribes the required position of the linear motor's shaft. The linear motors oscillate according to the given amplitude in a certain time interval. An almost harmonic movement is created by the inertance of the shaft and the connected flap kinematics. All flaps carry out synchronized movements and both the frequency and the amplitude of the oscillatory flap motion can be adjusted.

To realize the flap movement with a certain combination of frequency and amplitude, the appropriate PVT table has to be predetermined iteratively. This is due to the fact, that the current positions of the flap deviate from the desired positions listed in the PVT table. This is especially the case for higher flap frequencies. Within the Elmo Studio software, the shaft position can be measured and therefore the amplitude and the frequency of a flap oscillation can be derived.

Fig. 3.13 shows two examples of flap motion profiles for exemplary target frequencies $f_{flap} = 12\ Hz$ and $f_{flap} = 48\ Hz$ as well as a Fast Fourier transformation (FFT) for the latter signal. The quality of the harmonic position profile decays with higher frequencies. Additionally, the resolution of the recorded signal is limited to 3 msec. The maximum inaccuracy of the adjusted flap frequencies is less than 5 %.

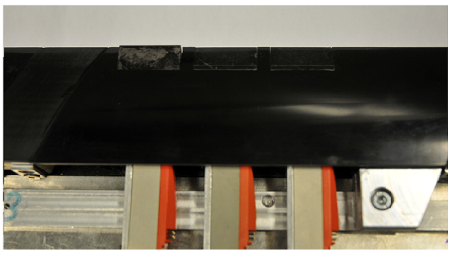

(a) Miniature leading edge flaps driven by linear motors

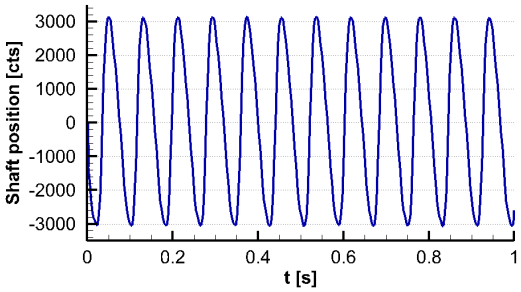

(b) Measured time series of shaft position for $f_{flap} = 12\ Hz$, $amplitude = 3000\ cts$

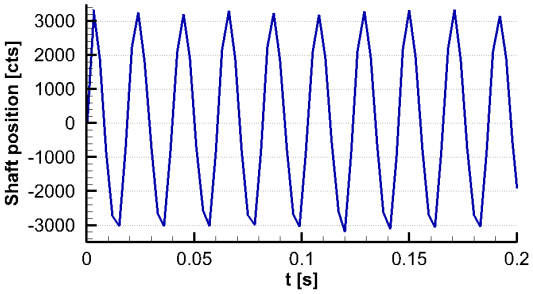

(c) Measured time series of shaft position for $f_{flap} = 48\ Hz$, $amplitude = 3000\ cts$

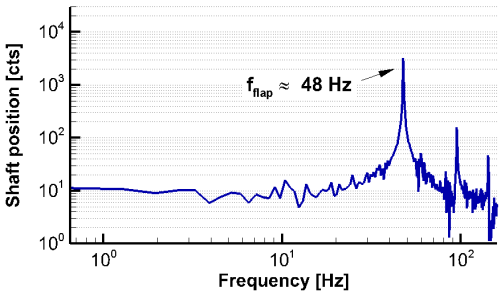

(d) Fast Fourier Transformation (FFT) of shaft position signal for $f_{flap} = 48\ Hz$ and $amplitude = 3000\ cts$

Figure 3.13.: Oscillating flap signal

In simplified terms, the motion of the flap tip can be modeled by a harmonic oscillation at the angular frequency ω, that describes the tangential deflection y_θ on a ring segment with the radius $r = 15\ mm$:

$$y_\theta = \hat{y}_\theta \, sin(\omega t + \delta) \tag{3.1}$$

with $\hat{y}_\theta = 2\pi r\hat{\delta}$ and $\omega = 2\pi f_{flap}$, $\hat{\delta}$ being the amplitude of the flap deflection angle. The speed of the flap tip is then described by

$$v_\theta = \omega \, \hat{y}_\theta \, cos(\omega t + \phi) \tag{3.2}$$

and the maximum speed of the flap tip reached at the zero-crossing is

$$\hat{v}_\theta = \omega \, \hat{y}_\theta = 2\pi f_{flap} \, \hat{y}_\theta. \tag{3.3}$$

With $\hat{y}_\theta = 4.71 \; mm$ for $\hat{\delta} = 18°$, the maximum flap tip speed is 0.355 m/s for $f_{flap} = 12 \; Hz$ and 1.42 m/s for $f_{flap} = 48 \; Hz$.

The flap oscillation causes a change in the effective or normal angle of attack α_N. In comparison to Equation 2.1, it results from

$$\alpha_N = arctan\frac{tan\alpha}{cos\phi} + \delta. \tag{3.4}$$

Therefore, the normal angle of attack is reduced when the flap is deflected downwards (i.e. negative flap deflection angles) and increased if the flap is deflected upwards (positive flap deflection angles).

3.2. Test conditions and measurement techniques

The experiments were conducted in the Göttingen type low-speed wind tunnel facilities of the Institute of Aerodynamics and Fluid Mechanics at Technische Universität München. Aerodynamic load, pressure and hot-wire measurements were undertaken at Wind Tunnel B (see Fig. 3.15, open test section with dimensions $1.2\ m \times 1.55\ m \times 2.8\ m$, $Tu_x \leq 0.4\%$, maximum fan power $P_{fan} = 130\ kW$, contraction ratio 5:1). The Stereo PIV measurements were carried out at Wind Tunnel A (see Fig. 3.14, open test section with dimensions $1.8\ m \times 2.4\ m \times 4.8\ m$, $Tu_x \leq 0.4\%$, maximum fan power $P_{fan} = 420\ kW$, contraction ratio 7:1).

(a) External view

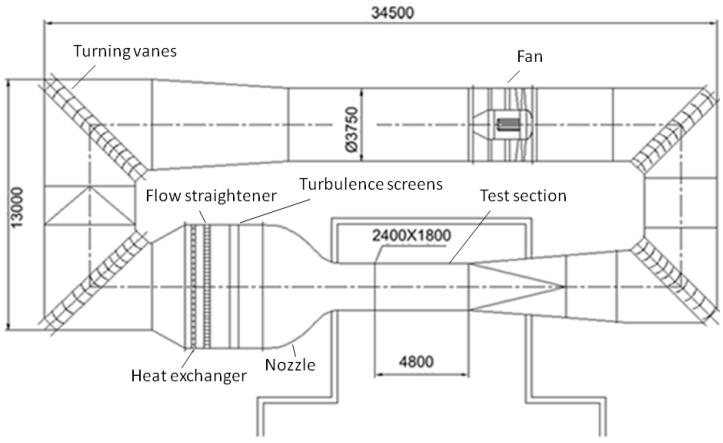

(b) Cross section

Figure 3.14.: Windtunnel A at Technische Universität München [3]

Two different free stream velocities have been investigated, namely $U_\infty = 12\ m/s$ and $24\ m/s$, corresponding to the Reynolds numbers based on the mean aerodynamic chord of the model $Re_{mac} \approx 5 \times 10^5$ and $Re_{mac} \approx 1 \times 10^6$, respectively. The maximum blockage ratio was less than 5%. The test section flow was carefully inspected and calibrated to

(a) External view [85]

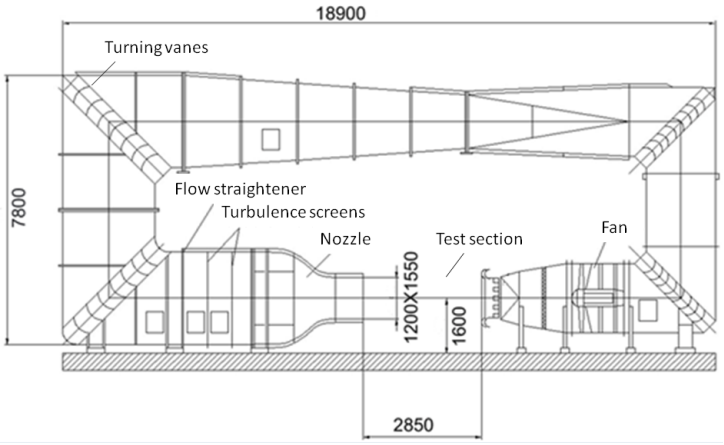

(b) Cross section [3]

Figure 3.15.: Windtunnel B at Technische Universität München

guarantee a turbulence level less than 0.4% along the relevant test section part. Uncertainties in the spatial and temporal mean velocity distributions were less than 0.067%. The different measurement techniques which were used to record the properties of the delta wing flow are presented in the following.

3.2.1. Force and moment measurements

The aerodynamic loads (forces and moments) are recorded in static load measurements by means of an external six-component under-floor balance, which is located below the test section. The measurement time was $t = 10s$. All results are averaged over the measurement time. The balance precision is ± 0.0022 for the lift coefficient C_L, ± 0.0011 for the drag coefficient C_D, ± 0.0005 for the yawing moment C_m and ± 0.0007 for the

rolling and yawing moment C_l and C_n (defined in Eqs. 3.5 to 3.9).

The loads are measured for the baseline case without actuation and for the flow cases with active blowing and active leading-edge flaps. Therefore, the effect of the active flow control devices compared to the baseline case can be quantified. The applied wing-fixed coordinate system and the orientation of the aerodynamic forces and moments is shown in Fig. 3.16. The moments are referred to the point $x = 2/3c_r$, $y = 0$, $z = 0$.

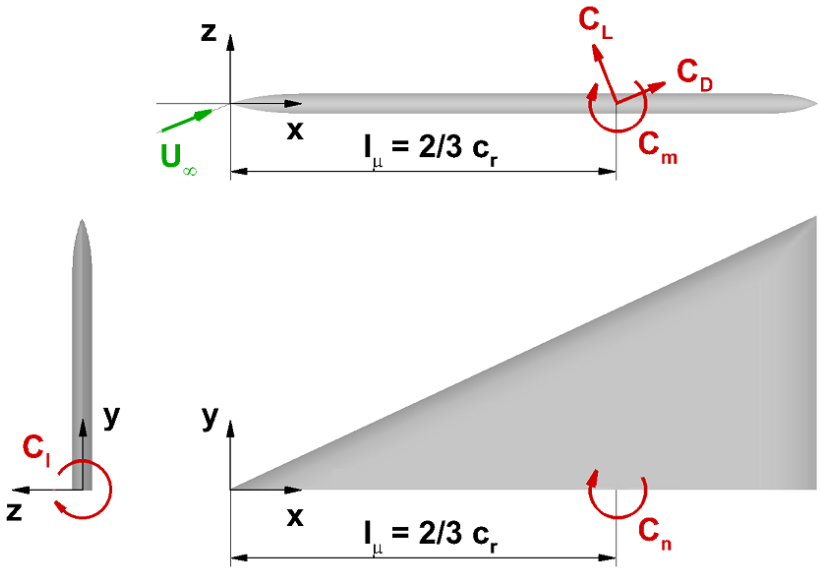

Figure 3.16.: Wing-fixed coordinate system and orientation of the aerodynamic loads

The lift and drag force coefficients C_L and C_D for the half wing model are defined as follows:

$$C_L = \frac{F_z cos\alpha - F_x sin\alpha}{q_\infty S/2}, \tag{3.5}$$

$$C_D = \frac{F_z sin\alpha + F_x cos\alpha}{q_\infty S/2}. \tag{3.6}$$

The definition of the rolling moment coefficient C_l, the pitching moment coefficient C_m and the yawing moment coefficient C_n is as follows:

$$C_l = -\frac{2M_x}{q_\infty S s}, \tag{3.7}$$

$$C_m = \frac{2M_y}{q_\infty S l_\mu}, \tag{3.8}$$

$$C_n = -\frac{2M_z}{q_\infty S s}. \tag{3.9}$$

3.2.2. Surface pressure measurements

By applying steady and unsteady surface pressure measurements, the mean pressure distribution C_p and the pressure fluctuations $C_{p,rms}$ are determined at three cross-sections $x/c_r = 0.4$, $x/c_r = 0.6$ and $x/c_r = 0.8$ of the wing. The measurement positions and the numbering of the sensors are listed in Tables A.1 and A.2. The accuracy of the pressure measurement is $\Delta C_p = \pm 0.007$ for the pressure coefficient with respect to the resulting flow.

3.2.2.1. Steady pressure measurements

The steady pressure is measured at 46 positions on the upper surface and 3 positions on the lower surface of the wing, using a Scanivalve-system with a sampling rate of 20 Hz and a measurement time of 30 s. A number of 600 samples is recorded for each station and averaged over the whole measurement time.

Table 3.2.: Parameters of steady surface pressure measurements

Parameter	Abbreviation	Value
sampling rate	f_{sample}	20 Hz
number of samples	n	600

3.2.2.2. Unsteady pressure measurements

The unsteady pressure measurements are performed using 29 piezoresistive sensors of type Kulite XCQ-107-093-5D with a sampling rate of 3000 Hz and a measurement time of 10 s. The cut-off frequency of the applied analog Butterworth low-pass filter is 1000 Hz.

Table 3.3.: Parameters of unsteady surface pressure measurements

Parameter	Abbreviation	Value
sampling rate	f_{sample}	3000 Hz
number of samples	n	30000
cut-off frequency Butterworth filter	f_c	1000 Hz

On the basis of the recorded time series, the mean pressure coefficients are determined as follows:

$$\overline{c_{p,i}(\boldsymbol{x})} = \frac{1}{n} \sum_{k=1}^{n=30000} c_{p,i}(\boldsymbol{x}). \tag{3.10}$$

Analogously to the velocity fluctuations, the fluctuations of the pressure coefficients are defined by

$$c_{p,rms}(\boldsymbol{x}) = \sqrt{\overline{C_p'^{\,2}(\boldsymbol{x})}}. \tag{3.11}$$

For the spectral analysis, the coefficient $C_p(\boldsymbol{x}, t)$ which is on hand in form of discrete time functions, is transferred to the frequency domain by a Fourier transformation:

$$X_{C_p}(\boldsymbol{x}, \omega) = \lim_{T\to\infty} \int_0^T C_p(\boldsymbol{x}, t) e^{-i\omega t} dt. \tag{3.12}$$

The power spectral density is then derived from the multiplication of the Fourier transform by its complex conjugate,

$$S_{C_p}(\boldsymbol{x}, \omega) = \lim_{T\to\infty} \frac{2}{T} X^*_{C_p}(\boldsymbol{x}, \omega) X^T_{C_p}(\boldsymbol{x}, \omega). \tag{3.13}$$

The normalized power spectral density of the pressure coefficient is defined by

$$S^N_{C_p}(\boldsymbol{x}, k) = \frac{U_\infty}{c_r} S_{C_p}(\boldsymbol{x}, k), \tag{3.14}$$

it can be expressed as a function of the reduced frequency k

$$k = \frac{f c_r}{U_\infty}. \tag{3.15}$$

3.2.3. Velocity measurements

The velocity measurements were carried out at up to four different stations located at chordwise positions $x/c_r = 0.2$, 0.4, 0.6 and 0.8. The measurement points span planes which are aligned orthogonally to the wing's horizontal symmetry plane. Fig. 3.17 shows the four different measurement planes on the upper side of the wing.

3.2.3.1. Hot-wire anemometry

The hot-wire anemometry (HWA) measurements were carried out with crosswire-type miniature probes of type Dantec 55P61 (see Fig. 3.18a) on the basis of constant temperature anemometry (CTA) and a look-up table technique, as described in [6]. They include a temperature correction, which normalizes all results to a reference temperature $T_{ref} = 20\ ^\circ C$. The calibration of the probes is carried out for an opening angle of $\alpha = \pm 45^\circ$ and axial velocities from $U_\infty \approx 4\ m/s$ to $U_\infty \approx 65\ m/s$. Fig. 3.18b shows an

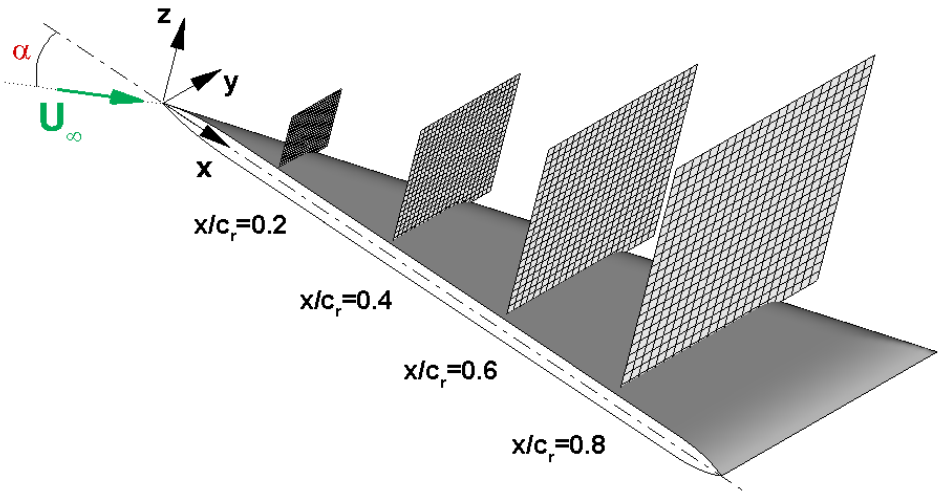

Figure 3.17.: Velocity measurement planes

example for a calibration of a crosswire-type probe, where two temperature-corrected wire voltages are correlated to each combination of angle of attack and free-stream velocity.

A sampling rate $f_s = 3000Hz$ is used for the measurements. The bridge output voltages were filtered by an analogue low-pass filter at a frequency $f_{lp} = 1400Hz$ before digitization. For each grid point, a time series of $N = 19200$ samples corresponding to a sampling time of 6.4 s is recorded and averaged to obtain the mean velocity values. The grid resolution of the measurement planes is $\Delta = s_l/20$ in the spanwise and vertical directions. The measured and temperature-corrected voltages are then combined with the calibration data in the look-up table and a time series for the velocity vector is calculated.

Within a single measurement, the axial and one cross-flow velocity component can be measured. To gain the third velocity component, the measurement has to be repeated with the probe being axially rotated by 90°. The mean velocity components u, v and w can be obtained from the measured time series of the velocity components by time averaging:

$$\overline{u_i}(\boldsymbol{x}) = \frac{1}{n} \sum_{k=1}^{n=19200} u_{i,k}(\boldsymbol{x}). \tag{3.16}$$

In order to analyze the unsteady flow phenomena, the fluctuations of the velocity components u_{rms}, v_{rms} and w_{rms} are calculated and normalized by the freestream velocity

$$\frac{u_{i,rms}(\boldsymbol{x})}{U_\infty} = \frac{\sqrt{\overline{u_i'^2}(\boldsymbol{x})}}{U_\infty}. \tag{3.17}$$

(a) Dantec probe 55P61

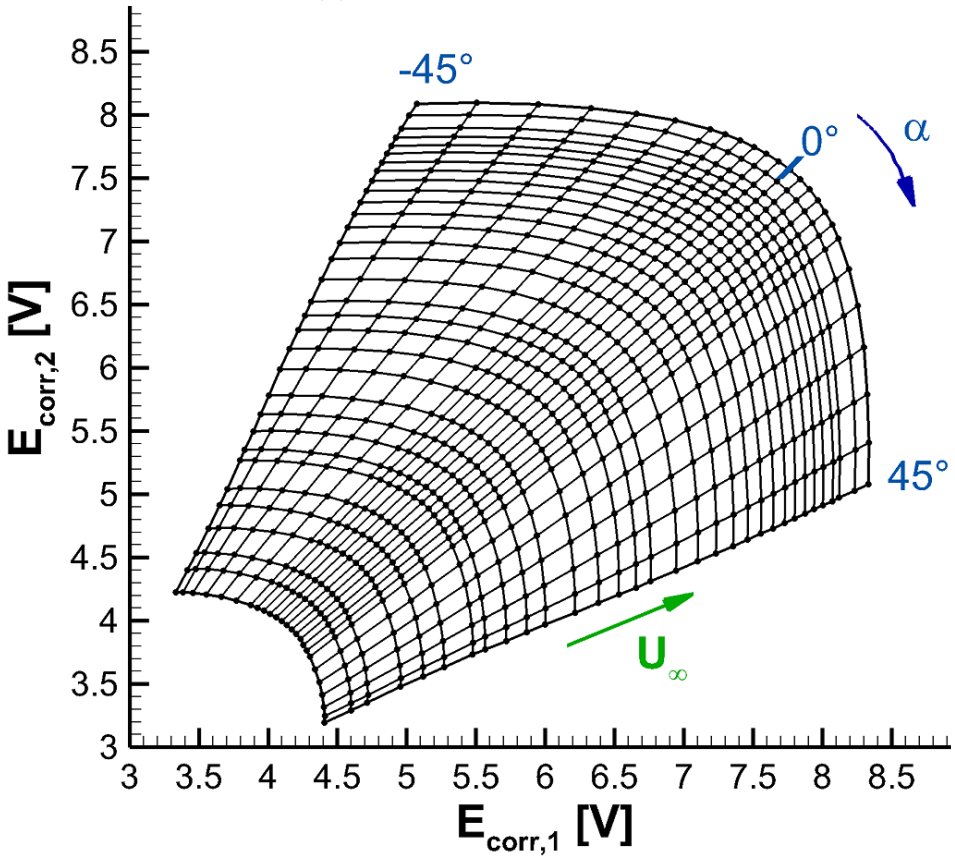

(b) Typical calibration of a probe

Figure 3.18.: Hot-wire anemometry by crosswire-type miniature probes

For the spectral analysis, the power spectral density is used. In analogy to Eq. 3.14, it is defined by

$$S_{u'}(\boldsymbol{x},\omega) = \lim_{T\to\infty} \frac{2}{T} X^*_{u'}(\boldsymbol{x},\omega) X^T_{u'}(\boldsymbol{x},\omega). \tag{3.18}$$

This spectrum is linearly averaged to $n = 1024$ bands.

Potential measurement inaccuracies can be caused by the following factors: inaccuracies in the probe calibration and the temperature measurement, resistance changes in the sensor line and a pollution of the wires. The measurement accuracy is estimated at 0.5% for the mean deviation, 2% for the standard deviation and 3.5% for the spectral density estimation.

Table 3.4.: Parameters of HWA measurements

Parameter	Abbreviation	Value
sampling rate	f_{sample}	3000 Hz
low-pass filter frequency	f_{lp}	1400 Hz
number of samples	n	19200 s
grid resolution	Δ	$s_l/20$

3.2.3.2. Stereo-PIV

For selected flow control cases, the mean velocity field quantities are also measured with Stereo Particle Image Velocimetry (Stereo PIV or 2D3C PIV, for measuring three velocity components in a plane). By applying this optical measurement technique, a disturbing influence on the vortex-dominated flow field can be excluded.

The PIV system consists of a 325 mJ double cavity Nd:YAG laser with a wavelength of 532 nm, an externally triggered control unit, a PIV synchronization unit and two sCMOS cameras. The laser has a maximum double pulse frequency of 15 Hz and is operated at 12 Hz for all measurements. The light sheet thickness is approximately set to 5 mm and the pulse delay is set to 40 μs. The laser is mounted on a three axis traverse system with a positioning accuracy of $12,5\ \mu m$. The cameras are equipped with a dual-frame-technique and a frame rate of 50 Hz at full resolution. The sensor resolution is 2560×2160 Pixel, corresponding to 0.04% – 0.08% of the local half wing span of the studied wind tunnel model.

In analogy to the HWA measurements, the measurement planes are aligned orthogonally to the wing's horizontal symmetry plane and root chord line, see Fig. 3.17. In order to

minimize laser light reflections on the wing surface, both the laser and the high-speed cameras were installed above and not besides the test section, see Fig. 3.19.

The DAVIS software was used for the execution of the measurements as well as for the pre- and post-processing. To account for a perspective distortion of the cameras, a camera calibration is performed by means of a three-dimensional target placed in the laser light sheet in the measurement area. Additionally, a fine-adjustment of the angle between the camera lens and the CMOS array is made with the help of Scheimpflug mounts right before the measurements to fulfill the Scheimpflug criterion and focus correctly [66].

As a further component of the measurement technique, a seeding generator is used to produce oil droplets with a size of $1 - 2\ \mu m$ for the measurements. It is placed behind the test section and can be turned on and off during the measurements to control the amount of seeding in the test section.

The whole area of interest could be recorded in one image for all chord-wise measurement planes, so that it was not necessary to record different images with a spatial offset and overlap. The raw particle images were discretized in 8265 interrogation areas with 25% overlap and a final size of 32×32 pixels and an adaptive correlation algorithm was applied to obtain the velocity field. The results of 400 instantaneous measurements were then used to calculate the statistically averaged flow field information.
The resulting measurement inaccuracy of the velocity components is estimated to be less than 2%.

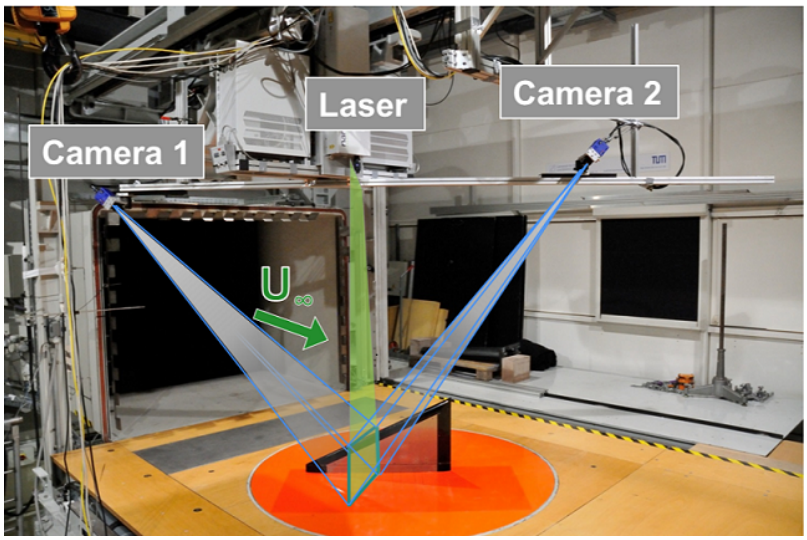

Figure 3.19.: Setup for the stereo PIV measurements in Wind Tunnel A of Technische Universität München

Table 3.5.: Parameters of PIV measurements

Parameter	Abbreviation	Value
Laser		
laser type		double cavity Nd:YAG
laser output	E_o	325 mJ
laser wavelength	λ	532 nm
pulse delay	t	20/40 μs ($U_\infty = 12/24\ m/s$)
double pulse frequency	f_{dp}	12 Hz
Cameras		
sensor type		sCMOS
sensor resolution		2560 × 2160 Pixel
frame rate		50 Hz

3.2.4. Flow visualization

To visualize the flow on the wing surface, wool tufts are attached to the upper side of the wing with adhesive tape. This technique is employed especially to the respective baseline flow cases. The wool tufts are 3 cm long and are evenly distributed over the whole wing in lateral and axial direction, see Fig. 3.20.

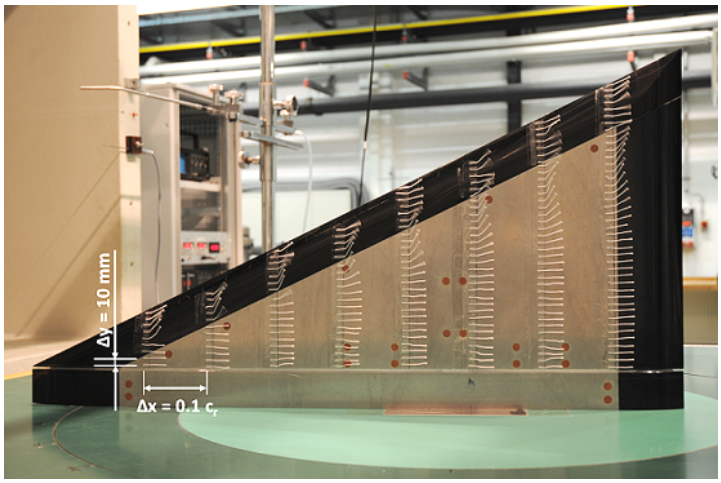

Figure 3.20.: Wool tuft flow visualization

4. Flow physics of the basic configuration

In this chapter, the low-speed aerodynamics of the basic VFE-2 configuration are analyzed for different angles of attack. The presented measurement results comprise the aerodynamic force and moment coefficients as well as the surface pressure and the velocity distributions on the suction side of the wing. All physical properties were measured at static conditions. In the analysis of the pressure distribution, five flow cases are presented: three pre-stall test-cases at the angles of attack $\alpha = 13°$, $\alpha = 18°$ and $\alpha = 23°$ and the Reynolds number $Re_{mac} = 1.0 \cdot 10^6$, a stall test-case at $\alpha = 35°$ and $Re_{mac} = 0.5 \cdot 10^6$ and a post-stall test-case at $\alpha = 45°$ and $Re_{mac} = 0.5 \cdot 10^6$. The velocity distribution is analyzed for the mentioned test cases at $\alpha = 23°$, $\alpha = 35°$ and $\alpha = 45°$.

These results form the basis for the choice of the actuation parameters for pulsed blowing and oscillating leading edge flaps. Furthermore, they are used as a reference to assess the effect of the flow control devices on the delta wing flow in Chapter 5 and 6.

4.1. Aerodynamic loads

The aerodynamic loads for the baseline configuration were recorded in the wind tunnel B (see Chapter 3.2) for the three different Reynolds numbers $Re_{mac} = 0.5 \cdot 10^6$, $Re_{mac} = 1.0 \cdot 10^6$ and $Re_{mac} = 1.5 \cdot 10^6$, cf. [24] and [85]. For this purpose, the model equipped for pulsed blowing was used with the blowing devices being switched off.

4.1.1. Forces

Fig. 4.1 shows the angle-of-attack polars of the aerodynamic lift and drag forces as well as the Lilienthal polar for the half delta wing model with the VFE-2 geometry. At first glance at the figure, the Reynolds similarity of the low-speed delta wing aerodynamics is evident. For all three Reynolds numbers, the characteristics of the aerodynamic loads are very similar. Only a small offset in the lift and moment polars is visible.

Lift. The lift curve (see Fig. 4.1a) is characterized by a linear increase at low angles of attack $\alpha = 0°$ to $\alpha \approx 10°$. Above an angle of attack $\alpha \approx 10°$, a non-linear increase in lift is observed. The additional lift component is called vortex lift, as it is caused by the primary vortex, that develops with increasing angle of attack (see also Section 2.2).

At approximately $\alpha = 18°$, the vortex reaches a fully-developed state. Accordingly, the shear layer feeding the primary vortex is separating along the whole leading edge. If the angle of attack is further increased, more fluid is transported into the vortex and its cross-section is enlarged.

The increase in the vortex cross section does also become noticeable on the wing surface. In Fig. 4.2, flow visualizations are shown for the three angles of attack $\alpha = 13°$, $\alpha = 18°$ and $\alpha = 23°$ at $Re_{mac} = 1 \cdot 10^6$, cf. [42], [72]. The wool tufts align themselves with the flow. In the area affected by the leading-edge vortex, they are deflected outboard due to the circumferential velocity components of the vortex close to the wing surface. Further inboard, in the area of reattached flow, the wool tufts are aligned in axial direction. The separation line between these two areas is called reattachment line. It is marked on the right pictures of Fig. 4.2. The results indicate that the reattachment line moves inboard with increasing angle of attack. Thus, the area affected by the vortex becomes larger.

At angles of attack from $\alpha = 20°$ to $\alpha = 25°$, a bump can be observed in the lift curve. The reason for this irregularity is that the vortices cannot grow in circumferential direction anymore, and their core is therefore moving vertically upwards. Thus, the increase in the circumferential velocities and the suction pressure on the wing surface is reduced.

By the phenomenon of vortex breakdown, the lift gradient is getting smaller until the lift curve flattens out and reaches the angle of attack α_{max}, corresponding to the maximum lift coefficient. This angle is approximately 34° to 36° (stall regime) and the maximum lift coefficient $C_{L,max}$ is 1.125 for $Re_{mac} = 0.5 \cdot 10^6$, 1.10 for $Re_{mac} = 1.0 \cdot 10^6$ and 1.08 for $Re_{mac} = 1.5 \cdot 10^6$. At this point, vortex breakdown has reached the apex. The maximum angle of attack of the configuration ($\alpha_{max} \approx 35°$) is followed by a region of moderate decline of the lift force up to $\alpha \approx 40°$. At greater incidences $\alpha > 40°$, a strong and abrupt decrease in the lift coefficient is observed, which is characterized by a gradient of almost $-0.3/°$ (post-stall regime). This lift decrease is caused by the abrupt transition from a burst vortex structure to a state with a detached shear layer, that does not roll up to form a leading vortex any more.

Drag. The polars of the drag coefficient are shown in Fig. 4.1b. They correspond very well for the three investigated Reynolds numbers. The drag gradient is continually increasing up to the angle of attack $\alpha \approx 30°$. In the adjacent stall regime, the drag gradient decreases until the maximum drag coefficient $C_{D,max} = 0.85$ is reached at $\alpha = 40°$. The collapse of the burst vortex structure at angles of attack $\alpha > 40°$ is accompanied by a considerate decrease of the drag coefficient to $C_D \approx 0.64$.

Lilienthal polar. In Fig. 4.1c, the lift coefficient is plotted over the drag coefficient for the different angles of attack (Lilienthal polar). As the configuration is symmetrical to the horizontal plane $Z = 0$, the lift and the drag coefficients are zero at zero angle of attack, $C_L(\alpha = 0°) = 0$; $C_D(\alpha = 0°) = 0$. The angle of attack of maximum drag is higher than the angle of attack of maximum lift.

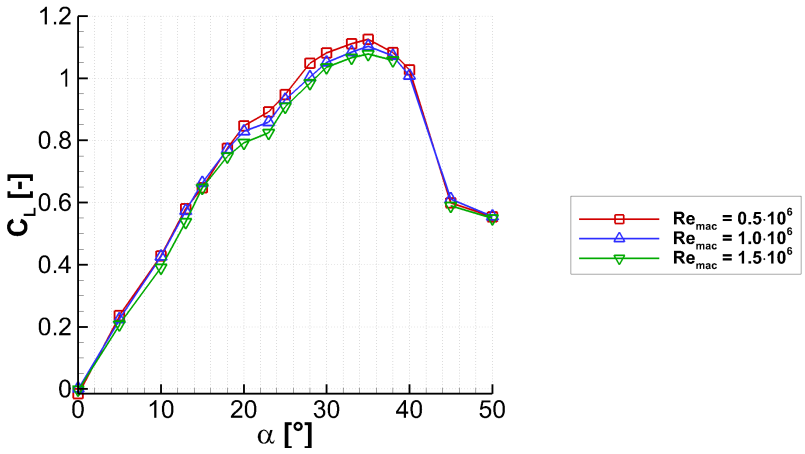

(a) Lift polar

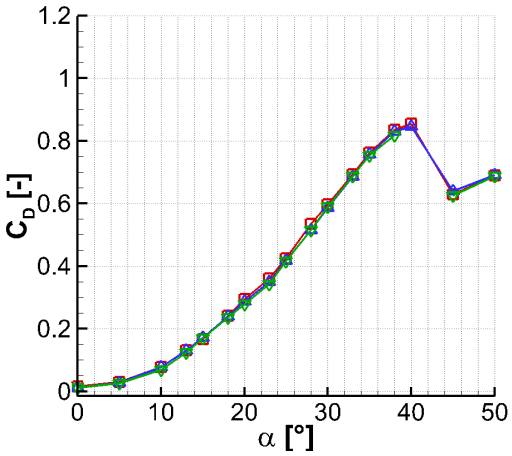

(b) Drag polar

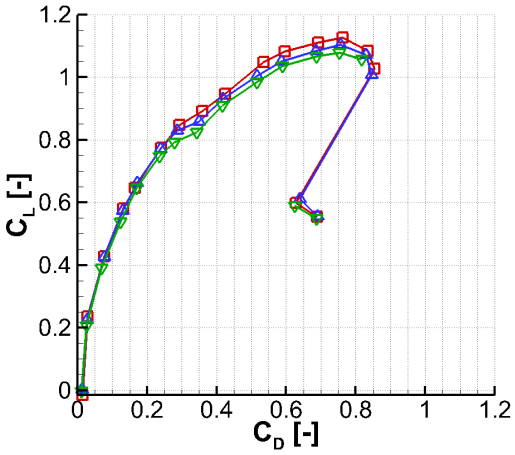

(c) Lilienthal polar

Figure 4.1.: Polars of the lift and the drag coefficient for the basic configuration

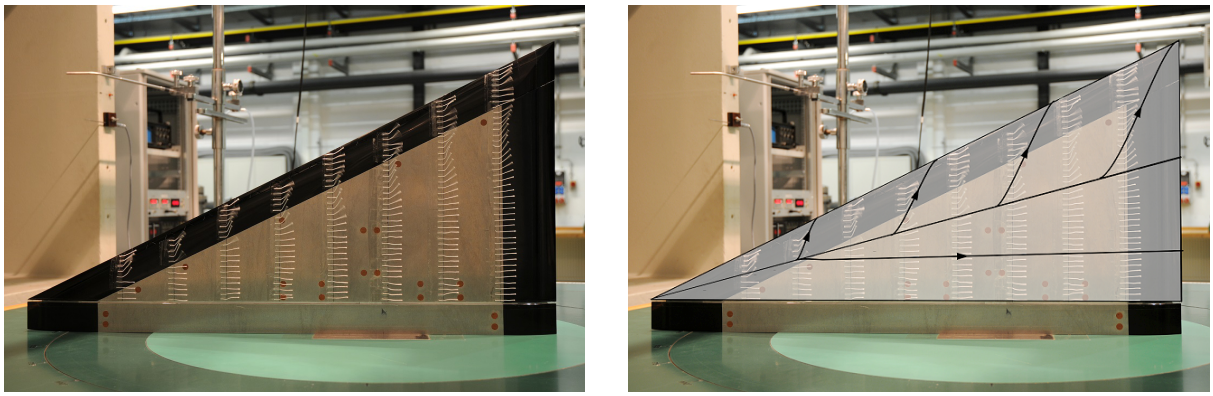

(a) $\alpha = 13°$

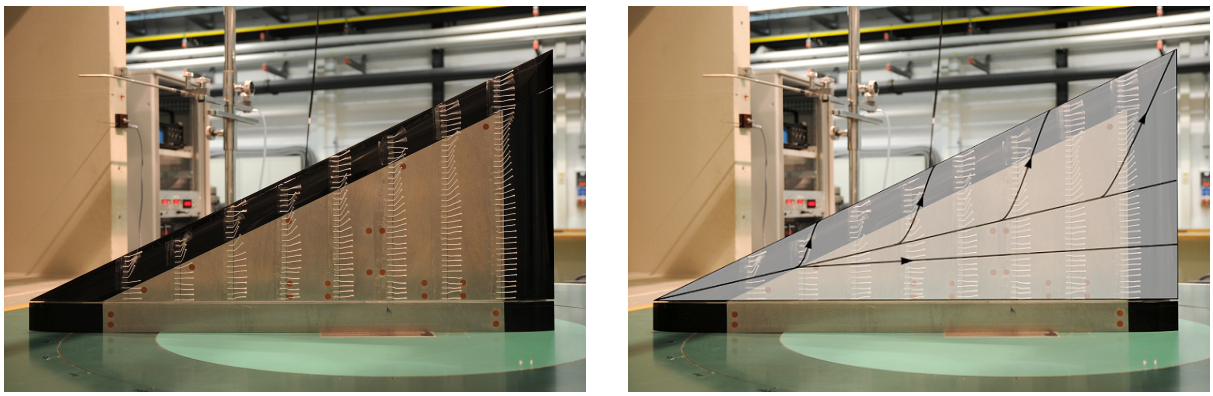

(b) $\alpha = 18°$

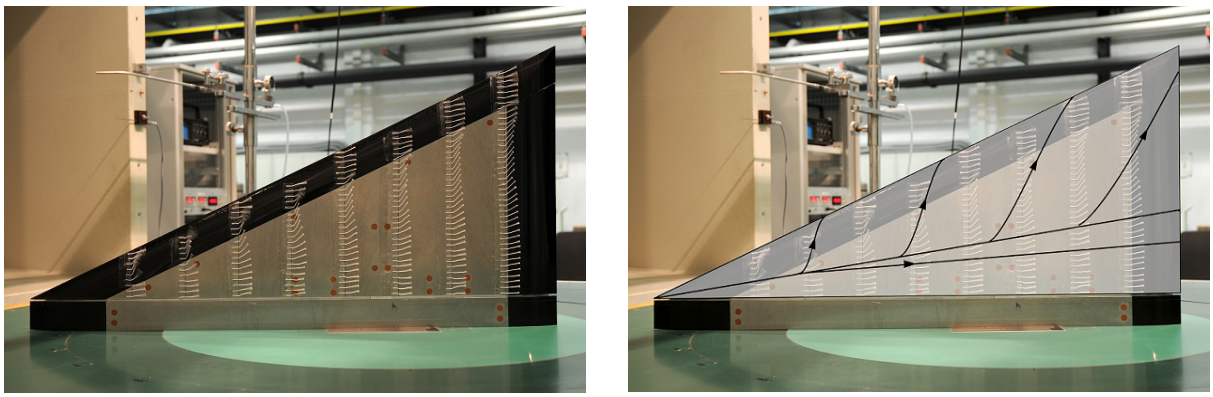

(c) $\alpha = 23°$

Figure 4.2.: Wool-tufts visualization on the wing upper side at different angles of attack, baseline configuration, $Re_{mac} = 1 \cdot 10^6$, and $M = 0.07$

4.1.2. Moments

The polars of the rolling moment, pitching moment and yawing moment coefficients are sketched in Fig. 4.3 for the three Reynolds numbers $Re_{mac} = 0.5 \cdot 10^6$, $Re_{mac} = 1.0 \cdot 10^6$ and $Re_{mac} = 1.5 \cdot 10^6$.

Rolling moment coefficient. Regarding the polars of the rolling moment coefficient shown in Fig. 4.3a and the yawing moment coefficient in Fig. 4.3c, it is important to note that these results were gained from measurements with a half delta wing model. For a full delta wing model at zero sideslip angle, the rolling moment resulting from the normal forces integrated over both sides of the wing would add up to values close to zero for symmetric vortex breakdown. The same holds for the yawing moment coefficient.

For the half delta wing model, the rolling moment is proportional to the normal force coefficient and therefore, the curve of the rolling moment coefficient polar strongly resembles that of the normal force polar and the lift polar. It also incorporates a bump at high angles of attack $\alpha \approx 20°$ to $25°$ with a local minimum at $\alpha = 23°$. The maximum rolling moment coefficient is $C_{l,max} = 0.33$ to 0.35. The highest value is reached for the lowest Reynolds number $Re_{mac} = 0.5 \cdot 10^6$. At $\alpha = 40°$ to $45°$, a strong decrease appears according to the lift polar. As the rolling moment coefficient is negative, it turns the right wing tip up.

Pitching moment coefficient The pitching moment coefficient shown in Fig. 4.3b is referred to $x = 2/3c_r$, see Section 3.2.1. The coefficient is positive in the whole measurement range, which means that the wing has a pitch-up tendency. The coefficient for a zero incidence is $C_{m,0} = 0$ due to the symmetric wing profile. It is increased for a rising angle of attack, until $\alpha_{max} = 35°$ is reached. Subsequently, the coefficient strongly decreases to values $C_m(\alpha = 45°) \approx 0.3\ C_{m,max}$.

Yawing moment coefficient. The yawing moment coefficient induced on the half delta wing model is shown in Fig. 4.3c. It is characterized by low positive values, which indicate that the moment reference point at $X = 2/3c_r$ is close to the center of pressure. The yawing moment is maximal at the angles of attack $\alpha = 30°$ to $36°$ and the positive coefficient indicates a moment turning the configuration right round.

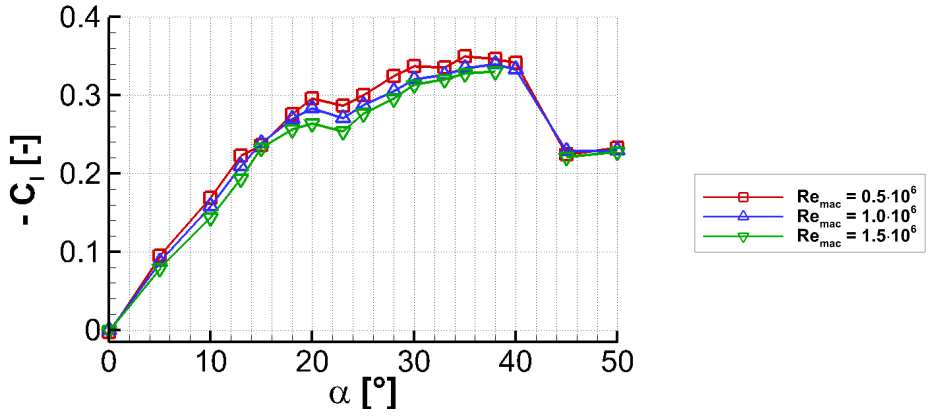

(a) Rolling moment coefficient

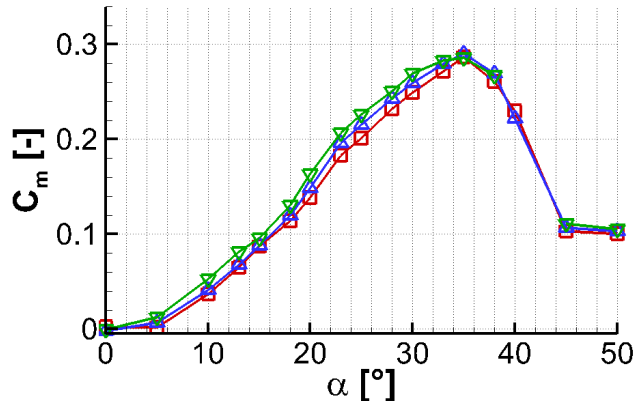

(b) Pitching moment coefficient

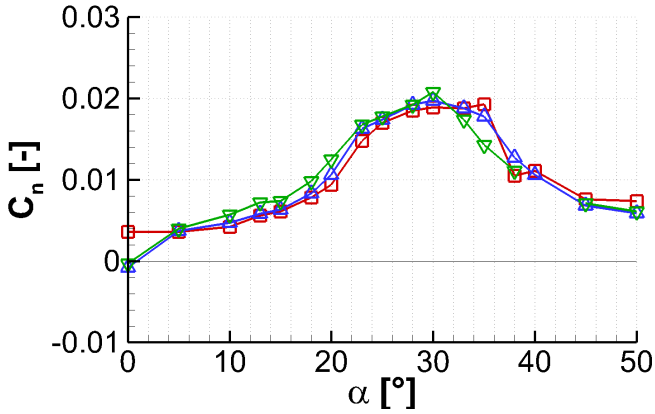

(c) Yawing moment coefficient

Figure 4.3.: Polars of the three moment coefficients for the half model configuration

4.1.3. Comparison with other results

In this subsection, the aerodynamic loads that were measured on the basic half model configuration including the pulsed blowing system in wind tunnel B are compared to results from measurements in wind tunnel A and to measurements with the basic half model with integrated flaps. Furthermore, a comparison with results from full models is carried out, which were investigated in different wind tunnel facilities.

Comparison with the flap model and with measurements in wind tunnel A. In Fig. 4.4, the lift coefficient polar that was measured in wind tunnel B of Technische Universität München with the model for pulsed blowing is compared to the results obtained from measurements in wind tunnel A. Additionally, the equivalent data obtained from measurements with the second wind tunnel model with integrated flaps is shown. While red lines correspond to the results for the model with integrated pulse actuators, the results for the flap model are shown in blue color. The solid lines belong to the measurement results recorded in wind tunnel A, and dashed lines represent the lift coefficients measured in wind tunnel B.

The characteristics of the different lift curves are very similar. However, one can observe smaller differences. First, the level of the lift curves measured in wind tunnel B is slightly higher than the lift curve level measured in wind tunnel A. Second, the bump observed at $\alpha = 20°$ to $\alpha = 25°$ in wind tunnel B occurs at higher angles of attack compared to the measurement results taken in wind tunnel A ($\alpha = 18°$ to $\alpha = 23°$). Third, the strong decrease in the post-stall regime appears at different angles of attack. For the flap model, the decrease is observed from $\alpha = 40°$ to $\alpha = 41°$ in wind tunnel A and from $\alpha = 42°$ to $\alpha = 43°$ in wind tunnel B. For the model with pulsed blowing actuators, the decrease occurs from $\alpha = 41°$ to $\alpha = 42°$ in wind tunnel A. In wind tunnel B, it is located between $\alpha = 40°$ and $\alpha = 45°$ for this model (no finer measurement resolution for this angle-of-attack range is available).

Table 4.1.: Abrupt lift decrease at very high angles of attack

Wind tunnel half model	Wind tunnel B	Wind tunnel A
Pulsed blowing	$\alpha = 40° \rightarrow \alpha = 45°$	$\alpha = 41° \rightarrow \alpha = 42°$
Leading edge flaps	$\alpha = 42° \rightarrow \alpha = 43°$	$\alpha = 40° \rightarrow \alpha = 41°$

The observed differences originate from the differences of the two wind tunnels: in comparison to wind tunnel B, the wind tunnel A has a remarkably larger test section. Both the cross section size and the test section length are of larger dimensions. Therefore, the blockage ratio in wind tunnel A is considerably lower compared to the wind tunnel B. Additionally, the run length from the beginning of the test section to the wind tunnel models is longer in wind tunnel A. According to this, another difference could be rooted

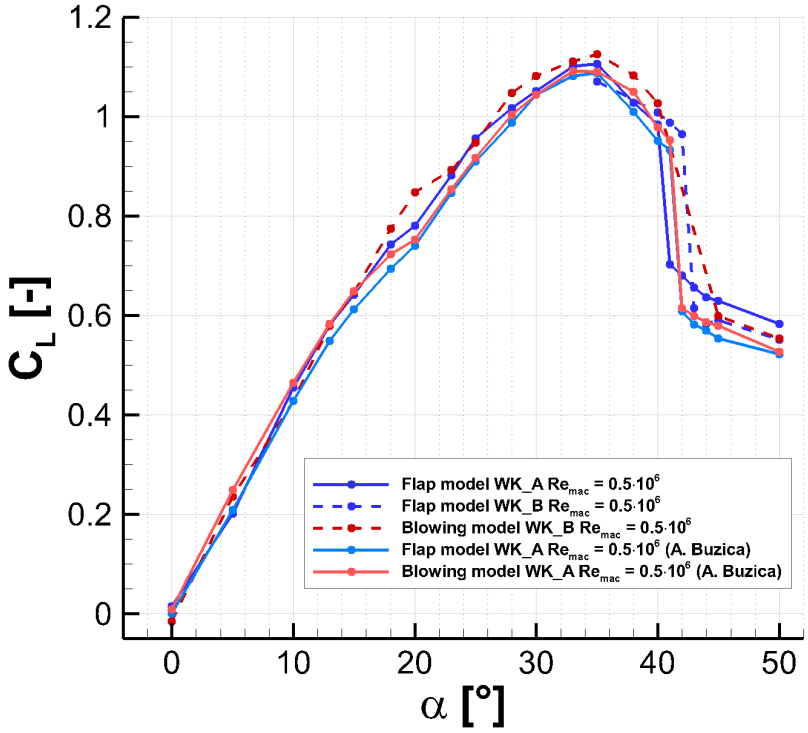

Figure 4.4.: Lift polar - comparison with results from wind tunnel A and from the flap model

in the different extent of the boundary layer, that develops on the bottom of the wind tunnel test section. Another potential source of differences in the measurement results are uncertainties in the adjustment of the angle of attack. The uncertainty in the adjustment of the incidence is estimated to be $\Delta\alpha = 0.5°$.

Comparison with the full model. In Fig. 4.5, the normal force coefficient is shown and compared to the results of measurements, which were carried out with full wing models at NASA, U.S. [50] as well as at ONERA, France [70] and at TUBITAK, Turkey, [43]. Although the measurements were conducted at different Reynolds numbers, they lie in the same range.

The characteristics of the normal force curve strongly resemble those of the lift curve shown see Fig. 4.1a. Compared to the curves measured at other institutes, the results are in good agreement for low to moderate angles of attack. Beginning at $\alpha = 18°$ (when the vortex is fully developed), the normal force coefficient of the half model is considerably lower than the coefficients measured for the full wing configurations.

This difference might be due to the use of a half delta wing model with a péniche.

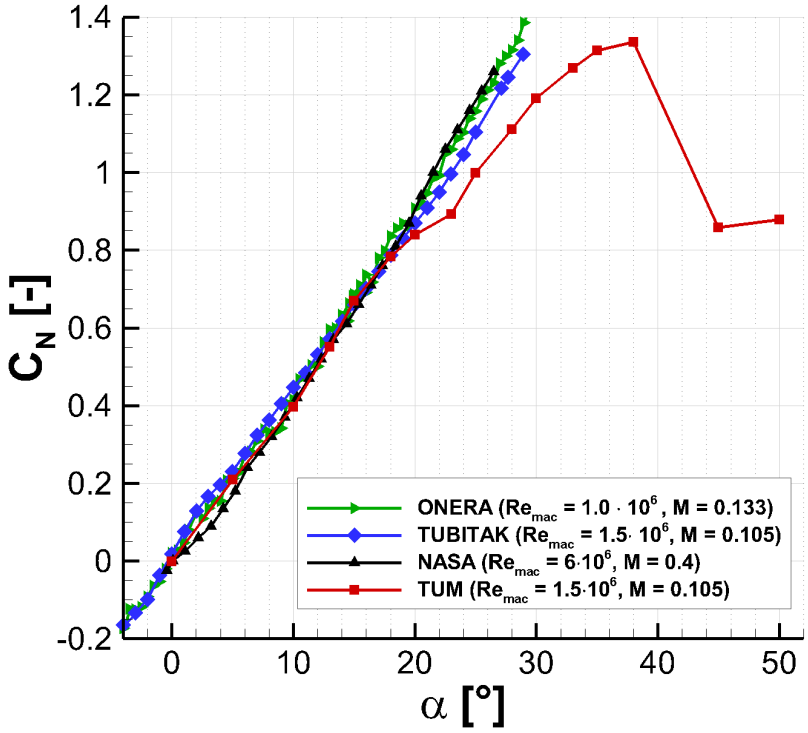

Figure 4.5.: Polar of the normal force coefficient - comparison with results from other institutes

Compared to the full wing configurations, the second primary vortex does not exist. In fact, the balance table also has a displacement effect on the vortex system, but by the use of a péniche with the height of 55 *mm* (see Section 3.1.1), the symmetry condition is not fulfilled. Therefore, a wider span-wise area on the wing is available for the vortex on the half delta wing.

An additional displacement effect on the full wing model comes from the model sting located symmetrically to the wing's symmetry plane (see Fig. 3.1). It does not exist on the half wing model and could therefore enforce the differences between the two configurations. As a consequence, the vortex structure on the half delta wing model is less concentrated and the suction peaks are reduced. Accordingly, the lift coefficients are lower compared to the full wing configuration.

4.2. Surface pressure distribution

In this section, the surface pressure distributions in the pre-stall, stall and post-stall regimes are presented, cf. [5], [37]. The measurements were carried out in wind tunnel B.

4.2.1. Time-averaged pressure and pressure fluctuations

In the following subsections, the coefficients of the mean pressure and the pressure fluctuations are shown for the three chord-wise measurement cross-sections $X = 0.4$, $X = 0.6$ and $X = 0.8$.

4.2.1.1. Pre-stall

In Figs. 4.6 to 4.8, the static surface pressure and the pressure fluctuation coefficients are shown for angles of attack $\alpha = 13°$, $\alpha = 18°$ and $\alpha = 23°$ at the Reynolds number $Re_{mac} = 1 \cdot 10^6$. In these plots, the results for the half delta wing model are compared to the results measured for the full VFE-2 model by Furman [17].

The figures for the mean pressure coefficient on the left contain the distribution on the upper side of the wing for both configurations, half and full wing model. Additionally, the lowest of the three pressure curves at each chord-wise station represents the static pressure measured by Furman on the lower side of the full delta wing. As the span-wise characteristics are quite homogenous and of less impact with respect to the flow control experiments on the upper wing side, only one control station per cross-section was installed on the lower side of the half delta wing model. The span-wise positions are $Y = 0.4$ for $X = 0.4$, $Y = 0.6$ for $X = 0.6$ and $Y = 0.6$ for $X = 0.8$. On the right hand side of the figures, the pressure fluctuations are shown, which were measured by the Kulites on the upper wing side of the delta wing models.

Low angle of attack ($\alpha = 13°$). At the low angle of attack, a weak suction peak is observed on the wing's upper side at all chord-wise measurement positions, see Fig. 4.6a. The highest suction level is $C_p = -1.5$ for $X = 0.4$, $C_p = -1.4$ for $X = 0.6$ and $C_p = -1.25$ for $X = 0.8$ in the case of the half wing model. The center of the peak is located at the respective span-wise position $X \approx 0.75$. It is caused by the early-stage fully-developed primary vortex, that is generated along the leading edge of the wing (see also Fig. 2.2 for a classification of the different angles of attack). The vortex-induced velocities cause negative pressures on the wing surface. The surface pressure reaches its minimum below the vortex core. Therefore, the span-wise location of the pressure minimum marks the span-wise position of the primary vortex' core. The suction peak slightly decreases in the chord-wise direction. Further inboard, a relatively low constant pressure level is observed. It does reflect the reattached flow inboard from the primary vortex.

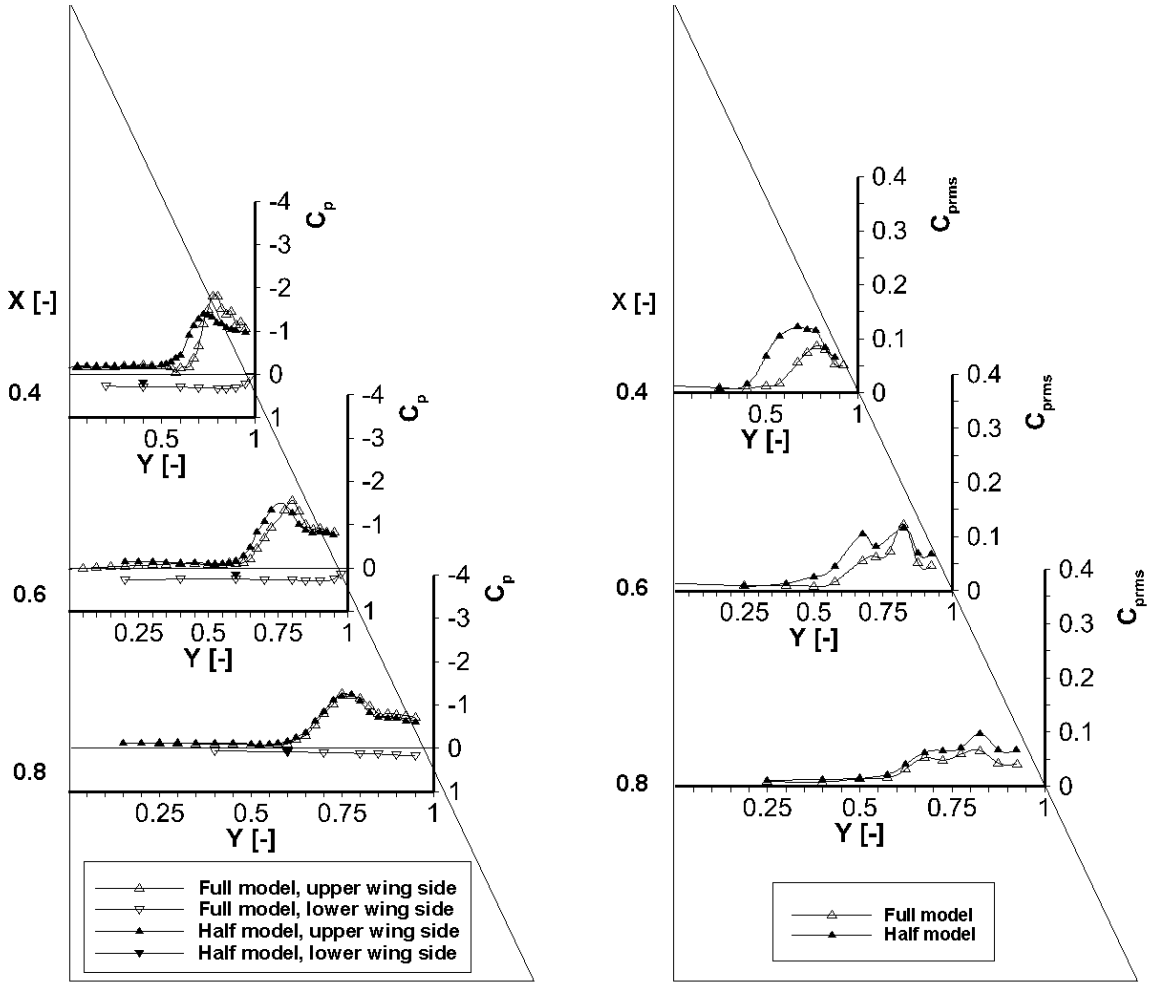

(a) Mean pressure (b) Pressure fluctuations

Figure 4.6.: Pressure distribution for $\alpha = 13°$, $Re_{mac} \approx 1.0 \times 10^6$, and $M = 0.07$

For the full model, the suction peak is slightly higher and it is located closer to the leading edge for $X = 0.4$ and $X = 0.6$. This difference might be caused by the lower displacement effects at the half model, which is equipped with a péniche. Here, the vortex has more space available to expand on the upper wing side. Moreover, a second local maximum in the mean pressure is observed for the full model at $X = 0.4$ and $Y = 0.88$. It is related to the secondary vortex. A second local maximum is not detected in the pressure distribution of the half wing model. This is most likely due to the fact than one sensor at the position ($X = 0.4$; $Y = 0.925$) was defective on the half model. At $X = 0.8$, the pressure distributions correspond very well for both models, only the level of the pressure fluctuations is slightly higher for the half wing model. The pressure at the control point on the pressure side of the half wing model agrees very well with the values measured on

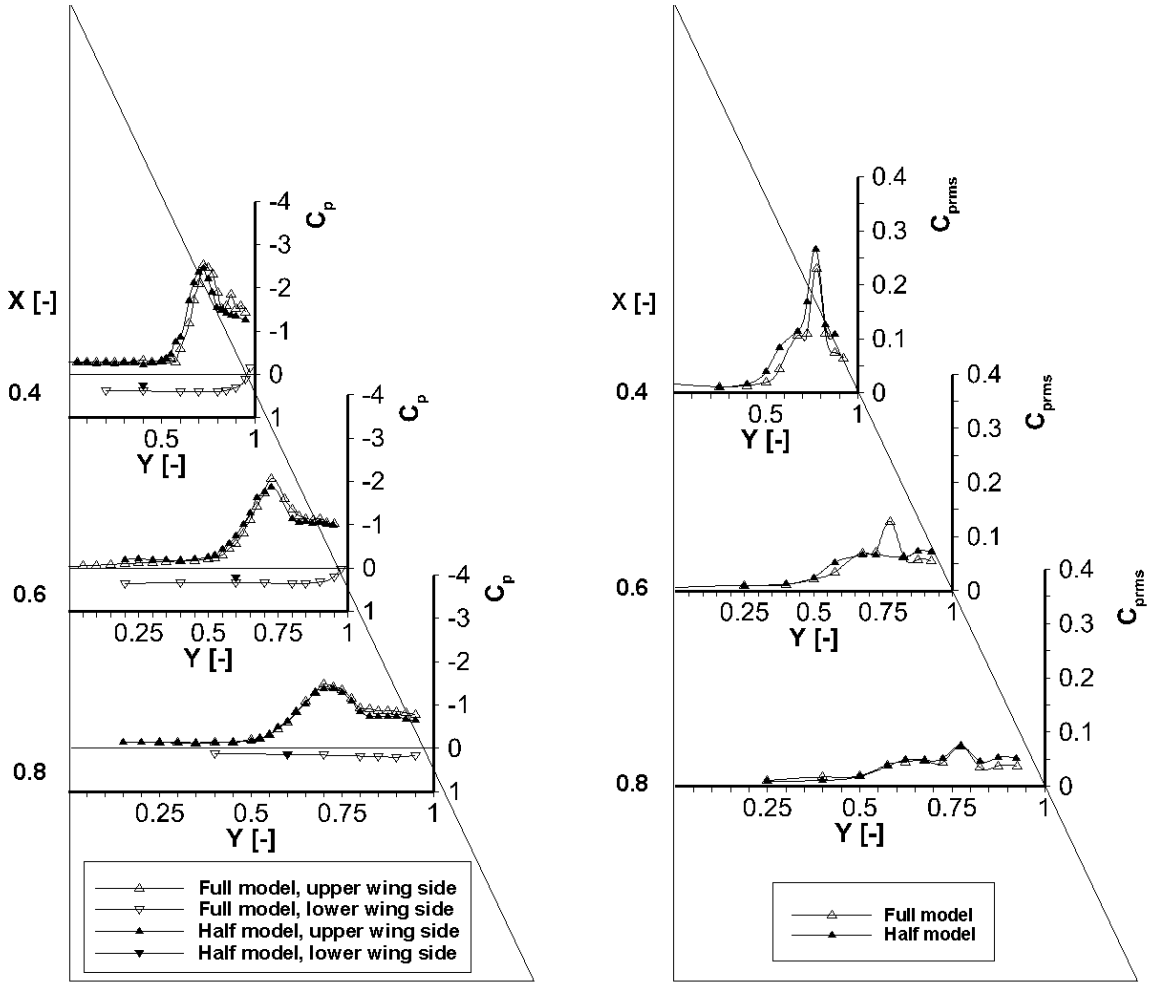

(a) Mean pressure (b) Pressure fluctuations

Figure 4.7.: Pressure distribution for $\alpha = 18°$, $Re_{mac} \approx 1.0 \times 10^6$, and $M = 0.07$

the full wing model.

The pressure fluctuations shown in Fig. 4.6b reveal a remarkably increased fluctuation level in the region of the suction peak compared to the attached flow further inboard. The maximum rms intensity is $C_{p,rms} = 0.122$. The values measured on the half model are slightly higher than on the full model.

Moderate angle of attack ($\alpha = 18°$). The pressure distribution at $\alpha = 18°$ shows a significantly higher suction peak ($C_{p,min} = -2.6$ at $X = 0.4$) and a larger span-wise extent of the fully-developed primary vortex compared to $\alpha = 13°$, see Fig. 4.7a. The pressure distributions agree very well for the half and the full wing model. The only difference is again in a second local pressure minimum, which is observed on the full wing

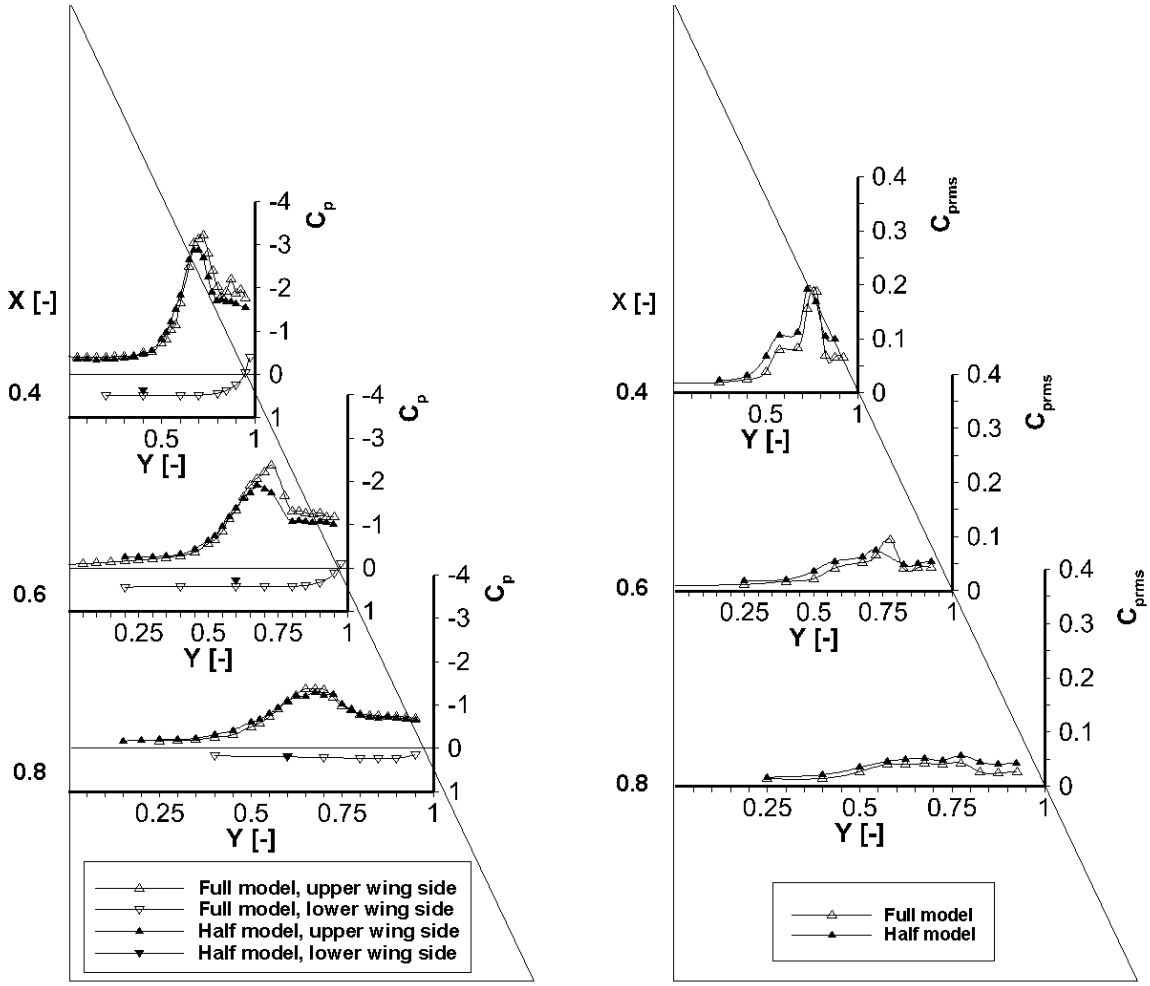

(a) Mean pressure (b) Pressure fluctuations

Figure 4.8.: Pressure distribution for $\alpha = 23°$, $Re_{mac} \approx 1.0 \times 10^6$, and $M = 0.07$

model at $X = 0.4$ and $Y \approx 0.87$ and does not occur on the half wing model.

In the distributions of the pressure fluctuations, a global maximum is observed at all three chord-wise measurement stations (Fig. 4.7b). It is missing only for $X = 0.6$ on the half delta wing model. This is most probably due to the lack of a sensor at this position (the sensor was defect). The local maxima are located a bit further outboard than the maxima in the mean pressure distribution, which are caused by the primary vortex. The highest peak appears in the first measurement cross section at $X = 0.4$, where $C_{p,rms} = 0.265$.

High angle of attack ($\alpha = 23°$). Increasing the angle of attack from $\alpha = 18°$ to $\alpha = 23°$, the suction level is further augmented in the measurement cross-section $X = 0.4$,

$C_{p,min} = -2.9$ (see Fig. 4.8a). This is not the case for the two rear cross-sections.

The following criterion can be applied to detect vortex breakdown: the vortex is burst at a position $X = const.$, if an increase of the angle of attack does not implicate a gain of the suction pressure level. Of course, this is only valid if the vortex axis does not veer away from the wing surface when the breakdown location crosses the trailing edge of the wing [6]. Applied to the results of the half wing model, it can be observed that the suction pressure stagnates in the chord-wise station $X = 0.6$ and decreases at $X = 0.8$ at the transition from $\alpha = 18°$ to $\alpha = 23°$. It can therefore be concluded, that vortex breakdown has reached the chord-wise position $X = 0.6$ at the higher angle of attack. At $\alpha = 18°$ and $X = 0.8$, the vortex is close to breakdown, because the suction pressure level is only marginally higher than for $\alpha = 13°$ at the same position (see Figs. 4.12a and 4.11a). This is an indication, that the vortex flow is very sensitive to an increase in the angle of attack. As already observed for $\alpha = 18°$, the distribution of the pressure fluctuations contains a local maximum slightly outboard of the suction peak at the high angle of attack $\alpha = 23°$ for $X = 0.4$ and $X = 0.6$ (see Fig. 4.8).

Table 4.2.: Vortex characteristics in the pre-stall regime for the half wing model, cf. [5]

	X [-]	13°	18°	23°
Position Y of the vortex axis	0.4	0.724	0.724	0.673
	0.6	0.725	0.725	0.675
	0.8	0.775	0.700	0.675
Suction peak level $C_{p,min}$	0.4	-1.38	-2.44	-2.88
	0.6	-1.34	-1.87	-1.91
	0.8	-1.24	-1.38	-1.29
Position Y of the reattachment line	0.4	0.500	0.500	0.300
	0.6	0.600	0.500	0.400
	0.8	0.575	0.525	0.350

The most important vortex characteristics derived from the pressure measurements in the pre-stall regime are summarized in Table 4.2. The following conclusions can be drawn:

- the span-wise position of the vortex axis is almost constant in the chord-wise direction; it moves inboard with increasing angle of attack,
- as already observed in Fig. 4.2, the reattachment line does also move inboard with higher incidence, and
- the suction peak level decreases in chord-wise direction; it increases with the angle of attack.

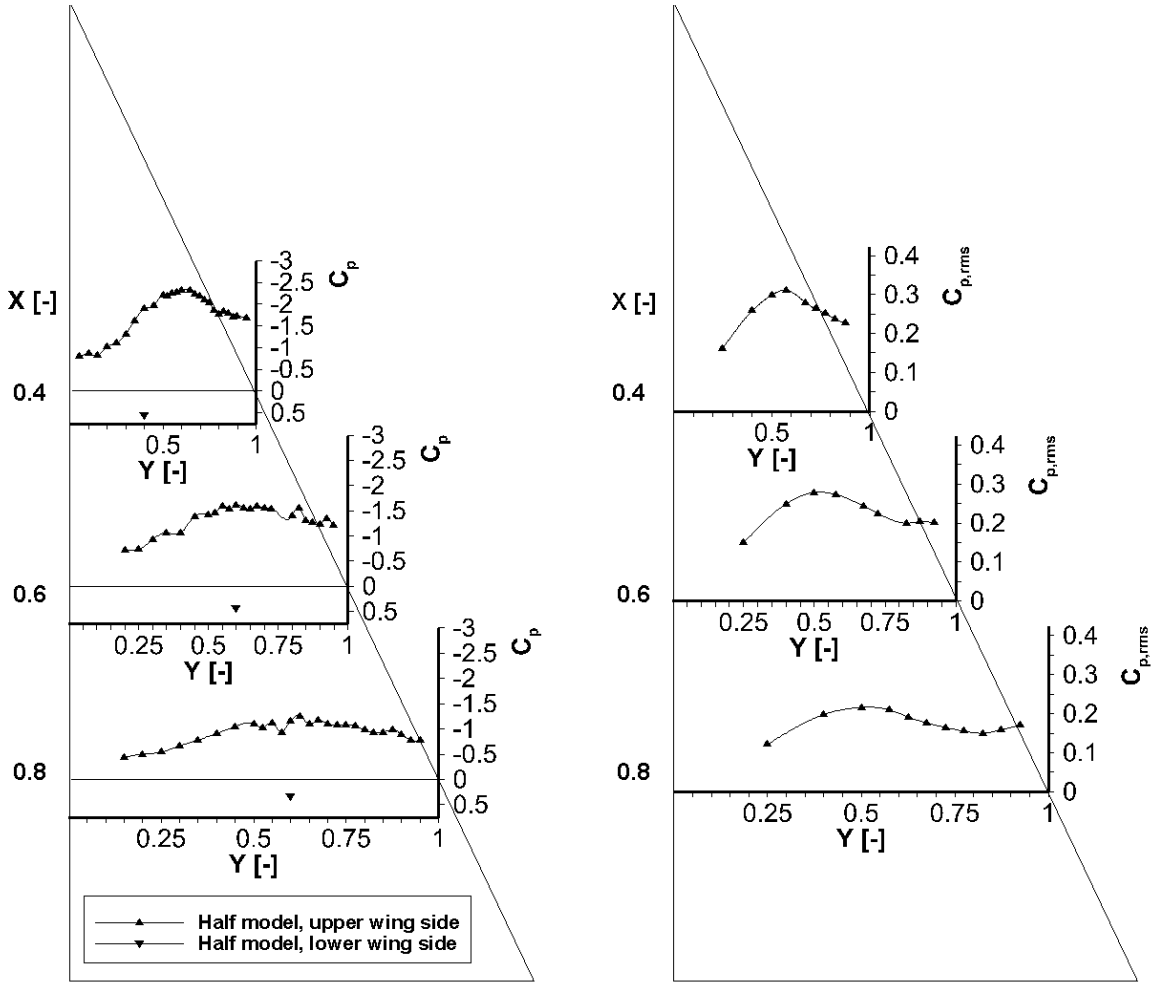

(a) Mean pressure (b) Pressure fluctuations

Figure 4.9.: Pressure distribution for $\alpha = 35°$, $Re_{mac} \approx 0.5 \times 10^6$, and $M = 0.035$

4.2.1.2. Stall

In Fig. 4.9, the pressure distribution for $\alpha = 35°$ and $Re_{mac} = 0.5 \cdot 10^6$ is plotted applying the same layout as used for the presentation of the pre-stall cases in subsection 4.2.1.1. The comparison to the full model is not considered, since this angle of attack was not investigated in the VFE-2 project.

At the stall angle $\alpha = 35°$, a suction peak $C_p = -2.3$ can be observed in the mean pressure distribution at $X = 0.4$, see Fig. 4.9a. This peak, that is much weaker than the peak observed at $\alpha = 23°$, indicates the presence of a leading-edge vortex, whose breakdown location is situated in front of $X = 0.4$. For the cross-sections $X = 0.6$ and $X = 0.8$, the pressure distribution is much flatter and the vortex is spread widely over the wing. Compared to the pre-stall cases, the suction pressure level is strongly

increased on the inner part of the wing. This corresponds to the maximum lift reached at this angle of attack ($\alpha_{max} = 35°$, see Section 4.1). From the suction peaks in inboard direction, a monotonous pressure increase is observed. This is an indication of a large vortex diameter that covers the whole area of the half delta wing. Hence, the vortex axis cannot move further inboard.

The vortex is also depicted by high pressure fluctuations. In the $C_{p,rms}$ distributions, local maxima are observed in each cross-section, see Fig. 4.9. $C_{p,rms}$ reaches a value of 0.31 for $X = 0.4$ and $Y = 0.575$, which reflects high turbulence intensity at the location under the burst vortex core.

4.2.1.3. Post-stall

The mean pressure distribution for $\alpha = 45°$ does not exhibit the typical patterns of a vortex flow (see Fig. 4.10a). In all cross-sections, the suction level is very low and evenly flat: on average, $C_p \approx -0.65$ for each cross-section. This is characteristic of a "dead-water" type flow region due to the very high angle of attack.

The pressure fluctuations plotted in Fig. 4.10b also exhibit very low values: for each cross-section, the average pressure fluctuations are about 2%. This confirms the presence of a dead-water area.

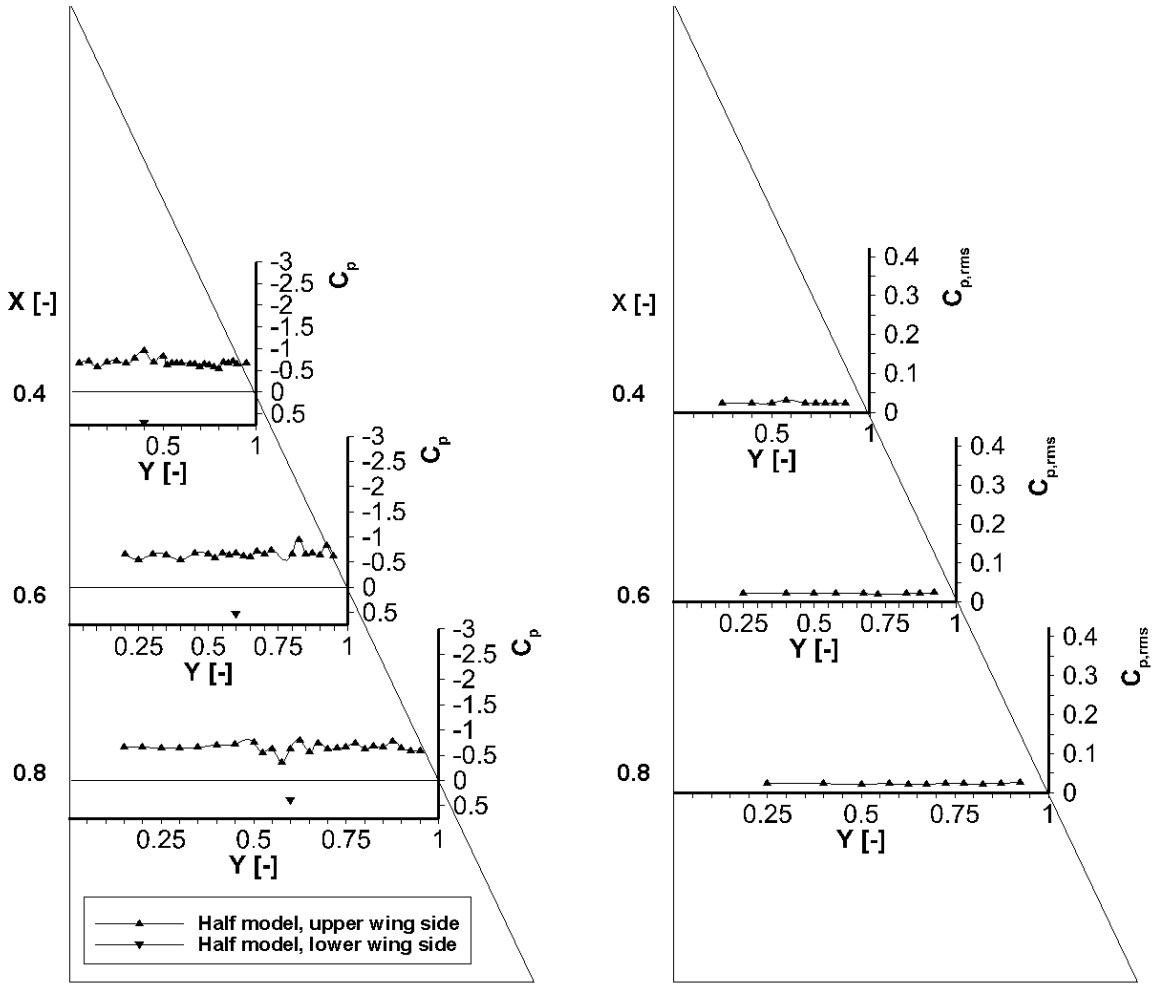

(a) Mean pressure

(b) Pressure fluctuations

Figure 4.10.: Pressure distribution for $\alpha = 45°$, $Re_{mac} \approx 0.5 \times 10^6$, and $M = 0.035$

4.2.2. Spectral analysis

In the following, the power spectral density of the pressure coefficient $S_{c_p}^N$ is presented to allow for a detailed analysis of the pressure fluctuations on the wing's upper surface at different angles of attack. The width of the frequency band is $\Delta k = 0.12$. Figs. 4.11 to 4.15 show the results at one specific span-wise position Y of the three chord-wise measurement planes ($X = 0.4; 0.6; 0.8$), where local mean pressure maxima and characteristic pressure fluctuation distributions were observed. Additionally, the span-wise distribution of the power spectral density is shown for one selected cross-plane.

4.2.2.1. Pre-stall

Low angle of attack ($\alpha = 13°$). The spectral distribution for $\alpha = 13°$ is shown in Fig. 4.11. It reveals a decline in the power spectral density with increasing frequencies, which is typical for turbulent spectra (see Fig. 4.11a). Furthermore, the level of the pressure fluctuations decreases in the chord-wise direction. In the whole measurement area, no noticeable energy concentrations are detected.

In the span-wise comparison for $X = 0.4$, see Fig. 4.11b, higher fluctuations are observed in the area affected by the suction peak of the primary vortex ($Y = 0.6$ to 0.8). They appear at relatively low reduced frequencies $k = 0$ to 2 and are associated with shear layer instabilities and the small discrete vortices that are shed at the leading edge and are transported into the vortex as the shear layer rolls up over the wing.

Moderate angle of attack ($\alpha = 18°$). The level of the power spectral density is remarkably increased for $\alpha = 18°$, as the strength of the vortex rises with the angle of attack, see Fig. 4.12. This is especially the case in the first measurement section $X = 0.4$, where a slight concentration of pressure fluctuations is observed at $k = 10$ to 18 (Fig. 4.12a).

In the detailed diagram for this cross plane shown in Fig. 4.12b, the distribution at the span-wise position $Y = 0.774$ is noticeable. It represents the global maximum in the pressure fluctuations, that appears in the region of the suction peak of the primary vortex. The energy is concentrated at reduced frequencies $k = 8$ to 16.

High angle of attack ($\alpha = 23°$). The properties of the spectral distributions are quite similar for $\alpha = 23°$ compared to the $\alpha = 18°$ case, apart from a slight concentration of pressure fluctuations in the frequency bands $k = 2$ to 5 at $X = 0.8$ and $k = 3$ to 8 at $X = 0.6$ (Fig. 4.13). This concentration is related to the vortex breakdown.

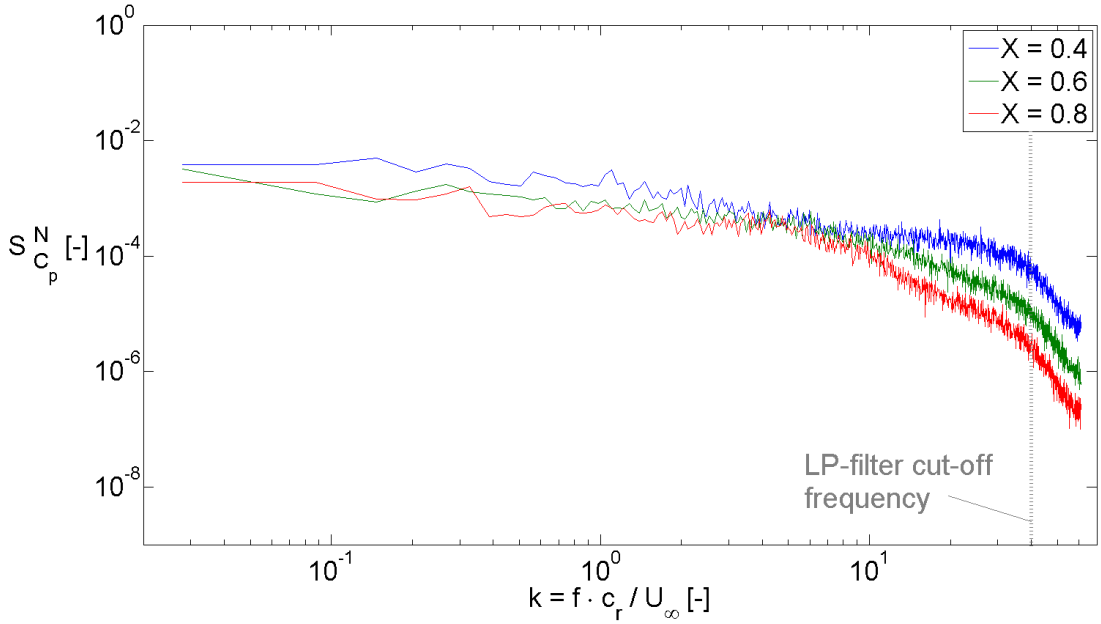

(a) Power spectral density for $Y = 0.725$

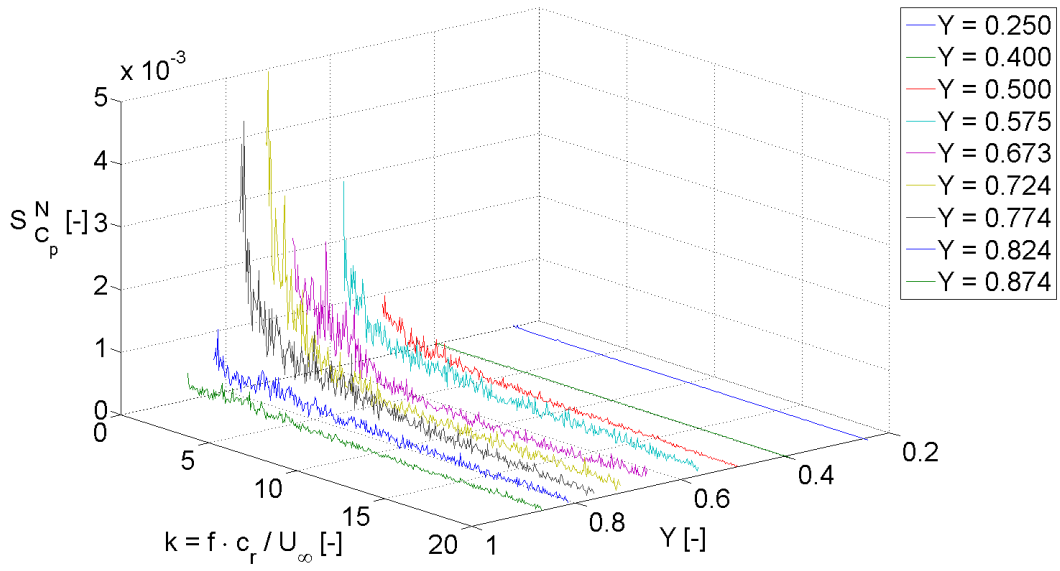

(b) Power spectral density for $X = 0.4$

Figure 4.11.: Spectral analysis for $\alpha = 13°$, $Re_{mac} \approx 1.0 \times 10^6$, and $M = 0.07$

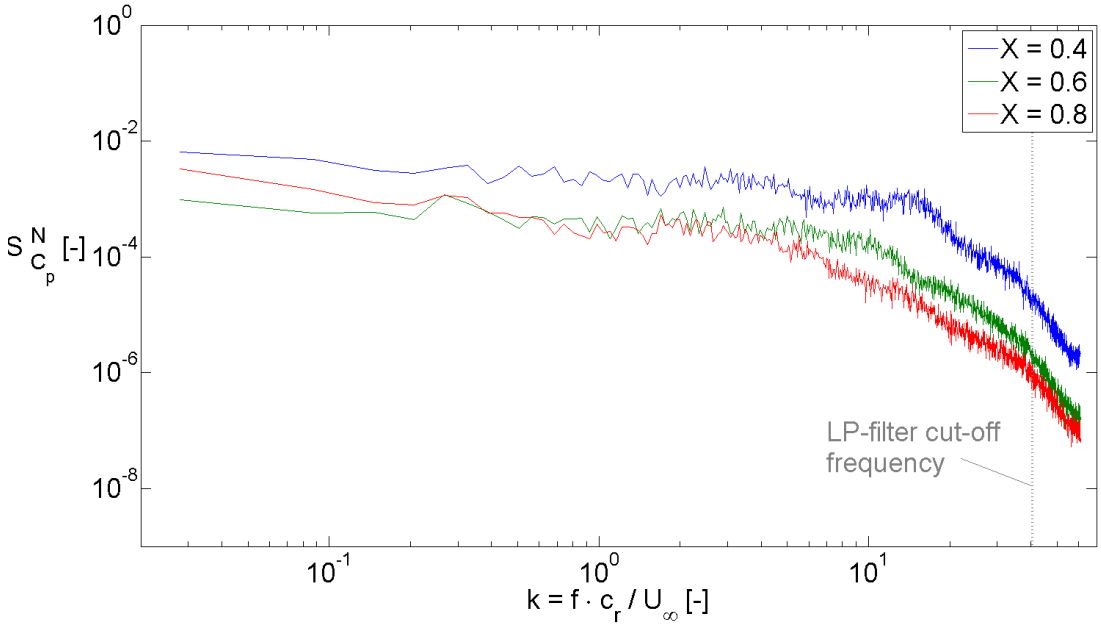

(a) Power spectral density for $Y = 0.725$

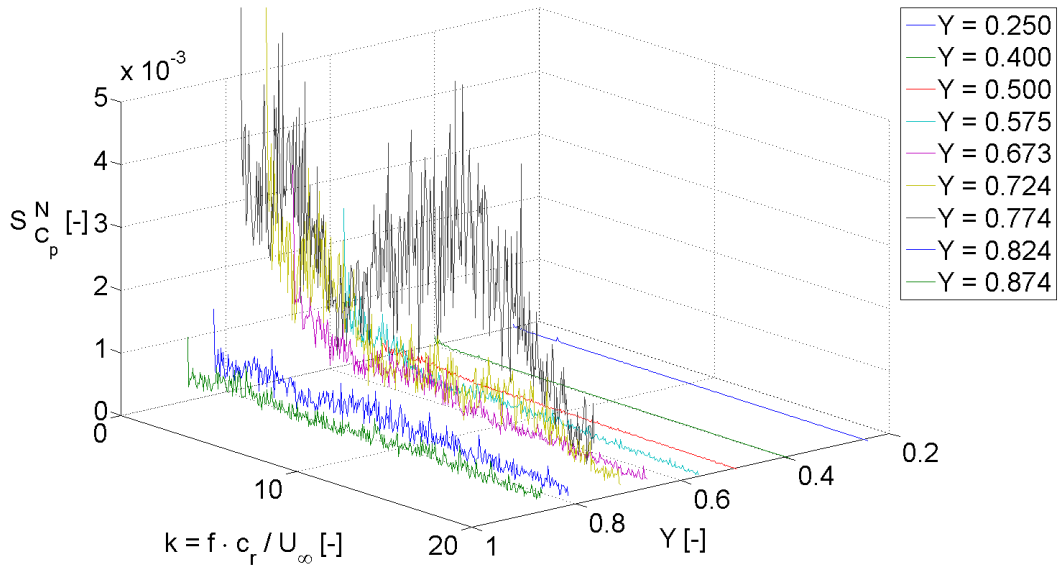

(b) Power spectral density for $X = 0.4$

Figure 4.12.: Spectral analysis for $\alpha = 18°$, $Re_{mac} \approx 1.0 \times 10^6$, and $M = 0.07$

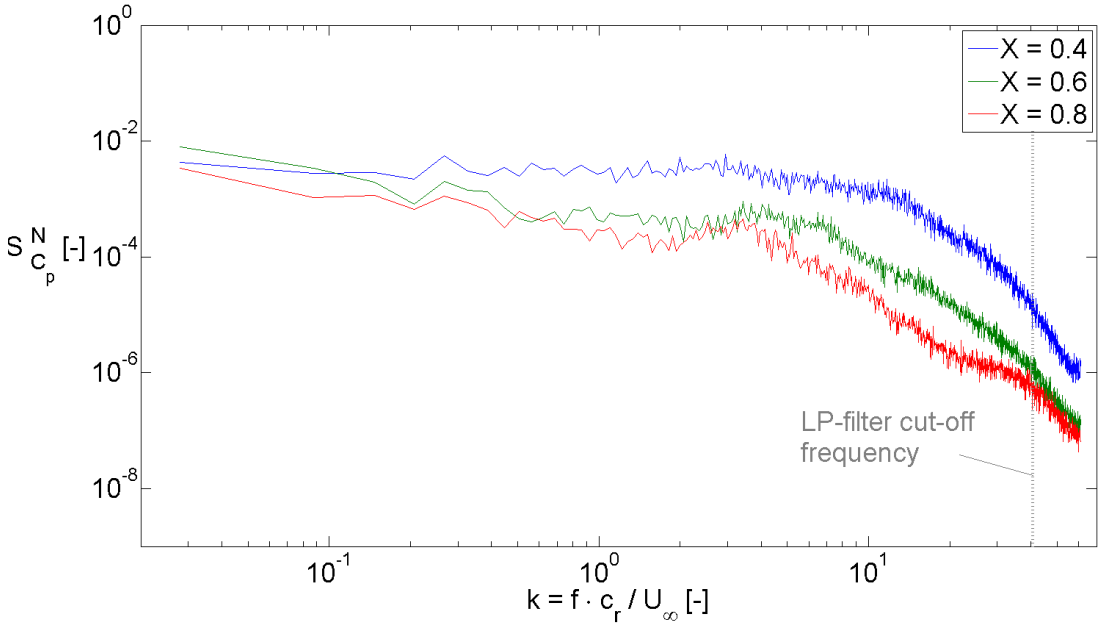

(a) Power spectral density for $Y = 0.725$

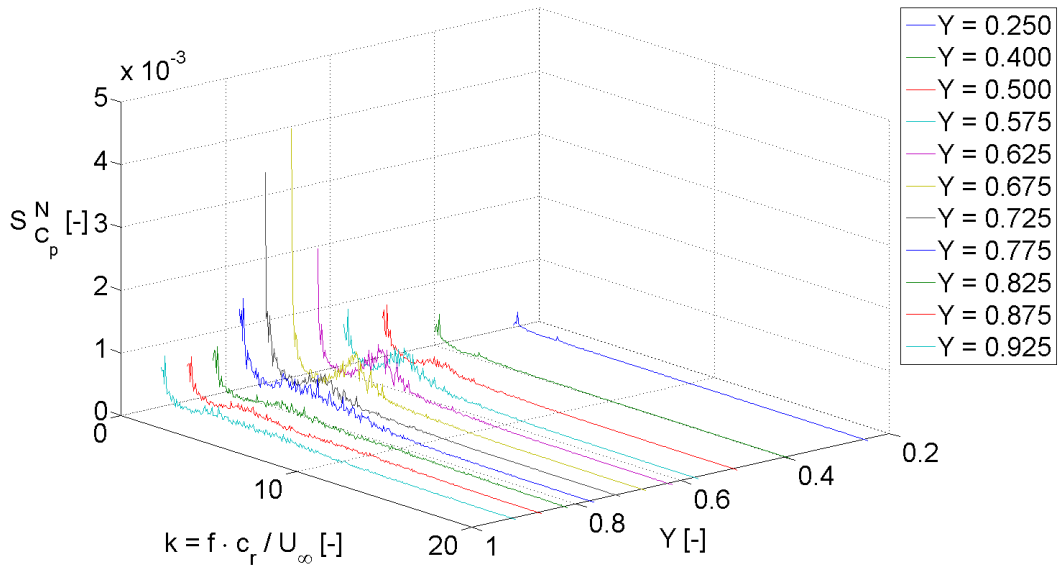

(b) Power spectral density for $X = 0.8$

Figure 4.13.: Spectral analysis for $\alpha = 23°$, $Re_{mac} \approx 1.0 \times 10^6$, and $M = 0.07$

Although vortex breakdown has already passed over the trailing edge at this angle of attack and the burst location is situated at $X \leq 0.6$, this is only weakly reflected by a rise in the spectral pressure distributions. This is due to the fact that the vortex breakdown manifests itself in different consecutive steps [6]. First, a structural change occurs in the vortex core. Second, the region of highest turbulence intensity is expanded in radial direction. Third, the surface pressure fluctuations will rise subsequently. Therefore, a difference related to the angle of incidence or the chord-wise location is observed for the maximum intensity of the velocity and the pressure fluctuations, respectively [6].

4.2.2.2. Stall

At the maximum angle of attack $\alpha = 35°$, vortex breakdown is located upstream of the cross-section $X = 0.4$. The level of the measured pressure fluctuations is very high (see Fig. 4.9b) and narrow-banded concentrations of the power spectral density occur in all measurement cross sections, see Fig. 4.14a. At $X = 0.4$, the dominant frequency peak is located at $k = 1.5$. For $X = 0.6$, it is observed at $k = 1.8$ and for $X = 0.8$ at $k = 2.8$. This reflects the frequency of the helical mode instability, that decays in stream-wise direction as the diameter of the vortex and of the spiral core flow grows in this direction.

The strong span-wise expansion of the vortex and the burst vortex core is evident in Fig. 4.14b, where this frequency peak dominates the spectrum at every measurement position. $S^N_{c_p}$ is maximal at $Y = 0.4$ to 0.6, where the vortex core flow is closest to the wing surface and the pressure fluctuations are impressed most intensively on the surface. The same phenomenon with even stronger peaks is observed downstream at $X = 0.6$ and $X = 0.8$. The results for all three measurement cross-sections are shown in Appendix B.

4.2.2.3. Post-stall

The spectral quantities at the post-stall angle of attack $\alpha = 45°$ differ significantly from the results at the other angles of attack. The flow on the upper side of the wing is characterized by a dead-water region. The spectra shown in Fig. 4.15a and Fig. 4.15b are close to isotropic turbulence, which is characterized by an energy decay proportional to $k^{-5/3}$. No further significant characteristics can be observed at this angle of attack.

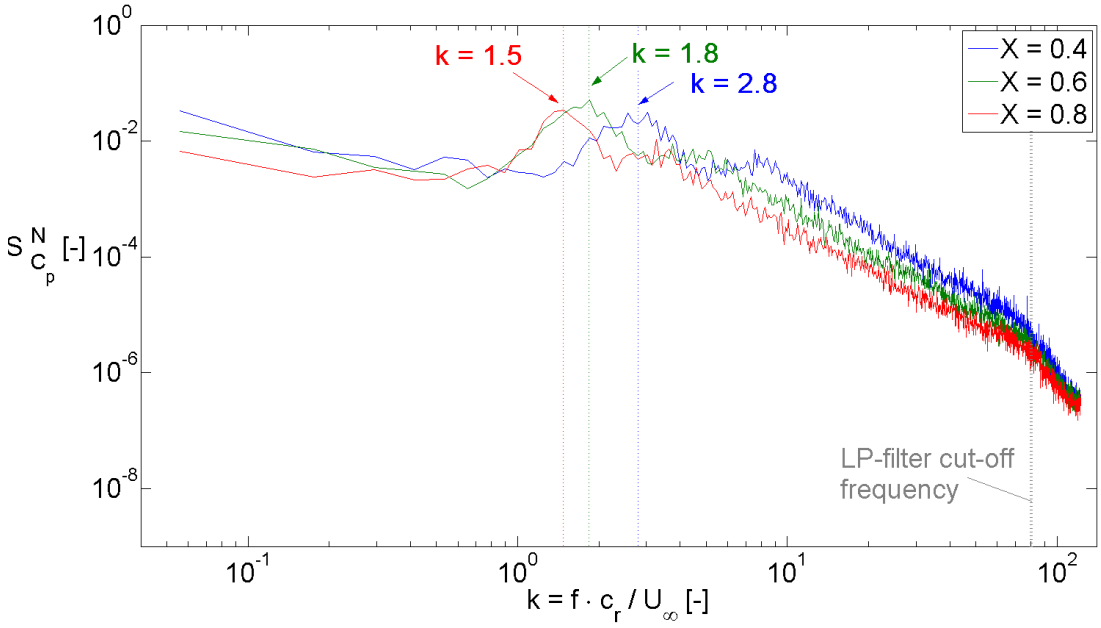

(a) Power spectral density for $Y = 0.5$

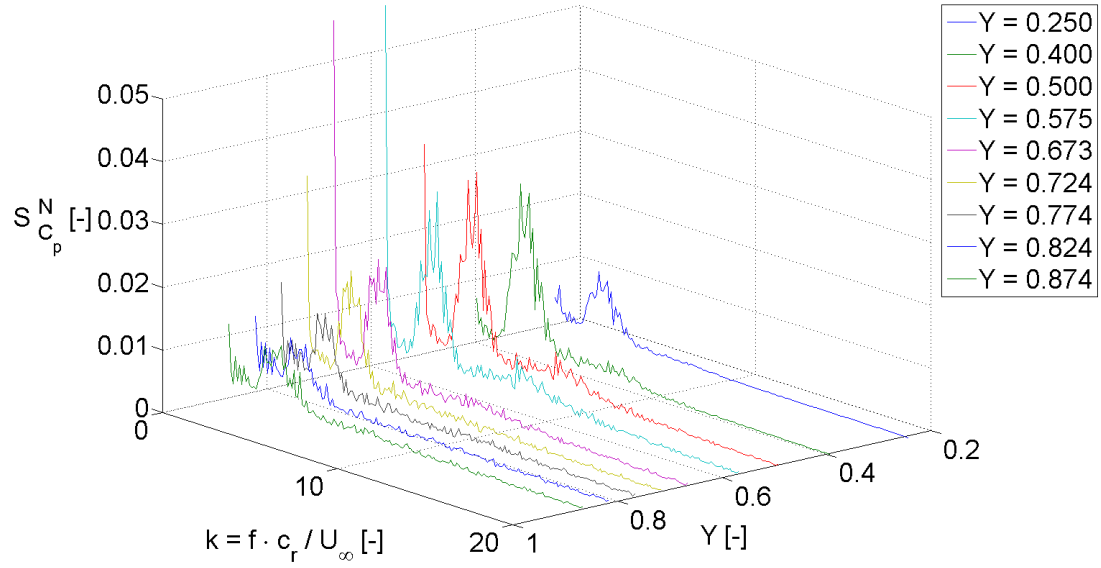

(b) Power spectral density for $X = 0.4$

Figure 4.14.: Spectral analysis for $\alpha = 35°$, $Re_{mac} \approx 0.5 \times 10^6$, and $M = 0.035$

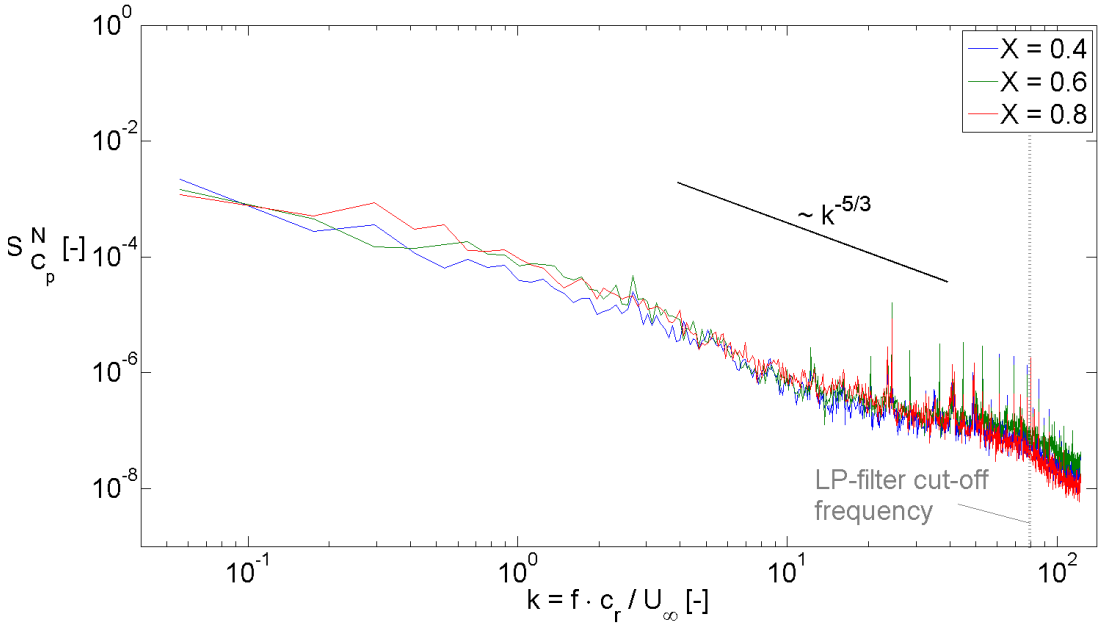

(a) Power spectral density for $Y = 0.875$

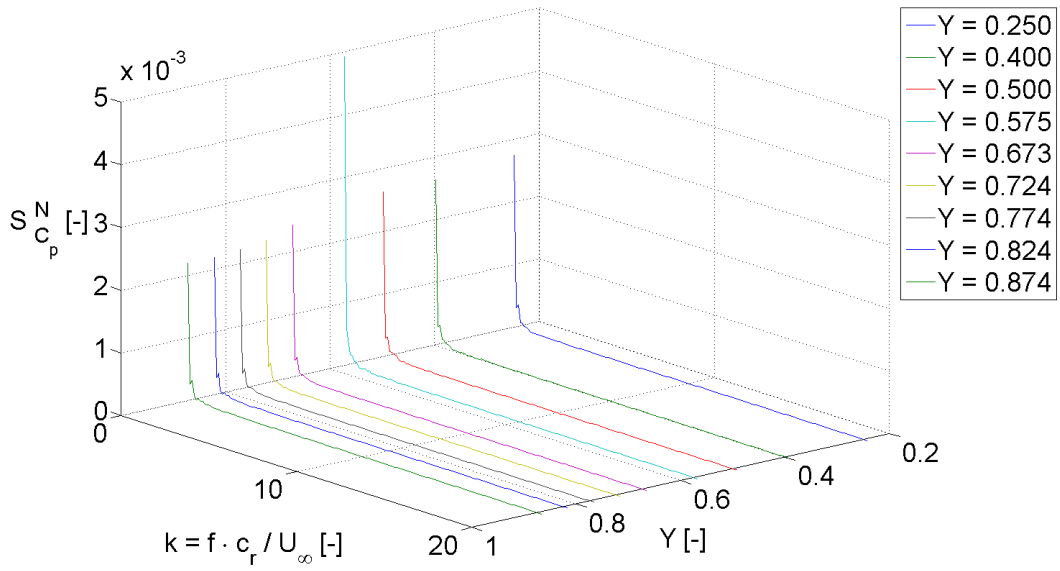

(b) Power spectral density for $X = 0.4$

Figure 4.15.: Spectral analysis for $\alpha = 45°$, $Re_{mac} \approx 0.5 \times 10^6$, and $M = 0.035$

4.3. Flow Field

In this section, the flow field is presented for the following combinations of angle of attack and Reynolds number: $\alpha = 23°$ at $Re_{mac} = 1.0 \cdot 10^6$, $\alpha = 35°$ at $Re_{mac} = 0.5 \cdot 10^6$ and $\alpha = 45°$ at $Re_{mac} = 0.5 \cdot 10^6$. The results were gained from HWA measurements on the basic half delta wing configuration in wind tunnel B of Technische Universität München.

In the first subsection, the mean and the turbulent velocity distributions are shown for each flow case. Subsequently, a spectral analysis is carried out for the velocity field above the wing.

4.3.1. Time-averaged flow field

The following flow field analysis refers to the contour plots of the mean axial velocity u/U_∞ and the axial turbulence intensity u_{rms}/U_∞ in the measurement planes on the wing's upper side, see Figs. 4.16 to 4.18. Both are shown as dimensionless quantities to enable a better comparison between the different angles of attack. The displayed axial velocity was gained from the HWA measurements with the vertical probe orientation. Hence, the vertical velocity component w was measured as the second velocity component. Additionally, measurements with horizontal probe orientation were conducted for all test cases to record the horizontal velocity component v. The sum of the time-averaged cross-velocities v and w of each measurement plane is displayed in vector form.

4.3.1.1. Pre-stall

The result for the angle of attack $\alpha = 23°$ at $Re_{mac} = 1.0 \cdot 10^6$ is shown in Fig. 4.16 [42], [41]. The vortex dimensions are illustrated by an increase in the turbulence intensity distributions in the plots on the right hand side. In lateral direction, the vortex system expands from $Y \approx 0.25$ to $Y = 1.0$, where the shear layer is shed along the leading edge. The vertical vortex dimension ranges from the wing's surface to $Z = 0.5$.

The vortex breakdown has already progressed from the rear part of the wing to a position in front of the first measurement cross-section ($X_{bd} < 0.4$). This is clearly depicted by the annular structure of local rms maxima of the axial velocity fluctuations in the cross sections at $X = 0.4$, $X = 0.6$ and $X = 0.8$ (Figs. 4.16a - c, right). The local u_{rms} maxima are at a very high level ($u_{rms}/U_\infty = 0.38$). The annular structure is caused by the spiral rotation of the vortex core flow (helical mode instability), that sets in at the breakdown location. The turbulence intensity of the core flow decreases in the chord-wise direction. The other local maximum of turbulence intensity near the leading edge and close to the wing's surface marks the position of the secondary vortex. It is also observed in all considered cross-sections.

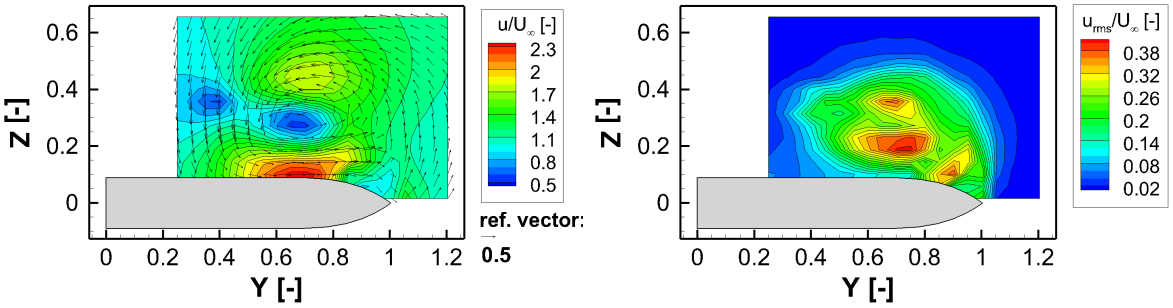

(a) $X = 0.4$

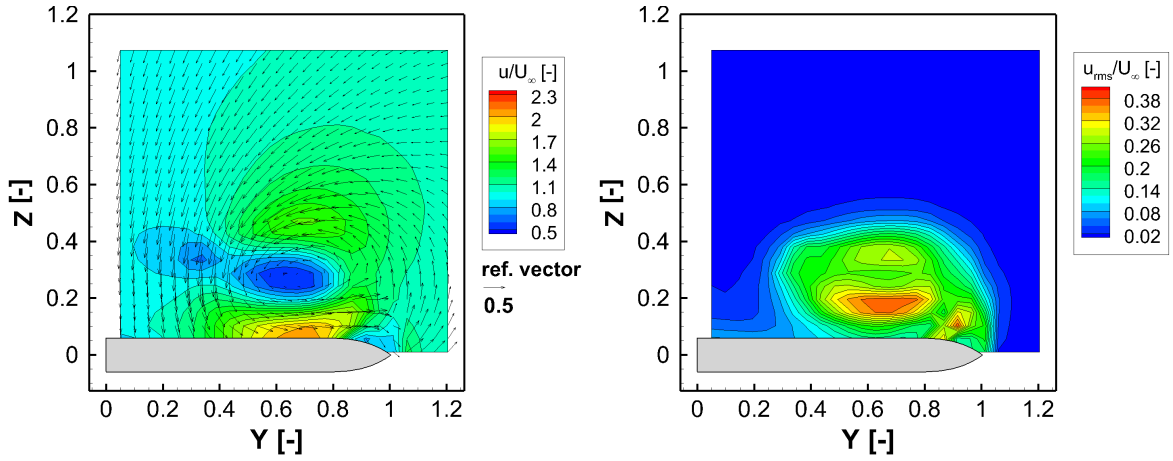

(b) $X = 0.6$

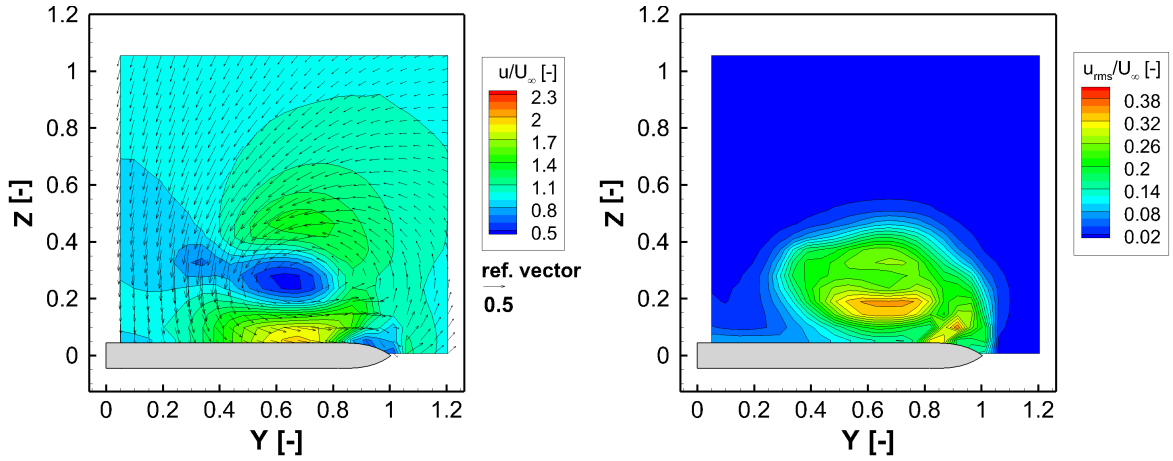

(c) $X = 0.8$

Figure 4.16.: Distribution of the axial velocity (left) and axial velocity fluctuations (right) at $\alpha = 23°$ for $Re_{mac} = 1.0 \cdot 10^6$, and $M = 0.07$; HWA measurement result

The vectors visualizing the cross-velocities v and w are shown in the left of Fig. 4.16. Their distribution is characteristic of a vortical flow structure and their center of rotation indicates the location of the vortex center. It is located at $Y \approx 0.65$ and $Z \approx 0.275$ in all considered measurement sections. The axial velocity distributions (left of Fig. 4.16) exhibit a typical structure with two local maxima, which was also observed in former HWA measurements [6]. The vortex-induced axial velocities are very high below the vortex center in the vicinity of the wing surface, and they reach $u/U_\infty = 2.35$ at $X = 0.4$. Noteworthy is an area of decelerated axial flow between these two local maxima, which occurs in the center of the vortex in all three measurement planes. It is another sign for the burst primary vortex at $\alpha = 23°$ and reaches values as low as $u/U_\infty = 0.55$. The axial core velocity is considerably smaller than the value of the free stream velocity ($U_\infty = 24\ m/s$) and the corresponding area expands in chord-wise direction.

Vortex breakdown location: comparison with PIV results. The chord-wise position of the burst location recorded in the HWA measurements is $X_{bd} < 0.4$. This value was confirmed in several repetitive measurements. However, it differs from the observations made in the PIV measurements at the same free-stream conditions. In the PIV measurements conducted with the half wing model in wind tunnel A, the burst location was found to be situated further downstream, between $X = 0.4$ and $X = 0.6$. This offset in the breakdown location between the results from HWA measurements at wind tunnel B and PIV measurements at wind tunnel A can also be observed in the measurement results by Furman on the full delta wing model [17].

The reason for this offset in the breakdown location lies in the following two parameters:

- The hot-wire probe and its support cause an increased positive pressure gradient in the downstream direction. This leads to an upward-shift of the vortex breakdown location during HWA measurements due to the sensitivity of the vortex flow to an increased pressure gradient. This is not the case for the PIV measurements, where no perturbing object is brought into the flow.

- As the velocity measurements were carried out in different wind tunnel facilities with different test section geometries (HWA in the smaller wind tunnel B, PIV in wind tunnel A), different blockage ratios prevailed during the two types of measurement. The higher blockage ratio during the HWA measurements in wind tunnel B might have caused a shift of the vortex breakdown location in upstream direction.

According to Table 4.3, a difference in the breakdown location on the full and the half wing model of $\Delta X_{bd} \approx 0.2$ can be deduced from the results. This observation is consistent with the pressure measurement result, where a significant difference in the suction peak at $X = 0.6$ is observed for $\alpha = 23°$, see Fig. 4.8.

Table 4.3.: Vortex breakdown location for $\alpha = 23°$ and $Re_{mac} = 1 \cdot 10^6$

	Full model [17]	Half model
HWA, wind tunnel B	$0.4 < X_{bd} < 0.6$	$X_{bd} < 0.4$
PIV, wind tunnel A	$0.6 < X_{bd} < 0.8$	$0.4 < X_{bd} < 0.6$

4.3.1.2. Stall

The results of the HWA measurements at the maximum angle of attack $\alpha = 35°$ and $Re_{mac} = 0.5 \cdot 10^6$ are presented in Fig. 4.17, cf. [24], [37]. The vortex has a large lateral and vertical expansion, and it dominates the whole flow on the suction side of the wing. Compared to $\alpha = 23°$, the vortex center has moved to a position further inboard and further upwards, away from the wing surface. It is located at $Y \approx 0.55$ and $Z \approx 0.4$. In contrast to the pre-stall case, no area of reattached flow is existent on the inboard side of the wing.

The axial velocity field reveals a burst vortex, whose breakdown already progressed to the wing's apex (left of Fig. 4.17). This is clearly reflected by the area of decelerated axial flow in the region of the vortex core. The minimum of the axial velocity is $u/U_\infty = 0.55$ in the measurement cross-sections $X = 0.4$ and $X = 0.6$. It is considerably below the value of the free stream velocity $U_\infty = 12\ m/s$. The corresponding area of decelerated axial flow expands in the chord-wise direction.

As similarly observed for $\alpha = 23°$, the maximum turbulence intensities form an annular structure around the vortex axis, but their local maxima are higher compared to the pre-stall case ($u_{rms,max}/U_\infty = 0.48$). Another peculiarity is that the turbulence intensity maxima of the vortex core flow and of the secondary vortex are conglomerated.

4.3.1.3. Post-stall

In Fig. 4.18, the velocity field is shown for the post-stall case $\alpha = 45°$ at $Re_{mac} = 0.5 \cdot 10^6$, cf. [53], [39]. As reflected by the vectors representing the cross-velocities on the left hand side, the angle of attack is that high that the flow separating along the entire leading edge does not roll up and reattach to the wing as observed in the pre-stall and stall regime. Instead, the flow field in the two measurement planes is characterized by a large dead water region above the wing and a detached shear layer originating along the leading edge and forming the transition from the stagnant flow over the wing to the approaching free-stream flow. The shear layer comprehends high velocity gradients. Its curvature at the rear measurement cross-section at $X = 0.6$ is higher than at $X = 0.2$. No vortical structure in terms of a leading edge vortex is detected.

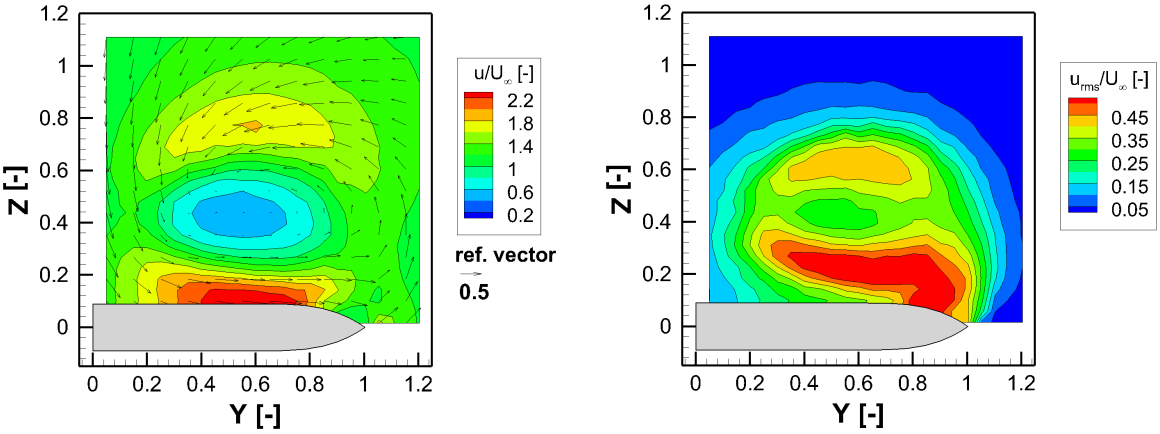

(a) $X = 0.4$

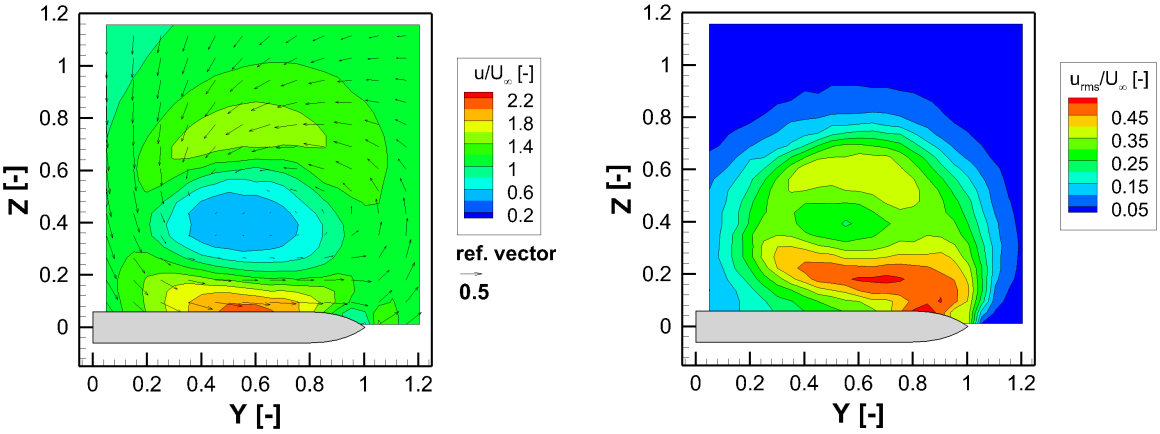

(b) $X = 0.6$

Figure 4.17.: Distribution of the axial velocity (left) and the axial velocity fluctuations (right) at $\alpha = 35°$ for $Re_{mac} = 0.5 \cdot 10^6$ and $M = 0.035$; HWA measurement result

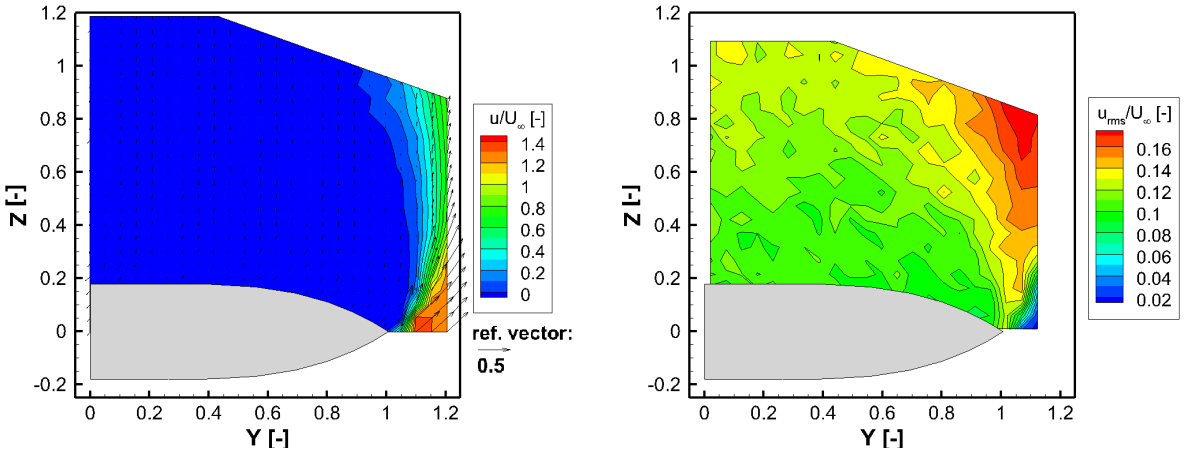

(a) $X = 0.2$

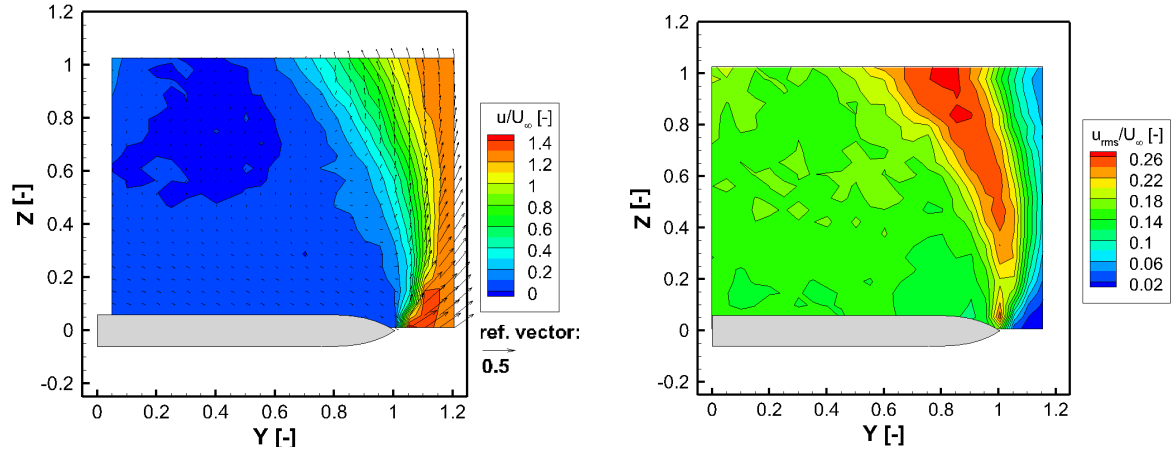

(b) $X = 0.6$

Figure 4.18.: Distribution of the axial velocity (left) and the axial velocity fluctuations (right) at $\alpha = 45°$ for $Re_{mac} = 0.5 \cdot 10^6$ and $M = 0.035$; HWA measurement result

The axial velocities gained from the HWA measurements are very small and close to zero above the wing, see left of Fig. 4.18. De facto, a back flow with low negative axial velocities dominates the region on the upper side of the wing, but these velocity conditions cannot be reflected correctly by the applied HWA measurement technique with a cross-wire type probe. The axial velocities are measured correctly in the PIV measurements, the results are shown in Section 5.4.2 for the post-stall case at $\alpha = 45°$.

The level of the turbulence intensities shown on the right of Fig. 4.18 amounts to $u_{rms}/U_\infty = 0.12 - 0.2$ above the wing. It is much lower than for the vortex structures observed at $\alpha = 23°$ and $\alpha = 35°$. The maxima in the velocity fluctuations ($u_{rms,max}/U_\infty = 0.26$) are found in the region of the shear layer, where the velocity gradient is maximal.

4.3.2. Spectral analyis

In analogy to chapter 4.2.2, the axial velocity fluctuations $S_{u'}$ are analyzed in the HWA measurement cross sections of the pre-stall, stall and post-stall regime. In the pre-stall and stall case, special attention will be paid to the helical mode instability of vortex bursting.

4.3.2.1. Pre-stall

In Fig. 4.19, the turbulence intensity distribution of the axial velocity component u_{rms} is shown for the rear measurement plane $X = 0.8$, $\alpha = 23°$ and $Re_{mac} = 1.0 \cdot 10^6$, cf. [42], [37]. It clearly reveals the annular structure of the burst vortex core. In addition, the power spectral density of the axial velocity fluctuations is plotted for three specific points in the vortex flow.

The turbulence intensity in the outer shear-layer region of the baseline vortex (measurement point 3) is remarkably higher than in the area not affected by the leading-edge vortex. A moderate increase of turbulent kinetic energy in a very broad frequency range from 80 to 400 Hz is observed. In the shear layer over the burst vortex core at measurement point (2), these amplitude peaks are slightly higher, but they strongly decline for increasing frequencies.

The highest values of turbulent kinetic energy appear in the annular core region of the burst vortex. They become manifest in narrow-band concentrations at a frequency of approximately 55 to 76 Hz, as can be seen from the result at measurement point 1. This concentration is linked to the helical mode instability of vortex bursting (see also Chapter 2.3).

In Fig. 4.20, the spectrum at measurement point 1 in Fig. 4.19 is contrasted with the spectra of two measurement points in the vortex core at the cross sections $X = 0.4$ and 0.6. At all three points, a narrow-band concentration of turbulent kinetic energy can be observed.

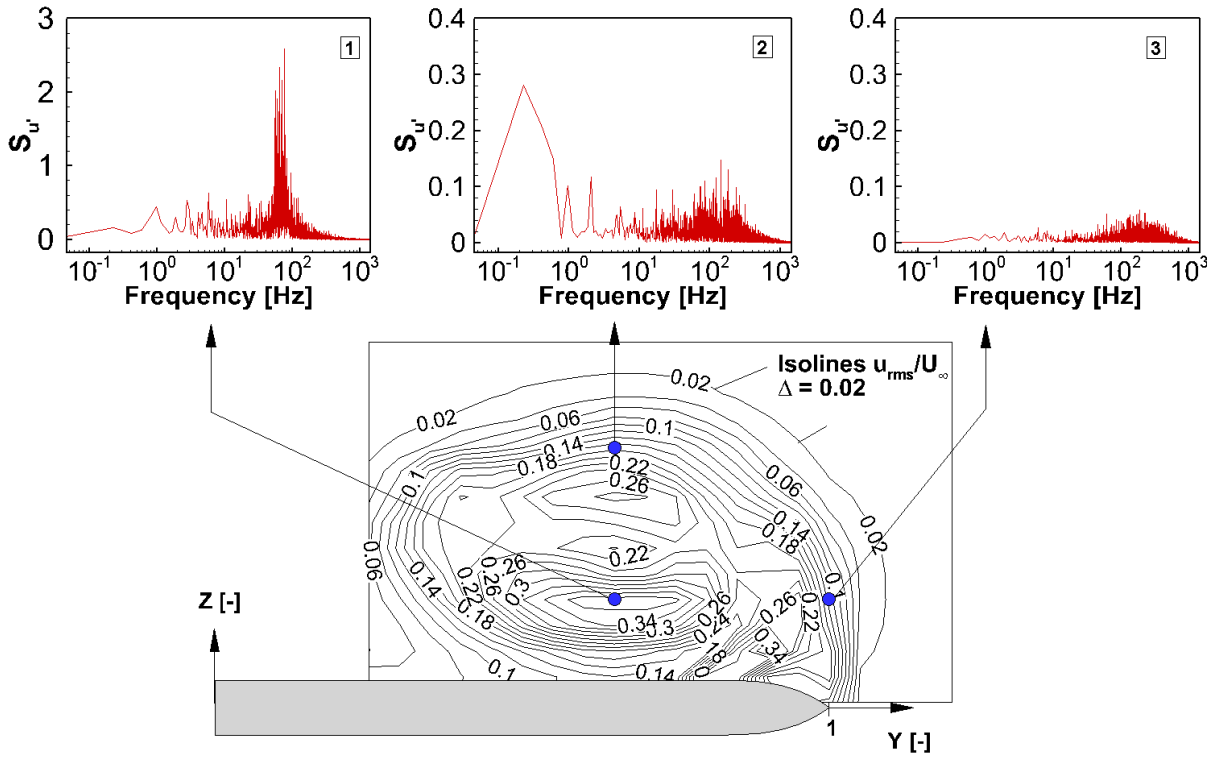

Figure 4.19.: Power spectral density for axial velocity fluctuations ($S_{u'}$) in the shear layer and the burst vortex core at $\alpha = 23°$, $X = 0.8$, $Re_{mac} = 1 \cdot 10^6$, and $M = 0.07$; baseline case, cf. [41]

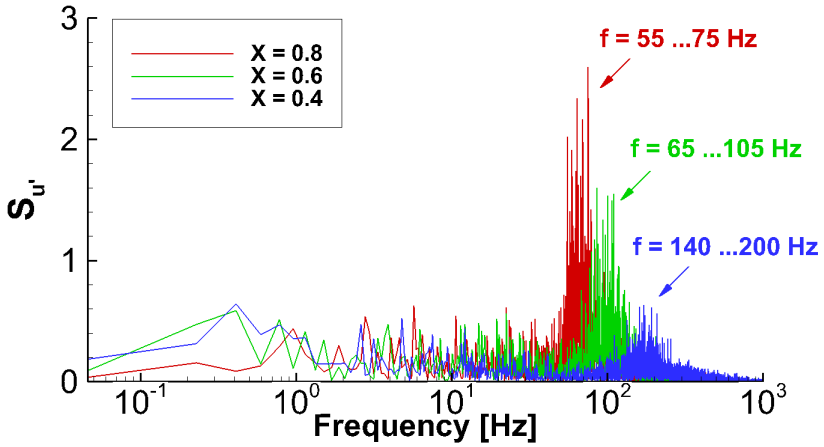

Figure 4.20.: Power spectral density for axial velocity fluctuations ($S_{u'}$) reflecting the helical mode instability at different chord-wise stations for $\alpha = 23°$, $Re_{mac} = 1 \cdot 10^6$ and $M = 0.07$; baseline case

For the fore cross-sections, this concentration of turbulent kinetic energy is detected at higher frequencies compared to those recorded at $X = 0.8$. For the second measurement plane ($X = 0.6$), the concentration of kinetic energy is measured at frequencies $f = 65\ Hz$ to 105 Hz. For the first measurement plane at $X = 0.4$, the concentration is found at frequencies $f \approx 140$ to 200 Hz. Additionally, several single peaks were detected in the flow field at the frequency $f = 4\ Hz$. It could be related to the frequency of the quasi-periodic fluctuations of the vortex breakdown location.

4.3.2.2. Stall

Fig. 4.21 shows the contour plot of the axial velocity fluctuations for $X = 0.6$, $\alpha = 35°$ and $Re_{mac} = 1.0 \cdot 10^6$. The large cross-section of the vortex core flow at $\alpha = 35°$ is clearly visible.

The dominating role of the burst vortex core in the whole vortex structure is also observed by the omnipresence of the narrow-banded frequency concentration of the helical mode instability. It is not only detected in the region of the vortex core as observed at $\alpha = 23°$, but in the whole vortex domain, including the region of the shear layer. The frequency concentration is found at $f \approx 15$ to 25 Hz with relatively low energy content right after the separation from the leading edge (see measurement point 2) and in the upper part of the vortex (measurement point 1). Very high values are observed in the lower part of the burst vortex core and also close to the wing's surface (points 3 and 4).

In agreement with the results for $\alpha = 23°$, a frequency shift of the narrow-banded concentration in turbulent kinetic energy is observed when the results for $\alpha = 35°$ are compared for different chord-wise stations (see Fig. 4.22). In comparison to $X = 0.6$, the spectrum is characterized by lower values at higher frequencies for the forward measurement sections $X = 0.4$ and $X = 0.2$.

4.3.2.3. Post-stall

In Fig. 4.23, the power spectral density is analyzed for different measurement points in the post-stall regime ($\alpha = 45°$). Three main areas are of interest at this angle of attack: the dead water area above the wing, the separated shear layer emanating from the leading edge, and the outer area of the shear layer, that is close to free-stream conditions.

Measurement point 1 is representing the region of the dead-water area above the wing. At this measurement station, the power spectral density is dominated by low-frequency fluctuations at $f \approx 1.5$ to 6 Hz. They reflect the oscillations that occur in the dead water and back-flow zone over the wing and could also be observed when a filament probe was brought in this region during the wind tunnel experiments.

Measurement points 2 and 5 lie in the inner region of the shear layer, where the axial turbulence intensity reaches its local maximum. Here, the spectrum is characterized by broad-banded large-amplitude velocity fluctuations at $f \approx 2$ to 50 Hz.

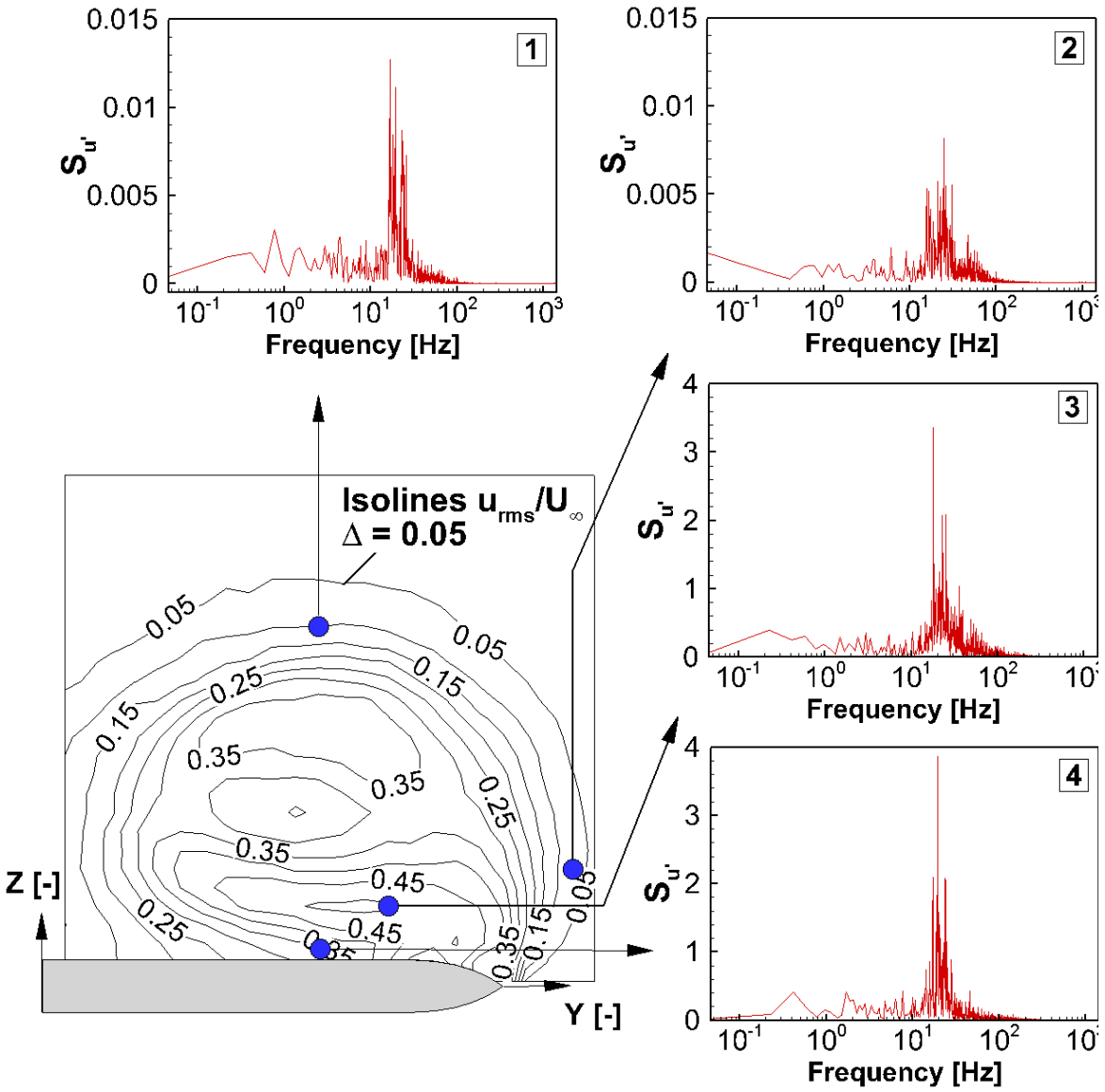

Figure 4.21.: Power spectral density for the axial velocity fluctuations ($S_{u'}$) in the shear layer and the burst vortex core at $\alpha = 35°$, $X = 0.6$, $Re_{mac} = 0.5 \cdot 10^6$ and $M = 0.035$; baseline case

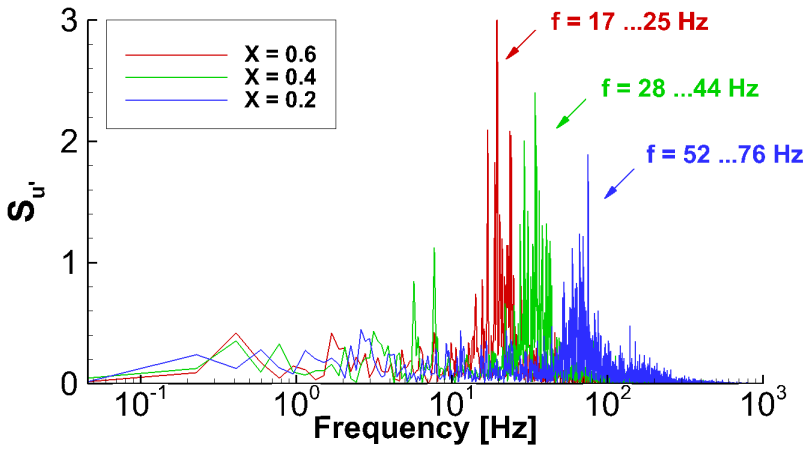

Figure 4.22.: Power spectral density for axial velocity fluctuations ($S_{u'}$) reflecting the helical mode instability at different chord-wise stations for $\alpha = 35°$, $Re_{mac} = 0.5 \cdot 10^6$ and $M = 0.035$; baseline case

More narrow-banded concentrations of small-amplitude axial velocity fluctuations occur at the outer edge of the shear layer, see the spectra at measurement points 3 and 4. In the vicinity of the leading edge, they are observed at relatively high frequencies, $f \approx 30$ to 120 Hz or $k \approx 0.4$ to 9.8 (point 4). In greater distance to the leading edge (point 3), the observed concentration is found at lower frequencies $f \approx 15$ to 50 Hz or $k \approx 1.2$ to 4. These narrow-banded concentrations of turbulent kinetic energy are related to the discrete vortices, that are shed along the leading edge of the wing (see also Chapter 2.2).

The observations in the spectra of the dead water area and in the region of highest turbulence intensity in measurement plane $X = 0.2$ resemble those from the rear measurement plane $X = 0.6$ shown in Fig. 4.23. Unfortunately, the outer edge of the shear layer was not covered by the measurement plane, so that the spectrum of the discrete vortices at this location cannot be analyzed or compared to $X = 0.6$.

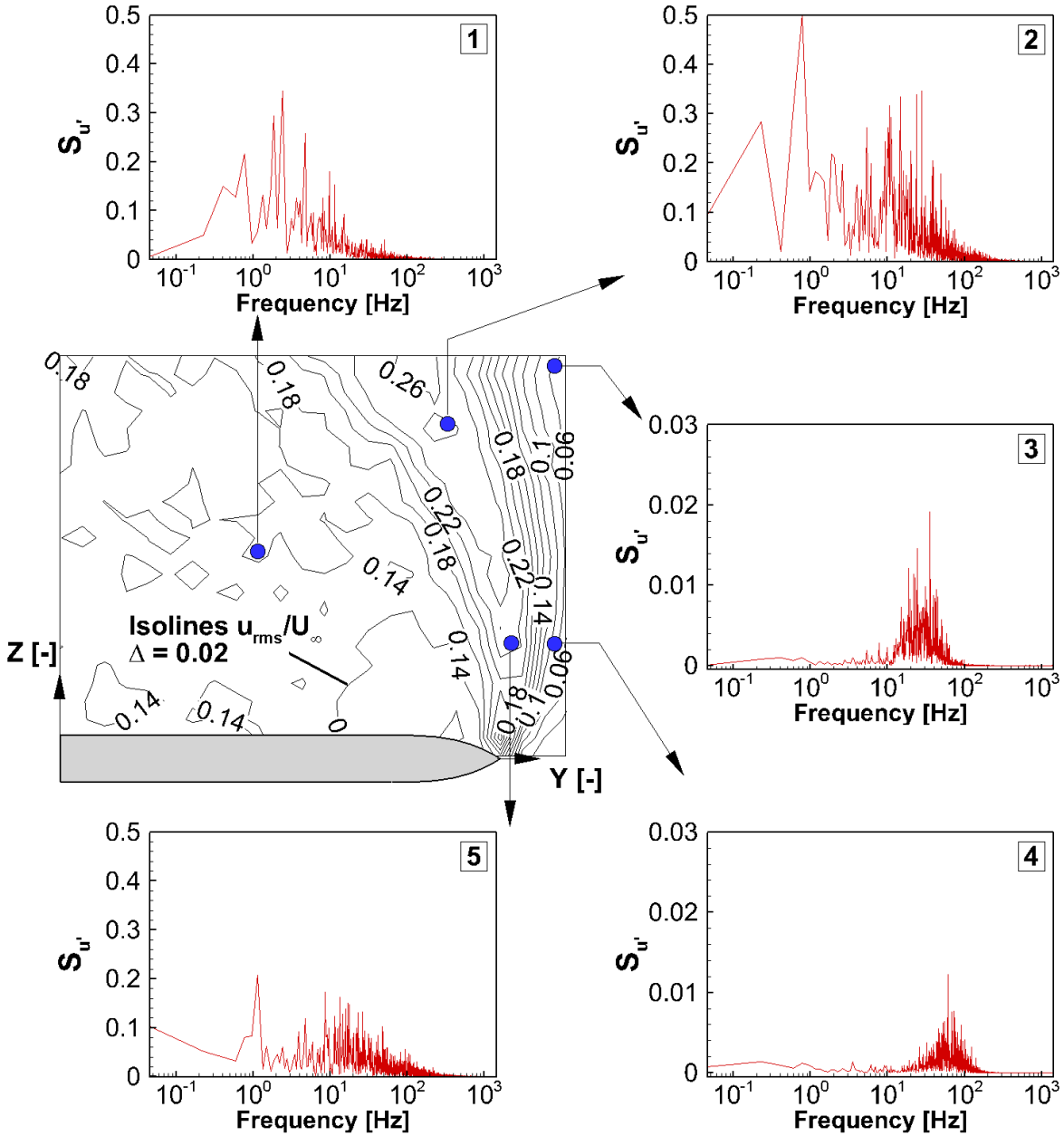

Figure 4.23.: Power spectral density for axial velocity fluctuations ($S_{u'}$) in the shear layer and the burst vortex core at $\alpha = 45°$, $X = 0.6$, $Re_{mac} = 0.5 \cdot 10^6$ and $M = 0.035$; baseline case

4.4. Synthesis

In this section, the main observations from the aerodynamic flow measurements are summarized for the angles of attack, that were studied for the basic half delta wing model. Subsequently, the flow instabilities observed in the spectral analysis of the pressure and the velocity fluctuations are compared to empirical relations derived from measurements for other delta wing configurations.

4.4.1. Stages of vortex development

Increasing the angle of attack from $\alpha = 13°$ to 23°, the evolution from a partially developed vortex at $\alpha = 13°$ passing the fully developed stage at $\alpha = 18°$ to a burst vortex at $\alpha = 23°$ can be observed on the half delta wing VFE-2 geometry. The vortex cross-section increases and the suction peak level caused by the primary vortex is highly enlarged from $\alpha = 13°$ to $\alpha = 23°$.

The following properties characterize the flow field of the burst vortex at $\underline{\alpha = 23°}$:

- Vortex breakdown is estimated to be located at $X = 0.3$. It causes a sudden expansion of the vortex core flow and the reformation from axially accelerated to axially decelerated vortex core flow ($u/U_\infty = 0.55$).
- Under the vortex axis close to the wing surface, very high axial velocity maxima are observed ($u/U_\infty = 2.8$). They correspond to significant suction peaks that are measured on the wing surface at the span-wise position of the vortex center ($C_p = -3.0$ at $X = 0.4$). Both axial velocities and suction peak decline in chordwise direction.
- As a result of high velocity gradients, intense velocity fluctuations are observed (for instance, $u_{rms}/U_\infty = 0.38$ at $X = 0.4$). In the spectral analysis, narrow-banded concentrations of turbulent kinetic energy are detected in the vortex core flow. They are linked to the helical mode instability.

If the angle of attack is further increased, the effect of vortex bursting is even amplified. The flow at the maximum angle of attack $\underline{\alpha = 35°}$ is governed by the following aspects:

- The primary vortex expands over the whole span of the half delta wing and the lift coefficient is maximal ($C_{L,max} \approx 1.1$).
- The burst location has reached the apex and the burst vortex core covers a large area of the vortex cross section. Compared to $\alpha = 23°$, the maximal axial velocities and the mean suction pressure peak are diminished ($u_{max}/U_\infty = 2.2$, $C_{p,min} = -2.3$ at $X = 0.4$). In the rear part of the wing at $X = 0.6$ and 0.8, no distinctive suction peak is observed.

- The velocity and surface pressure fluctuations are even more intense compared to $\alpha = 23°$, namely $u_{rms,max} = 0.48$. Narrow-banded concentrations of the turbulent kinetic energy related to the helical mode instability dominate the vortex system.

After the collapse of the vortex structure for angles of attack beyond the stall region, completely different flow patterns are observed. The angle of attack $\underline{\alpha = 45°}$ in the post-stall regime is characterized as follows:

- The flow is governed by a dead water area over the wing as well as a detached shear layer that forms the transition zone to the free-stream flow. These flow properties strongly resemble the 2D-like flow case of an inclined flat plate. Due to the absence of the vortex system, the lift coefficient is significantly reduced ($C_L = 0.6$).
- In the dead water area above the wing, low and even negative axial velocities are observed. Therefore, the surface pressure level is very low.
- Close to the wing surface, low pressures and velocity fluctuations are observed. In contrast, increased velocity fluctuations are detected in the shear layer.

4.4.2. Observed flow instabilities

In the spectral analysis of the flow quantities, two types of instabilities related to leading edge vortex systems were of great importance: the discrete vortices that are shed along the leading edge of the wing and the helical mode instability of vortex bursting. In the following, the measurement results on the half wing model are compared to observations from other experiments.

Discrete vortices. In [19], Gad-el-Hak and Blackwelder conducted water tunnel experiments to investigate the properties of the substructures that feed the primary vortex of a delta wing. They concluded that the shear layer separating along the leading edge of a delta wing rolls up immediately to form discrete vortices parallel to the leading edge. The discrete vortices undergo a pairing process, in which two discrete vortices merge to one bigger vortex [19]. Thereby, the shear layer is growing with increasing distance from the leading edge. In the pre-stall and stall regime, the shear layer is wrapped up to form the primary vortex. At even higher angles of attack in the post-stall regime, the vortical structures are transported downstream without rolling-up and forming a primary vortex [68].

Moreover, Gad-el-Hak and Blackwelder studied the shedding frequency of the discrete vortices for different angles of attack. They made the following observations [19]:

- For a constant free-stream velocity U_∞, the shedding frequency decreases as the angle of attack is increased.
- At constant incidence, the shedding frequency is proportional to $\sqrt{U_\infty}$.

- The following empirical relation for the shedding frequency f was found in the experiments with a 45° swept delta wing at Reynolds numbers $Re_{mac} = 1.25 \cdot 10^4$ to $3.33 \cdot 10^5$:

$$f c_r / U_\infty = 1625 / \sqrt{Re_{mac}}. \tag{4.1}$$

Applied to the test case at $\alpha = 45°$ and a root chord Reynolds number $Re_{mac} = 0.5 \cdot 10^6$, the shedding frequency derived from Eq. 4.1 is $k = 5.144$. This corresponds to $f = 63\ Hz$ for $c_r = 0.98\ m$ and $U_\infty = 12\ m/s$. In the experimental results, narrow-banded concentrations in the spectral analysis of the axial velocity fluctuations were detected at $f \approx 30\ Hz$ to $120\ Hz$ in the vicinity of the leading edge, see Section 4.3.2.3. Therefore, one can conclude that experimental results correspond very well to the predicted frequency of vortex shedding.

Helical mode instability. In conjunction with vortex breakdown, narrow-banded concentrations can be observed in the spectral distribution of turbulent kinetic energy. This holds for both velocities and surface pressures downstream the breakdown location. As observed in the measurements at $\alpha = 23°$ and 35°, the dominating frequencies decrease in chord-wise direction, see Figs. 4.20 and 4.22.

On the basis of the flow field measurements on two different delta wing configurations, Breitsamter derived a universal frequency parameter k^*_{dom} [7]. It relates the dominating frequency f_{dom} arising in pressure and velocity fluctuations in the breakdown flow field to the delta wing geometry (ϕ), the free-stream conditions (U_∞, α) and the chord-wise location x:

$$k^*_{dom} = \frac{f_{dom} x}{U_\infty} \cot\phi \, \sin\alpha = 0.28 \pm 0.025. \tag{4.2}$$

On this basis, the dominating frequency of the helical mode instability can be estimated:

$$f_{dom} = \frac{1}{x \cot\phi} \frac{U_\infty}{\sin\alpha} (0.28 \pm 0.025). \tag{4.3}$$

Table 4.4.: Dominating frequencies related to the helical mode instability, listing for different chord-wise positions; values in Hz

	$\alpha = 23°$, $Re_{mac} = 1 \cdot 10^6$			$\alpha = 35°$, $Re_{mac} = 0.5 \cdot 10^6$		
chord-wise position	f_{dom} [7]	from $S_{u'}$	from $S^N_{c_p}$	f_{dom} [7]	from $S_{u'}$	from $S^N_{c_p}$
X = 0.4	85 - 102	140 - 200	-	29 - 35	52 - 76	20 - 51
X = 0.6	57 - 68	65 - 105	73 - 196	19 - 23	28 - 44	14 - 32
X = 0.8	43 - 51	55 - 75	49 - 122	15 - 17	17 - 25	11 - 26

In Table 4.4, the theoretical values for f_{dom} are listed for the two test cases at $\alpha = 23°$ ($U_\infty = 24\ m/s$) and $\alpha = 35°$ ($U_\infty = 12\ m/s$). In addition, the experimental results from the velocity and the surface pressure field analysis on the half delta wing are specified. The theoretical and experimental results lie in the same range. Nevertheless, the concentrations of turbulent kinetic energy observed in the experiment with the half wing configuration are observed at higher frequencies than predicted by the empirical relation.

4.4.3. Suggestions for a frequency-based actuation strategy

In the experiments presented in the following two chapters, frequency-dependent forcing is carried out on the half delta wing model by pulsed leading-edge blowing on the one hand and oscillating leading-edge flaps on the other. The results of the spectral analysis and the flow instabilities observed on the basic configuration find their way in the choice of the actuation frequencies.

For the pre-stall and stall regime, it is suggested to examine the effect of actuation frequencies that lie in the range of the helical mode instability observed in the pre-stall and stall regime (see Table 4.4 for distinct values). The peculiarity is, that this instability does not only vary with the angle of attack and the free-stream velocity, but also with the chord-wise position on the wing. Moreover, the measured shedding frequency should be tested as actuation frequency. It lies a bit higher than the helical mode instability and does also occur in the post-stall regime.
Additionally, a variation of the active actuation segments would be useful to examine if the location along the leading edge, where the flow control method is applied, does matter.

On this basis, force and flow field measurements will be carried out for both flow control methods. Thereby, the receptivity and the sensitivity of the flow to controlled disturbances is evaluated.

5. Pulsed blowing

In this chapter, the results obtained with pulsed blowing are analyzed. First, a parameter study is presented for different angles of attack. Subsequently, one test case at each angle of attack regime (pre-stall, stall and post-stall) is described in more detail including the results of pressure and velocity measurements.

5.1. Parameter study

The following parameters of the pulsed blowing system can be varied (see Chapter 3.1.2):

- the pulse frequency f_{pulse},
- the jet velocity U_{jet},
- the Duty Cycle DC,
- and the active segments.

In order to detect the optimal actuation parameters, force and HWA measurements are carried out in the framework of a parameter study. Primarily, the influence of different pulse frequencies and jet velocities is studied. Additionally, the duty cycle and the choice of the active segments are varied for particular parameter sets.

5.1.1. Pre-stall

A parameter study in the pre-stall regime is conducted by HWA for $\alpha = 23°$, $Re_{mac} = 1 \cdot 10^6$ and $M = 0.07$. The study focuses on the variation of the pulse frequency for $DC = 25\%$ and $p_{valve} = 5\ bar$, cf. [41].

HWA measurements for different actuation frequencies were carried out. The pulse frequencies are chosen on the basis of the spectral analysis of the baseline velocity field, see Section 4.3.2.1. In this analysis of the power spectral density, several peaks are detected at single values of $f = 65\ Hz$ and $f = 76\ Hz$ in the annular structure of the vortex core at $X = 0.8$. For the second measurement plane ($X = 0.6$), the concentration of turbulent kinetic energy is measured at $f = 65\ Hz$ to $f = 105\ Hz$. Therefore, the following frequencies are studied in the HWA measurements: $f_{pulse} = 52, 65, 76$, and $103\ Hz$, corresponding to $F^+ = 2.1, 2.6, 3.1$ and 4.3. These four frequencies lie in the range of the helical mode instability. Furthermore, one very low frequency ($f_{pulse} = 4\ Hz$

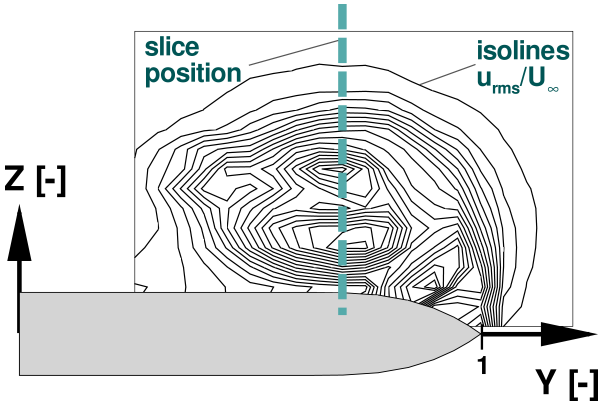

(a) Position of vertical slice

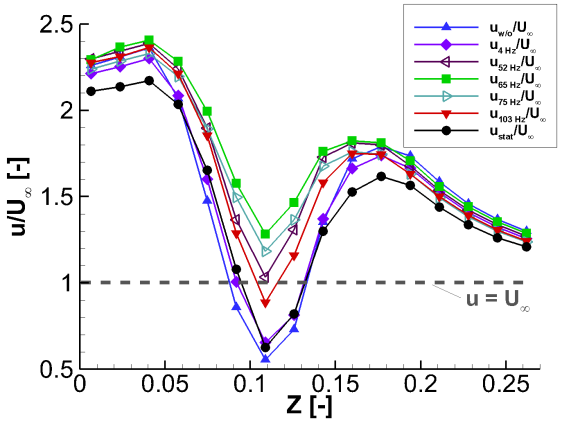

(b) Axial velocity component

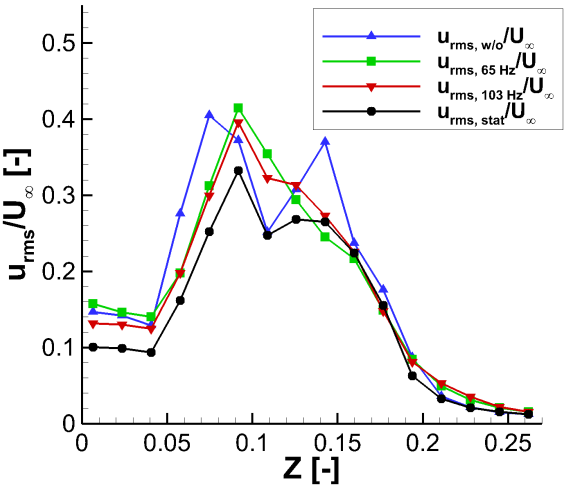

(c) Axial turbulence intensity

Figure 5.1.: Axial velocity component u and its turbulence intensity u_{rms} in vertical slices through the vortex center at $\alpha = 23°$, $X = 0.4$, $Re_{mac} = 1{\cdot}10^6$, and $M = 0.07$

corresponding to $F^+ = 0.16$) was tested, as several peaks were detected at this frequency in the spectral analysis of the velocities for the baseline case. It could be related to the frequency of the quasi-periodic fluctuations of the vortex breakdown location.
In the investigations, the same pulse frequency was applied to all slots without phase displacement. The chosen duty cycle is $DC = 25\%$.

The comparison of the amplitude of the mean axial velocity and its turbulence intensity is shown in Fig. 5.1 for different blowing profiles in a vertical slice through the vortex center at the measurement plane $X = 0.4$. The diagram comprises the curves of the baseline case (index “w/o”), the case of steady blowing (index “stat”), and pulsed blowing at the

frequencies $f_{pulse} = 4, 52, 65, 75$, and 103 Hz (indices 4 Hz to 103 Hz). All slices are extracted at the respective span-wise position of the vortex center (see Fig. 5.1a as an example for the baseline case).

Whereas the baseline case is characterized by the distinctive deficit in axial velocity ($u/U_\infty \approx 0.5$ at the vertical position $Z = 0.11$) and two local maxima in the axial turbulence intensity distribution, these criteria for a burst vortex are attenuated considerably by dynamic active blowing. Most impact is exerted by the pulse frequency of 65 Hz ($F^+ \approx 2.6$). In this case, the deficit in axial velocity is suppressed and the axial velocity component is increased to $u/U_\infty = 1.3$. Moreover, the turbulence intensity does only contain one local maximum, which indicates that the vortex breakdown location is shifted downstream.

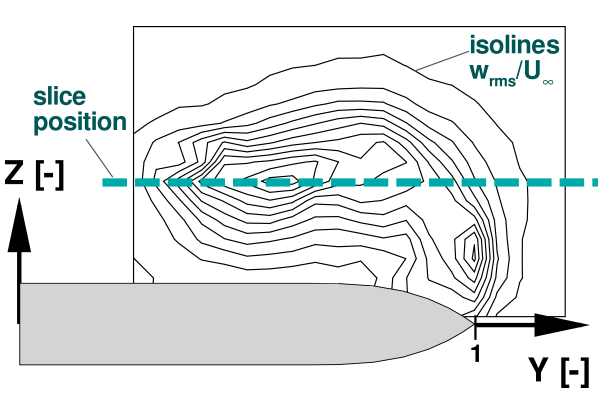

(a) Position of horizontal slice

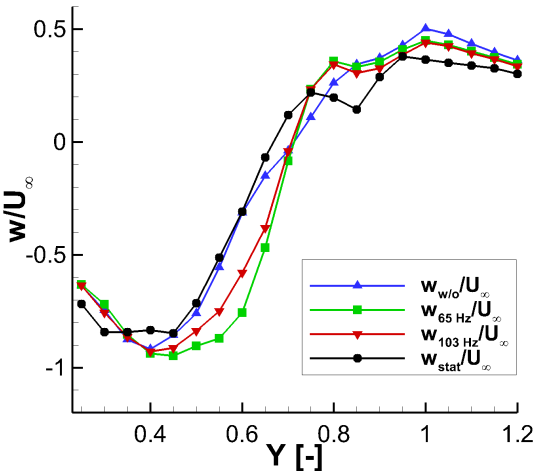

(b) Vertical velocity component

Figure 5.2.: Vertical velocity component w in horizontal slices through the vortex center at $\alpha = 23°$, $X = 0.4$, $Re_{mac} = 1 \cdot 10^6$, and $M = 0.07$

In Fig. 5.2b, the vertical velocity is plotted for a horizontal slice at $X = 0.4$ for both the baseline and the actuated cases. The slice is located at the vortex center, which corresponds to the position of the maximum w_{rms} value (see Fig. 5.2a). The gradient of the vertical velocity component is considerably increased by all types of blowing. As observed in the axial velocity component, the effect is strongest for blowing with $f_{pulse} = 65\ Hz$ ($F^+ \approx 2.6$).

In a nutshell, the plots visualize the concentration of the vortex as a result of blowing along the leading edge. It is also shown that the impact of the blowing is increased by applying a pulsed jet velocity profile in contrast to steady blowing. Furthermore, the results depend strongly on the chosen frequency. For all studied cases, the pulsing with $f_{pulse} = 65\ Hz$, which corresponds to the frequency related to the helical mode instability

measured at $X = 0.8$ and 0.6 (see Figs. 4.19 and 4.20), was most efficient. The results for frequencies to some extent below and above the value of the dominant instability frequency ($f_{pulse} = 52\ Hz$ and $f_{pulse} = 76\ Hz$) show almost the same characteristics, but the impact, in the sense of a decrease of the velocity deficit, is reduced. Hence, the test case of $f_{pulse} = 65\ Hz$ ($F^+ \approx 2.6$) will be analyzed in detail in the next subsection 5.2.

5.1.2. Pre-stall and stall

A series of three pulse frequencies was tested at angles of attack from $\alpha = 15°$ to 40° and the three Reynolds numbers $Re_{mac} = 0.5 \cdot 10^6, 1.0 \cdot 10^6$ and $1.5 \cdot 10^6$, see Figs. 5.3 to 5.7. The force measurements were carried out for $DC = 25\%$ and $p_{valve} = 4\ bar$, cf. [24]. The diagramed coefficients symbolize the alterations of the coefficients when pulsed blowing is active in comparison to the baseline case presented in Section 4.1, e.g.:

$$\Delta C_L = (C_{L,active\,blowing} - C_{L,baseline})/C_{L,baseline} \tag{5.1}$$

The choice of test frequencies is based on the results in the previous subsection. Therefore, $f_{pulse} = 65\ Hz$ is chosen as test frequency. Additionally, $f_{pulse} = 32\ Hz$ and $97\ Hz$ are tested. These frequencies are derived from the scaling of the first pulse frequency to the two other Reynolds numbers $Re_{mac} = 0.5 \cdot 10^6$ and $Re_{mac} = 1.5 \cdot 10^6$ based on the formula $f_{pulse,new} = 65\ Hz/(1 \cdot 10^6) \cdot Re_{mac,new}$.

Fig. 5.3 shows the effect of pulsed blowing on the lift coefficient. It is negative for angles of attack $\alpha < 23°$ and all three Reynolds numbers. In these cases, the vortex is not burst over the wing and the helical mode instability does not exist in the flow field over the wing. The actuation seems to disturb the (fully developed) vortex system in a way that the lift coefficient is reduced. In contrast, an increase in lift is observed for $\alpha \geq 23°$, $Re_{mac} = 0.5 \cdot 10^6$ and $f_{pulse} = 32\ Hz$ ($F^+ = 2.6$). The changes in the lift coefficient amount to 1 to 4% for the different angles of attack. ΔC_L is negative for the other two pulse frequencies $f_{pulse} = 65\ Hz$ and $97\ Hz$, whereupon the losses are higher for the higher pulse frequency. At $Re_{mac} = 1.0 \cdot 10^6$, the lift coefficient increases for all three actuation frequencies, only at $\alpha = 25°$ and $\alpha = 38°$ to 40° a slight decline in lift is recognized. At this Reynolds number, the frequency $f_{pulse} = 65\ Hz$ ($F^+ = 2.6$) is most efficient, but the average increase in lift is lower than at $Re_{mac} = 0.5 \cdot 10^6$ and $f_{pulse} = 32\ Hz$. At the highest Reynolds number $Re_{mac} = 1.5 \cdot 10^6$, pulsed blowing causes only small changes in the lift coefficients for $\alpha \geq 23°$. Summarizing, pulsed blowing at $F^+ = 2.6$ seems to stabilize the burst vortex system for the two lower Reynolds numbers, resulting in a slight increase of the lift coefficient.

The impact on the drag coefficient is plotted in Fig. 5.4. An improvement in the aerodynamic efficiency C_L/C_D would be highly desirable. It could be achieved if ΔC_L is higher than ΔC_D. In most instances, the changes in the drag coefficient compared to the baseline case correlate with the changes in the lift coefficient. If C_L is increased by pulsed blowing, the drag coefficient C_D does also increase. Only for a few particular

cases the aerodynamic efficiency is slightly improved, for instance for $Re_{mac} = 0.5 \cdot 10^6$, $f_{pulse} = 32\ Hz$ and $\alpha = 25°, 28°$ and $38°$.

As the rolling moment shown in Fig. 5.5 is measured for a semi span model, an increase in lift (see Fig. 5.3) leads to a reduction of the rolling moment, and a loss of lift causes an increase of the rolling moment, vice versa (see Fig. 3.16 for the definition of the positive aerodynamic moments). Transferred to a full-span configuration, the trend would be similar if pulsed blowing was applied only on one wing side with respect to a full-span model. Therefore, an influence on the rolling moment coefficient would become possible by pulsed blowing.

As a lift reduction is caused by pulsed blowing for $\alpha = 15°$ to $20°$, an increase in the rolling moment is induced. Analogously, a reduction of the rolling moment is observed for $f_{pulse} = 32\ Hz$ and $Re_{mac} = 0.5 \cdot 10^6$ and for the cases at $Re_{mac} = 1.0 \cdot 10^6$, where a lift increase was measured with active pulsed blowing. Thereby, two observations are noteworthy: first, the reduction of the rolling moment is relatively small in proportion to the lift increase observed for $f_{pulse} = 32\ Hz$ and $\alpha = 38°$ to $40°$ in Fig. 5.3. This can be taken as an indicator, that the additional lift forces caused by pulsed blowing occur relatively far inboard, close to the chord line. Second, another irregularity is observed at $Re_{mac} = 1.0 \cdot 10^6$ and $\alpha = 40°$: the rolling moment increases for $f_{pulse} = 65\ Hz$ and $97\ Hz$, although an increase in the overall lift is detected in Fig. 5.3. The reason could be a redistribution of the lift forces in chord-wise direction.

The pitching moment coefficient diminishes for all tested pulse frequencies at $\alpha = 15°$ to $23°$ and $Re_{mac} = 0.5 \cdot 10^6$, see Fig. 5.6. As the reference point for the pitching moment is situated at $x/c_r = 2/3$, one can conclude that the lift reduction observed in Fig. 5.3a mainly occurs in front of this reference point. An increase in the pitching moment is detected for $\alpha \geq 25°$ and $f_{pulse} = 32\ Hz$ ($F^+ = 2.6$), indicating that the additional lift forces arise at the front part of the wing. A slight increase of the pitching moment is noticed for almost all angles of attack and pulse frequencies at $Re_{mac} = 1.0 \cdot 10^6$. The only exception is found at $\alpha = 40°$, where C_m increases by 12% to 17% at all pulse frequencies. At $Re_{mac} = 1.5 \cdot 10^6$, the changes of the pitching moment coefficient are relatively low.

The yawing moment is significantly increased for all pulse frequencies and Reynolds numbers, apart from some particular cases as $\alpha = 23°$ and $25°$ at $Re_{mac} = 0.5 \cdot 10^6$ as well as $\alpha = 28°$ and $38°$ at $Re_{mac} = 1.5 \cdot 10^6$. Here, a reduction of the yawing moment is observed at all pulse frequencies, see Fig. 5.7.

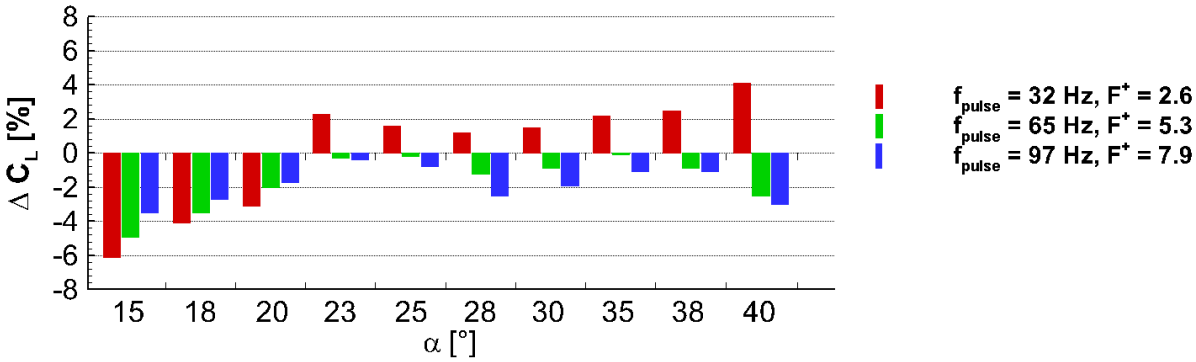

(a) $Re_{mac} = 0.5 \cdot 10^6$

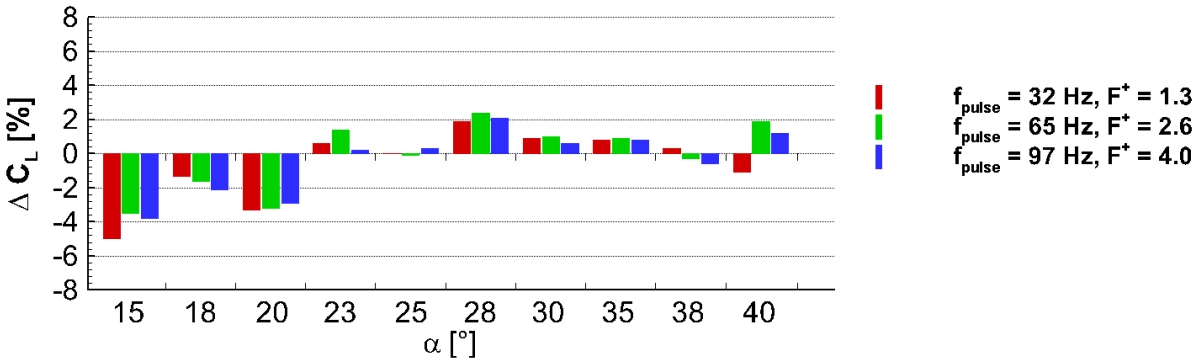

(b) $Re_{mac} = 1.0 \cdot 10^6$

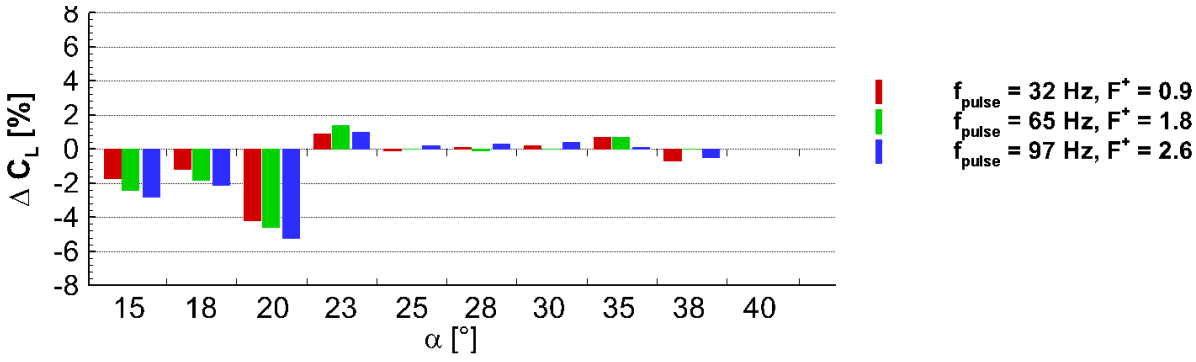

(c) $Re_{mac} = 1.5 \cdot 10^6$

Figure 5.3.: Effect of pulsed blowing on the lift coefficient, $DC = 25\%$, $p_{valve} = 4\ bar$

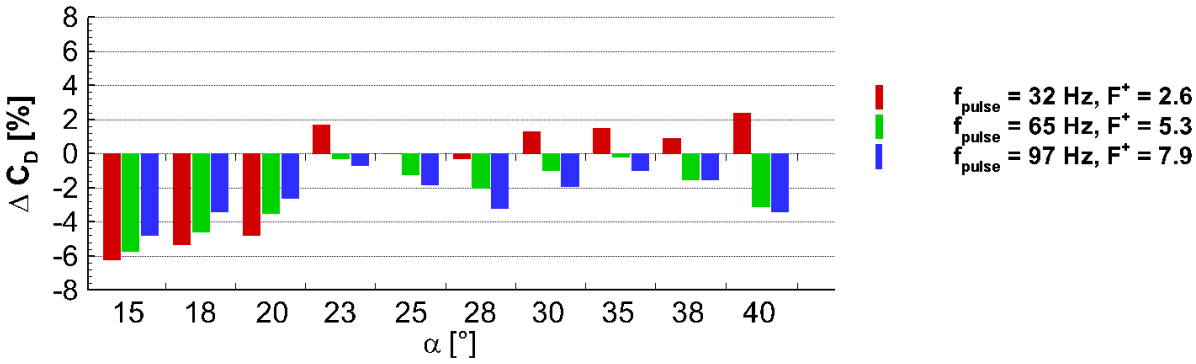

(a) $Re_{mac} = 0.5 \cdot 10^6$

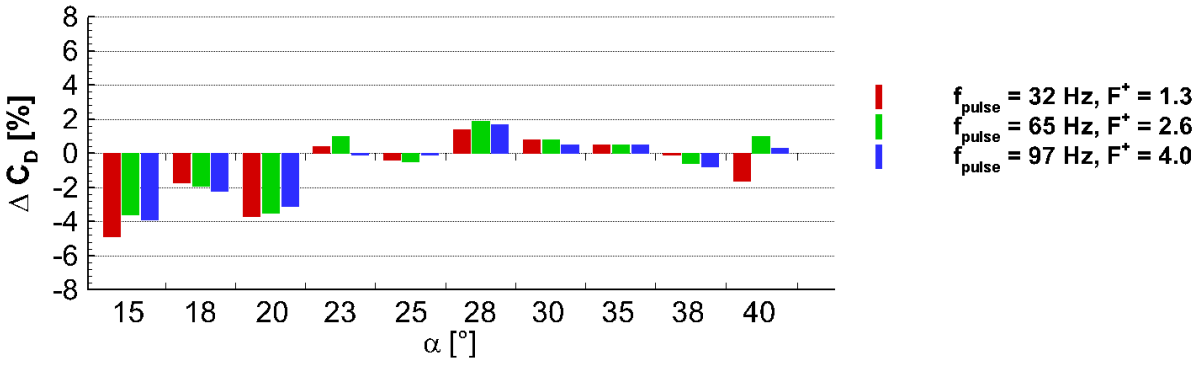

(b) $Re_{mac} = 1.0 \cdot 10^6$

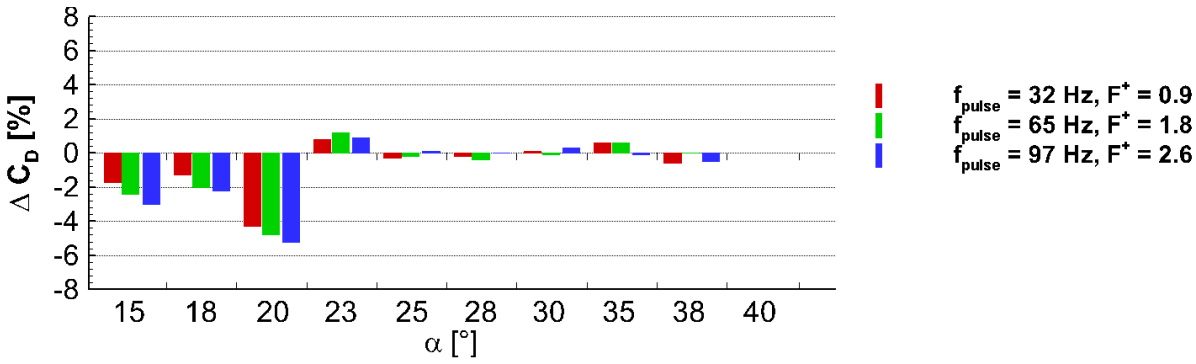

(c) $Re_{mac} = 1.5 \cdot 10^6$

Figure 5.4.: Effect of pulsed blowing on the drag coefficient, $DC = 25\%$, $p_{valve} = 4\ bar$

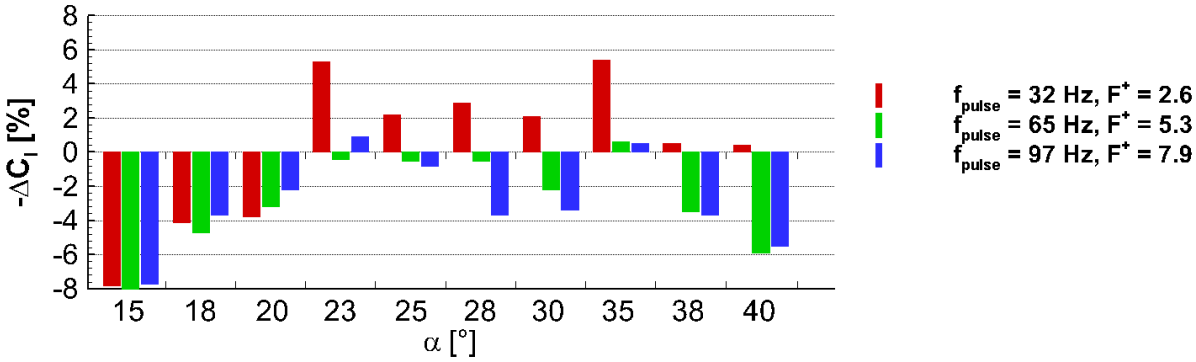

(a) $Re_{mac} = 0.5 \cdot 10^6$

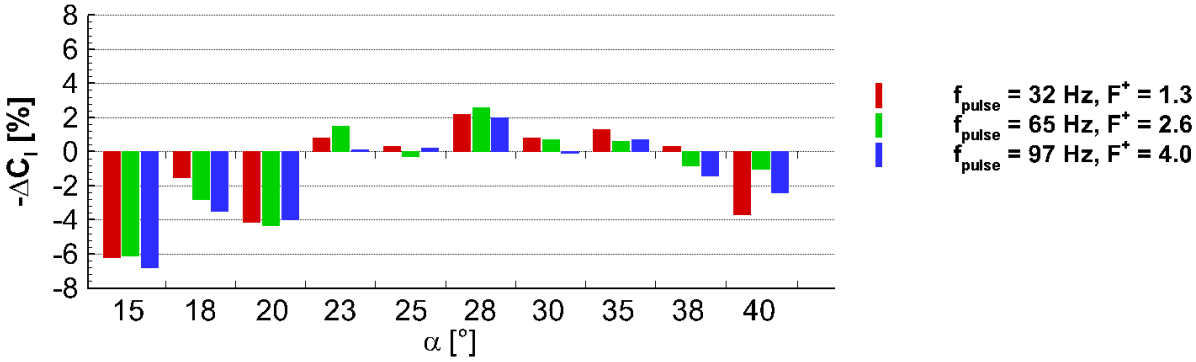

(b) $Re_{mac} = 1.0 \cdot 10^6$

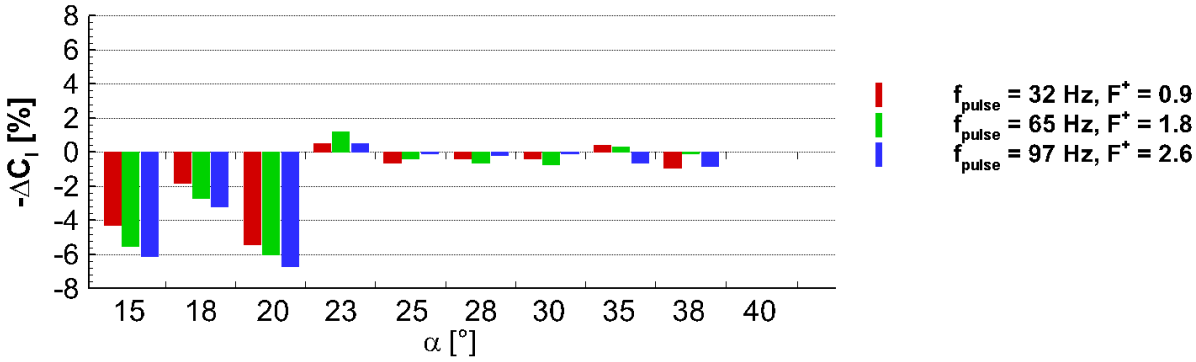

(c) $Re_{mac} = 1.5 \cdot 10^6$

Figure 5.5.: Effect of pulsed blowing on the rolling moment coefficient, $DC = 25\%$, $p_{valve} = 4\ bar$

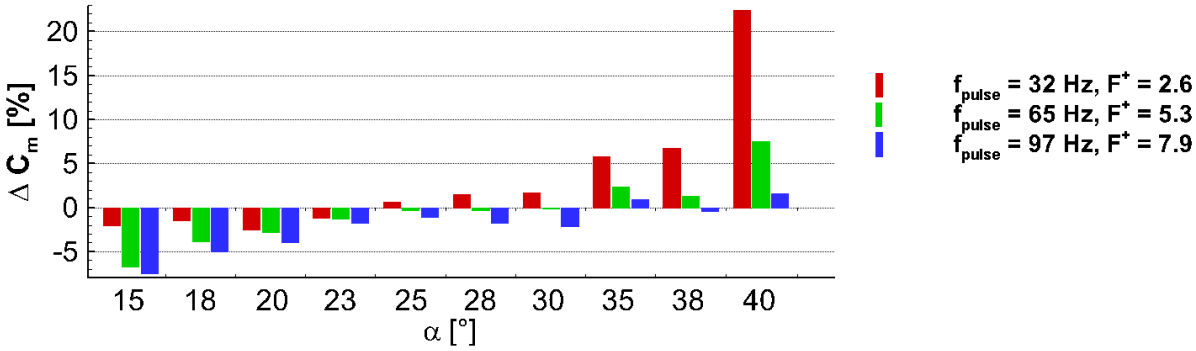

(a) $Re_{mac} = 0.5 \cdot 10^6$

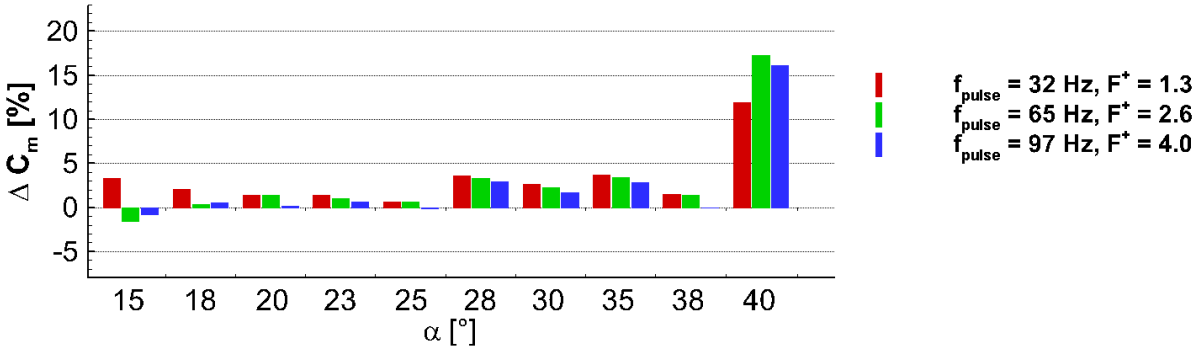

(b) $Re_{mac} = 1.0 \cdot 10^6$

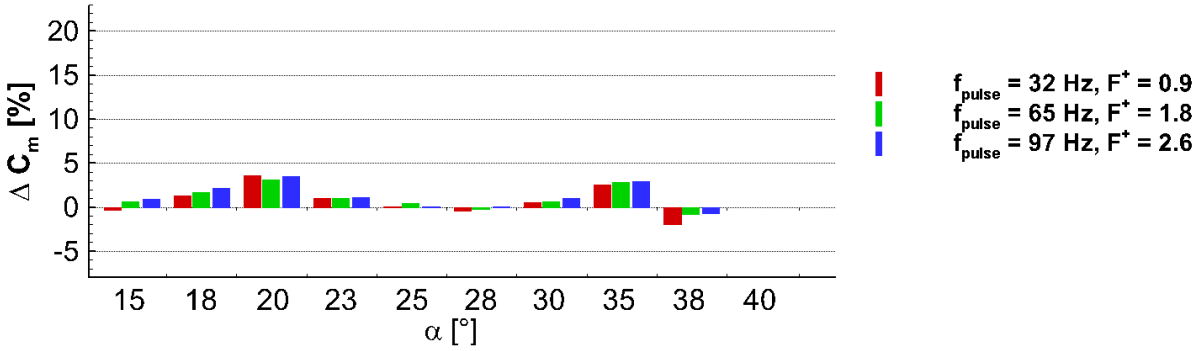

(c) $Re_{mac} = 1.5 \cdot 10^6$

Figure 5.6.: Effect of pulsed blowing on the pitching moment coefficient, $DC = 25\%$, $p_{valve} = 4\ bar$

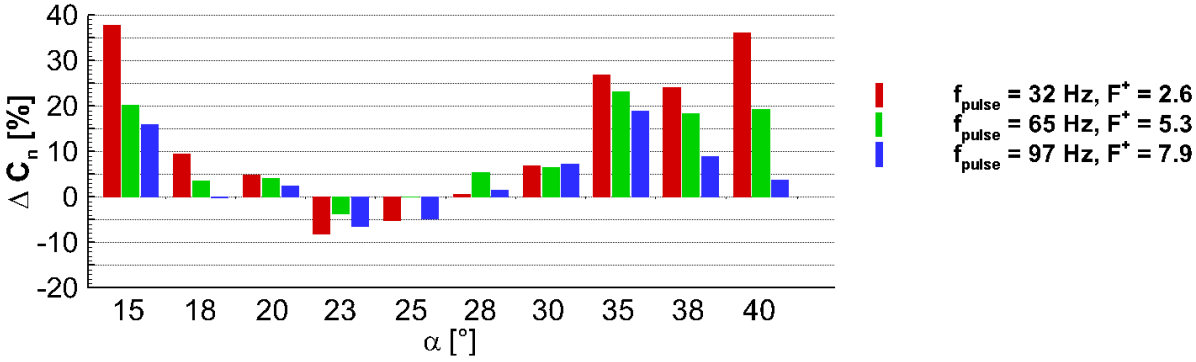

(a) $Re_{mac} = 0.5 \cdot 10^6$

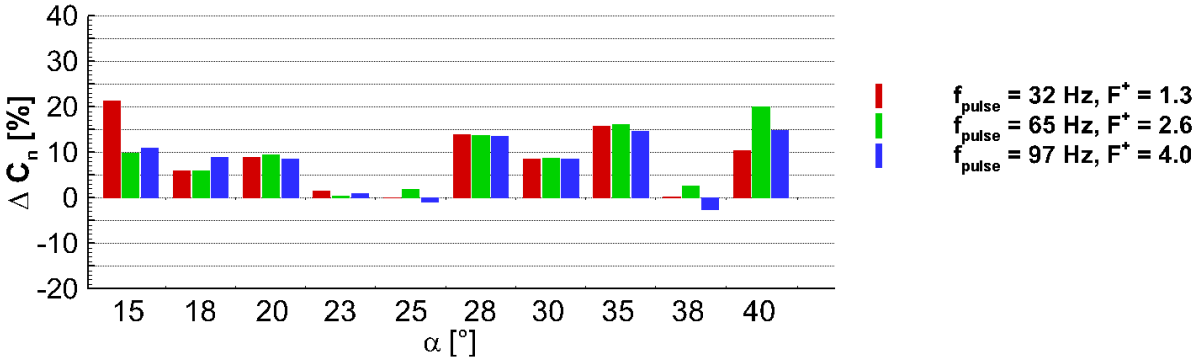

(b) $Re_{mac} = 1.0 \cdot 10^6$

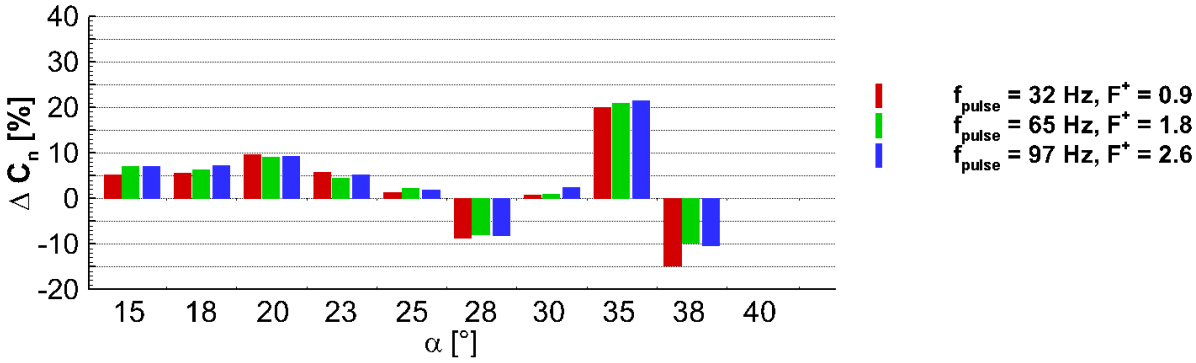

(c) $Re_{mac} = 1.5 \cdot 10^6$

Figure 5.7.: Effect of pulsed blowing on the yawing moment coefficient, $DC = 25\%$, $p_{valve} = 4\ bar$

5.1.3. Post-stall

In the post-stall regime, a variation of the pulse frequency f_{pulse} and the duty cycle DC is conducted in the force measurements under the flow conditions $\alpha = 45°$ and $Re_{mac} = 0.5 \cdot 10^6$, cf. [24], [85], [39]. Subsequently, the influence of the pressure in front of the valves and the effectiveness of the different blowing segments is studied for selected pulse frequencies.

Variation of pulse frequency and duty cycle. Figs. 5.8, 5.9 and 5.10 show the results of the frequency and duty cycle variation. The following frequencies are tested: $f_{pulse} = 6, 12, 18, 24, 36$ and 72 Hz, corresponding to $F^+ = 0.5, 1, 1.5, 2, 3$ and 6. At the same time, the duty cycle is varied from $DC = 5\%$ to 90%. The pressure in front of the closed valves is kept constant at $p_{valve} = 5\ bar$.

Pulsed blowing has a significant effect on the lift coefficient for all blowing frequencies $f_{pulse} \leq 36\ Hz$ ($F^+ \leq 3$) in the whole duty cycle range (DC = 5 - 90 %), see Fig. 5.8a. The two frequencies $f_{pulse} = 12\ Hz$ and 18 Hz are most effective, especially for $DC = 20\%$ to 50%. A lift increase of approximately 50% is obtained for this parameter set. This observation is in compliance with the findings in literature, that an actuation at a reduced frequency $F^+ \approx 1 - 2$ leads to a strong increase in lift in the post-stall regime [55], [81]. Fig. 5.8b shows, that the change in the drag coefficient evoked by pulsed blowing is almost identical to the effects observed for the lift coefficient.

The rolling moment coefficient has almost the same characteristics as the lift and drag coefficients for the pulse frequency and duty cycle variation, but with the opposite sign, see Fig. 5.9a. The absolute value of the rolling moment coefficient is increased by 25% to 30% for all $f_{pulse} \leq 36\ Hz$ ($F^+ \leq 3$). Pulsed blowing does also have a considerable effect on the pitching moment coefficient, whereupon this coefficient depends a bit stronger on the duty cycle than the other force and moment coefficients, cf. Fig. 5.9b. The increase of the pitching moment is greatest for $DC = 40\%$. In this case, C_m is increased from 0.1 to 0.25. As both the lift and the pitching moment coefficient do increase, it can be concluded that the additional lift does mainly occur in front of the pitching moment reference point at $X = 2/3c_r$. The yawing moment is reduced to maximal $\Delta C_n = -0.01$ to -0.015 for $f_{pulse} = 12\ Hz$ to 24 Hz and $DC = 20\%$ to 70%.

Variation of p_{valve} and the active segments for $f_{pulse} = 12\ Hz/18\ Hz$. As the effect of pulsed blowing is most effective at reduced pulse frequencies $F^+ = 1$ to 2, the pulse frequencies $f_{pulse} = 12\ Hz$ and 18 Hz corresponding to $F^+ = 1$ and 1.5, respectively, are studied in more detail.

Fig. 5.11 shows the force measurement results for a variation of the pressure in front of the closed valves, p_{valve}, and for the duty cycle DC varied from 2.5% to 30%. Furthermore, the lift coefficient for steady blowing is depicted. Steady blowing evokes only a small increase in lift of approximately 5%.

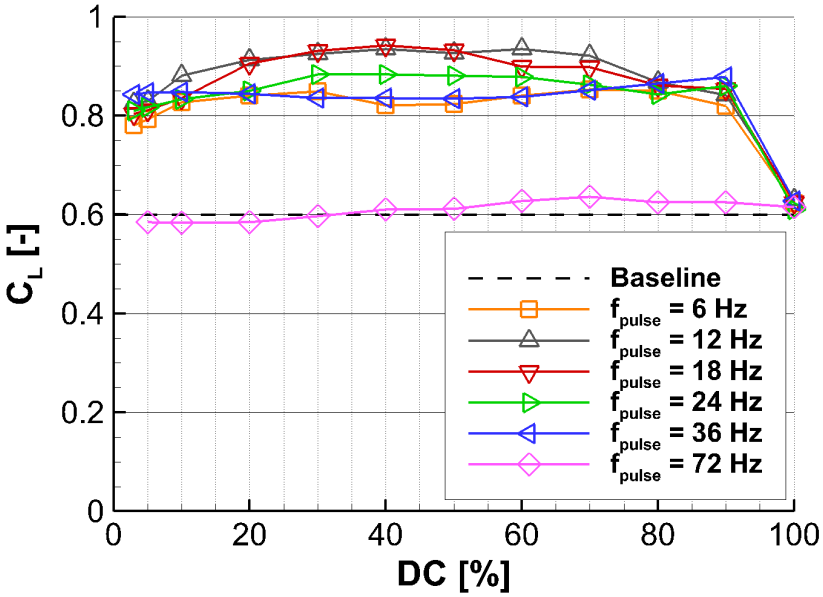

(a) Lift coefficient

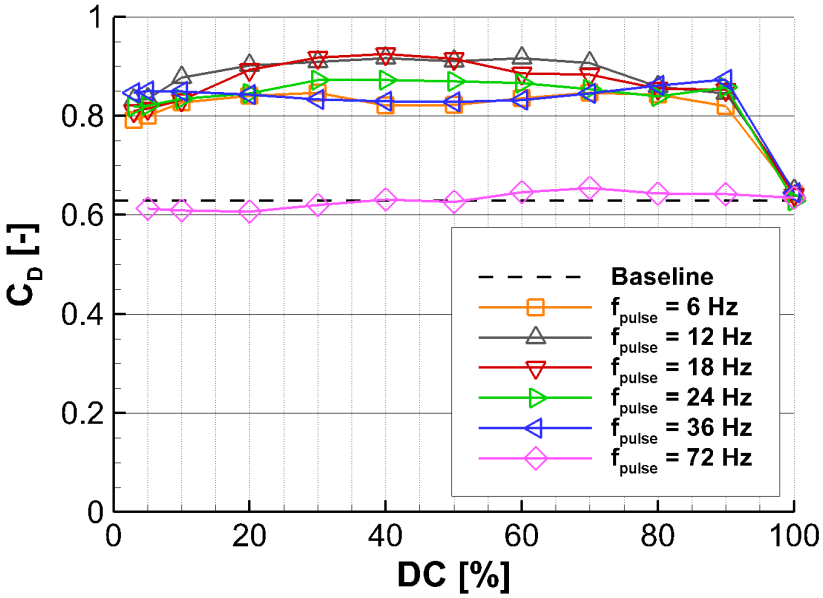

(b) Drag coefficient

Figure 5.8.: Force coefficients for the variation of DC and f_{pulse} ($F^+ = 0.5$ to 6) at $\alpha = 45°$, $Re_{mac} = 0.5 \cdot 10^6$ and $M = 0.035$; pulsed blowing at $p_{valve} = 5\ bar$

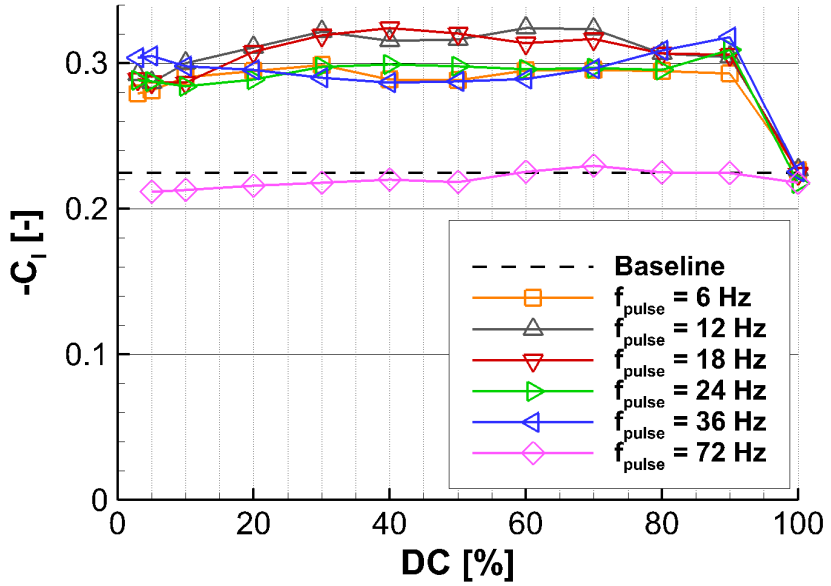

(a) Rolling moment coefficient

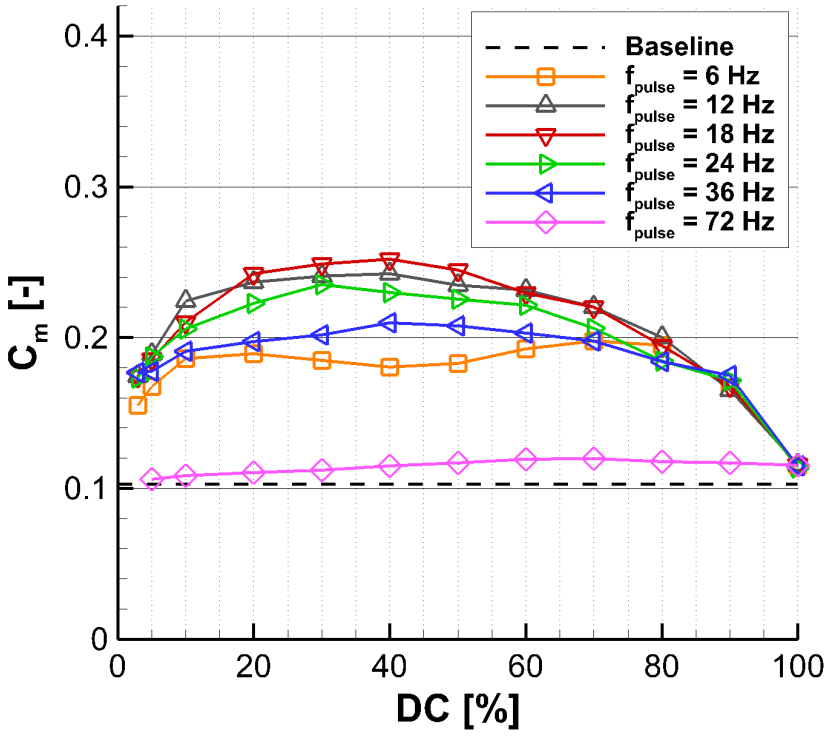

(b) Pitching moment coefficient

Figure 5.9.: Rolling and pitching moment coefficients for the variation of DC and f_{pulse} ($F^+ = 0.5$ to 6) at $\alpha = 45°$, $Re_{mac} = 0.5 \cdot 10^6$ and $M = 0.035$; pulsed blowing at $p_{valve} = 5\ bar$

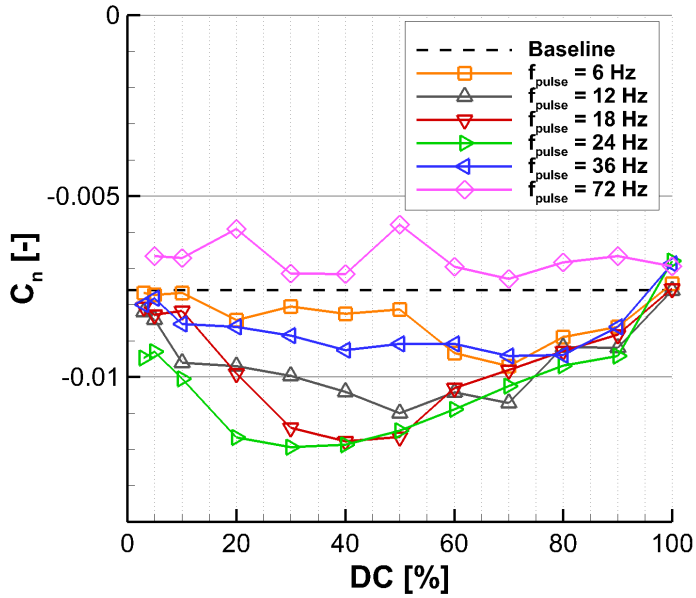

Figure 5.10.: Yawing moment coefficient for the variation of DC and f_{pulse} ($F^+ = 0.5$ to 6) at $\alpha = 45°$, $Re_{mac} = 0.5 \cdot 10^6$ and $M = 0.035$; pulsed blowing at $p_{valve} = 5\ bar$

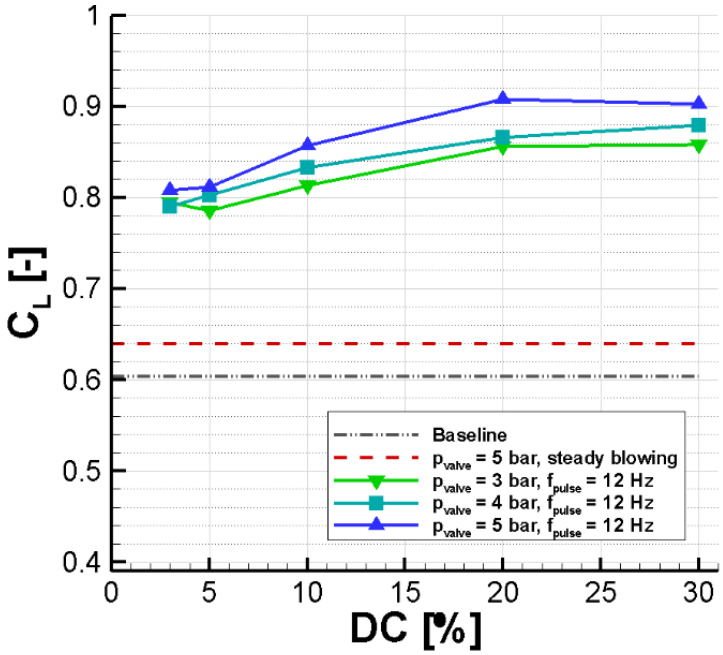

Figure 5.11.: Lift coefficient for the variation of DC and p_{valve} at $\alpha = 45°$, $Re_{mac} = 0.5{\cdot}10^6$ and $M = 0.035$; pulsed blowing at $f_{pulse} = 12\ Hz$ ($F^+ = 1$)

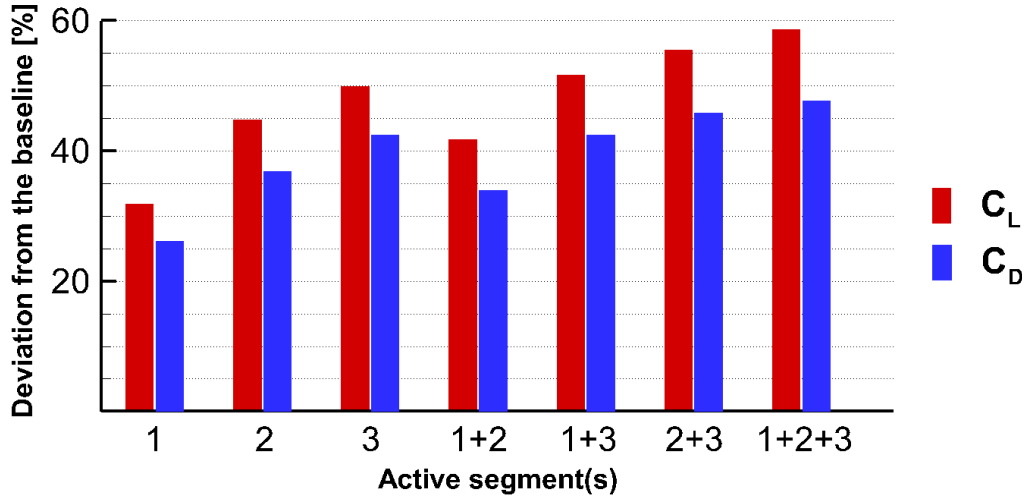

(a) Forces

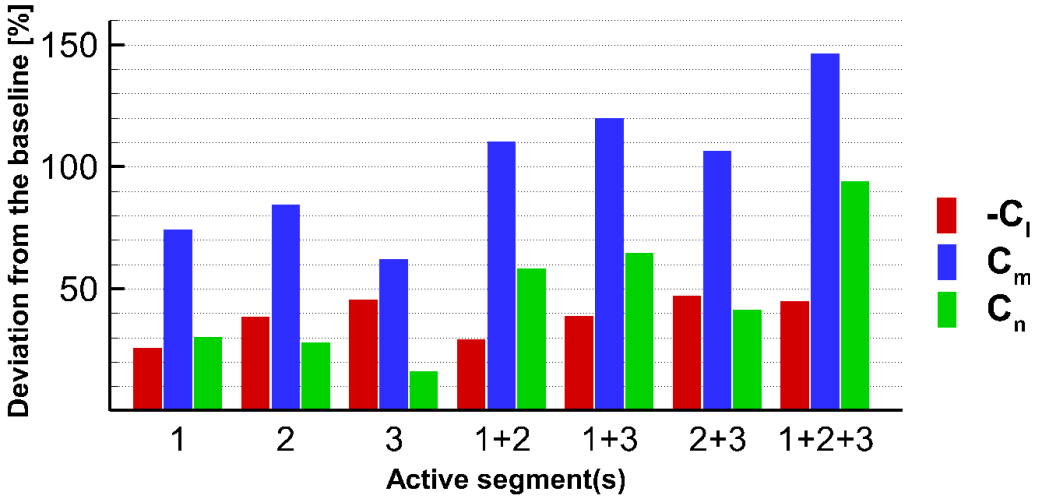

(b) Moments

Figure 5.12.: Variation of active segments in the post-stall regime at $\alpha = 45°$ and $Re_{mac} = 0.5 \cdot 10^6$; pulsed blowing at $f_{pulse} = 18\ Hz$ ($F^+ = 1.5$), $DC = 25\%$ and $U_{jet} \approx 60\ m/s$

Compared to this result, pulsed blowing at $f_{pulse} = 12\ Hz$ is much more efficient. The increase in lift augments with the pressure in front of the valves and is maximal for $p_{valve} = 5\ bar$. Moreover, the lift coefficient is maximal for $DC = 20$ to 30%.
Fig. 5.12 shows the results of the segment variation for the parameter set $f_{pulse} = 18\ Hz$, $DC = 25\%$ and $p_{valve} = 5\ bar$, cf. [24]. Both the activation of the three single segments and the different combinations of two segments are considered, as well as the case when all three segments are active at the same time.

Pulsed blowing from all three segments along the leading edge leads to an increase in lift of approximately 60%, see Fig. 5.12a. The drag coefficient is increased by 48%. If only one single segment is active, an increase in lift is still observed in all cases, and the efficiency is highest for the segment 3 in the rear part of the leading edge. While the third segment leads to a remarkable lift increase that amounts to 85% of the lift increase measured when all segments are active, this portion is 76% for the second and 54% for the first blowing segment. The absolute gain in the drag coefficient is a bit lower compared to the lift coefficient, leading to a slight improvement of the aerodynamic efficiency in all actuated cases. The combination of two blowing segments results in higher lift coefficients than measured for the respective single segments. Again, the combination of the two rear segments is most efficient. It can be concluded that, with respect to the lift coefficient, the rear segment has the biggest influence. This could be a hint that pulsed blowing is most effective at the rear part of the wing, at least in the post-stall case.

The moment coefficients are relatively high in change compared to the baseline case, see Fig. 5.12b. The pitching and the yawing moment coefficient are increased by the pulsed blowing. The combination of all three blowing segments provides the highest increase in the pitching and yawing moment and the contribution of segment 3 is lower than that of segment 1 or 2. In contrast, the change in the rolling moment is negative and it is most considerable for the rear segment. The absolute value of ΔC_l increases, if two blowing segments are combined.

5.1.4. Definition of the test cases

Three test cases are analyzed more elaborately. The corresponding free-stream conditions and the actuation parameters are listed in Table 5.1. At $\alpha = 23°$ and $Re_{mac} = 1.0 \cdot 10^6$, the pulse frequency $f_{pulse} = 65\ Hz$ leads to a significant alteration of the velocity profile close to the vortex breakdown position, see Section 5.1.1. Therefore, this parameter combination is explored in more detail for the pre-stall regime. The combination of $\alpha = 35°$, $Re_{mac} = 0.5 \cdot 10^6$ and $f_{pulse} = 32\ Hz$ is studied by additional flow measurements, because a slight increase in lift was observed for the stall regime in the force measurements. The post-stall test case is $\alpha = 45°$ and $Re_{mac} = 0.5 \cdot 10^6$ and $f_{pulse} = 12\ Hz$. Here, a significant effect on the force, but also on the moment coefficients was noted.

For the detailed analysis, surface pressure measurements and velocity measurements were carried out by HWA. For the test cases at $\alpha = 23°$ and $\alpha = 35°$, additional PIV meas-

urements were conducted. The results are discussed in the following sections.

Table 5.1.: Pulsed blowing test cases

Domain	α	Re_{mac}	U_∞	M	f_{pulse}	F^+	U_{jet}	DC	C_μ
Pre-stall	23°	$1 \cdot 10^6$	24 m/s	0.07	65 Hz	≈ 2.6	55 m/s	25%	0.0014
Stall	35°	$0.5 \cdot 10^6$	12 m/s	0.035	32 Hz	≈ 2.6	55 m/s	25%	0.0056
Post-stall	45°	$0.5 \cdot 10^6$	12 m/s	0.035	12 Hz	1	60 m/s	25%	0.0067

5.2. Pre-stall test case

In the following, the results of the pressure and flow field measurements are shown for pulsed blowing with $f_{pulse} = 65\ Hz$ and $U_{jet} \approx 50\ m/s$ at $\alpha = 23°$ and $Re_{mac} \approx 1 \cdot 10^6$ ($M = 0.07$), see Table 5.1.

5.2.1. Surface-pressure distributions

The mean pressure distribution is plotted in Fig. 5.13a for the baseline and the actuated case, cf. [5]. The mean surface pressure field of the actuated case is very similar to that of the baseline case. The pressure distributions at $X = 0.6$ and 0.8 are almost identical. An effect of pulsed blowing on the mean pressure distribution is observed only at the first measurement station $X = 0.4$, where blowing at $f_{pulse} = 65\ Hz$ leads to a slight reduction of the suction peak on the upper wing side. The location of the primary vortex suction peak remains the same as in the baseline case.

The pressure fluctuations are significantly increased at all measurement stations in the case of active pulsed blowing. The amplitudes are more than doubled at most of the measurement points. Nevertheless, the main characteristics of the $C_{p,rms}$ distribution are retained. Only two peculiarities can be observed: at $X = 0.4$ and $Y = 0.55$, a second local maximum appears which was not observed in the baseline case. It is located inboard from the suction peak, at a position where the gradient of the mean pressure is very high in chord-wise direction. At $X = 0.6$ the maximal pressure fluctuations occur close to the leading edge at $Y = 0.93$. This measurement point is in the vicinity of the slots, where the pulsed jets are generated.

As shown by Fig. 5.14a on the example of $X = 0.4$, high-amplitude peaks at the actuation frequency and its higher harmonic frequencies are found at all span-wise positions in the spectral analysis of the pressure signals recorded by the Kulite sensors. According to Fig. 5.13, they are maximal at the locations slightly inboard and outboard from the suction peak. The characteristics of the curve shown in Fig. 5.14b are very similar to those of the baseline case, apart from the distinctive peaks at the actuation frequency and its higher harmonic frequencies.

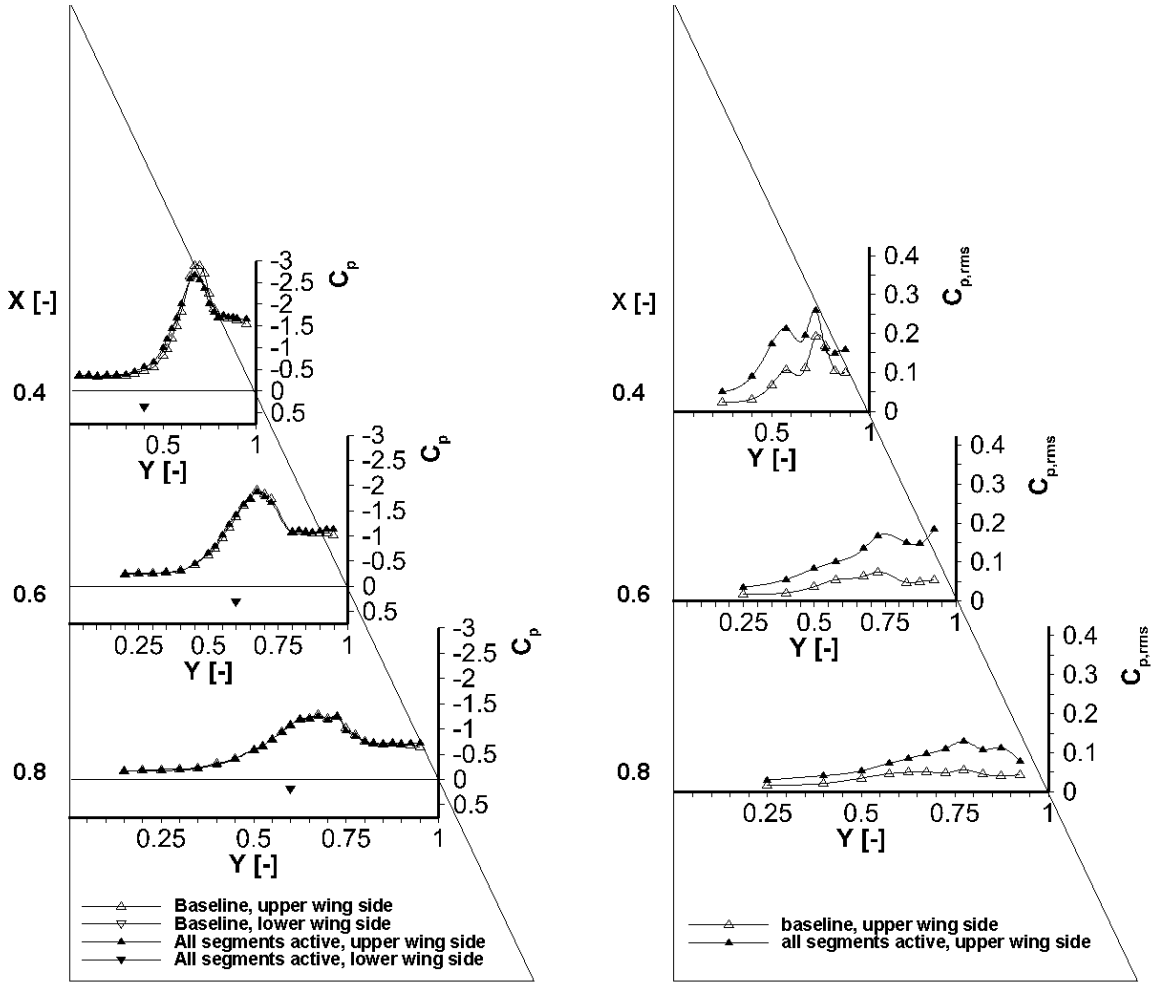

(a) Mean pressure (b) Pressure fluctuations

Figure 5.13.: Mean pressure and pressure fluctuation distribution for the non-actuated and actuated cases at $\alpha = 23°$ for $Re_{mac} \approx 1.0 \times 10^6$, and $M = 0.07$; pulsed blowing at $f_{pulse} = 65\ Hz$ ($F^+ = 2.6$), $U_{jet} \approx 50\ m/s$

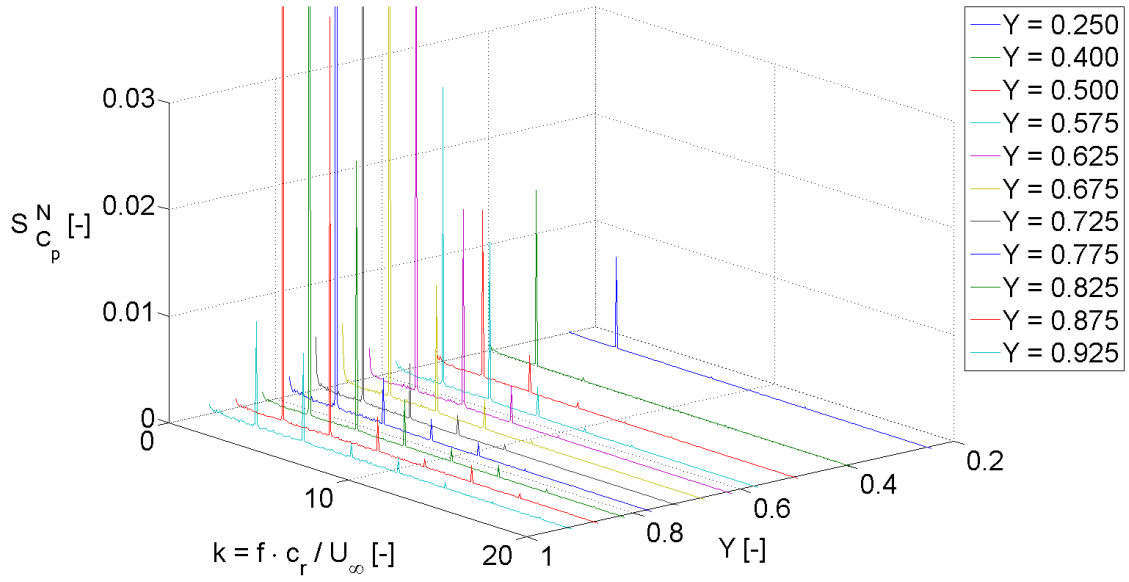

(a) Power spectral density for $X = 0.4$

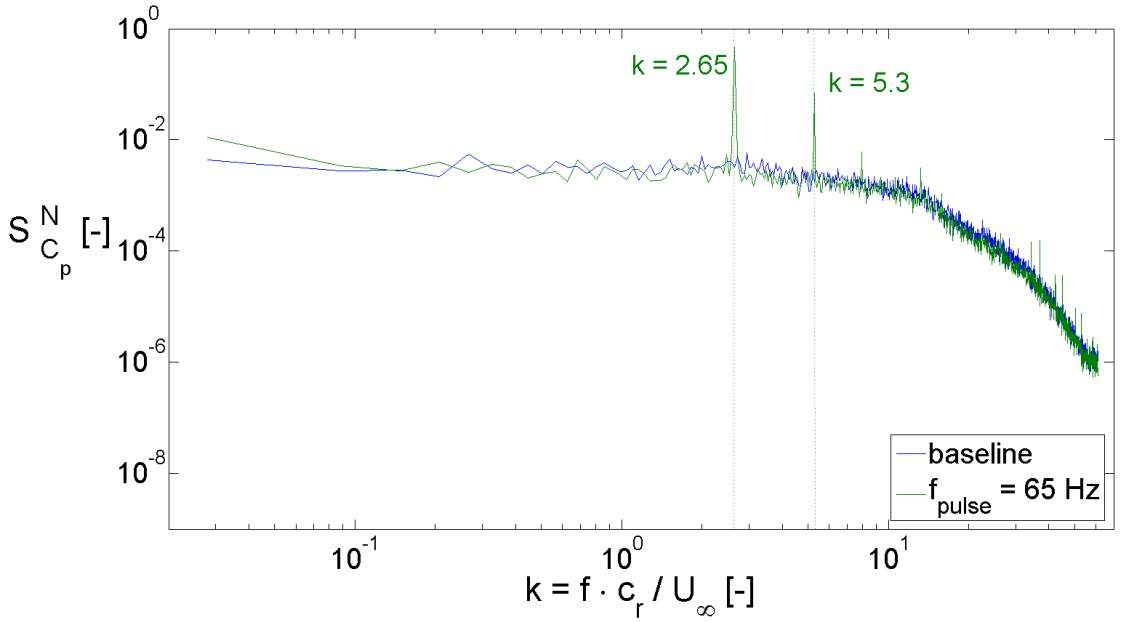

(b) Power spectral density for $X = 0.4$ and $Y = 0.725$

Figure 5.14.: Spectral analysis of the pressure coefficient for $\alpha = 23°$, $Re_{mac} \approx 1.0 \times 10^6$, and $M = 0.07$, pulsed blowing at $f_{pulse} = 65\ Hz$ ($F^+ = 2.6$), $DC = 25\%$ and $U_{jet} \approx 50\ m/s$

5.2.2. Flowfield

Baseline PIV results. The basic axial velocity field gained from PIV measurements is shown on the left hand side of Fig. 5.15. It looks slightly different compared to the HWA results for the same free-stream conditions in Fig. 4.16. This difference is attributed to the perturbation of the binormal component at the HWA measurements. It does not occur when non-intrusive measurement methods like PIV are applied. The flow field in the PIV cross-sections $X = 0.2$ and $X = 0.4$ is characterized by a region of axially accelerated flow inboard from the vortex center as well as a region of axially decelerated flow outboard and below the vortex center. This velocity pattern is typical for a fully developed leading edge vortex. At $X = 0.6$ and $X = 0.8$, a second region of axially decelerated flow is observed in the vortex center. It indicates a burst vortex. In contrast to the HWA measurement results presented in Section 4.3.1, the region of decelerated axial flow in the vortex center does not appear until $X = 0.6$. Therefore, one can conclude that the breakdown location is situated between $X = 0.4$ and $X = 0.6$ in the baseline case.

Fig. 5.16 shows the distribution of the turbulent kinetic energy. The position of the vortex center is located at $Y \approx 0.6$ and $Z \approx 0.3$ in the measurement planes $X \geq 0.4$ of the baseline case. In the first two measurement planes, the turbulent kinetic energy is strongly concentrated in the vortex center. Downstream the vortex breakdown location, at $X = 0.6$ and 0.8, the maximum of the TKE strongly declines and the structures with maximal turbulent kinetic energy appear rather diffused.

Pulsed blowing - PIV results. The results for active pulsed blowing at $f_{pulse} = 65\ Hz$ are shown on the right hand side of Fig. 5.15 and Fig. 5.16. No considerable upstream effect on the flow field is determined for the axial velocity distribution in the measurement plane $X = 0.2$, which is located in front of the first blowing segment. In the second measurement plane $X = 0.4$, the global maximum of the axial velocity component is slightly reduced compared to the baseline case. Here, u_{max}/U_∞ is 3.8 for active blowing instead of 4.1 in the baseline case. At the two rear cross sections $X = 0.6$ and $X = 0.8$, the region of axially decelerated flow is diminished and the axial velocity is significantly increased. At $X = 0.6$, u_{min}/U_∞ has increased from 0.1 in the baseline case to 0.8 with active pulsed blowing. This is an indicator for a highly-desired downstream-shift of the vortex breakdown location.

The distribution of the TKE appears to be very similar compared to the baseline case for $X = 0.2, 0.4$ and 0.8. A significant difference is observed at $X = 0.6$, where the global TKE maximum is more concentrated when pulsed blowing is active. Additionally, the maximal TKE values are increased compared to the baseline case. Fig. 5.17 shows a 3D-plot of the TKE in the baseline case with stream traces visualizing the cross-flow velocities (v and w) in the respective measurement plane.

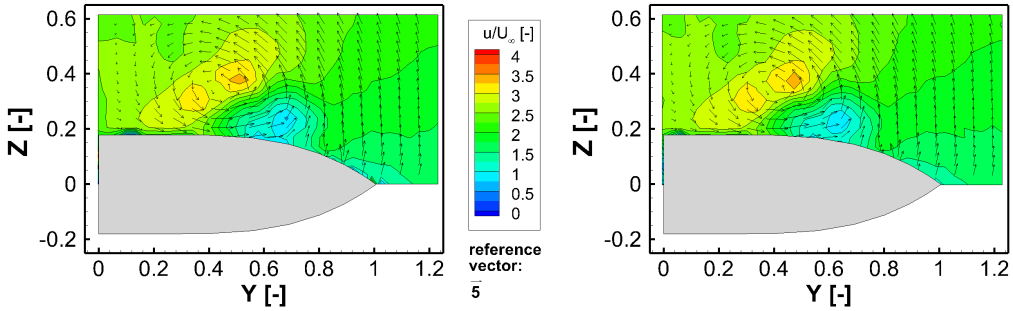

(a) $X = 0.2$

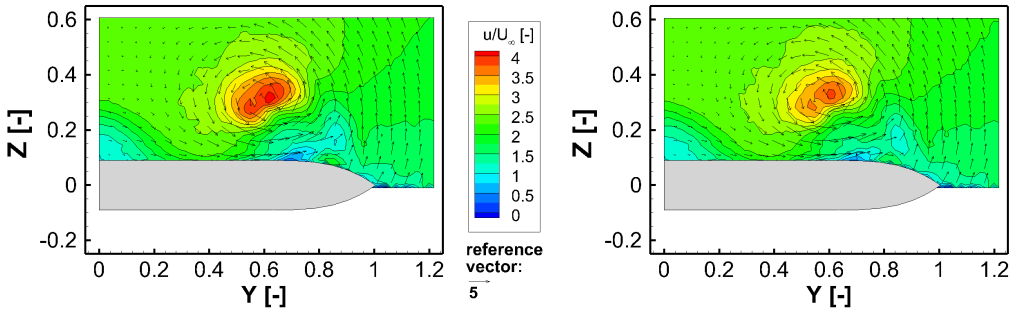

(b) $X = 0.4$

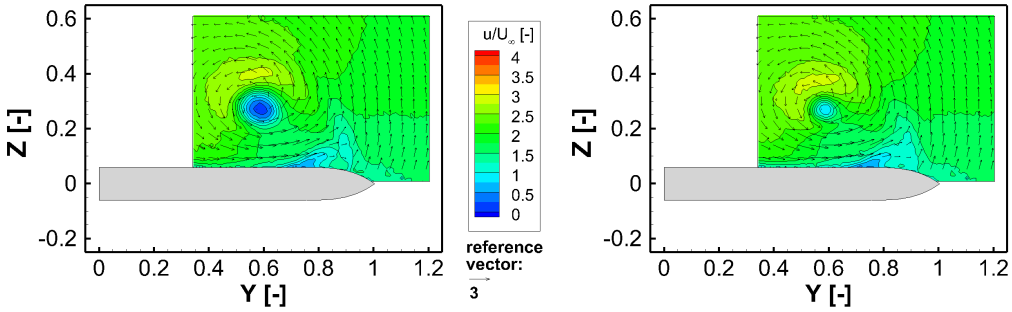

(c) $X = 0.6$

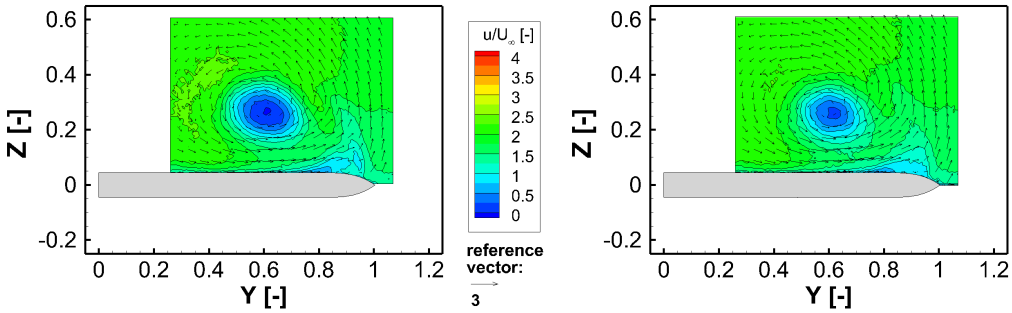

(d) $X = 0.8$

Figure 5.15.: Distribution of the axial velocity for the non-actuated (left) and actuated cases (right) at $\alpha = 23°$ for $Re_{mac} = 1.0 \cdot 10^6$, and $M = 0.07$; pulsed blowing at $f_{pulse} = 65\ Hz$ ($F^+ = 2.6$), $DC = 25\%$ and $U_{jet} \approx 50\ m/s$; PIV measurement result

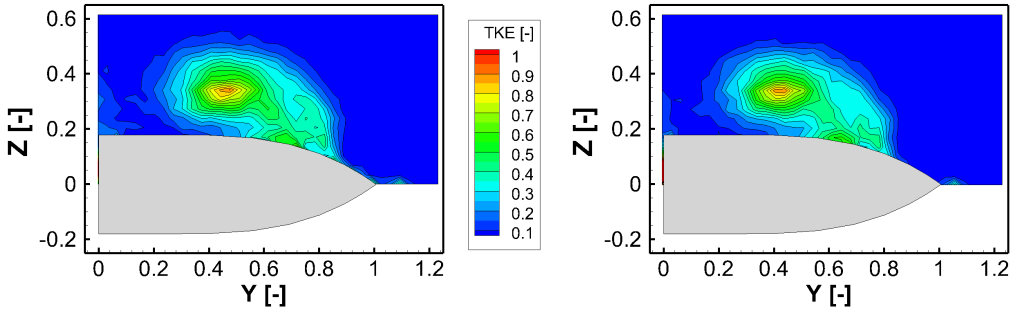

(a) $X = 0.2$

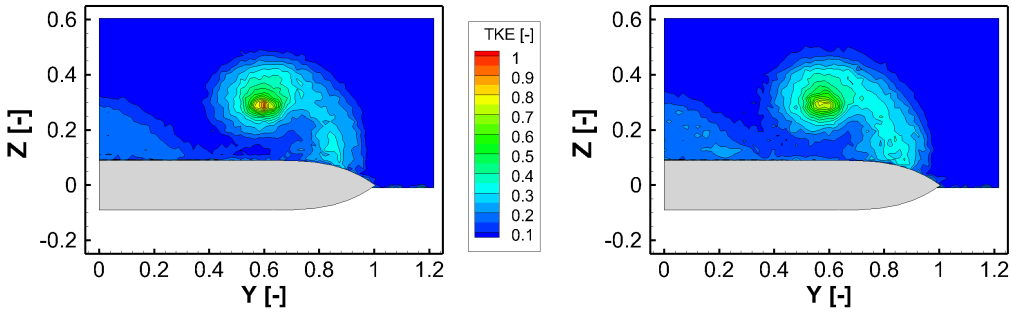

(b) $X = 0.4$

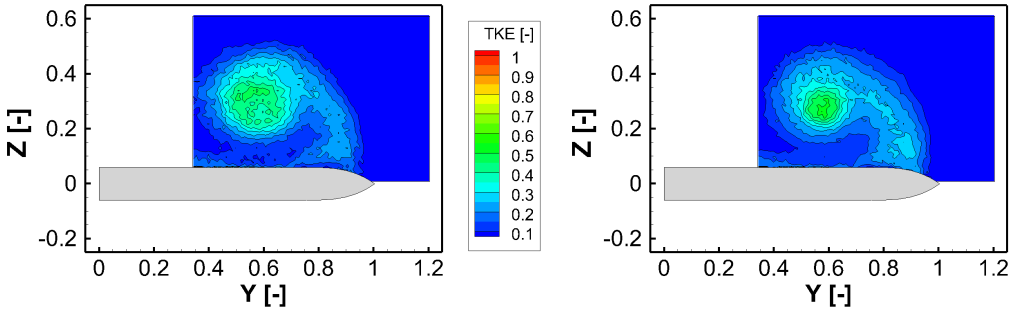

(c) $X = 0.6$

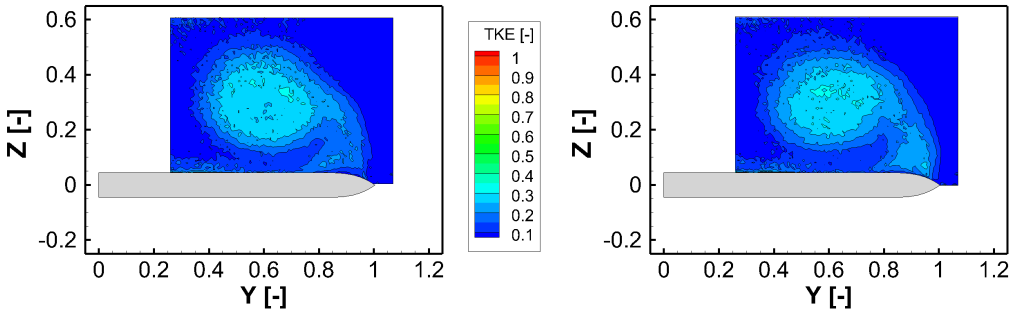

(d) $X = 0.8$

Figure 5.16.: Distribution of the turbulent kinetic energy for the non-actuated (left) and actuated cases (right) at $\alpha = 23°$ for $Re_{mac} = 1.0{\cdot}10^6$, and $M = 0.07$; pulsed blowing at $f_{pulse} = 65\ Hz$ ($F^+ = 2.6$), $DC = 25\%$ and $U_{jet} \approx 50\ m/s$; PIV measurement result

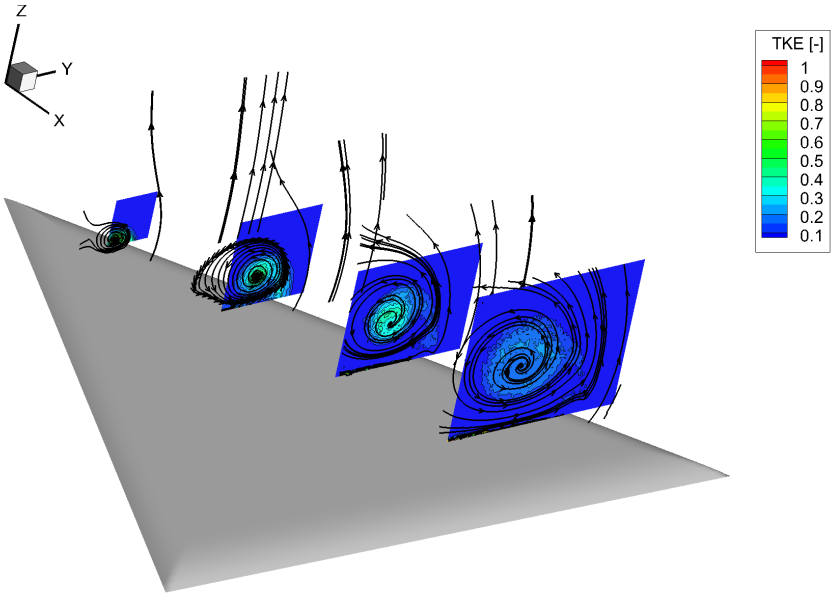

Figure 5.17.: Distribution of the turbulent kinetic energy streamtraces at $\alpha = 23°$ for $Re_{mac} = 1.0 \cdot 10^6$, and $M = 0.07$; PIV measurement result

Pulsed blowing - HWA results. The results from the HWA measurements are shown in Appendix C for the same test case and the cross-sections $X = 0.4$ and $X = 0.6$. The plots comprise the distributions of the axial and vertical velocity component as well as the respective velocity fluctuations. In the measurement plane at $X = 0.4$, the axial velocity deficit is completely removed when pulsed blowing is active, see Fig. C.1 in the Appendix. Moreover, the annular structure formed by the maxima of axial velocity fluctuations transforms to a concentrated peak for pulsed blowing. Therefore, it is to conclude that vortex breakdown is shifted downstream.

Spectral analysis of the axial velocities. In Fig. 5.18 the spectrum of the axial velocity component is compared for different measurement positions in the baseline and the actuated case, cf. [41]. The time series of the velocity components were recorded in the HWA measurements (see Appendix C for the contour plots of the flow field).

For the actuated case, the spectra of all measurement points show high-amplitude peaks at the pulse frequency $f_{pulse} = 65\ Hz$ ($F^+ = 2.6$) and corresponding higher harmonic frequencies, respectively. The detected values of power spectral density at the pulse frequencies are approximately one order of magnitude higher than the values of the baseline case. This verifies the receptivity of the shear layer with respect to pulsed blowing. Besides these dominant peaks, the spectral characteristics for measurement points 2 and 3 are quite similar to those of the uncontrolled ones. This is not the case for measurement point 1 in the core; the spectrum reveals the former concentration of TKE at the narrow frequency band of the helical mode instability neither at this point nor at other measurement stations of the core region, cf. [41].

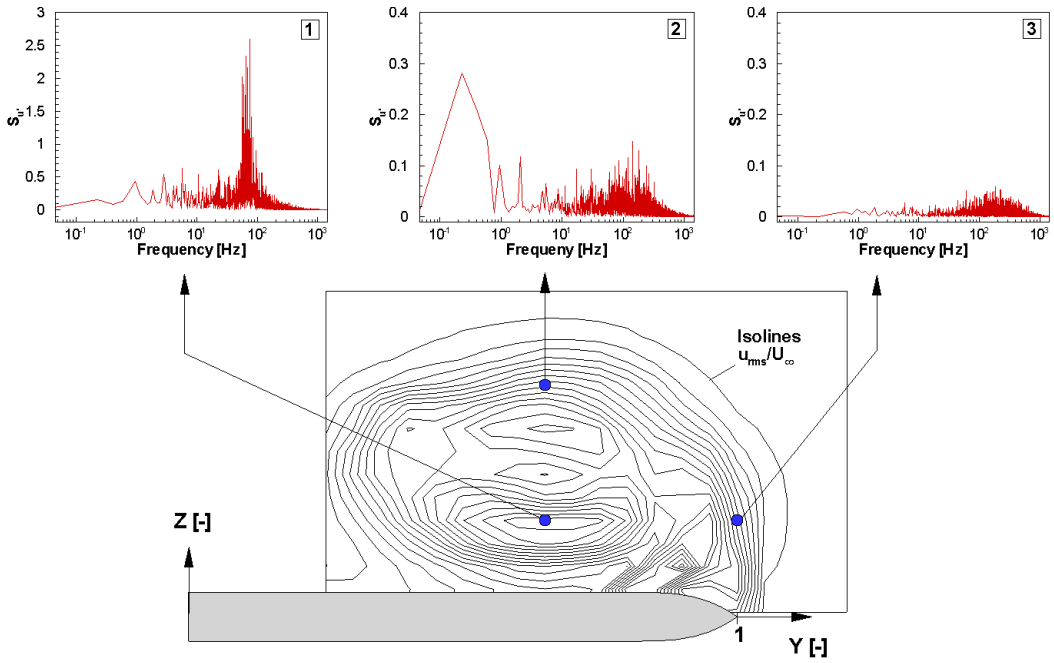

(a) Baseline case

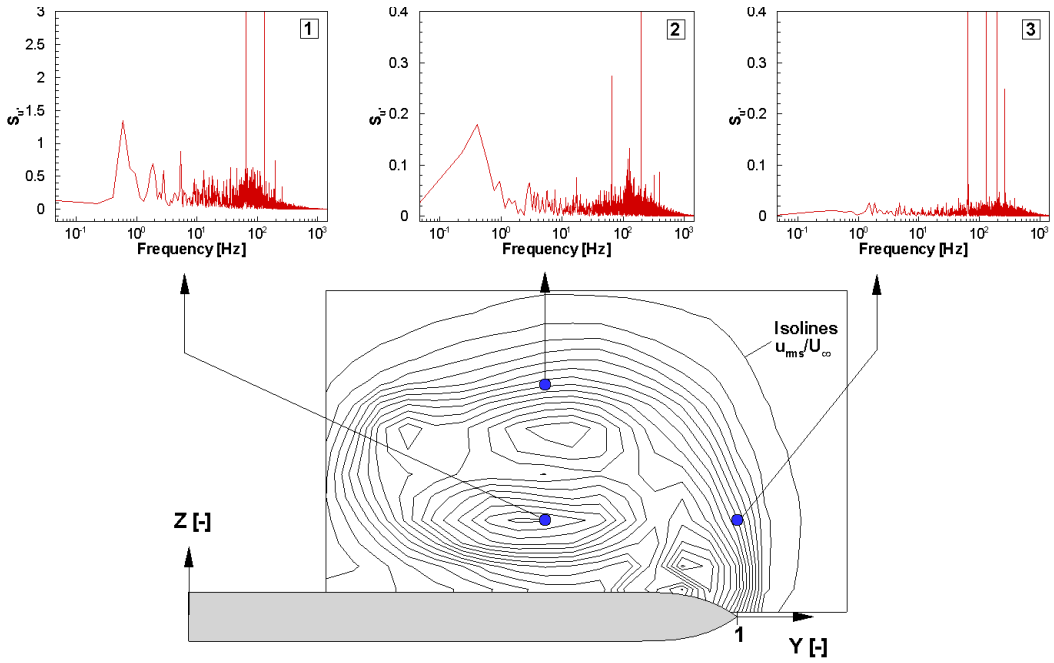

(b) Pulsed blowing at $f_{pulse} = 65\ Hz$ ($F^+ = 2.6$), $U_{jet} \approx 55\ m/s$, $DC = 25\%$

Figure 5.18.: Comparison of the power spectral densities for axial velocity fluctuations ($S_{u'}$) in the shear layer and the burst vortex core at $\alpha = 23°$, $X = 0.6$, $Re_{mac} = 1 \cdot 10^6$, and $M = 0.07$

5.3. Stall test case

In this subsection, the measurement results for the stall case at $\alpha = 35°$, $Re_{mac} \approx 0.5 \cdot 10^6$ and $M = 0.035$ are discussed for pulsed blowing with $f_{pulse} = 32\ Hz$ and $U_{jet} \approx 50\ m/s$ (see Table 5.1 for the whole parameter set).

5.3.1. Surface-pressure distributions

The mean pressure and the pressure fluctuation intensities are shown in Fig. 5.19, cf. [5], [37]. With pulsed blowing at $f_{pulse} = 32\ Hz$, the suction level of the mean pressure distribution is slightly higher compared to the baseline case. This effect is especially observed in the cross-section at $X = 0.4$, where the suction level increases by 10% for span-wise coordinates $Y \approx 0.5 - 1.0$ [37]. The surface pressure is also reduced close to the leading edge.

The results for the pressure fluctuations are visualized in Fig. 5.19b. They indicate a stabilization of the vortex flow, as the pressure fluctuations $C_{p,rms}$ diminish under the vortex in the case of pulsed blowing. This positive effect is observed at all three chord-wise measurement stations. At $X = 0.4$ under the vortex axis, $C_{p,rms}$ decreases by 24%. The pressure fluctuations increase near the leading-edge in each cross-section, as these pressure measurement sensors are located close to the blowing slots [37].

Similarly to the pre-stall test case, the pulse frequency is measurable in the surface pressure signal at all measurement stations. The power spectral density distribution for the first measurement plane $X = 0.4$ is shown in Fig. 5.20a, cf. [5]. It exhibits high-amplitude fluctuations at the pulse frequency and the higher harmonic frequencies at all chord-wise stations. The comparison of the spectra measured at $Y = 0.5$ is shown in Fig. 5.20b for $X = 0.4$ and in Figs. 5.21a and 5.21b for $X = 0.6$ and 0.8. In general, the level of the power spectral density is a bit lower in the actuated case compared to the baseline case for $X = 0.4$ and 0.6, if the peaks at the actuation frequency and its higher harmonics are disregarded. This observation is especially made at $X = 0.4$. Here, the former narrow-banded concentration of TKE, which is observed at the reduced frequencies $k \approx 1.6$ to 4.2 in the baseline case, is significantly reduced and replaced by a distinctive peak at the pulse frequency ($k_{pulse} = 2.56$). At $X = 0.6$ and 0.8, the pulse frequency $k = 2.56$ does not meet the frequency band of the narrow-banded concentration of pressure fluctuations related to the helical mode instability ($k \approx 1.8$ at $X = 0.6$ and $k \approx 1.5$ at $X = 0.8$ in the baseline case). Certainly, the PSD is reduced in this bands, but the effect is less dominant than at $X = 0.4$.

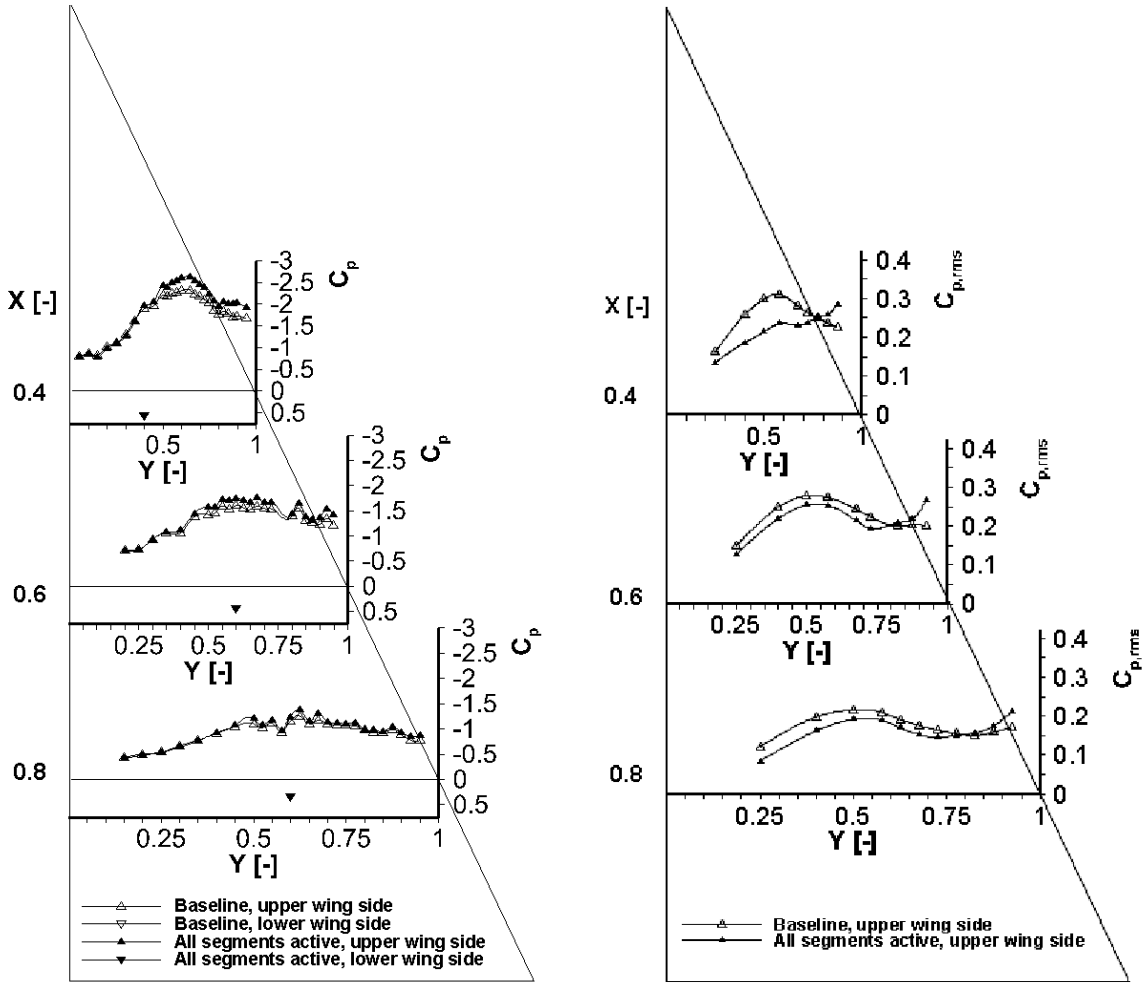

(a) Mean pressure

(b) Pressure fluctuations

Figure 5.19.: Mean pressure and pressure fluctuation distribution for the non-actuated and actuated cases at $\alpha = 35°$ for $Re_{mac} \approx 0.5 \times 10^6$, and $M = 0.035$; pulsed blowing at $f_{pulse} = 32\ Hz$ ($F^+ \approx 2.6$), $U_{jet} \approx 50\ m/s$

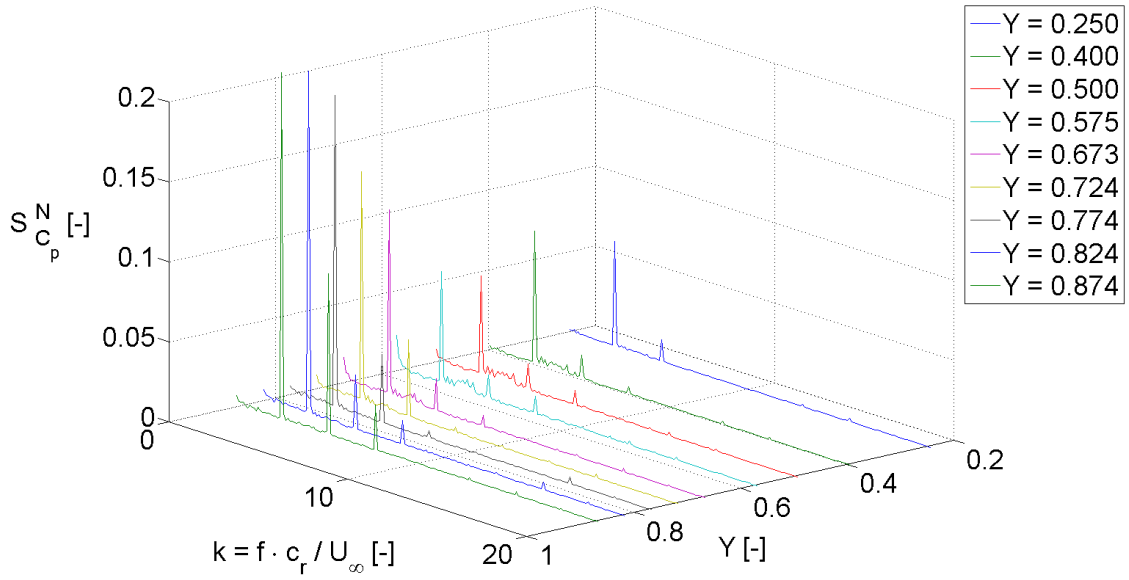

(a) Power spectral density for $X = 0.4$

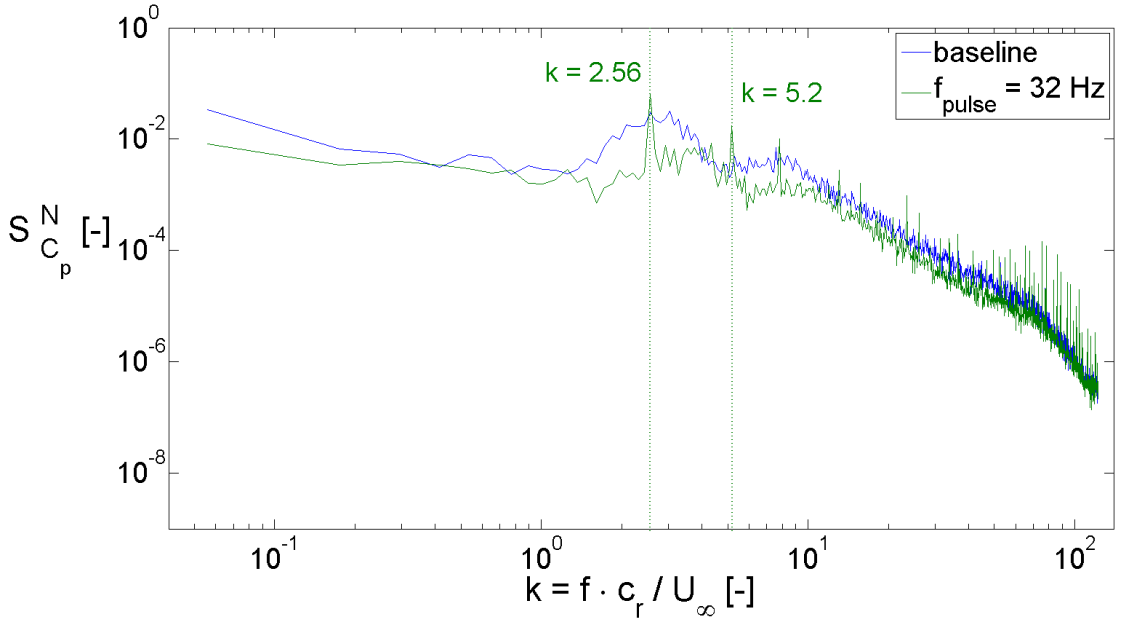

(b) Power spectral density for $X = 0.4$ and $Y = 0.5$

Figure 5.20.: Spectral analysis of the pressure coefficient for $\alpha = 35°$, $Re_{mac} \approx 0.5 \times 10^6$, and $M = 0.035$, pulsed blowing at $f_{pulse} = 32\ Hz$ ($F^+ \approx 2.6$)

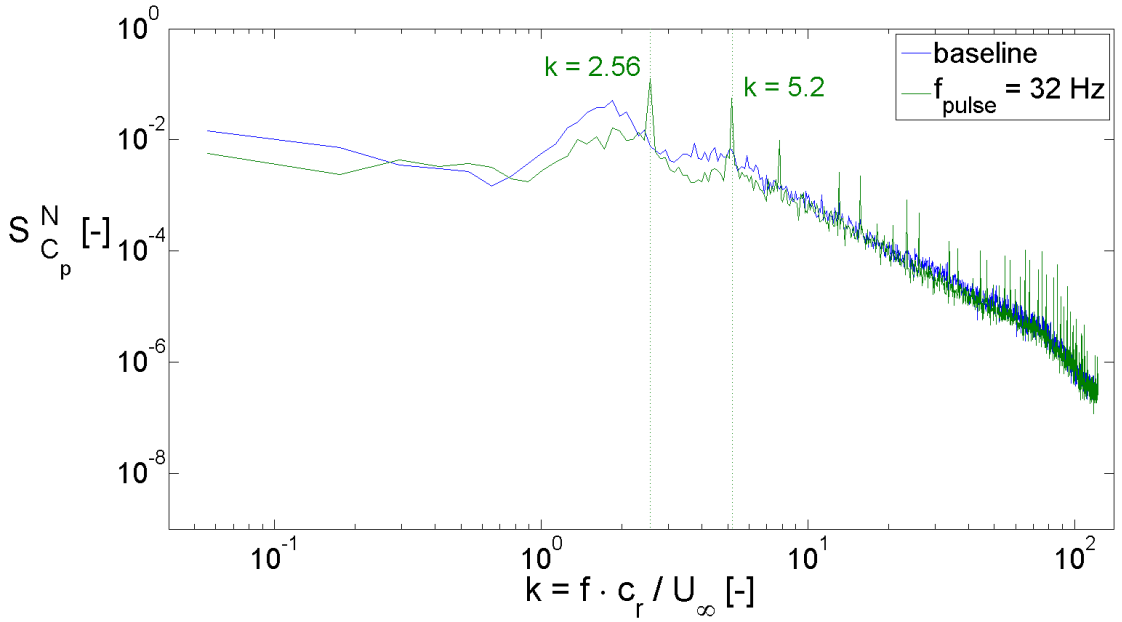

(a) Power spectral density for $X = 0.6$ and $Y = 0.5$

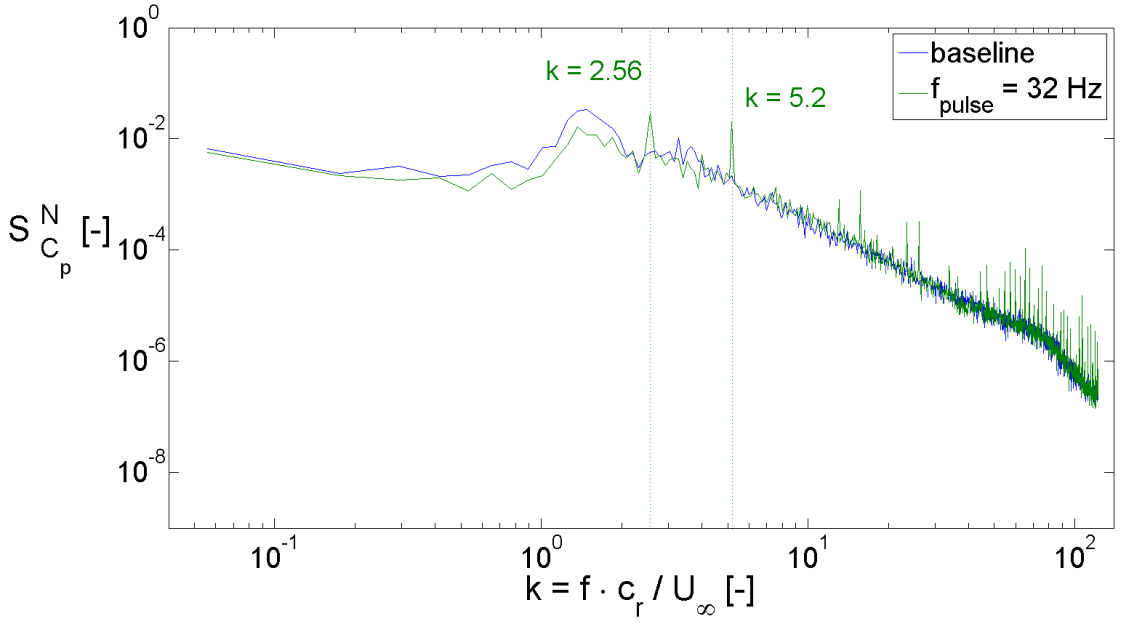

(b) Power spectral density for $X = 0.8$ and $Y = 0.5$

Figure 5.21.: Spectral analysis of the pressure coefficient for $\alpha = 35°$, $Re_{mac} \approx 0.5 \times 10^6$, and $M = 0.035$, pulsed blowing at $f_{pulse} = 32\ Hz$ ($F^+ \approx 2.6$)

5.3.2. Flowfield

The following two figures show the distribution of the axial velocity field (see Fig. 5.22) and the turbulent kinetic energy (see Fig. 5.23) recorded in the HWA measurements, cf. [24], [37].

Pulsed blowing - HWA results. For the controlled case with pulsed blowing at 32 Hz, similar effects are observed as at the rear measurement planes of the pre-stall test case. The region of decelerated axial flow between the two local maxima is minimized and the velocity deficit of the axial velocity component is increased from $u/U_\infty = 0.49$ to 0.53 at $X = 0.4$, see Fig. 5.22. In addition, the axial peak velocity on the wing surface is slightly increased from $u/U_\infty = 2.3$ to $u/U_\infty = 2.4$ [37].

The turbulent kinetic energy is shown in Fig. 5.23 for the baseline and the actuated case. It is slightly increased in the vortex center and diminished in the outer annular region of the burst core by pulsed blowing. This is a sign for an attenuation of vortex breakdown. Additionally, the vertical and horizontal dimensions of the vortex have diminished, indicating a stabilization of the vortex structure.

Spectral analysis of the axial velocities. Fig. 5.24 shows the spectral analysis of the axial velocity signal measured by HWA. The contour plot of the axial velocity fluctuations reveals a large area of high-amplitude fluctuations in the burst vortex core (see the plot at the bottom left). The plots for the four measurement points show the PSD of u'. Whereas the red line represents the PSD measured in the actuated case, the gray line marks the baseline case (see Fig. 4.21) and serves as a reference. Like observed in the spectral analysis of the surface pressures, the TKE concentrates in distinct peaks at the pulse frequency and its higher harmonics. This effect is mainly observed at measurement points 1 to 3. The concentration at a slightly broader band, which appears in the baseline case and is related to the helical mode instability, is significantly reduced and shifted to the pulse frequency. Thus, it is to be assumed that the frequency related to the helical mode instability could be shifted to the pulse frequency by the active blowing. This effect is also known as lock-in effect.

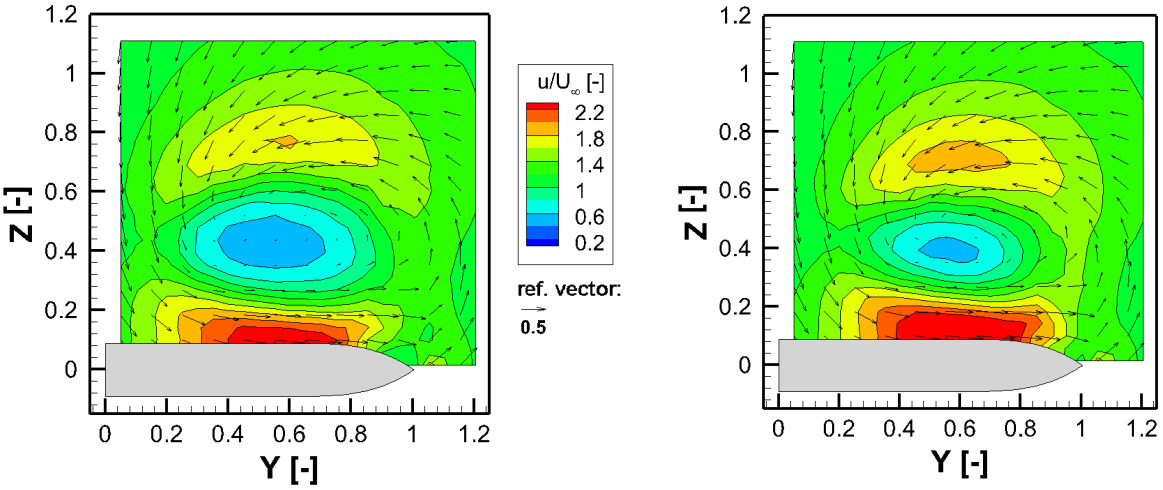

(a) $X = 0.4$

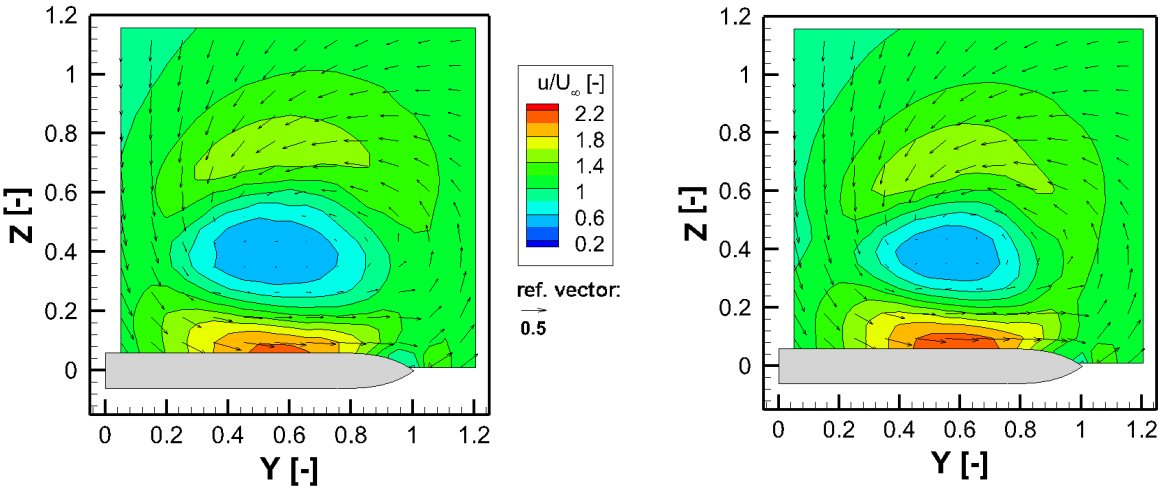

(b) $X = 0.6$

Figure 5.22.: Distribution of the axial velocity for the non-actuated (left) and actuated cases (right) at $\alpha = 35°$ for $Re_{mac} = 0.5 \cdot 10^6$, and $M = 0.035$; pulsed blowing at $f_{pulse} = 32\ Hz$ ($F^+ \approx 2.6$), $DC = 25\%$ and $U_{jet} \approx 50\ m/s$; HWA measurement result

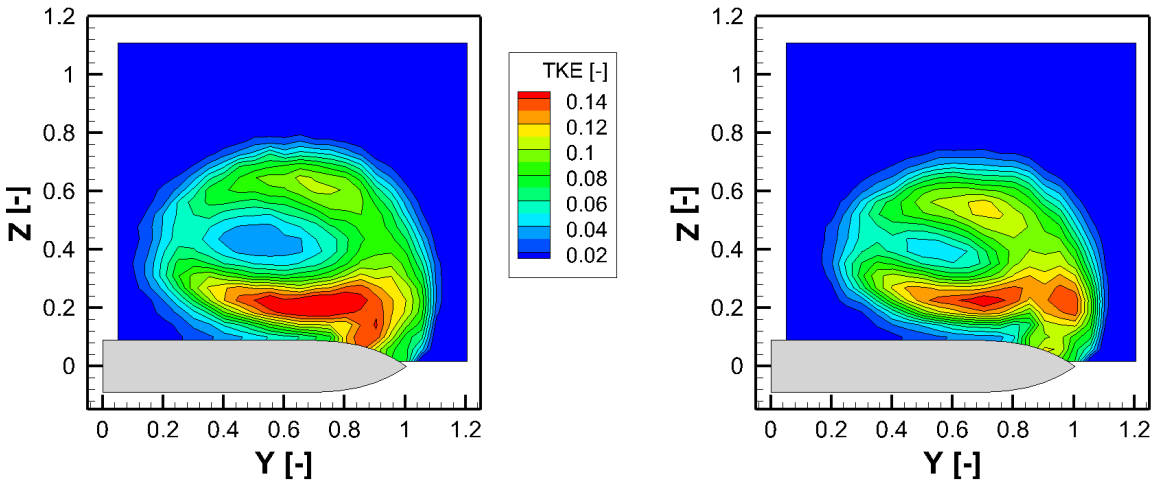

(a) $X = 0.4$

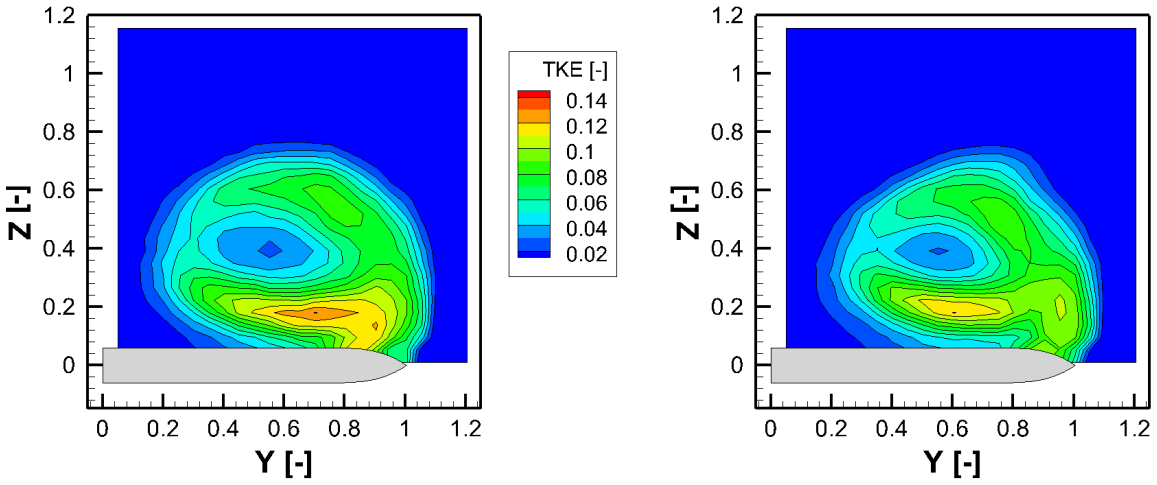

(b) $X = 0.6$

Figure 5.23.: Distribution of the turbulent kinetic energy for the non-actuated (left) and actuated cases (right) at $\alpha = 35°$ for $Re_{mac} = 0.5 \cdot 10^6$, and $M = 0.035$; pulsed blowing at $f_{pulse} = 32\,Hz$ ($F^+ \approx 2.6$), $DC = 25\%$ and $U_{jet} \approx 50\,m/s$; HWA measurement result

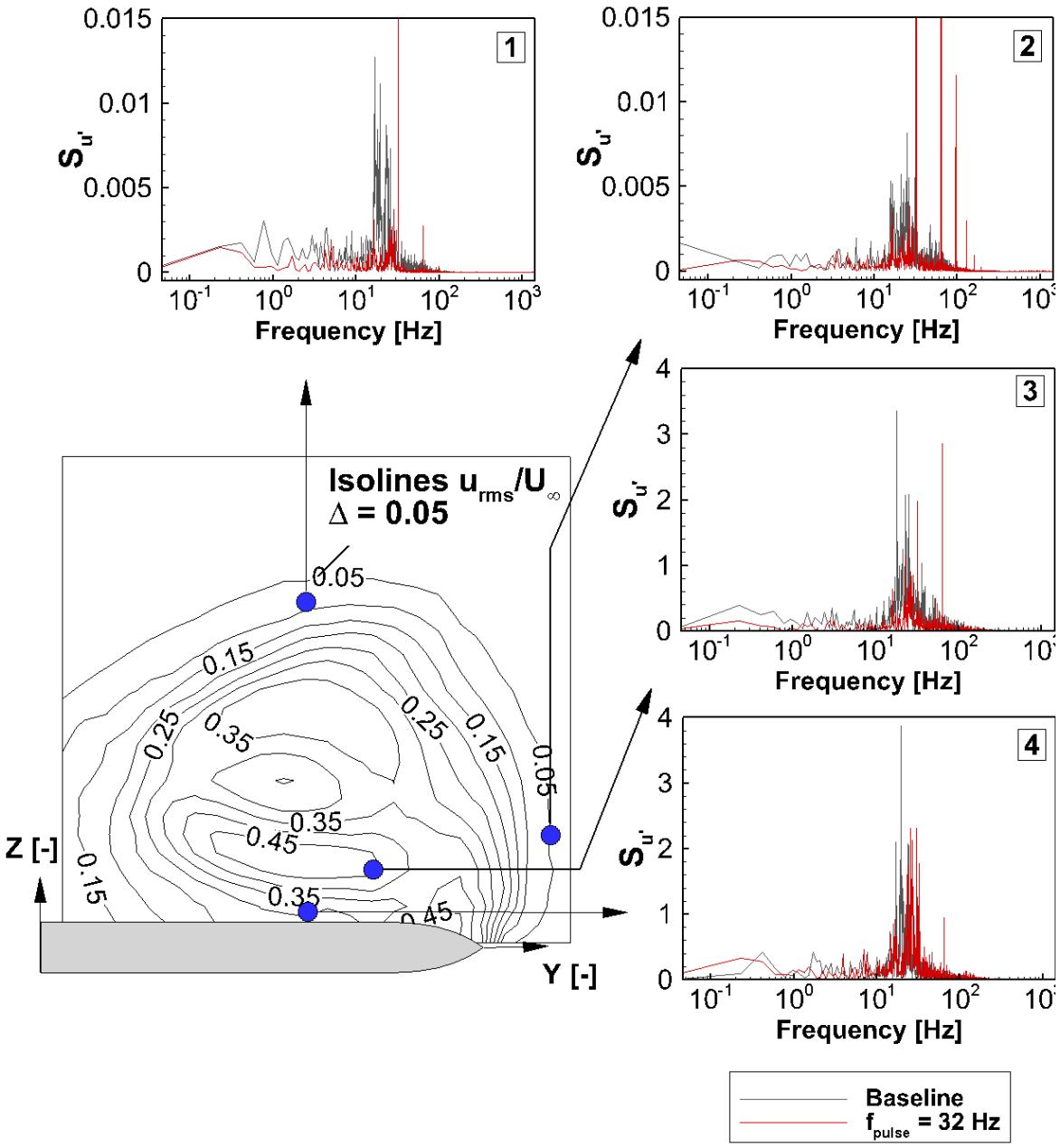

Figure 5.24.: Power spectral density for the axial velocity fluctuations ($S_{u'}$) in the shear layer and the burst vortex core at $\alpha = 35°$, $X = 0.6$, $Re_{mac} = 0.5 \cdot 10^6$ and $M = 0.035$; pulsed blowing at $f_{pulse} = 32\ Hz$ ($F^+ \approx 2.6$)

5.4. Post-stall test case

This subsection contains the results for pulsed blowing at $f_{pulse} = 12\ Hz$ and $U_{jet} \approx 55\ m/s$ at the free-stream conditions $\alpha = 45°$, $Re_{mac} \approx 0.5 \cdot 10^6$ and $M = 0.035$. Two actuation cases are considered: first, pulsed blowing at all three leading edge sections and second, pulsed blowing only at the rear segment.

5.4.1. Surface-pressure distributions

The effect of pulsed blowing is shown for the mean pressure and pressure fluctuations (Fig. 5.25) as well as for the PSD of the pressure coefficient (Figs. 5.26 and 5.27), cf. [5], [37].

According to the mean pressure distribution shown in Fig. 5.25a, the suction level on the upper wing side is highly increased by pulsed blowing. This holds for both active blowing from all three segments and active blowing at the last segment only. The activation of all blowing slots results in a suction pressure increase of approximately 100% at $X = 0.4$ between $Y = 0.3$ and $Y = 0.9$. At $X = 0.6$ and $X = 0.8$, the effect is a bit weaker, but still significant. Furthermore, the results demonstrate the important role of the last blowing segment: at $X = 0.4$, the increase in the suction level is 90% of the suction level observed when all three blowing segments are active. For this reason, a strong upstream effect is detected. In the rear cross sections at $X = 0.6$ and 0.8, the achieved suction level is even highest if only the third blowing segment is active [37].

The pressure fluctuations increase significantly (up to $C_{p,rms} = 0.4$), when pulsed blowing is active. Besides, the fluctuation amplitudes rise with the number of active blowing segments. Local $C_{p,rms}$ maxima are recorded inboard for each cross-section. If all blowing segments are active, the fluctuations increase near the leading-edge, because of the proximity of the slots.

These effects are also observed in the spectral analysis, see Figs. 5.26 and 5.27. Distinctive peaks at the pulse frequency characterize the spectrum of both actuation cases, see Fig. 5.26a and b. If all segments are active, the amplitudes are considerably higher and additional peaks at the higher harmonic frequencies of f_{pulse} occur. The whole spectrum is increased in comparison to the baseline case, see Fig. 5.27.

Fig. 5.28 shows two snapshots of the delta wing equipped with wool tufts on the upper wing side at the flow conditions $\alpha = 45°$ and $Re_{mac} = 0.5 \cdot 10^6$. In the first flow visualization for the baseline case, the filaments are not aligned in a certain direction and no high spatial fluctuations are observed. This implies low velocities and low flow fluctuations in the vicinity of the wing surface. Additionally, some of the filaments indicate a backward flow in the rear part of the wing. On the other hand, the filaments are much stronger aligned by the flow in the actuated case. Hence, the velocities close to the wing surface must be significantly increased. Moreover, the filaments conduct high-amplitude spatial fluctuations, when pulsed blowing is active at $f_{pulse} = 12\ Hz$.

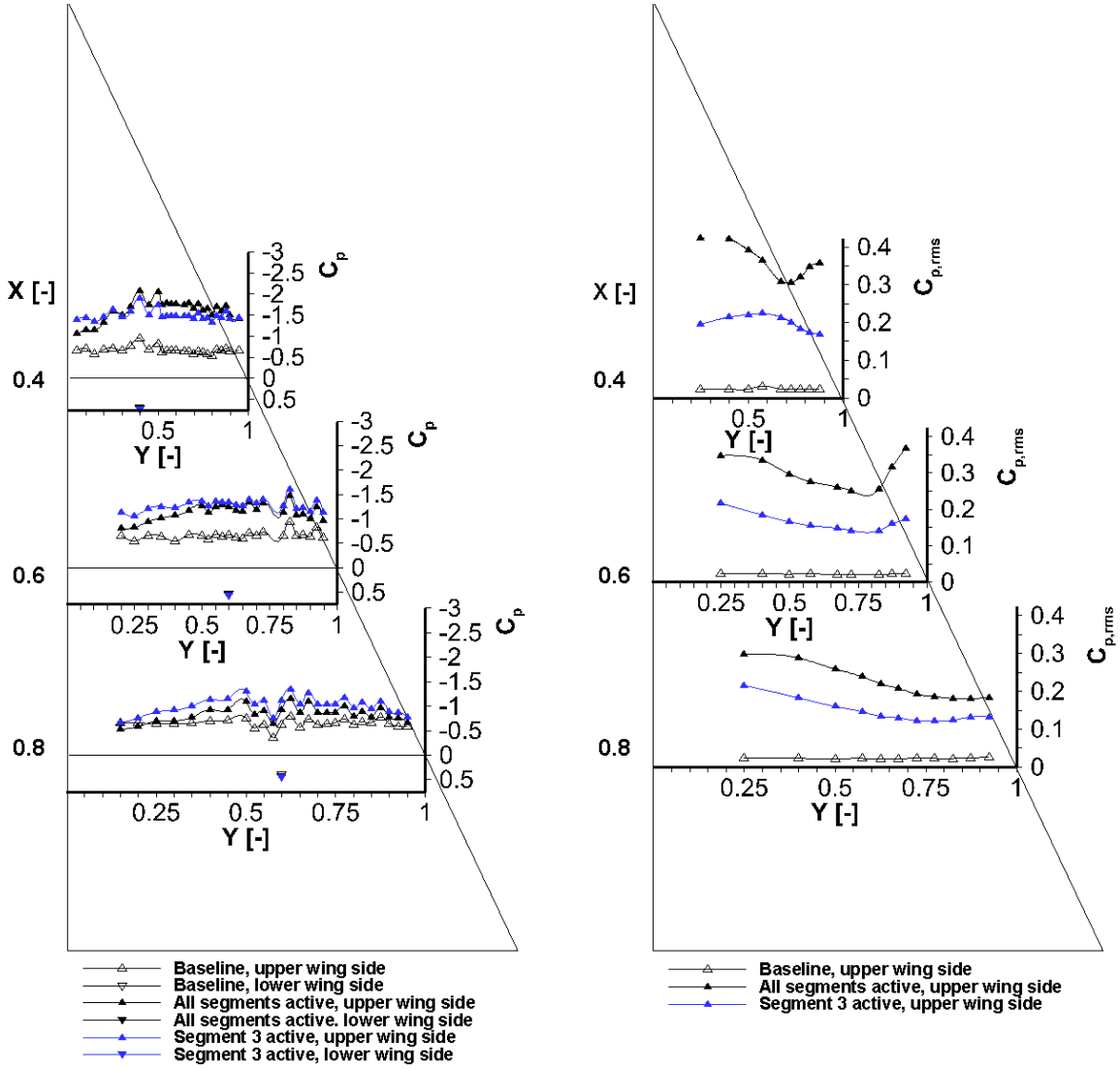

(a) Mean pressure

(b) Pressure fluctuations

Figure 5.25.: Mean pressure and pressure fluctuation distribution for the non-actuated and actuated cases at $\alpha = 45°$ for $Re_{mac} \approx 0.5 \times 10^6$, and $M = 0.035$; pulsed blowing at $f_{pulse} = 12\ Hz$ ($F^+ = 1$), $DC = 25\%$ and $U_{jet} \approx 55\ m/s$, cf. [37]

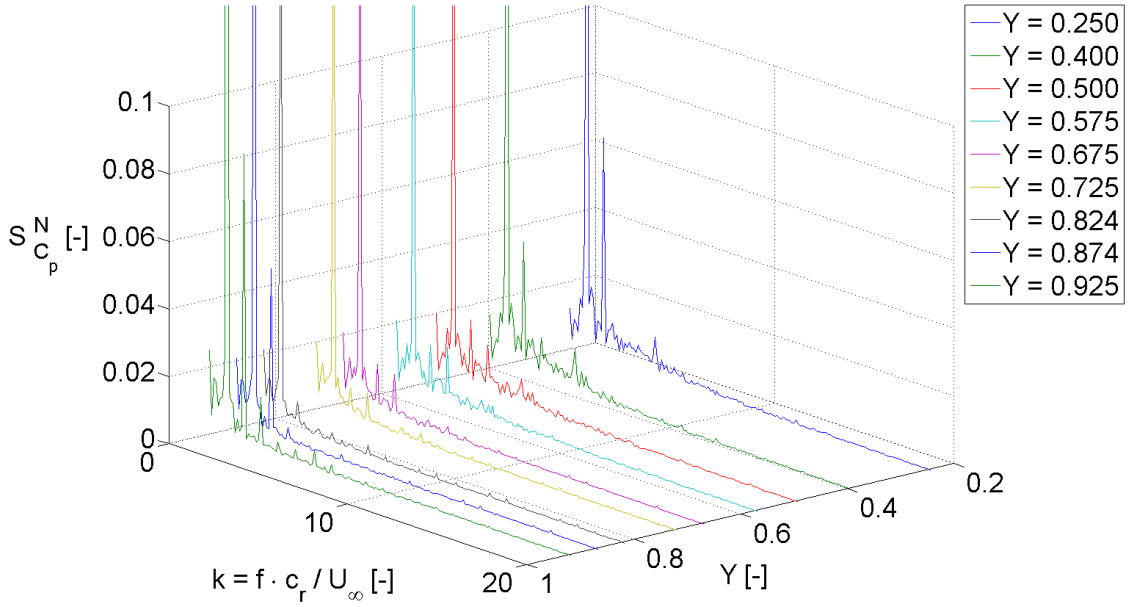

(a) Power spectral density for $X = 0.6$, all segments active

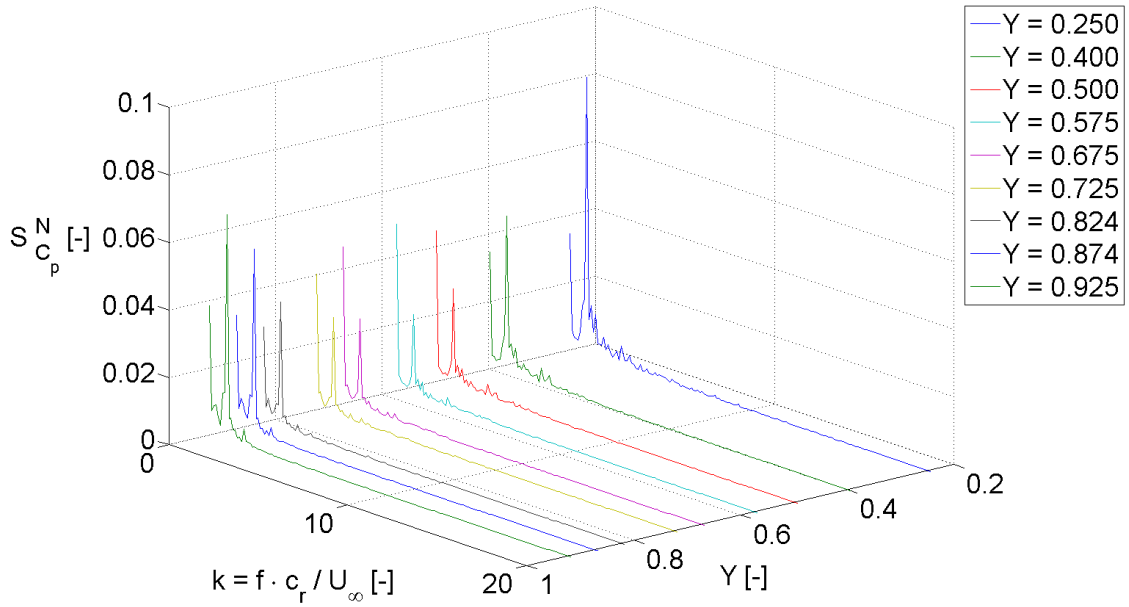

(b) Power spectral density for $X = 0.6$, segment 3 active

Figure 5.26.: Spectral analysis of the pressure coefficient for $\alpha = 45°$, $Re_{mac} \approx 0.5 \times 10^6$, and $M = 0.035$, pulsed blowing at $f_{pulse} = 12\ Hz$ ($F^+ = 1$), $DC = 25\%$ and $U_{jet} \approx 55\ m/s$,

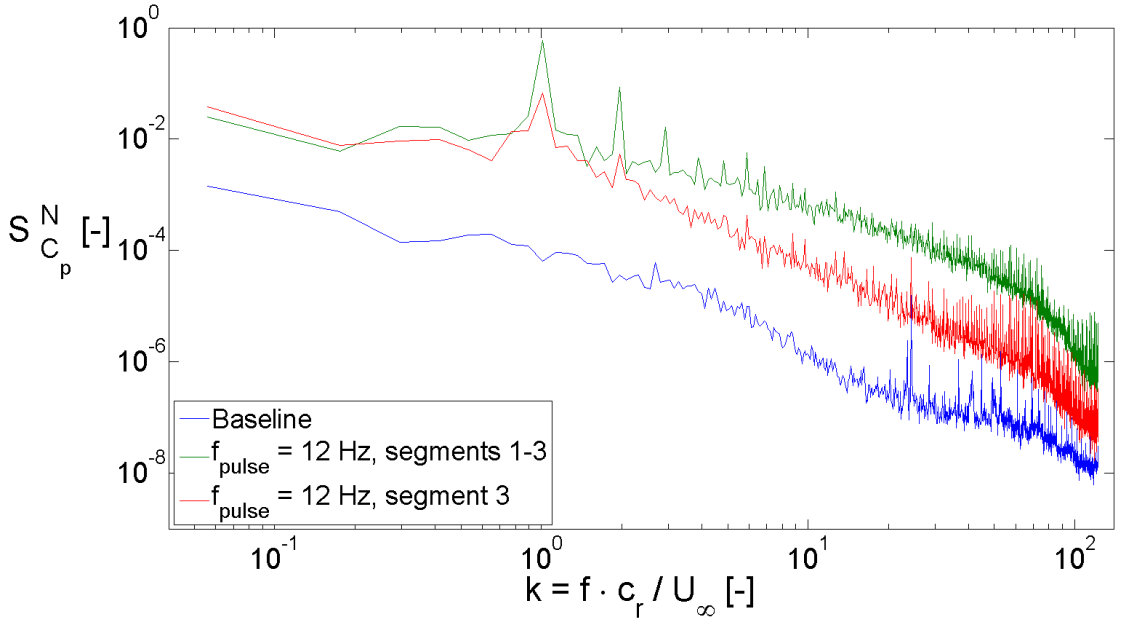

Figure 5.27.: Spectral analysis for $\alpha = 45°$, $Re_{mac} \approx 0.5 \times 10^6$, and $M = 0.035$, pulsed blowing at $f_{pulse} = 12\ Hz$ ($F^+ = 1$), $DC = 25\%$ and $U_{jet} \approx 55\ m/s$, PSD for $X = 0.6$ and $Y = 0.925$

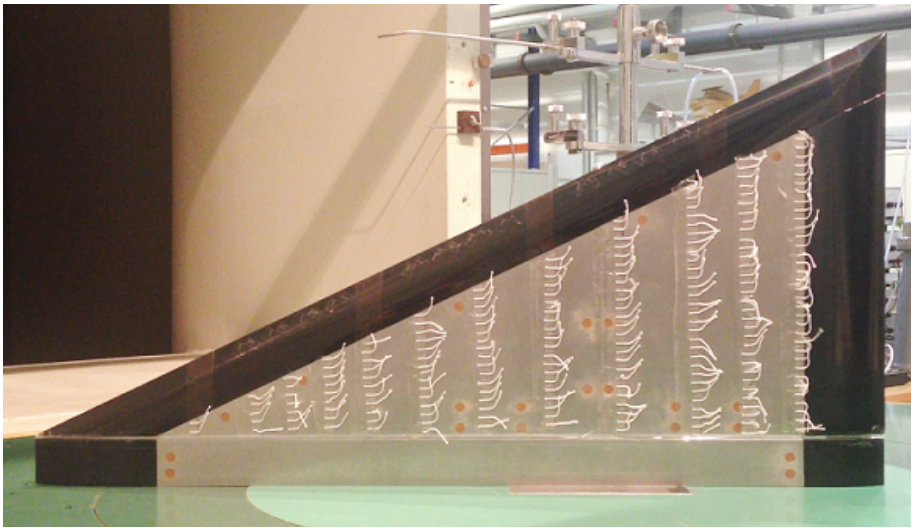

(a) Baseline case

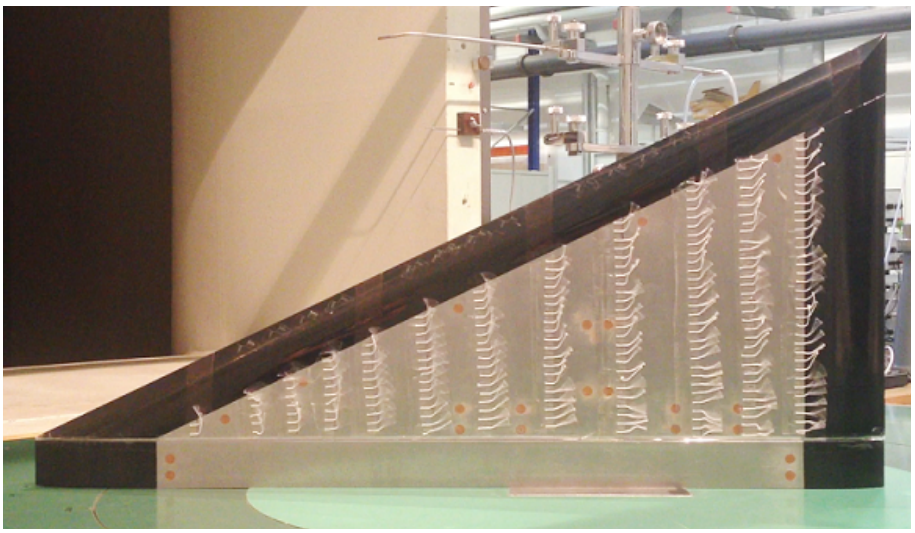

(b) Pulsed blowing at $f_{pulse} = 12\ Hz$ ($F^+ = 1$), $U_{jet} = 60\ m/s$, $DC = 25\%$, all segments active

Figure 5.28.: Wool-tufts visualization on the upper wing side at $\alpha = 45°$, $Re_{mac} = 0.5 \cdot 10^6$ and $M = 0.035$

5.4.2. Flowfield

Baseline PIV results. The axial velocity field and the TKE recorded by PIV are shown in Figs. 5.29a and 5.30a for the post-stall flow conditions, cf. [40]. The shape of the contour plots looks very similar to the pattern recorded in the HWA measurements (see Fig. 4.18). Nevertheless, a big difference is observed: negative axial velocities are detected above the wing by the PIV measurements. This backward flow could not be depicted in the HWA measurements, because an X-wire probe was used that is incapable of detecting negative axial velocities. The turbulent kinetic energy is slightly increased above the wing. The maximal TKE value is 0.06.

Pulsed blowing - PIV results. Figs. 5.29b and 5.30b represent the flow field in the actuated case, cf. [40]. By applying pulsed blowing at all three segments along the leading edge, a massive flow transformation is induced, see also Fig. 5.31 for a direct comparison. A large burst vortex structure is formed that spans over the whole wing half. The vortex comprises an area of decelerated axial flow located in the vortex center. In this area, negative axial velocities are measured, $u/U_\infty = -0.65$ at $X = 0.2$ and $u/U_\infty = -0.45$ at $X = 0.6$. In the second measurement plane the axial velocity is slightly higher: $u/U_\infty = -0.15$. A second local minimum in axial velocity is observed at $X = 0.4$ and 0.6 close to the leading edge. It could be related to a secondary vortex. Moreover, the flow field is characterized by an area of accelerated axial velocity close to the wing surface and further inboard. It is strongest in the second measurement cross-plane $X = 0.4$ and correlates with the higher suction pressure level observed in the actuated case, see Fig. 5.25. The cross-flow velocities indicate a motion around a position that is located below the area of decelerated axial flow, see Fig. 5.31.

The TKE shown in Fig. 5.30 is strongly increased in comparison to the baseline case. The highest fluctuations are observed in the regions above and below the burst vortex core.

Spectral analysis of the axial velocities. The PSD of the axial fluctuations is shown for several positions at $X = 0.6$ in Fig. 5.32. Similarly to the TKE distribution, the fluctuations of the axial velocity component are increased in the whole measurement plane. Additionally, local maxima are found above and below the burst vortex core. The pulse frequency is dominant in the spectra of the points located in the shear layer (point 3) and in the regions where the axial velocity fluctuations are maximal (points 2 and 6). The pulse frequency is less dominant in the areas where the fluctuations reach a local minimum (points 1, 4 and 5).

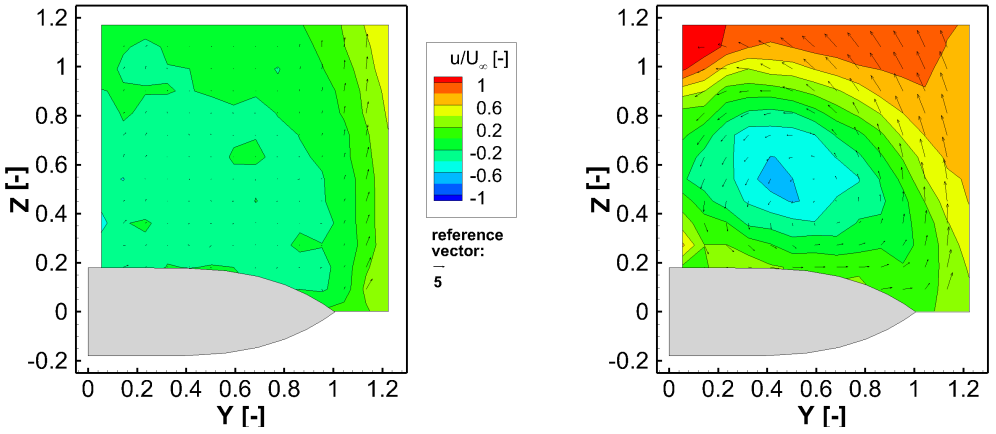

(a) $X = 0.2$

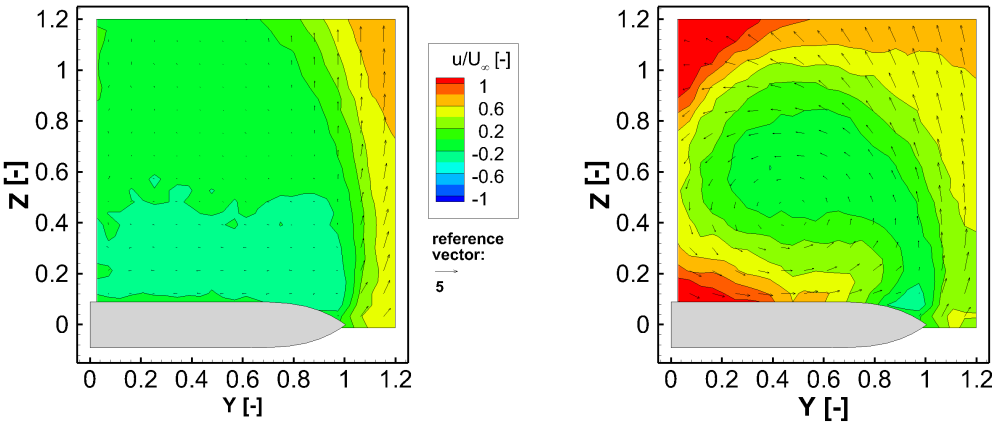

(b) $X = 0.4$

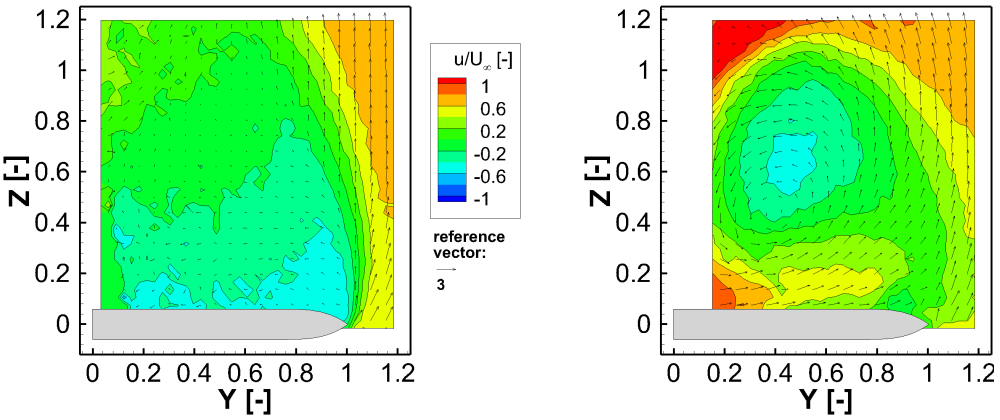

(c) $X = 0.6$

Figure 5.29.: Distribution of the axial velocity for the non-actuated (left) and actuated cases (right) at $\alpha = 45°$ for $Re_{mac} = 0.5 \cdot 10^6$, and $M = 0.035$; pulsed blowing at $f_{pulse} = 12\ Hz$ ($F^+ = 1$), $DC = 25\%$ and $U_{jet} \approx 55\ m/s$; PIV measurement result

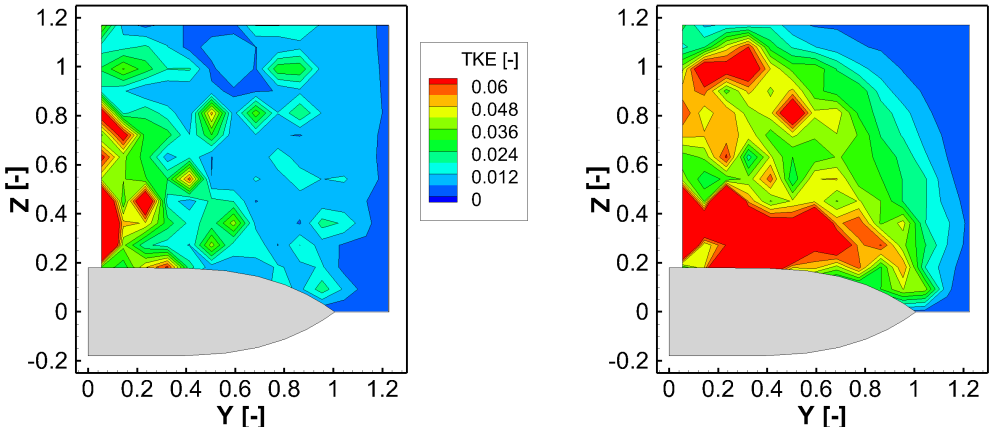

(a) $X = 0.2$

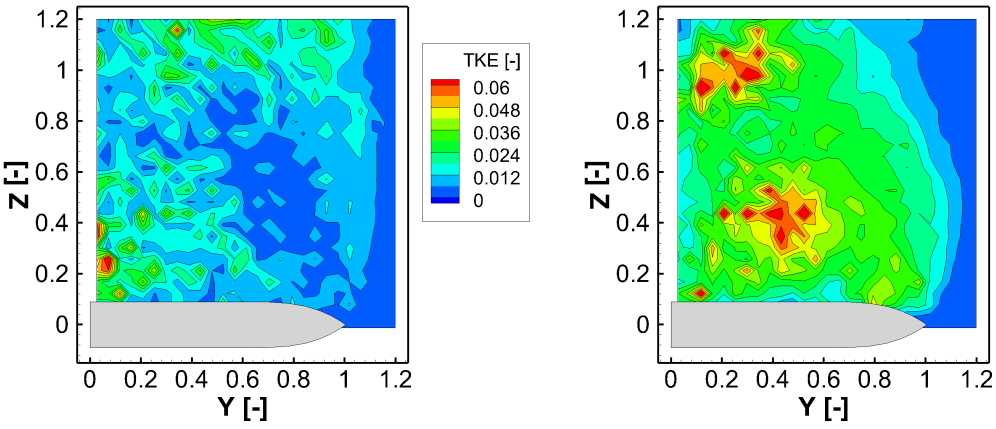

(b) $X = 0.4$

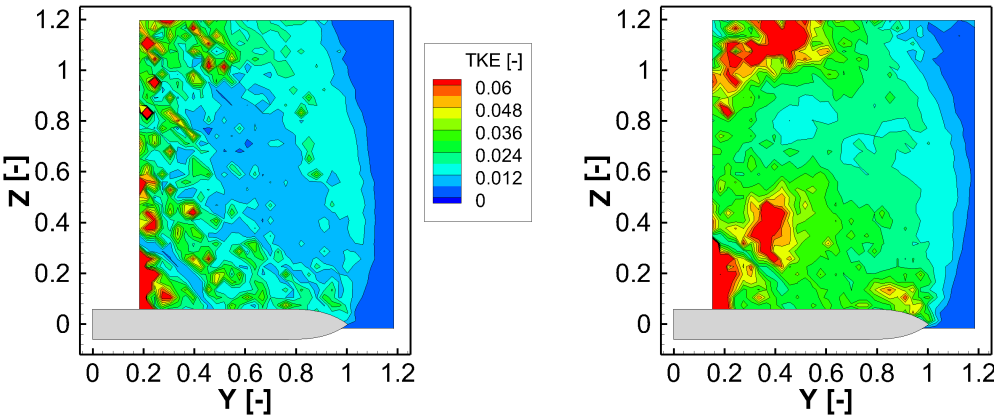

(c) $X = 0.6$

Figure 5.30.: Distribution of the turbulent kinetic energy for the non-actuated (left) and actuated cases (right) at $\alpha = 45°$ for $Re_{mac} = 0.5 \cdot 10^6$, and $M = 0.035$; pulsed blowing at $f_{pulse} = 12\ Hz$ ($F^+ = 1$), $DC = 25\%$ and $U_{jet} \approx 55\ m/s$; PIV measurement result

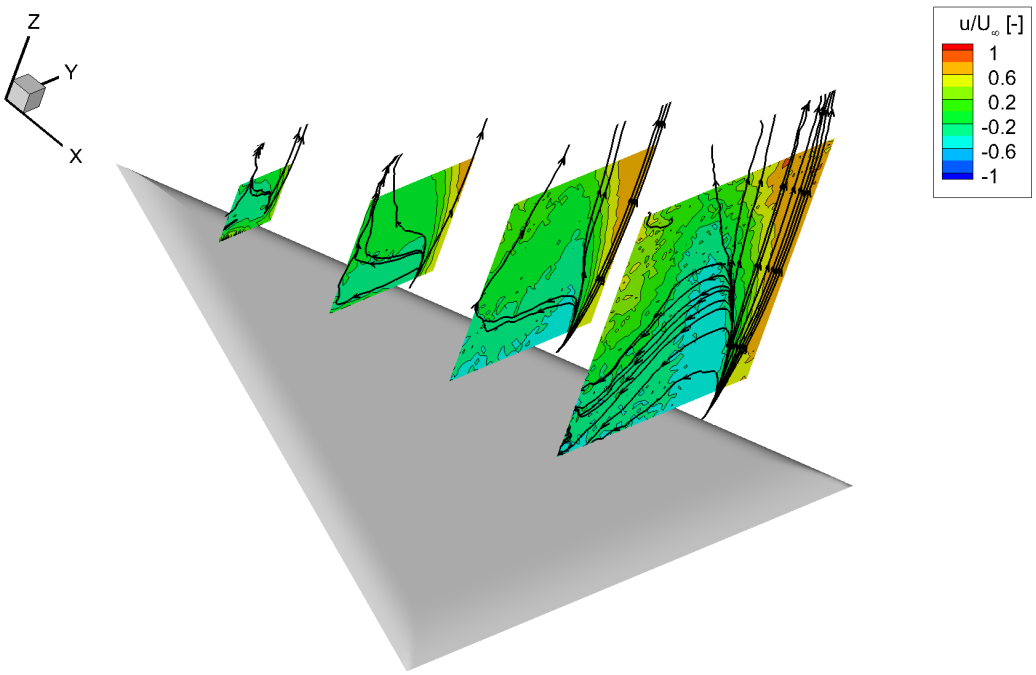

(a) Baseline case

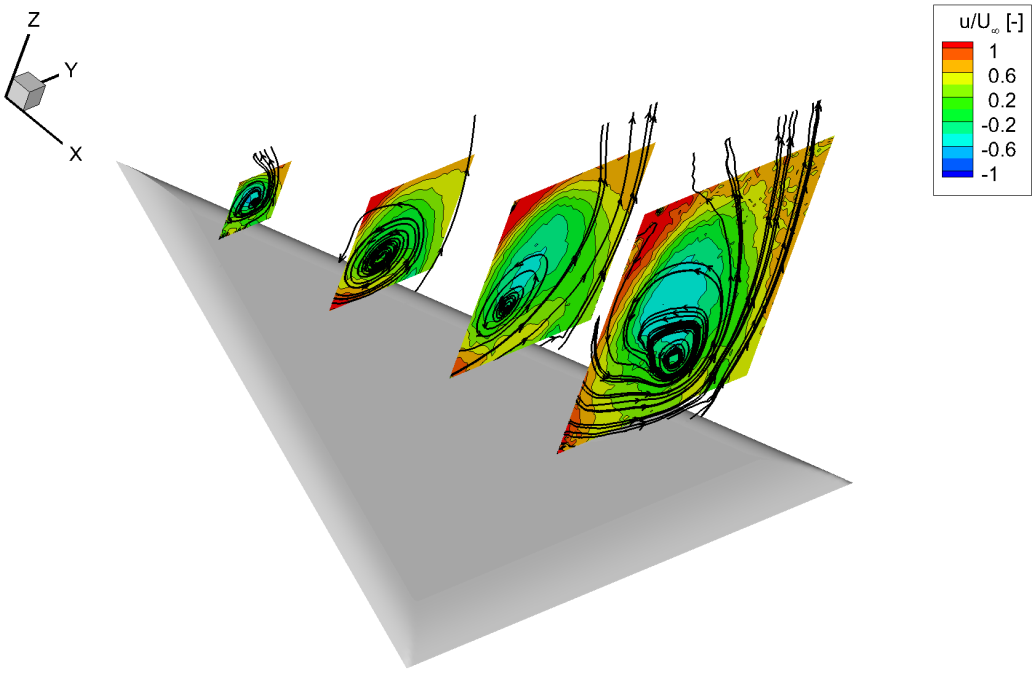

(b) Actuated case

Figure 5.31.: Distribution of the axial velocity and streamtraces at $\alpha = 45°$ for $Re_{mac} = 0.5 \cdot 10^6$, and $M = 0.035$; pulsed blowing at $f_{pulse} = 12\ Hz$ ($F^+ = 1$), $DC = 25\%$ and $U_{jet} \approx 55\ m/s$; PIV measurement result

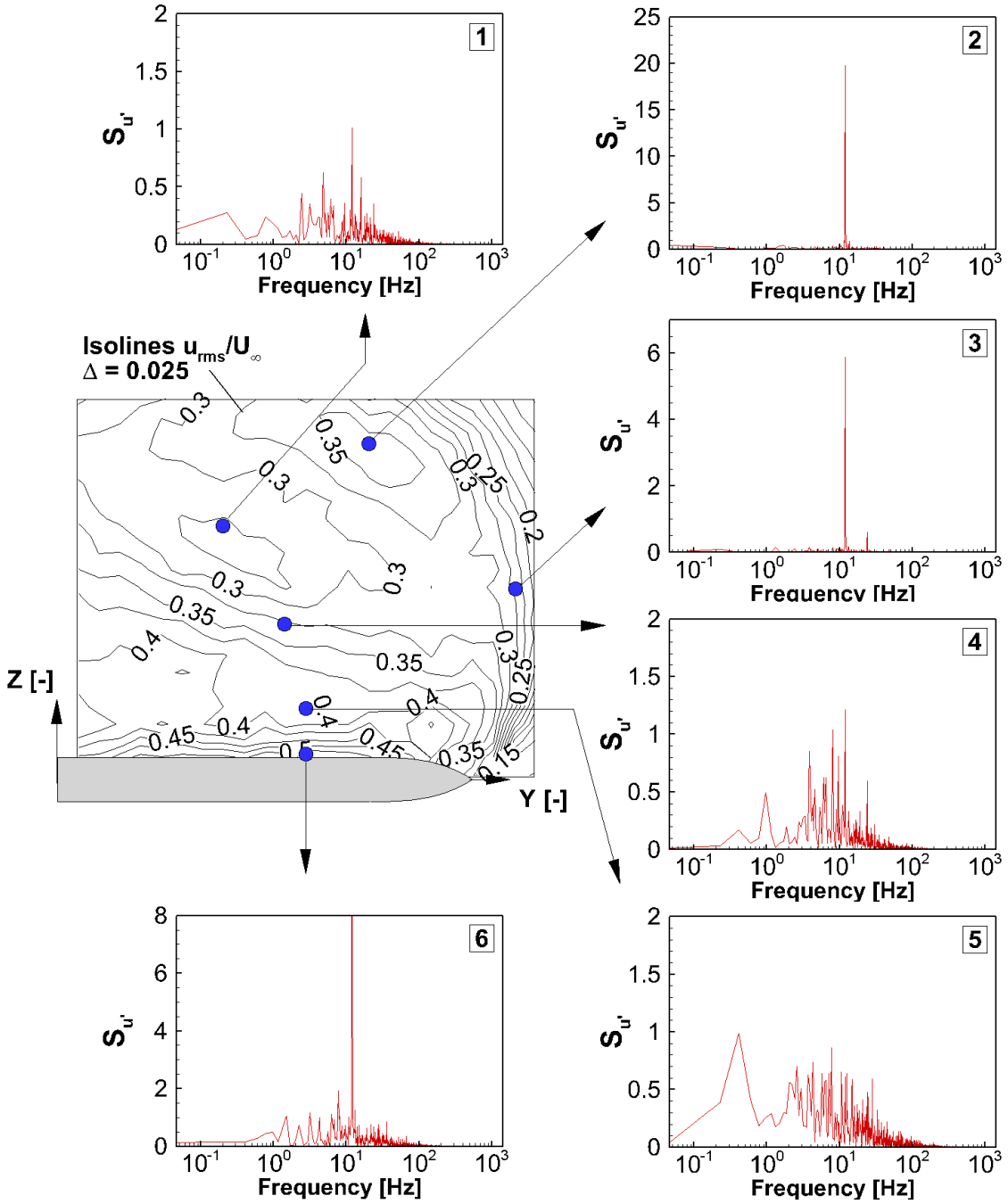

Figure 5.32.: Power spectral density for the axial velocity fluctuations ($S_{u'}$) at $\alpha = 45°$, $X = 0.6$, $Re_{mac} = 0.5 \cdot 10^6$ and $M = 0.035$; pulsed blowing at $f_{pulse} = 12\ Hz$ ($F^+ = 1$)

5.5. Summary

In this chapter, active blowing has been studied with pulsed jets ejected on the upper wing surface close to the leading edge. In the first step, a parameter study was carried out in order to find the optimal actuation parameters. On this basis, the effect of pulsed blowing was investigated for three different test cases. The optimal parameters and their effect on the flow field are summarized in this subsection.

In all test cases, unsteady excitation had a greater effect than steady blowing. Moreover, the respective actuation frequency was detected in the flow field above the wing, both in the shear layer emanating from the leading edge and in the vortex. This confirms the receptivity of the shear layer for periodic forcing.

The following conclusions can be drawn for pulsed blowing in the pre-stall regime:

- Pulsed blowing at $F^+ \approx 2.6$ causes a downstream-shift of the vortex breakdown location, $\Delta x_{bd} \approx 0.2$.
- The narrow-banded concentration of the power spectral density, that is observed related to the helical mode instability in the baseline case without actuation, is concentrated in a very high peak at the pulse frequency of active blowing in the actuated flow case.
- The influence on the aerodynamic force and moment coefficients is very small.

In the stall regime, similar effects as in the pre-stall regime are observed:

- An actuation at $F^+ \approx 2.6$ leads to a slight increase in lift.
- The vortex breakdown is attenuated and the primary vortex is stabilized.
- The effect on the moment coefficients is marginal.

In the post-stall regime, the following observations are made:

- Pulsed blowing at reduced frequencies F^+ from 1 to 2 leads to a massive flow transformation from a detached shear layer to a large burst vortex structure.
- The increase in axial and circumferential velocities close to the wing surface causes a significant increase in the suction pressure and thereby, the generation of lift induced by pulsed blowing ($\Delta C_L = +60\%$). This optimum is reached for a duty cycle DC between 20% and 50% and the highest tested jet velocity ($U_{jet} \approx 60\ m/s$, $U_{jet}/U_\infty \approx 5$, $C_\mu \approx 0.0067$ for $f_{pulse} = 12\ Hz$ and $18\ Hz$ and $DC = 25\%$).
- At the same time, the drag coefficient increases and an additional negative rolling moment as well as an increase in the yawing and the pitching moment is observed for half wing blowing, the latter summing up to $\geq +140\%$.

- With respect to the lift coefficient, the highest impact is observed if all blowing segments are active. Nevertheless, it has to be highlighted that the rear blowing segment is the most efficient one, generating 85% of the lift increase compared to the mode when all three segments are active. This could be a hint that the roll-up process generated by pulsed blowing in the post-stall case begins at the rear part of the wing, as it is analogously the case when the primary vortex system develops at low angles of attack in the pre-stall regime.

6. Leading-edge flaps

The results obtained with oscillating leading-edge flaps are presented in this chapter. The chapter structure is in analogy with the previous chapter. At the beginning, a parameter study with respect to force measurement results covering the pre-stall, stall and post-stall regime is presented. Subsequently, one test case in the post-stall regime is described in more detail including the results of pressure and velocity measurements.

6.1. Parameter study

The following parameters can be adjusted in the leading edge flap system (see Chapter 3.1.3):

- the oscillation frequency of the flap f_{flap},
- the flap deflection angle $\hat{\delta}$,
- and the active segments.

A parameter study with force measurements is conducted in order to detect the optimal actuation parameters. Primarily, the influence of different flap frequencies is studied. Besides, the choice of the active segments and the deflection angle regime are varied for particular parameter sets. In all test cases, the flaps were driven in synchronous oscillation mode.

6.1.1. Frequency variation for the pre-stall, stall and post-stall regime

Figs. 6.1 and 6.2 show the results of the flap frequency variation for the angle-of-attack regime from $\alpha = 23°$ to $50°$. The flap frequency was varied from $f_{flap} = 12\ Hz$ ($F^+ = 1$) to 66 Hz ($F^+ \approx 5.4$) and nine different frequencies were tested. Namely, these were $f_{flap} = 12, 18, 24, 33, 38, 44, 48, 56$ and 66 Hz ($F^+ = 1, 1.5, 2, 2.7, 3.1, 3.6, 4, 4.6$ and 5.4). The flap deflection angle was $\hat{\delta} = 18°$ for all actuation test cases. This experiment was conducted in the wind tunnel B, see Chapter 3.2.

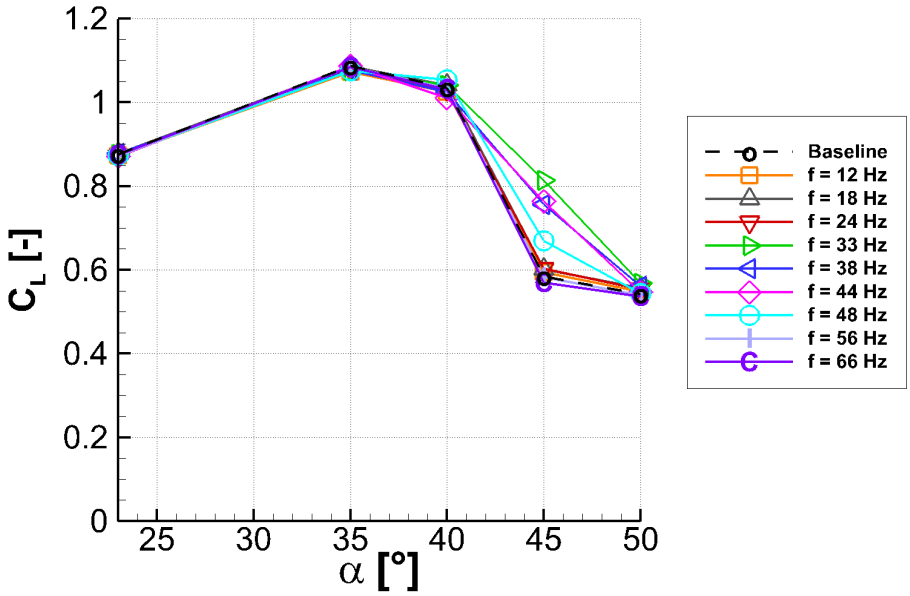

(a) Lift coefficient

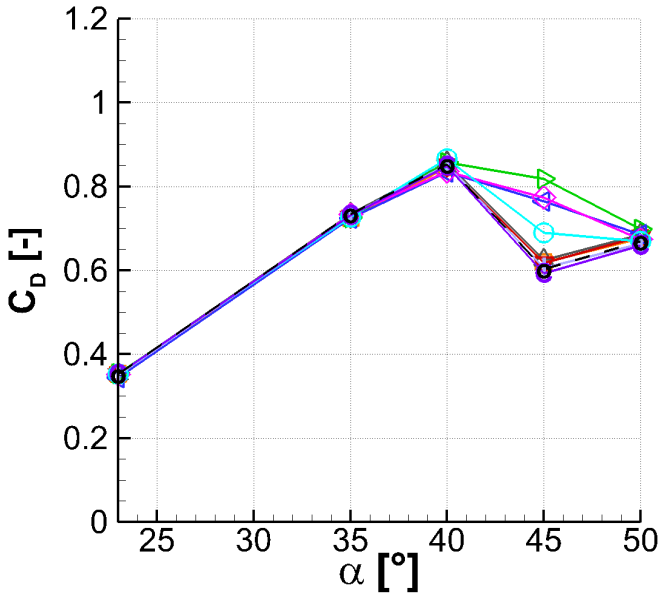

(b) Drag coefficient

Figure 6.1.: Force coefficients for the variation of f_{flap} ($F^+ = 1$ to 5.4) at $\alpha = 23°$ to $\alpha = 50°$, $Re_{mac} = 0.5 \cdot 10^6$ and $M = 0.035$; flap amplitude $\hat{\delta} \approx 18°$; measurement in wind tunnel B

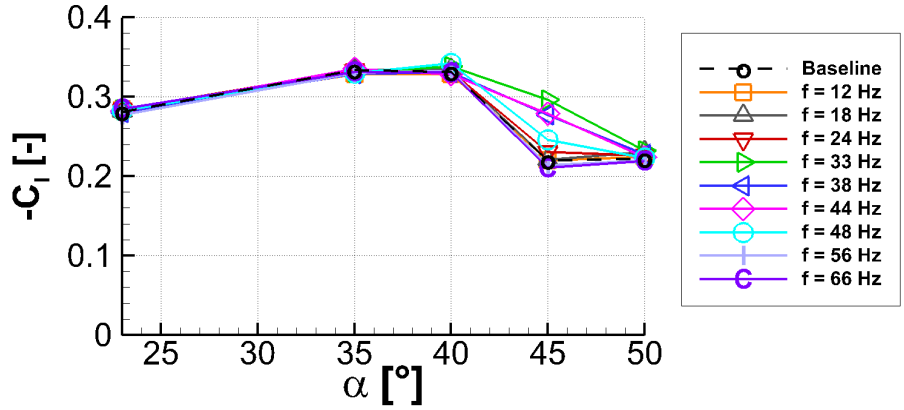

(a) Rolling moment coefficient

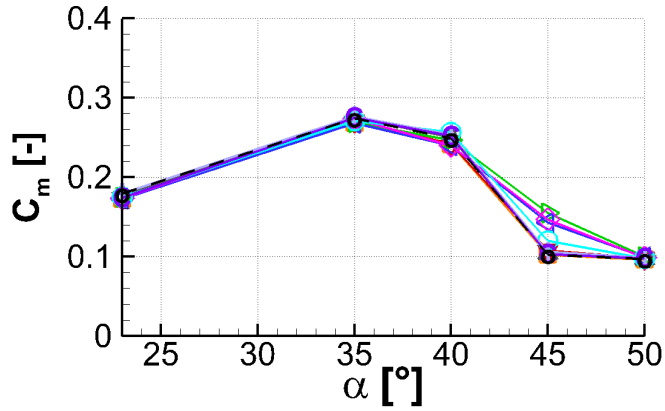

(b) Pitching moment coefficient

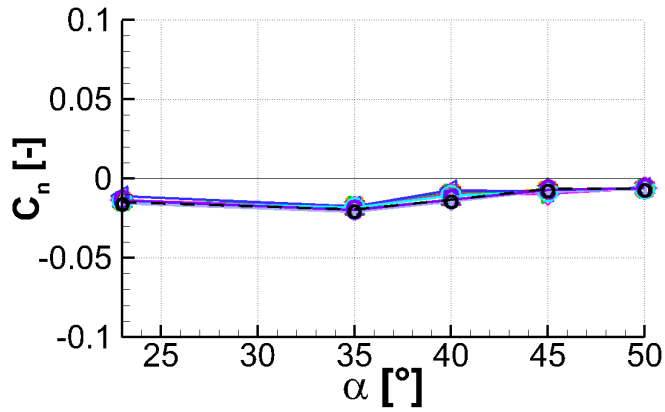

(c) Yawing moment coefficient

Figure 6.2.: Moment coefficients for the variation of f_{flap} ($F^+ = 1$ to 5.4) at $\alpha = 23°$ to $\alpha = 50°$, $Re_{mac} = 0.5 \cdot 10^6$ and $M = 0.035$; flap amplitude $\hat{\delta} \approx 18°$; measurement in wind tunnel B

The force coefficients C_L and C_D shown in Fig. 6.1 are rarely changed by the flap oscillation in the pre-stall and stall regime ($\alpha = 23°$ and $\alpha = 35°$). In contrast, a significant effect is observed in the post-stall regime, and especially for $\alpha = 45°$. Here, the flap frequencies $f_{flap} = 33\ Hz$ to $48\ Hz$ ($F^+ = 2.7$ to 4) cause an increase in lift of $\Delta C_L = +15\%$ to $+40\%$. It is maximal for $f_{flap} = 33\ Hz$ ($F^+ = 2.7$), where the lift coefficient increases from $C_{L,baseline} = 0.57$ to $C_{L,33Hz} \approx 0.8$. Additionally, an increase in drag is associated with the lift increase observed at $\alpha = 45°$. The increase in drag is also maximal for $f_{flap} = 33\ Hz$ ($F^+ = 2.7$). The increase relative to the baseline case is slightly lower than the increase in lift ($\Delta C_{D,33\ Hz} = +35\%$).

The moment coefficients for the flap frequency variation are depicted in Fig. 6.2. They are almost identical to the coefficients of the baseline case for $\alpha = 23°$ and $\alpha = 35°$. In the post-stall regime, a decrease of the rolling moment and an increase of the pitching moment are caused by the flap oscillation $f_{flap} = 33\ Hz$ to $48\ Hz$ ($F^+ = 2.7$ to 4). The yawing moment is barely effected by the flap oscillations.

6.1.2. Additional investigations in the post-stall regime

Since the results achieved with the oscillating flaps were most considerable for $\alpha = 45°$, the actuation was investigated in more detail for this angle of attack. Thereby, the active segments and the flap frequencies were varied in one experiment. Additionally, one experiment was carried out with the flap oscillating only on the upper side of the wing.

Variation of the active segments Fig. 6.3 shows the lift coefficient recorded for the variation of the active segments at $\alpha = 45°$ for the flap frequencies $f_{flap} = 12\ Hz$ to $66\ Hz$ ($F^+ = 1$ to 5.4). In one case, only the first three flaps were oscillating (red line) and in the other case, only flaps 4 to 6 in the rear part of the model were active (green line). The blue line symbolizes the case when all six flaps were activated. In this case, the increase in lift is maximal for $f_{flap} \approx 33\ Hz$ to $44\ Hz$ ($F^+ = 2.7$ to 3.6). This was already described in the last section. If only the rear flaps are oscillating, no lift increase is measured for all flap frequencies studied. In contrast, if the front flaps are active, an increase in lift is observed for $f_{flap} = 33\ Hz$ to $48\ Hz$ ($F^+ = 2.7$ to 4). The maximum is observed for $f_{flap} = 38\ Hz$ ($F^+ = 3.6$), where $C_L = 0.74$ is reached.

Variation of the flap deflection In Fig. 6.4, the comparison of two different flap actuation profiles is shown for the flap frequencies $f_{flap} = 12\ Hz$ to $66\ Hz$ ($F^+ = 1$ to 5.4). Whereas the blue line marks the results for the standard configuration with an oscillation between the two flap deflection angles $\delta = \pm 18°$, the red line represents the results of an oscillation only on the upper wing side, between the two flap deflection angles $\delta = 0°$ and $+18°$. It becomes clear that the oscillation solely on the upper wing side, when the effective angle of attack is periodically increased by the flap deflection, has a much less influence on the flow field then if the flaps cause a periodical change between an increase and a reduction of the effective angle of attack at the leading edge.

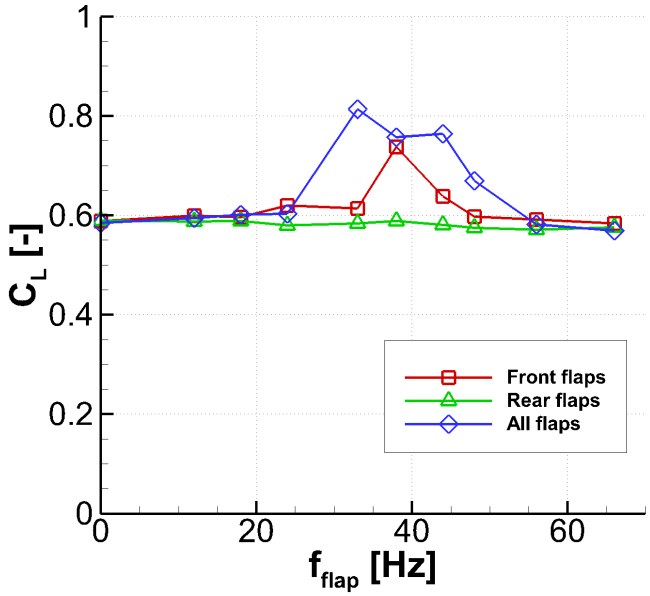

Figure 6.3.: Lift coefficient for the variation of the active flap segments at $\alpha = 45°$, $Re_{mac} = 0.5 \cdot 10^6$ and $M = 0.035$; variation of the flap frequency from $f_{flap} = 12\ Hz$ to $66\ Hz$ ($F^+ = 1$ to 5.4); measurement in wind tunnel B

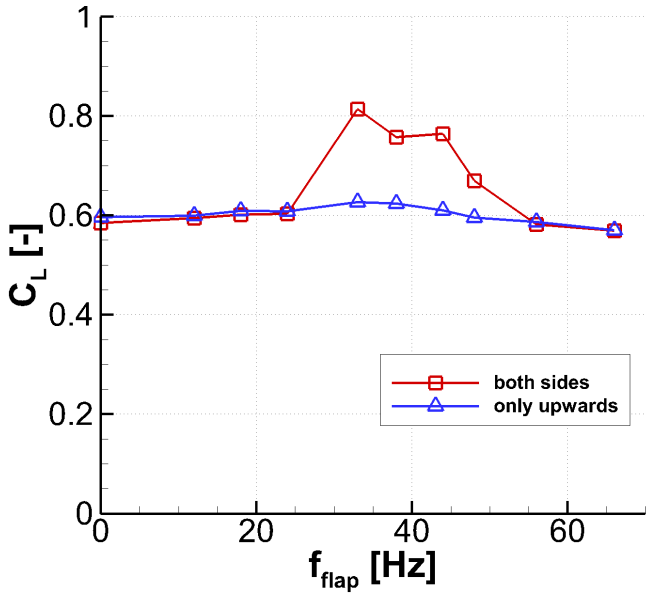

Figure 6.4.: Lift coefficient for the comparison of the flaps oscillating only on the upper wing side and on both sides at $\alpha = 45°$, $Re_{mac} = 0.5 \cdot 10^6$ and $M = 0.035$; variation of the flap frequency from $f_{flap} = 12\ Hz$ to $66\ Hz$ ($F^+ = 1$ to 5.4); measurement in wind tunnel B

6.1.3. Definition of the test case

The effect of the flap system was studied in more detail for the post-stall regime. Based on the results from the force measurements recorded in wind tunnel B, a flap frequency range of $f_{flap} = 33\ Hz$ to $44\ Hz$ ($F^+ = 2.7$ to 3.6) is most efficient at $\alpha = 45°$ and $Re_{mac} = 0.5 \cdot 10^6$. Therefore, the flap frequency $f_{flap} = 38\ Hz$ ($F^+ = 3.1$) was studied in more detail for an oscillation amplitude $\hat{\delta} = 18°$.

Pressure measurements were conducted at $\alpha = 45°$ in wind tunnel B. Additionally, PIV flow field measurements were carried out in wind tunnel A. Thereby, one important aspect had to be considered: the baseline force measurement results which were recorded with the flap model in wind tunnel A differ from those recorded in wind tunnel B (see Chapter 4.1.3), due to the different blockage ratios in the two wind tunnel facilities, see Chapter 3.2. Amongst others, the lift decay after the collapse of the primary vortex system appears at lower angles of attack, from $\alpha = 40°$ to $41°$ in the bigger wind tunnel A, instead of from $\alpha = 42°$ to $43°$ in wind tunnel B. For this reason, the force measurements with oscillating flaps were repeated for the mentioned post-stall test case in wind tunnel A. As a result, it was observed that the region where the lift coefficient can be increased by the flap oscillation is shifted to lower angles of attack compared to wind tunnel B. A significant increase in lift can be achieved at $\alpha = 41°$ to $42°$. In this case, the optimal flap frequency is $f_{flap} = 44\ Hz$ ($F^+ = 3.6$).

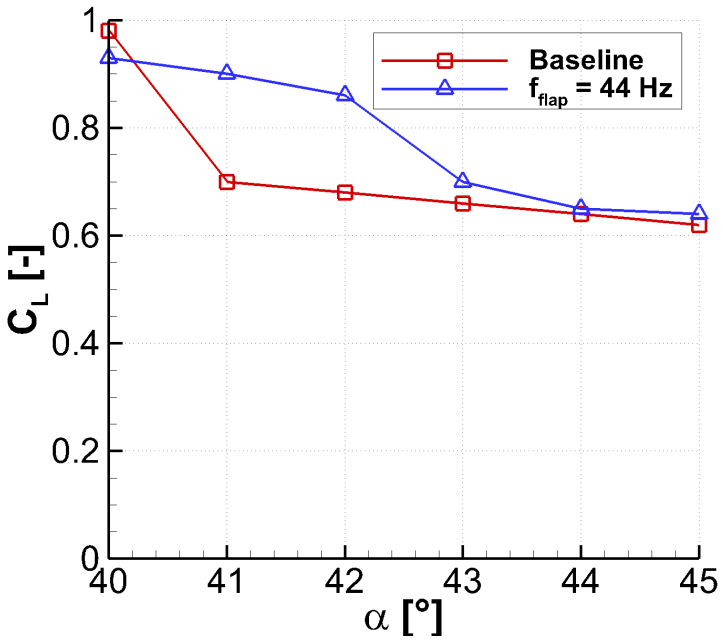

Figure 6.5.: Lift coefficient for $f_{flap} = 44\ Hz$ ($F^+ = 3.6$) and $\hat{\delta} = 18°$ at $\alpha = 40°$ to $\alpha = 45°$, $Re_{mac} = 0.5 \cdot 10^6$ and $M = 0.035$; measurement in wind tunnel A

The force measurement results for this actuation frequency are shown in Fig. 6.5. As the effect of the flap oscillation is very low at $\alpha = 45°$, it was decided to carry out the PIV measurements at the smaller angle of attack $\alpha = 42°$ in wind tunnel A. The flow and actuation parameters during the different measurements are summarized in Table 6.1.

Table 6.1.: Flap oscillation test case

Domain	Measurement type	α	Re_{mac}	U_∞	M	f_{flap}	F^+	$\hat{\delta}$
Post-stall	Pressure measurement	42°	$0.5 \cdot 10^6$	12 m/s	0.035	38 Hz	3.1	18°
Post-stall	PIV measurement	42°	$0.5 \cdot 10^6$	12 m/s	0.035	44 Hz	3.6	18°

6.2. Post-stall test case

In this subsection the results for the flap oscillation at $f_{flap} = 38\ Hz$ and 44 Hz ($F^+ = 3.1$ and 3.6) are presented for the free-stream conditions $\alpha = 45°$ and 42° at $Re_{mac} = 0.5 \cdot 10^6$ and $M = 0.035$.

6.2.1. Surface pressure distributions

The distribution of the mean pressure and the pressure fluctuations is depicted in Fig. 6.6 for the baseline and the actuated case ($f_{flap} = 38\ Hz$, $F^+ = 3.1$). Figs. 6.7 and 6.8 show the spectral analysis at the positions of the unsteady pressure transducers.

Similarly to the example shown for active pulsed blowing in the post-stall regime in Fig. 5.25 of the last Chapter, the suction pressure is increased by the flap oscillation at all three chord-wise measurement sections, albeit the observed effect is lower than for active pulsed blowing. In the first measurement plane at $X = 0.4$, the mean suction pressure level is increased from $-C_p = 0.6$ to $-C_p = 1.0$. The enhancement is lower at $X = 0.6$ and $X = 0.8$. Simultaneously, the pressure fluctuations are increased from $C_{p,rms} \approx 0.025$ in the baseline case to $C_{p,rms}$ values between 0.06 and 0.1 in the actuated case with flap oscillation. On average, the pressure fluctuations are highest at the front measurement plane $X = 0.4$.

Compared to the baseline case, the spectral analysis of the pressure coefficient signals reveals distinctive peaks at the flap oscillation frequency $f_{flap} = 38\ Hz$ ($F^+ = 3.1$) at $X = 0.4$, see Fig. 6.7b. They are most obvious for the span-wise positions at $Y \geq 0.75$ and the amplitudes are highest close to the leading edge. Nevertheless, the amplitudes of the fluctuations evoked by the flap oscillation are much lower than those observed with pulsed blowing. The same holds for the rear measurement plane at $X = 0.8$. At $X = 0.6$, the amplitude at the flap oscillation frequency is very low, which is due to the fact that no flaps are installed at the location between $X = 0.4$ and $X = 0.6$.

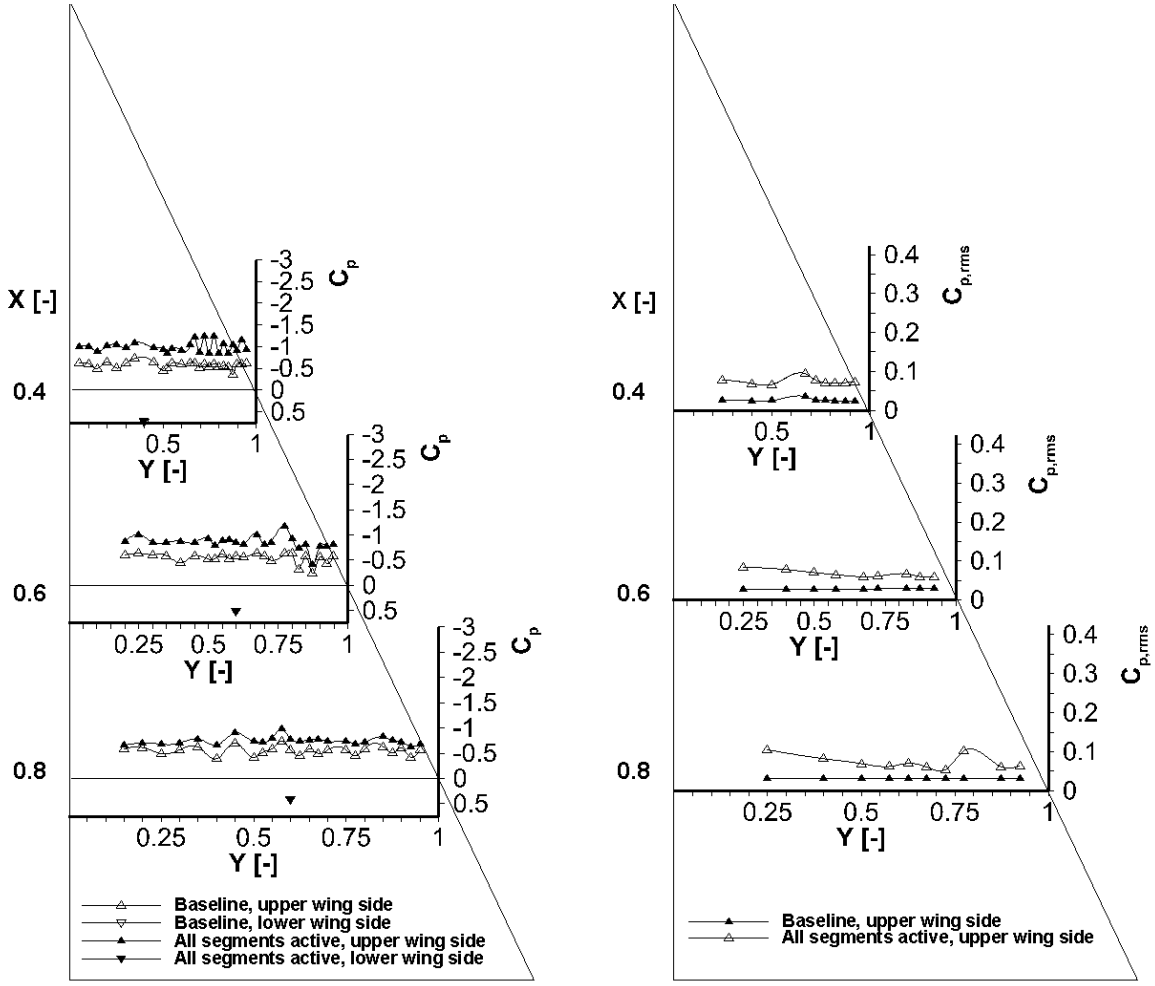

(a) Mean pressure

(b) Pressure fluctuations

Figure 6.6.: Mean pressure and pressure fluctuation distribution for the non-actuated and actuated cases at $\alpha = 45°$ for $Re_{mac} \approx 0.5 \times 10^6$, and $M = 0.035$; flaps oscillating at $f_{flap} = 38\ Hz$ ($F^+ = 3.1$) and $\hat{\delta} = 18°$

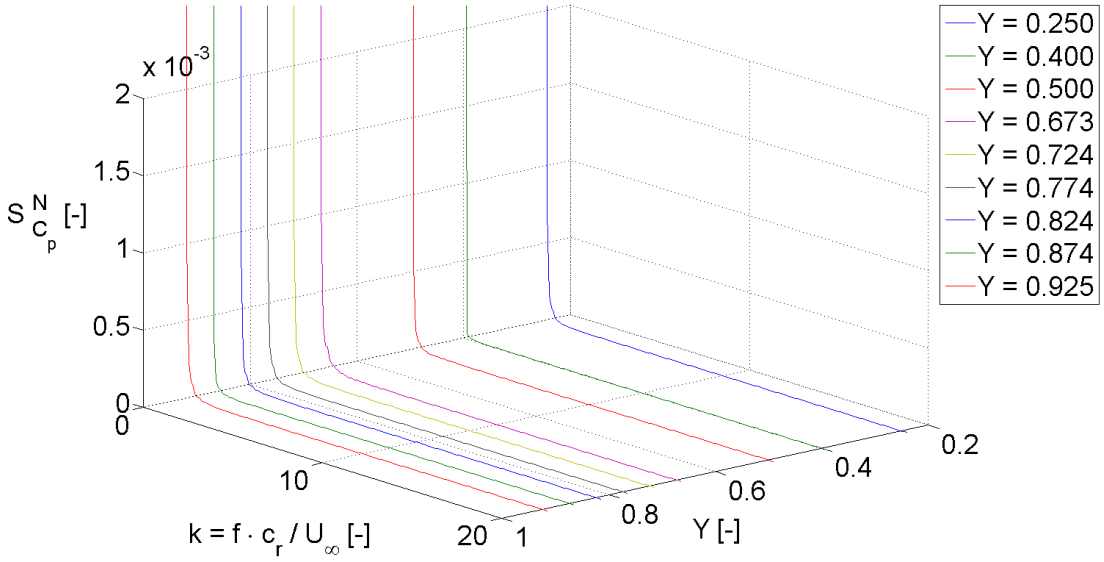

(a) Power spectral density for $X = 0.4$, baseline

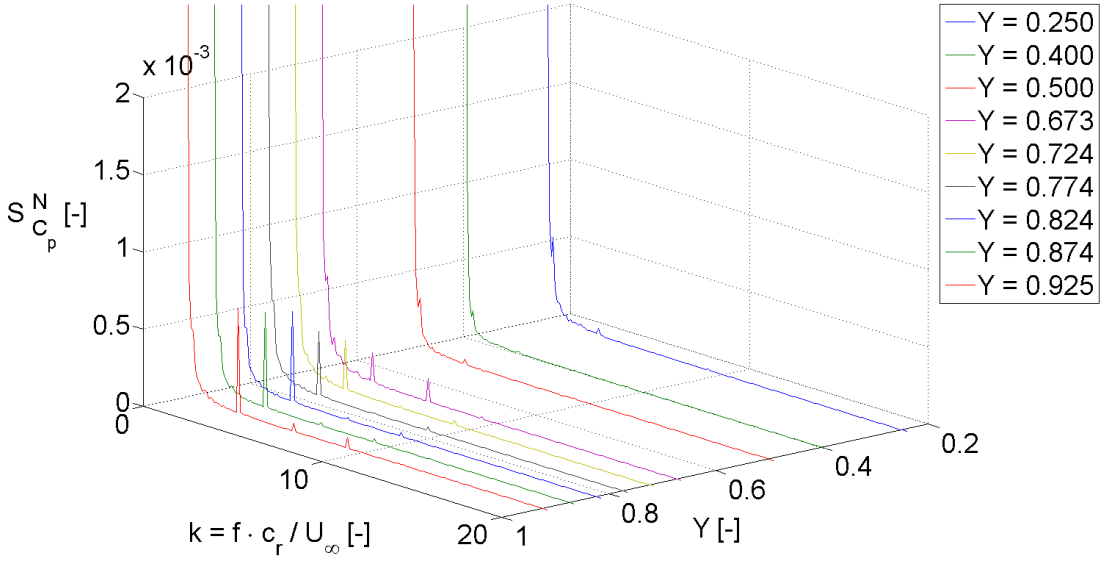

(b) Power spectral density for $X = 0.4$, all segments active

Figure 6.7.: Spectral analysis of the pressure coefficient for $\alpha = 45°$, $Re_{mac} \approx 0.5 \times 10^6$, and $M = 0.035$, oscillating flaps at $f_{pulse} = 38\ Hz$ ($F^+ = 3.1$) and $\hat{\delta} = 18°$, all flaps active

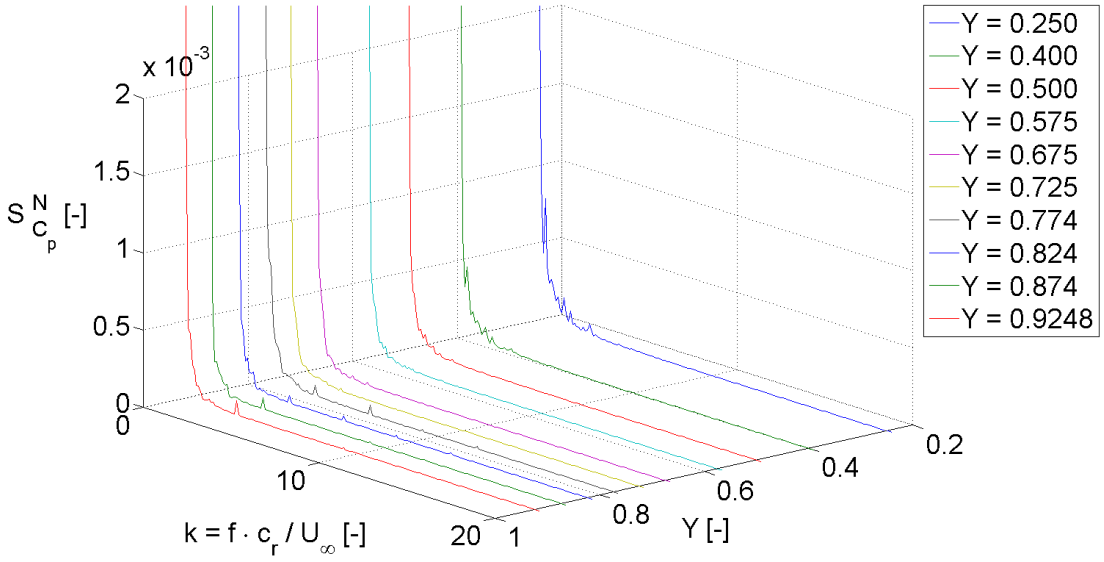

(a) Power spectral density for $X = 0.6$

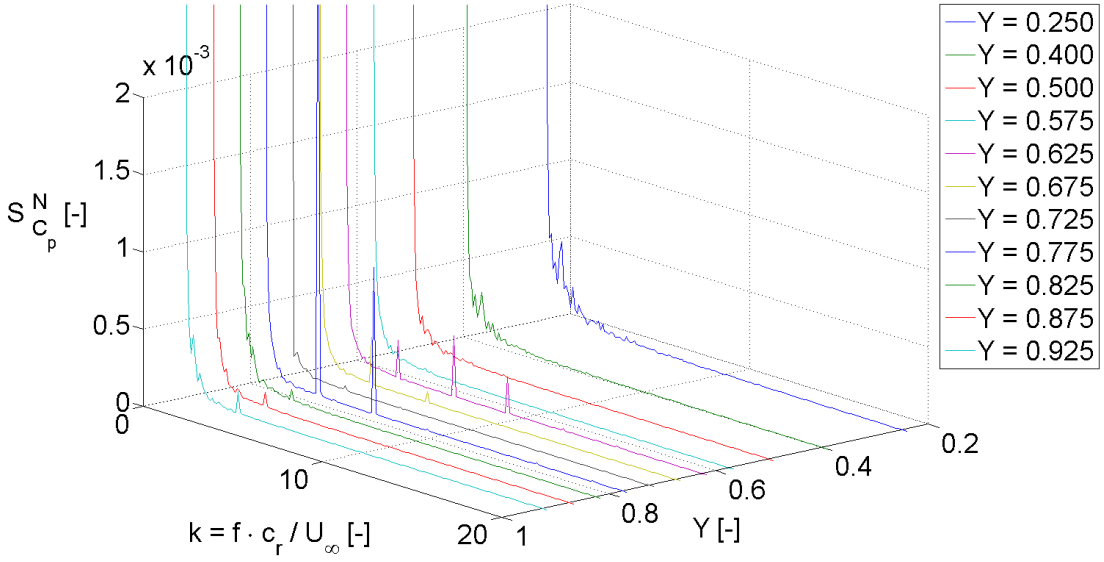

(b) Power spectral density for $X = 0.8$

Figure 6.8.: Spectral analysis of the pressure coefficient for $\alpha = 45°$, $Re_{mac} \approx 0.5 \times 10^6$, and $M = 0.035$, oscillating flaps at $f_{pulse} = 38\ Hz$ ($F^+ = 3.1$) and $\hat{\delta} = 18°$, all flaps active

6.2.2. Flowfield

Figs. 6.9 and 6.10 show the axial velocity and the turbulent kinetic energy for the test case at $\alpha = 42°$ and $Re_{mac} = 0.5 \cdot 10^6$, cf. [63], [40]. The flap actuation was carried out at $f_{flap} = 44\ Hz$ ($F^+ = 3.6$) and with the amplitude $\hat{\delta} = 18°$.

Baseline PIV results. The flow field for the baseline case at $\alpha = 42°$ is shown on the left of Figs. 6.9 and 6.10. The flow field strongly resembles the case at $\alpha = 45°$, which was shown in Figs. 5.29 and 5.30. A shear layer detaching at the leading edge is observed in all measurement planes. It does not roll up above the wing. The shear layer is bent further inboard for $\alpha = 42°$ in comparison to the higher angle of attack $\alpha = 45°$. The velocity distribution exhibits areas of negative axial velocities (backward flow) in the center of the measurement planes. The turbulent kinetic energy is increased above the wing, both in the region of the shear layer and further inboard.

Flap oscillation - PIV results. In the case with flap oscillation, the shear layer rolls up above the wing to form a burst vortex structure. This is clearly visible in the measurement planes behind the location of the first flap segment at $X = 0.4$ and $X = 0.6$. The primary vortex is located closer to the wing surface compared to the case with active pulsed blowing at $\alpha = 45°$. Furthermore, the vertical dimension of the vortex is a bit smaller for the case with flap oscillation and the vortex is less developed at $X = 0.2$ than with pulsed blowing at $\alpha = 45°$. In the inner part of the vortex structure, negative axial velocities up to $u/U_\infty = -0.55$ are measured. Positive axial velocities are observed close to the wing surface, below the primary vortex. The turbulent kinetic energy forms an annular structure in the actuated case and is clearly increased in comparison to the baseline case, especially at the measurement points, where the gradient of the axial velocity is relatively high. A local minimum of the turbulent kinetic energy is observed in the region of backward flow in the center of the vortex, where the velocity distribution is relatively homogenous.

Fig. 6.11 shows a three-dimensional plot of the axial velocity field and the stream traces formed by the cross flow velocities in the measurement planes $X = 0.2$ to $X = 0.8$. The presence of the vortex is also observed in the rear measurement plane $X = 0.8$.

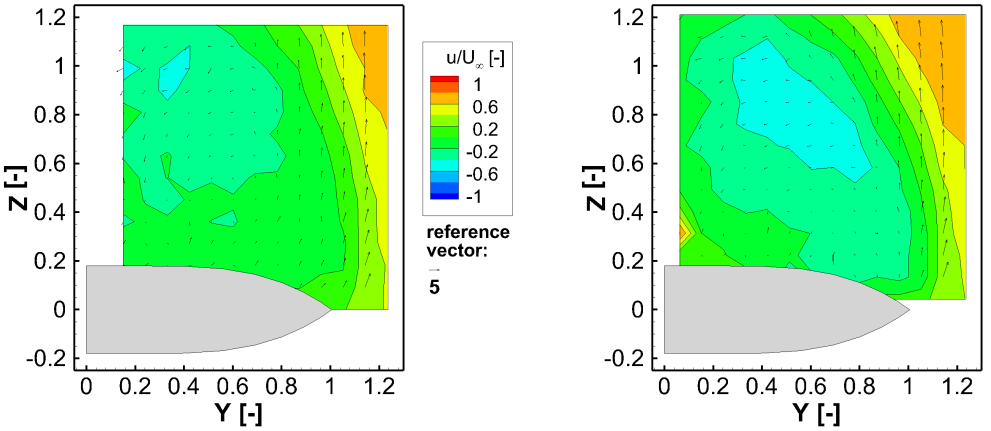

(a) $X = 0.2$

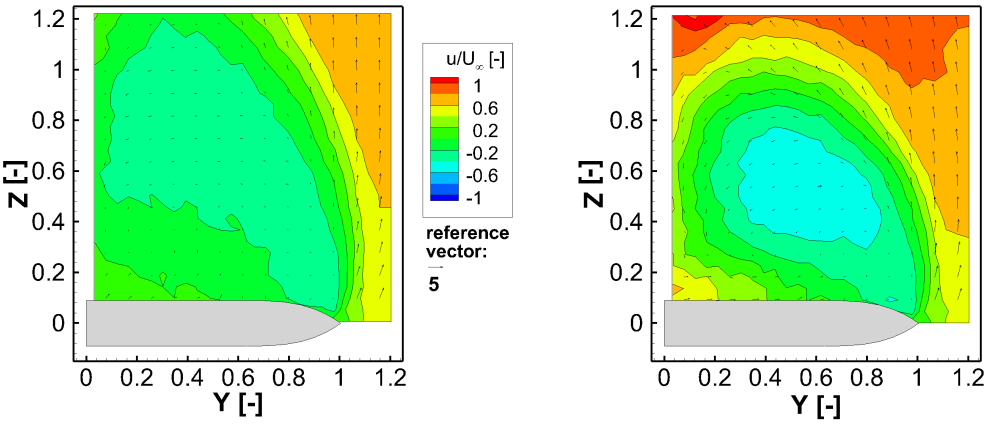

(b) $X = 0.4$

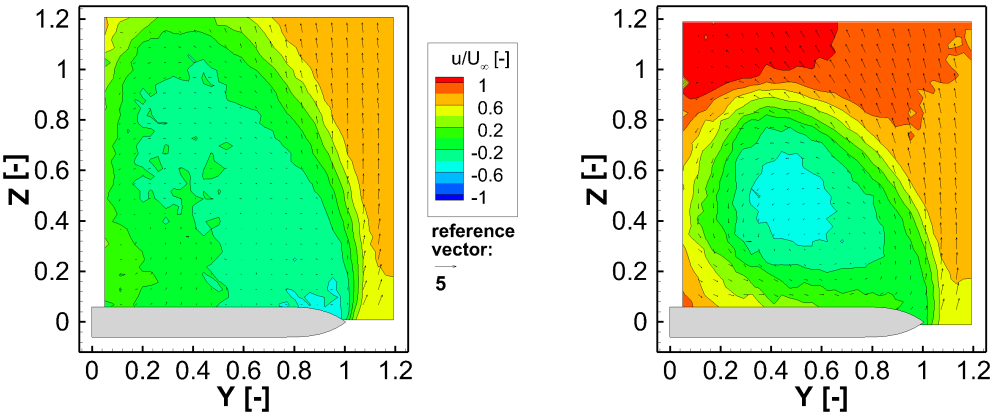

(c) $X = 0.6$

Figure 6.9.: Distribution of the axial velocity for the non-actuated (left) and actuated cases (right) at $\alpha = 42°$ for $Re_{mac} = 0.5 \cdot 10^6$, and $M = 0.035$; flaps oscillating at $f_{flap} = 44\ Hz$ ($F^+ = 3.6$) and $\hat{\delta} \approx 18°$; PIV measurement result

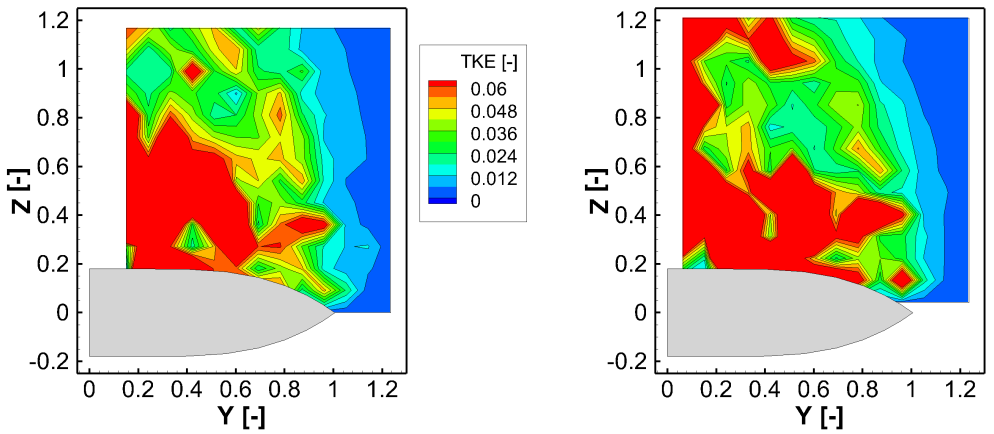

(a) $X = 0.2$

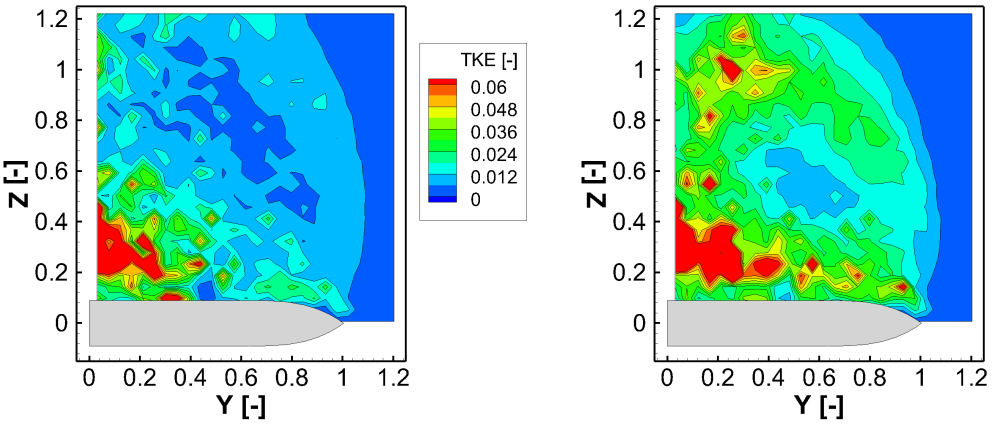

(b) $X = 0.4$

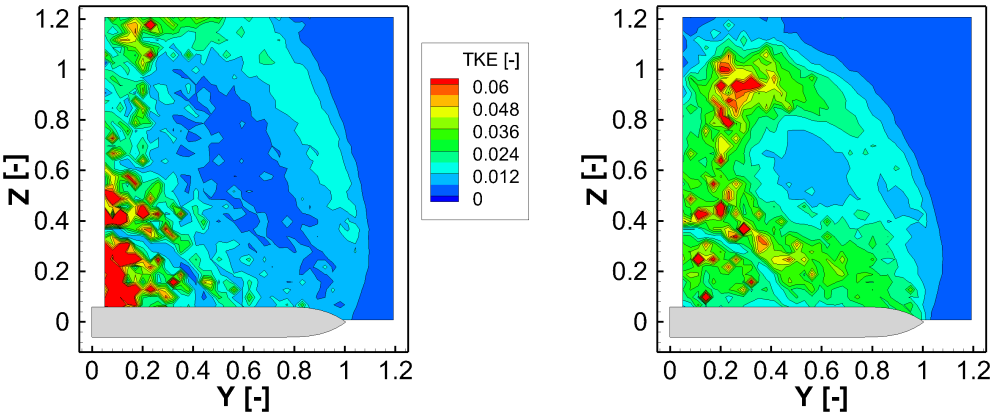

(c) $X = 0.6$

Figure 6.10.: Distribution of the turbulent kinetic energy for the non-actuated (left) and actuated cases (right) at $\alpha = 42°$ for $Re_{mac} = 0.5 \cdot 10^6$, and $M = 0.035$; flaps oscillating at $f_{flap} = 44\ Hz$ ($F^+ = 3.6$) and $\hat{\delta} \approx 18°$; PIV measurement result

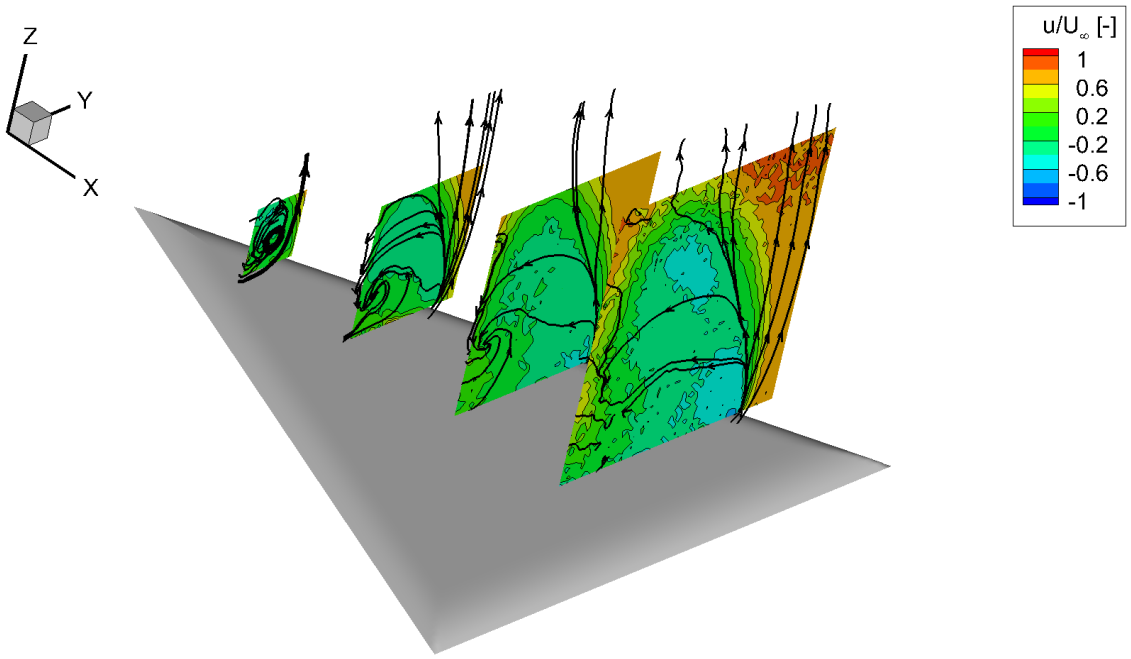

(a) Baseline case

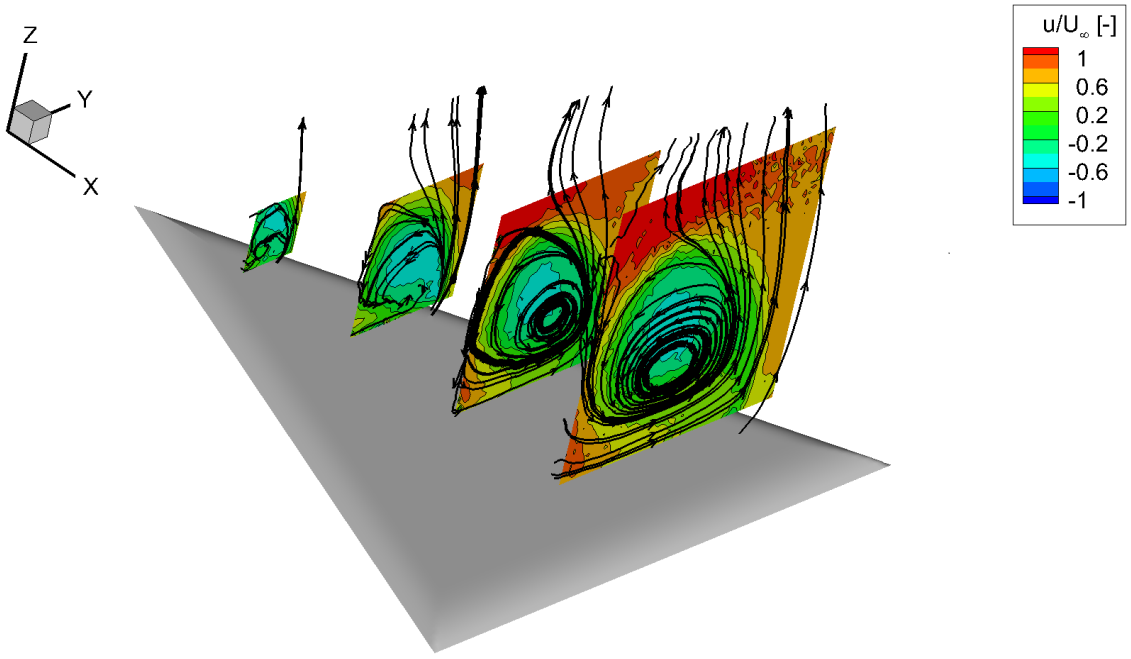

(b) Actuated case

Figure 6.11.: Distribution of the axial velocity and streamtraces at $\alpha = 42°$ for $Re_{mac} = 0.5 \cdot 10^6$, and $M = 0.035$; flaps oscillating at $f_{flap} = 44\ Hz$ ($F^+ = 3.6$) and $\hat{\delta} = 18°$; PIV measurement result

6.3. Summary

In this chapter, the effect of oscillating leading-edge flaps has been studied on the VFE-2 delta wing configuration. A parameter study was conducted by means of force measurements, in which mainly the flap frequency and the active segments during the flap oscillations were investigated. On this basis, the effects caused by the flap oscillation were studied in more detail for one test case in the post-stall regime.

The general effect of the oscillating miniature flaps is as follows:

- When the flaps are oscillating, the normal angle of attack α_N is changed locally and periodically along the leading edge. It is reduced for negative flap deflection angles and increased for positive ones.
- Moreover, the flap motion causes a motion-induced normal velocity, which depends on the amplitude as well as the frequency of the flap oscillation and is superimposed on the normal velocity component of the free stream.
- Moreover, the flap oscillation has a spectral impact on the flow field and minivortices detach from the miniature flaps to merge into the shear layer originating from the leading edge.

In the pre-stall and stall regime, only marginal effects are observed in the force measurements when the flap oscillation is active. For the post-stall regime, the following conclusions can be drawn:

- The flap oscillation at reduced frequencies in the regime from $F^+ \approx 2.7$ to 3.6 leads to a significant increase of the suction pressure on the upper wing surface and therefore, an increase in lift of up to $\Delta C_L = +40\%$. The shear layer rolls up above the wing to form a burst vortex structure and the axial and circumferential velocities increase close to the wing surface.
- The drag coefficient is increased by $\Delta C_D \approx +35\%$. Additionally, an increase of the pitching moment and a reduction of the rolling moment is observed.
- The flap oscillation frequency is detectable in the surface pressure signal recorded in the measurement planes behind the first flap segment. The amplitude of the power spectral density is significantly lower compared to the values observed with pulsed blowing.
- In contrast to pulsed blowing, the front flap segment plays an important role in the actuation. If this segment is not active, almost no effect on the lift coefficient can be achieved. This is reasonable, as the effective angle of attack, which is locally changed by the miniature flaps, is of major importance close to the apex of a delta wing than in the rear wing section.

6.4. Comparison of the two flow control methods

Finally, the two applied flow control methods, pulsed leading edge blowing and oscillating miniature leading edge flaps, are compared in this subsection. Several commonalities can be pointed out between the two studied flow control methods:

- Both methods are more effective, if they are applied for an unsteady excitation of the flow. This was clearly observed in the force measurement results of the parameter studies, where steady and frequency-based forcing were compared.
- Both methods induce additional velocities in the flow in the unsteady operation mode. In the case of pulsed blowing, the additional velocity corresponds to the velocity of the jet, that enters the flow on the wing's upper side at the location of the slots. For the investigated post-stall test case with $f_{pulse} = 12\ Hz$, it was relatively high ($U_{jet} \approx 60\ m/s$, $U_{jet}/U_\infty \approx 5$). The additional velocity induced by the oscillating flaps approximately corresponds to the velocity of the flap tip and is much lower at the same frequeny ($\hat{V}_\theta \approx 0.355\ m/s$ for $f_{flap} = 12\ Hz$).
- Active pulsed blowing has more impact on the flow than the oscillating leading-edge flaps, especially in the pre-stall and stall regime. This result is comprehensible, as an additional momentum is brought into the flow by the blowing, which is not the case in the second flow control method. Therefore, the energy expenditure by pulsed blowing is higher than in the case of the flap oscillation.

Two significant differences are observed in the post-stall regime:

- First, the optimal actuation frequency of pulsed blowing is much lower than the preferable frequency of the flap oscillation ($F^+_{pulse,opt} \approx 1$ to 2 versus $F^+_{flap,opt} \approx 3.2 - 3.6$).
- Second, the rear segment makes the most important contribution to the lift enhancement by pulsed blowing, while the front segment is essential in the case of the flap oscillation. Additionally, the upstream effect of the flap oscillation is less intense than with pulsed blowing. This is an indication, that different mechanisms could be addressed in the flow by pulsed blowing and the flap oscillation in the presented post-stall test cases.

7. Summary and conclusion

In this thesis, frequency-dependent forcing is experimentally investigated on a generic delta wing configuration at low Mach numbers. Therefore, two active flow control methods are applied, namely pulsed blowing from slots positioned along the leading edge on the upper wing side and oscillating miniature leading edge flaps. The study covers flow field experiments for the three different flow regimes pre-stall, stall and post-stall, for which the effect of the frequency-dependent forcing is investigated in detail and for different actuation parameters. The results offer a set of actuation parameters that lead to an improvement of the aerodynamic characteristics. Moreover, the understanding of the underlying physical processes can be improved.

The delta wing flow at low Mach numbers is characterized by a shear layer, that detaches at the leading edge. The shear layer is then rolling up to form a vortex system at moderate and high angles of attack of the pre-stall and stall regime. At high angles of attack, the primary vortex attains a critical stage called vortex bursting that causes strong flow fluctuations and can lead to severe damage of the aircraft. If the angle of attack is further increased to the post-stall regime, the vortex system starts collapsing, as the shear layer does not achieve to roll up in the presence of the strongly increased adverse pressure gradient. In order to address all three angle-of-attack regimes from pre-stall to post-stall, it is thus reasonable to execute flow actuation at the leading edge of the wing, where the shear layer emanates. Furthermore, the conclusions from former research studies on delta wing configurations recommend an unsteady actuation, as it is noticeably more efficient than steady actuation. This is comprehensible given the fact that the delta wing flow field is characterized by various instabilities at different time scales. For this reason, two unsteady flow control devices were developed, which permit a frequency-based intervention close to the leading edge.

In order to investigate the unsteady flow control methods in wind tunnel experiments, two half delta wing models were built, one for each flow control method. The models' geometry corresponds to one that was used in the Vortex Flow Experiment 2 (VFE-2).
The model with the pulsed blowing system has twelve slot pairs integrated along the leading edge, where pulsed jets are ejected on the upper wing side. The jet pairs form small vortical structures, that merge into the shear layer emanating from the sharp leading edge. The pulse frequency, duty cycle and jet velocity can be controlled for the pulsed jets. Additionally, a variation of the active segments which are located at the front, the middle and the rear part of the leading edge, is possible.
The second half model is equipped with two segments of three miniature leading-edge

flaps each. One segment is located at the front of the leading edge and the other at the rear. The flaps are actuated by linear motors and perform oscillatory movements around the mid-plane of the wing. At positive angles of attack, the free-stream flow arriving from the lower side of the wing detaches at the edges of the miniature flaps and likewise forms small vortical structures, that are generated by the motion of the oscillating flap. The flap-induced vortices are transported to the upper wing side. The frequency and the amplitude of the flap oscillation can be controlled.

In the first step of the experiments, the flow field of the basic configuration was analyzed considering wool tuft flow visualization, force and pressure measurements as well as velocity measurements by hot-wire anemometry (HWA) and Stereo Particle Image Velocimetry (Stereo PIV).
In the first step of the experiments, the flow field of the basic configuration was analyzed considering force, pressure and velocity measurements as well as wool tuft flow visualization. Special attention was paid to the fluctuation quantities and the spectral analysis of the surface pressure and velocity field to get access to the flow-inherent instabilities, such as the helical mode instability and the Kelvin-Helmholtz instability. Thereby, three representative low-speed flow cases were in focus:

- The first test case is assigned to the pre-stall regime at an angle of attack $\alpha = 23°$. It is characterized by a leading-edge vortex that is burst at the rear part over the wing.

- The second test case refers to the stall regime at $\alpha = 35°$. Here, the burst location has reached the apex and the helical mode instability can be detected at all chordwise planes above the wing.

- The third and last test case represents the flow field in the post-stall regime at angles of attack $\alpha = 45°$ for pulsed blowing and $\alpha = 42°$ for the oscillating flaps, respectively. They are characterized by a detached shear layer originating at the sharp leading edge and a "dead-water type" flow above the wing.

In the next step, a parameter analysis for the two flow control methods was carried out on the basis of the results from the spectral analysis and from findings in the literature. More elaborate measurements were then carried out for the test cases with the most promising parameter sets. The experiments were conducted repeatedly to ensure reproducibility of the results. The main results with pulsed blowing are:

- For the pre-stall test case at $\alpha = 23°$, active pulsed blowing leads to a downstream-shift of the burst location of $\Delta x_{bd} \approx 0.2$, if the actuation is carried out at reduced frequencies $F^+ \approx 2.6$. This optimal pulse frequency could be linked with the frequency of the helical mode instability of vortex bursting, which is in the same order of magnitude. Nevertheless, this cannot be proven definitely, because another instability, namely the shear layer instability, lies in the same frequency range.

- In the stall regime, similar observations are made: pulsed blowing at $F^+ \approx 2.6$ causes a stabilization of the primary vortex and vortex breakdown is attenuated. Furthermore, a small increase in lift is observed.

- The most significant transformation is observed in the post-stall test case, where pulse frequencies at the order of unity lead to a remarkable lift increase of up to 60%. Here, the pulsed momentum excites the shear layer to roll up over the delta wing and to form a large-scale burst vortex structure. Although this effect is highly desirable, it has to be considered that the additional lift induces an additional drag component and the flow transformation also effectuates a significant positive pitching moment and a negative rolling moment. Moreover, a substantial energy expenditure is necessary to reach the reformation of the leading-edge vortex.

Concerning the oscillating miniature flaps, the following observations are made:

- In the pre-stall and stall regime, no significant effects on the force and moment coefficients are observed in the parameter study for the flap oscillation.

- In the post-stall regime, a similar transformation of the detached shear layer to a burst vortex is caused by a flap oscillation at $F^+ \approx 2.7$ to 3.6, as it was observed with active pulsed blowing. The possible increase in the lift mounts up to 40%. Nevertheless, an increase in the drag and moment coefficients is also observed in this case. Moreover, the angle-of-attack regime, where the flap oscillation is effective, is remarkably smaller compared to pulsed blowing.

Several commonalities and differences can be pointed out between the two studied flow control methods:

- Both methods are more effective, if they are applied for an unsteady excitation of the flow.

- Nevertheless, active pulsed blowing has more impact on the flow than the oscillating leading-edge flaps, especially in the pre-stall and stall regime. This result is comprehensible, as an additional momentum is brought into the flow by the blowing, which is not the case in the second flow control method. Therefore, the energy expenditure by pulsed blowing is higher than in the case of the flap oscillation.

- Two significant differences are observed in the post-stall regime: first, the optimal actuation frequency of pulsed blowing is much lower than the preferable frequency of the flap oscillation. Second, the rear segment makes the most important contribution to the lift enhancement by pulsed blowing, while the front segment is essential in the case of the flap oscillation. Additionally, the upstream effect of the flap oscillation is less intense than with pulsed blowing. This is an indication, that different mechanisms could be addressed in the flow by pulsed blowing and the flap oscillation in the presented post-stall test cases.

Summarizing, a comprehensive study of the two flow control methods was carried out, which offers a detailed data base of the effects induced by pulsed blowing and flap oscillation on a generic delta wing configuration for different actuation parameters. Moreover, it can serve as a high-fidelity experimental data base for the development and improvement of advanced numerical methods.

The attained results suggest several starting points for supplementary experimental investigations:

- Firstly, continuing measurements would be valuable to improve the understanding of the observed mechanisms called forth by the active flow control methods. One important aspect would be the recording and analysis of the vortical structures, that are induced by the pulsed jets and the oscillating flaps, respectively. It is suggested to conduct PIV measurements with a new alignment of the measurement planes, in which additional flow field information is gathered in vertically staggered planes aligned parallel - instead of orthogonal - to the wing's horizontal mid-plane. This configuration would allow for a detection of the mini-vortices generated at the blowing slots and the oscillating flaps, that are then swept away in the shear layer in vertical direction. Furthermore, the interaction between these generated mini-vortices with the shear layer and the primary vortex system could be studied in more detail. In addition, a measurement plane aligned along the vortex core would give interesting insight in the flow properties in front and behind the vortex breakdown location. Moreover, the location of vortex breakdown could be determined with higher precision and certainty in the baseline and actuated flow cases.

- Secondly, it would be helpful to trigger the recording of the PIV frames of the actuated flow field with the flow control devices (the pulsed blowing signal and the flap deflection signal, respectively). Applied to the pre-stall and stall cases, this measurement set-up will improve the understanding of the interaction of the generated mini-vortices and the primary vortex structure. In the post-stall cases, the roll-up process during the reformation of the large vortex structure could be further investigated by this set-up.

- Furthermore, HWA measurements with at least two HWA probes at different flow field positions and a simultaneous signal recording would give valuable information about the influence, propagation and development of the motion-induced additional velocities. One probe could for example be positioned in the vicinity of the actuation device, where the additional velocity is generated. The other probe could be positioned at a certain point of interest. If the two probe signals are compared and correlated, conclusions on the frequency and the amplitude development as well as the run-time of the actuation signal to the point of the probe location can be drawn.

Bibliography

[1] Eurofighter Jagdflugzeug GmbH, Multimedia, URL: https://www.eurofighter.com/multimedia/details/italian-eurofighter-typhoon-at-the-royal-international-air-tattoo-2014-1649 [cited: 21st March 2016, 16:35].

[2] From Wikimedia Commons, the free media repository, photographer: Arpingstone, URL: https://de.wikipedia.org/wiki/Concorde#/media/File:Concorde_on_Bristol.jpg [cited: 21st March 2016, 16:40].

[3] Technische Universität München, Lehrstuhl für Aerodynamik und Strömungsmechanik, Wind tunnels, URL: http://www.aer.mw.tum.de/en/wind-tunnels/ [cited: 5th March 2016, 12:47].

[4] T. B. Benjamin. Theory of the vortex breakdown phenomenon. *Journal of Fluid Mechanics*, 14(4): pp. 593–629., 1962.

[5] S. Blanchard. Analysis of the pressure distribution on a delta wing at high angles of attack for pulsed leading-edge blowing. Master's thesis, Technische Universität München, Lehrstuhl für Aerodynamik und Strömungsmechanik, 2014.

[6] C. Breitsamter. *Turbulente Strömungsstrukturen an Flugzeugkonfigurationen mit Vorderkantenwirbeln*. PhD thesis, Technische Universität München, Herbert Utz Verlag Wissenschaft (ISBN 3-89675-201-4), 1997.

[7] C. Breitsamter. Unsteady flow phenomena associated with leading-edge vortices. *Progress in Aerospace Science*, 44: pp. 48–65, 2008.

[8] Z. Celik and L. Roberts. Vortical flow control on a delta wing by lateral blowing. In *AIAA-94-0509, 32nd Aerospace Sciences Meeting and Exhibit, Aerospace Sciences Meetings,*, Reno, NV, U.S.A., 1994.

[9] J. Chu and J. M. Luckring. Experimental surface pressure data obtained on 65° delta wing across reynolds number and mach number ranges. *NASA TM 4645*, 1996.

[10] Q. Deng and I. Gursul. Effect of leading-edge flaps on vortices and vortex breakdown. *Journal of Aircraft*, 33(6): pp. 1079–1086, 1996.

[11] Q. Deng and I. Gursul. Effect of oscillating leading-egde flaps on vortices over a delta wing. *AIAA Paper 1997-1972*, 1997.

[12] Q. Deng and I. Gursul. Vortex breakdown over a delta wing with oscillating leading edge flaps. *Experiments in Fluids*, 23: pp. 347–352, 1997.

[13] J. M. Délery. Aspects of vortex breakdown. *Progress in Aerospace Sciences*, 30(1): pp. 1–59, 1994.

[14] M. Escudier. Vortex breakdown: observations and explanations. *Progress in Aerospace Science*, 25: pp. 189–229, 1988.

[15] J. Fellerhoff. Entwicklung eines aktiven Ausblassystems zur Strömungsbeeinflussung an einer Deltaflügelkonfiguration, Diploma thesis, Technische Universität München, Lehrstuhl für Aerodynamik und Strömungsmechanik, 2011.

[16] A. Furman and C. Breitsamter. Turbulent and unsteady flow characteristics of delta wing vortex systems. In *46th AIAA Aerospace Sciences Meeting and Exhibit, Reno, Nevada*, 2008.

[17] A. Furman and C. Breitsamter. *Summary report of Task Group RTO-TR-AVT-11: Understanding and Modeling Vortical Flows to Improve the Technology Readiness Level for Military Aircraft*, chapter Experimental investigations on the VFE-2 configuration at TU Munich, Germany. ISBN 978-92-837-0073-9, 2009.

[18] M. Gad-el Hak. *Flow Control - Passive, Active, and Reactive Flow Management*. Cambridge University Press, 2008.

[19] M. Gad-el Hak and R.F. Blackwelder. The discrete vortices from a delta wing. *AIAA Journal*, 23(6): pp. 961–962, 1985.

[20] M. Gad-el Hak and R.F. Blackwelder. Control of the discrete vortices from a delta wing. *AIAA Journal*, 25(8): pp. 1042–1049, 1987.

[21] D. Greenblatt, Y. Kastantin, C. N. Nayeri, and C. O. Paschereit. Delta-wing flow control using dielectric barrier discharge actuators. *AIAA Journal*, 46(6): pp. 1554–1560, 2008.

[22] D. Greenblatt and I. J. Wygnanski. The control of flow separation by periodic excitation. *Progress in Aerospace Science*, 36: pp. 487–545, 2000.

[23] D. I. Greenwell and N. J. Wood. Roll moment characteristics of asymmetric tangential leading-edge blowing on a delta wing. *Journal of Aircraft*, 31(1):pp. 161–169, 1994.

[24] F. Greif. Experimentelle Untersuchung der Deltaflügelumströmung bei Beeinflussung mit aktivem Ausblassystem im Stall-Bereich, Term paper, Technische Universität München, Lehrstuhl für Aerodynamik und Strömungsmechanik, 2013, 2013.

[25] S. Guillot, E. J. Gutmark, and T. J. Garrison. Delay of vortex breakdown over a delta wing via near core blowing. *AIAA Paper 1998 - 0315*, 1998.

[26] I. Gursul. Unsteady aspects of leading-edge vortices. *RTO Rep-084 Chapter 10*, 2004.

[27] I. Gursul, S. Srinivas, and G. Batta. Active control of vortex breakdown over a delta wing. *AIAA Journal*, 33(9): pp. 1743–1745, 1995.

[28] I. Gursul, Z. Wang, and E. Vardaki. Review of flow control mechanisms of leading-edge vortices. *Progress in Aerospace Sciences*, 43: pp. 246 – 270, 2007.

[29] I. Gursul and W. Xie. Origin of vortex wandering over delta wings. *Journal of Aircraft*, 37(2): pp. 348–350, 2000.

[30] H. E. Helin and C. W. Watry. Effects of trailing-edge jet entrainment on delta wing vortices. *AIAA Journal*, 32(4):pp. 802–804, 1994.

[31] J. S. Hong, Z. Z. Celik, and L. Roberts. Effects of leading-edge lateral blowing on delta wing aerodynamics. *AIAA Journal*, 34:pp. 2471–2478, 1996.

[32] D. Hummel. Review of the second international vortex flow experiment (vfe-2). *AIAA Paper 2008-377*, 2008.

[33] D. Hummel and H. C. Oelker. Vortex interference effects on close-coupled canard configuration at low speed. *Aerodynamics of Combat Aircraft Controls and Ground Effects*, CP-465, AGARD: pp. 7–1 – 7–18, 1989.

[34] P. Jiang, Z. Wang, and I. Gursul. Effects of unsteady trailing-edge blowing on delta wing aerodynamics. *Journal of Aircraft*, 47(2): pp. 591–602, 2010.

[35] C. Kauer. Entwicklung eines aktiven Klappensystems zur Strömungsbeeinflussung an einer Deltakonfiguration, Diploma thesis, Technische Universität München, Lehrstuhl für Aerodynamik und Strömungsmechanik, 2011.

[36] S. M. Klute, O. K. Rediniotis, and D. P. Telionis. Flow control over a maneuvering delta wing at high angle of attack. *AIAA Journal*, 34(4): pp. 662–668, 1996.

[37] A. Kölzsch, S. Blanchard, and C. Breitsamter. *New Results in Numerical and Experimental Fluid Mechanics X*, chapter Dynamic Actuation for Delta Wing Post Stall Flow Control. Notes on Numerical Fluid Mechanics and Multidisciplinary Design. Springer Verlag, 2015.

[38] A. Kölzsch and C. Breitsamter. Vortex flow manipulation on a generic delta wing configuration. In *28th International Congress of the Aeronautical Sciences, Brisbane*, 2012.

[39] A. Kölzsch and C. Breitsamter. Vortex flow manipulation by pulsed leading-edge blowing. In *Specialists' Meeting on Innovative Control Effectors for Military Vehicles, STO-MP-AVT-215-P-16*, Stockholm, Sweden, 2013.

[40] A. Kölzsch and C. Breitsamter. Delta wing flow control for the stall and post-stall regime. In *Deutscher Luft- und Raumfahrtkongress, Augsburg*, 2014.

[41] A. Kölzsch and C. Breitsamter. Vortex-flow manipulation on a generic delta wing configuration. *Journal of Aircraft*, 51(5): pp. 1380–1390, 2014.

[42] M. E. Kügler. Windkanaluntersuchung eines aktiven Ausblassystems an einer Deltaflügelkonfiguration bei aufgeplatzten Vorderkantenwirbeln, Bachelor's thesis, Technische Universität München, Lehrstuhl für Aerodynamik und Strömungsmechanik, 2012.

[43] S. Kurun. *Summary report of Task Group RTO-TR-AVT-11: Understanding and Modeling Vortical Flows to Improve the Technology Readiness Level for Military Aircraft*, chapter Experimental investigations on the VFE-2 configuration at TUBITAK-SAGE, Turkey. ISBN 978-92-837-0073-9, 2009.

[44] J.E. Lamar and J.F. Campbell. Vortex flaps – advanced control devices for supercruise fighters. *Aerospace America*, pages pp. 95–99, 1984.

[45] N. C. Lambourne and D. W. Bryer. The bursting of leading-edge vortices–some observations and discussion of the phenomenon. *Aeronautical Research Council Reports and Memoranda*, (3282), 1961.

[46] M. Lee and C.-M. Ho. *Lecture Notes in Engineering - Frontiers in Experimental Fluid Mechanics*, chapter Vortex Dynamics of Delta Wings, pages 365 – 427. Springer Verlag, 1989.

[47] S. Leibovich. Vortex stability and breakdown: survey and extension. *AIAA Journal*, 22(9): pp. 1192–1206, 1983.

[48] M. V. Lowson. Visualization measurements of vortex flows. *Journal of Aircraft*, 28(5): pp. 320–327, 1991.

[49] J. M. Luckring. Reynolds number and lealeading-edge bluntness effects on a 65° delta wing. In *40th AIAA Aerospace Sciences Meeting & Exhibit, Reno, Nevada*, 2002.

[50] J. M. Luckring. *Summary report of Task Group RTO-TR-AVT-11: Understanding and Modeling Vortical Flows to Improve the Technology Readiness Level for Military Aircraft*, chapter Initial experiments and analysis of blunt-edge vortex flows. ISBN 978-92-837-0073-9, 2009.

[51] J. M. Luckring and D. Hummel. What was learned from the vfe-2 experiments? *AIAA Paper 2008-383*, 2008.

[52] R. Lynn and I. Gursul. Vortex dynamics on a generic ucav configuration. In *AIAA-2006-0061, 44th Aerospace Sciences Meeting and Exhibit*, Reno, NV, January 9–12 2006.

[53] G. Mack. Windkanaluntersuchung eines aktiven Ausblassystems an einer Deltaflügelkonfiguration im Pre- und Poststallbereich, Term paper, Technische Universität München, Lehrstuhl für Aerodynamik und Strömungsmechanik, 2013, 2013.

[54] J. F. Marchman. Effect of heating on leading edge vortices in subsonic flow. *Journal of Aircraft*, 12(2): pp. 121–123, 1975.

[55] S. Margalit, D. Greenblatt, A. Seifert, and I. Wygnanski. Delta wing stall and roll control using segmented piezoelectric fluidic actuators. *Journal of Aircraft*, 42(3): pp. 698–709, 2005.

[56] S. McCormick and I. Gursul. Effect of shear layer control on leading edge vortices. *Journal of Aircraft*, 33(6):pp. 1087–93, 1996.

[57] M. Menke, H. Yang, and I. Gursul. Experiments on the unsteady nature of vortex breakdown over delta wings. *Experiments in Fluids*, 27: pp. 262–272, 1999.

[58] D. S. Miller and R. M. Wood. An investigation of wing leading-edge vortices at supersonic speeds. *Proceedings of the AIAA Applied Aerodynamics Conference, Danvers, Massachusetts*, 1983.

[59] A. M. Mitchell and J. Delery. Research into vortex breakdown control. *Progress in Aerospace Sciences*, 37: pp. 385–418, 2001.

[60] A. M. Mitchell, P. Molton, D. Barberis, and J. Delery. Control of leading-edge vortex breakdown by trailing edge injection. In *Fluid Dynamics and Co-located Conferences*. American Institute of Aeronautics and Astronautics, June 1999.

[61] R. Y. Myose, S. Hayashibara, P. C. Yeong, and L. S. Miller. Effects of canards on delta wing vortex breakdown during dynamic pitching. *Journal of Aircraft*, 34(2): pp. 168–173, 1997.

[62] R.C. Nelson and A. Pelletier. The unsteady aerodynamics of slender wings and aircraft undergoing large amplitude maneuvers. *Progress in Aerospace Science*, 39: pp. 185–248, 2003.

[63] J. O. Olthoff. Integration eines Klappenaktuierungssystems an einer Deltaflügelkonfiguration und Windkanaluntersuchung zur aktiven Strömungsbeeinflussung, Diploma thesis, Technische Universität München, Lehrstuhl für Aerodynamik und Strömungsmechanik, 2014.

[64] F.M. Payne. *The structure of leading edge vortex flows including vortex breakdown*. PhD thesis, University of Notre Dame, 1987.

[65] S. Phillips, C. Lambert, and I. Gursul. Effect of a trailing-edge jet on fin buffeting. *Journal of Aircraft*, 40(3): pp. 590–599, 2003.

[66] M. Raffel, C.E. Willert, S. Wereley, and J. Kompenhans. *Particle Image Velocimetry - A Practical Guide*. 2007.

[67] O. K. Rediniotis, H. Stapountzis, and D. P. Telionis. Vortex shedding over delta wings. *AIAA Journal*, 28(5): pp. 944–946, 1990.

[68] O. K. Rediniotis, H. Stapountzis, and D. P. Telionis. Periodic vortex shedding over delta wings. *AIAA Journal*, 31(9): pp. 1555–1562, 1993.

[69] D. Rockwell, W. Gu, and O. Robinson. Control of vortices on a delta wing by leading-edge injection. *AIAA Journal*, 31(7): pp. 1177–1186, 1993.

[70] O. Rodriguez. *Summary report of Task Group RTO-TR-AVT-11: Understanding and Modeling Vortical Flows to Improve the Technology Readiness Level for Military Aircraft*, chapter Experimental investigations on the VFE-2 configuration at ONERA, France. ISBN 978-92-837-0073-9, 2009.

[71] H. Rotering. Strömungsbeeinflussung mittels Miniaturklappen an einer generischen Deltaflügelkonstruktion, Diploma thesis, Technische Universität München, Lehrstuhl für Aerodynamik und Strömungsmechanik, 2010.

[72] S. Selmeier. Windkanaluntersuchung eines aktiven Ausblassystems an einer Deltaflügelkonfiguration bei voll entwickeltem Vorderkantenwirbel, Bachelor's thesis, Technische Universität München, Lehrstuhl für Aerodynamik und Strömungsmechanik, 2012.

[73] S. G. Siegel, T. E. Mclaughlin, and J.A. Albertson. Partial leading edge forcing of a delta wing at high angles of attack. *AIAA Paper 2002-3268*, 2002.

[74] S. G. Siegel, T. E. McLaughlin, and J. A. Morrow. Piv measurements on a delta wing with periodic blowing and suction. *AIAA Paper 2001-2436*, 2001.

[75] A. Stanbrook and L.C. Squire. Possible types of flow at swept leading edge. *Aeronautical Quarterly*, XV: pp. 72–82, 1964.

[76] W. Staudacher. *Die Beeinflussung von Vorderkantenwirbelsystemen schlanker Tragflügel*. PhD thesis, Universität Stuttgart, 1992.

[77] G. Taylor, Z. Wang, E. Vardaki, and I. Gursul. Lift enhancement over flexible nonslender delta wings. *AIAA Journal*, 45(12): pp. 2979–2993, 2007.

[78] N. G Verhaagen, L. N. Jenkins, S. B. Kern, and A. E. Washburn. A study of the vortex flow over a 76/40-deg double-delta wing. In *AIAA 95-0650, 33rd Aerospace Sciences Meeting and Exhibit*, Reno, NV, January 9–12 1995.

[79] K. D. et al. Visser. Control of leading edge vortex breakdown by blowing. *AIAA Paper 1988-0504*, 1988.

[80] H. Werlé. Quelques resultats expérimentaux sur les ailes en flèche, aux faibles vitesses, obtenues en tunnel hydrodynamique. *La Recherche Aéronautique*, (41), 1954.

[81] N. M. Williams, Z. Wang, and I. Gursul. Active flow control on a nonslender delta wing. *Journal of Aircraft*, 45(6): pp. 2100–2110, 2008.

[82] M. Winter. Umsetzung eines aktiven Klappensystems zur Strömungsbeeinflussung an einer Deltaflügelkonfiguration, Term paper, Technische Universität München, Lehrstuhl für Aerodynamik und Strömungsmechanik, 2012.

[83] N. J. Wood and L. Roberts. Control of vortical lift on delta wings by tangential leading-edge blowing. *Journal of Aircraft*, 25(3): pp. 236–243, 1988.

[84] R. M. Wood and D. S. Miller. Assessment of preliminary prediction techniques for wing leading-edge vortex flows at supersonic speeds. *Journal of Aircraft*, 22(6): pp. 473 – 478, 1985.

[85] D. Zimmermann. Strömungsbeeinflussung an einem Deltaflügel mittels aktivem Ausblasen bei sehr hohen Anstellwinkeln, Term paper, Technische Universität München, Lehrstuhl für Aerodynamik und Strömungsmechanik, 2013.

A. Positions of the pressure sensors

The following tables give an overview of the positions and the numbering of the sensors for steady and unsteady pressure measurements.

Table A.1.: Sensor Coordinates [5]

Position of the sensors - Upper side								
$x/c_r = 0.4$			$x/c_r = 0.6$			$x/c_r = 0.8$		
$\eta = 2y/s_l$	$x[mm]$	$y[mm]$	$\eta = 2y/s_l$	$x[mm]$	$y[mm]$	$\eta = 2y/s_l$	$x[mm]$	$y[mm]$
Edge			Shaft			Shaft		
0.050	390.2	9.1						
0.100	390.2	18.2						
0.150	390.2	27.3	Edge			0.150	782.4	54.7
0.200	390.2	36.4	0.200	586.3	54.7	0.200	782.4	73.0
0.250	390.2	45.5	0.250	586.3	68.3	0.250	782.4	91.2
0.300	390.2	54.6	0.300	586.3	82.0	0.300	782.4	109.4
0.350	390.2	63.7	0.350	586.3	95.7	0.350	782.4	127.7
0.400	390.2	72.8	0.400	586.3	109.3	0.400	782.4	145.9
0.450	390.2	81.9	0.450	586.3	123.0	0.450	782.4	164.2
0.500	390.2	91.0	0.500	586.3	136.7	0.500	782.4	182.4
0.525	390.2	95.5	0.525	586.3	143.5	0.525	782.4	191.5
0.550	390.2	100.1	0.550	586.3	150.4	0.550	782.4	200.6
0.575	390.2	104.6	0.575	586.3	157.2	0.575	782.4	209.8
0.600	390.2	109.2	0.600	586.3	164.0	0.600	782.4	218.9
			0.625	586.3	170.9	0.625	782.4	228.0
0.648	390.2	118.0	0.650	586.3	177.7	0.650	782.4	237.1
0.673	390.2	122.5	0.675	586.3	184.5	0.675	782.4	246.2
0.698	390.2	127.1	0.700	586.3	191.4	0.700	782.4	255.4
0.724	390.2	131.7	0.725	586.3	198.2	0.725	782.4	264.5
0.749	390.2	136.3				0.750	782.4	273.6
0.774	390.2	140.8	*0.774 (d)*	*586.3*	*211.6*	0.775	782.4	282.7
0.799	390.2	145.4	0.799	586.3	218.5	0.800	782.4	291.8
0.824	390.2	150.0	0.824	586.3	225.3	0.825	782.4	300.8
0.849	390.2	154.5	0.850	586.3	232.2	0.850	782.4	309.9
0.874	390.2	159.1	0.874	586.3	239.0	0.875	782.4	319.0
0.900	390.2	163.7	0.900	586.3	245.9	0.900	782.4	328.2
0.925 (d)	*390.2*	*168.3*	0.925	586.3	252.7	0.925	782.4	337.3
0.950	390.2	172.8	0.950	586.3	259.6	0.950	782.4	346.5
Leading-edge			Leading-edge			Leading-edge		
Position of the sensors - Lower side								
0.400	390.2	72.8	0.600	586.3	164.0	0.600	782.4	218.9
d - sensor defect								

Table A.2.: Labels and numbers of the sensors [5]

Upper side											
$x/c_r = 0.4$				$x/c_r = 0.6$				$x/c_r = 0.8$			
Label	n°	n_S°	n_K°	Label	n°	n_S°	n_K°	Label	n°	n_S°	n_K°
Edge				Shaft				Shaft			
A1S	1	1									
A2S	2	2									
A3S	3	3		Edge				C1S	54	34	
A4S	4	4		B1S	29	19		C2S	55	35	
A5K	5		1	B2K	30		11	C3K	56		21
A6S	6	5		B3S	31	20		C4S	57	36	
A7S	7	6		B4S	32	21		C5S	58	37	
A8K	8		2	B5K	33		12	C6K	59		22
A9S	9	7		B6S	34	22		C7S	60	38	
A10K	10		3	B7K	35		13	C8K	61		23
A11S	11	8		B8S	36	23		C9S	62	39	
A12S	12	9		B9S	37	24		C10S	63	40	
A13K	13		4	B10K	38		14	C11K	64		24
A14S	14	10		B11S	39	25		C12S	65	41	
				B12S	40	26		C13K	66		25
A15S	15	11		B13S	41	27		C14S	67	42	
A16K	16		5	B14K	42		15	C15K	68		26
A17S	17	12		B15S	43	28		C16S	69	43	
A18K	18		6	B16K	44		16	C17K	70		27
A19S	19	13						C18S	71	44	
A20K	20		7	B17K	45		17	C19K	72		28
A21S	21	14		B18S	46	29		C20S	73	45	
A22K	22		8	B19K	47		18	C21K	74		29
A23S	23	15		B20S	48	30		C22S	75	46	
A24K	24		9	B21K	49		19	C23K	76		30
A25S	25	16		B22S	50	31		C24S	77	47	
A26K	26		10	B23K	51		20	C25K	78		31
A27S	27	17		B24S	52	32		C26S	79	48	
Leading-edge				Leading-edge				Leading-edge			
Lower side											
A28U	28	18		B25U	53	33		C27U	80	49	

B. Power spectral density for $\alpha = 35^{\circ}$

The following plots show the detailed analysis of the power spectral density for the surface pressure signal at $\alpha = 35^{\circ}$, $Re_{mac} \approx 0.5 \times 10^6$, and $M = 0.035$ and the measurement planes $X = 0.4$, $X = 0.6$ and $X = 0.8$ (baseline case). The narrow-banded concentrations of the pressure fluctuations can be clearly observed in all measurement planes.

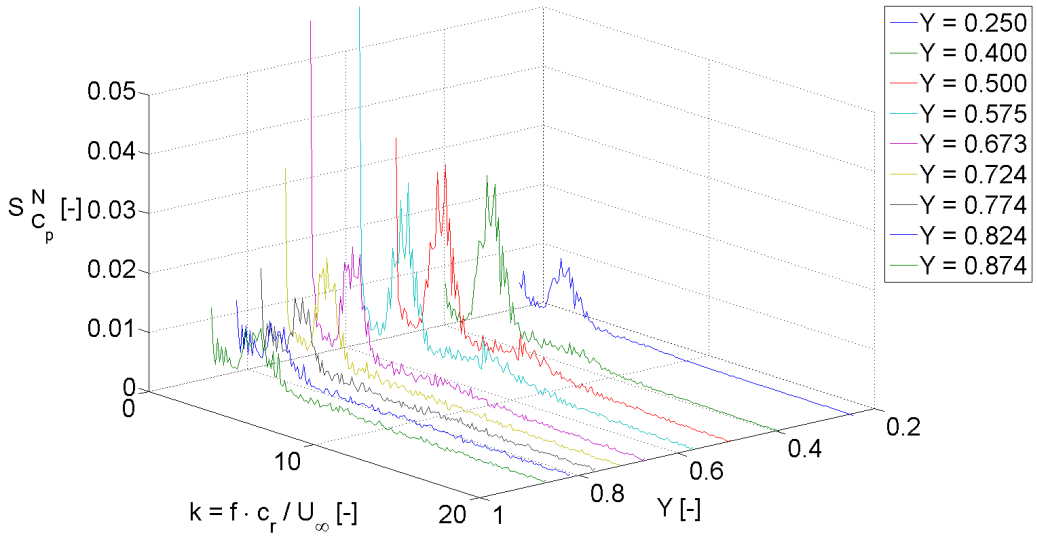

Figure B.1.: Power spectral density of the pressure signal at $X = 0.4$ for $\alpha = 35°$, $Re_{mac} \approx 0.5 \times 10^6$, and $M = 0.035$

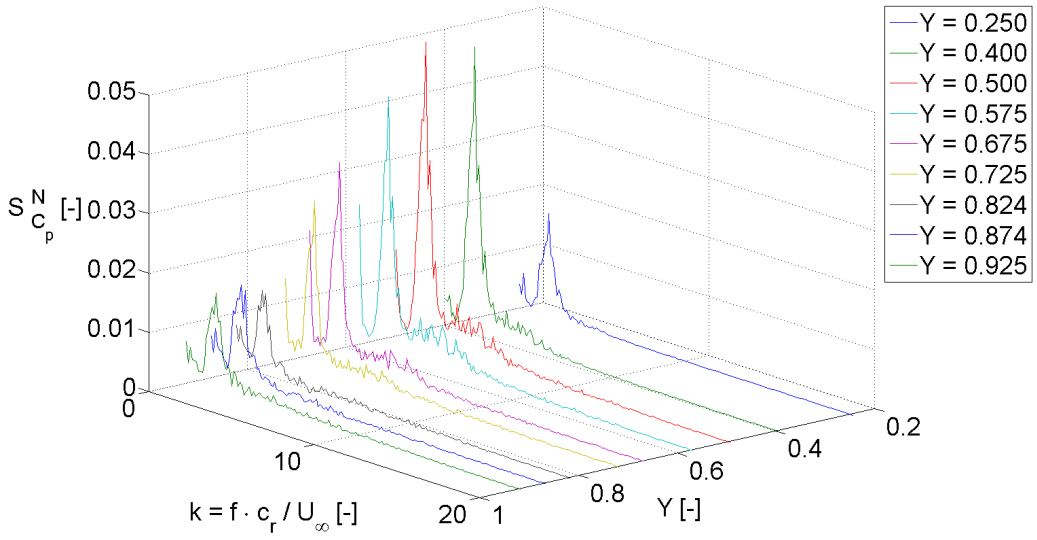

Figure B.2.: Power spectral density of the pressure signal at $X = 0.6$ for $\alpha = 35°$, $Re_{mac} \approx 0.5 \times 10^6$, and $M = 0.035$

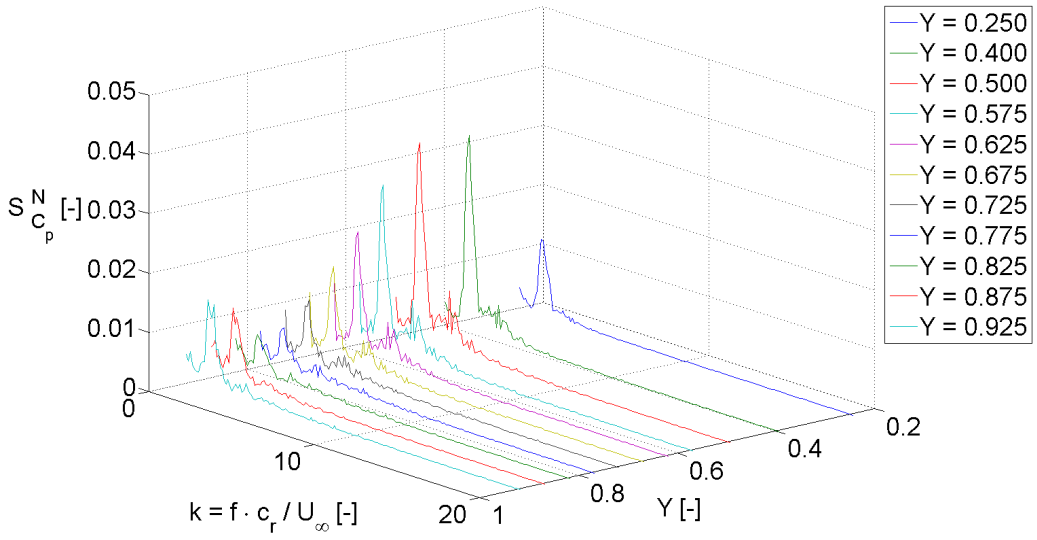

Figure B.3.: Power spectral density of the pressure signal at $X = 0.8$ for $\alpha = 35°$, $Re_{mac} \approx 0.5 \times 10^6$, and $M = 0.035$

C. Flow field results

In figures C.1 to C.5, additional information is provided for the flow field results measured in the pre-stall test case at $\alpha = 23°$, $Re_{mac} = 1 \cdot 10^6$ and $M = 0.07$. The measurement results for pulsed blowing at $f_{pulse} = 65\ Hz$ ($F^+ = 2.6$), $DC = 25\%$ and $U_{jet} \approx 50\ m/s$ are compared to the baseline case. Figures C.1 to C.4 show the axial velocity component on the left and the axial turbulent intensity on the right. At the bottom of the plots, the difference between the actuated case and the baseline case is shown for the respective quantity (e.g. $\Delta u/U_\infty = (u_{f_{pulse=65\ Hz}} - u_{baseline})/U_\infty$ for the dimensionless axial velocity component). Fig. C.5 contrasts the axial vorticity for the baseline case with the distribution in the actuated case.

Figures C.6 and C.7 show HWA measurement results in the post-stall test case at $\alpha = 45°$, $Re_{mac} = 0.5 \cdot 10^6$ and $M = 0.035$. The measurement results for pulsed blowing at $f_{pulse} = 12\ Hz$ ($F^+ = 1$), $DC = 25\%$ and $U_{jet} \approx 55\ m/s$ are compared to the baseline case. The flow field is visualized by the axial velocity component, the axial turbulent intensity and the axial vorticity.

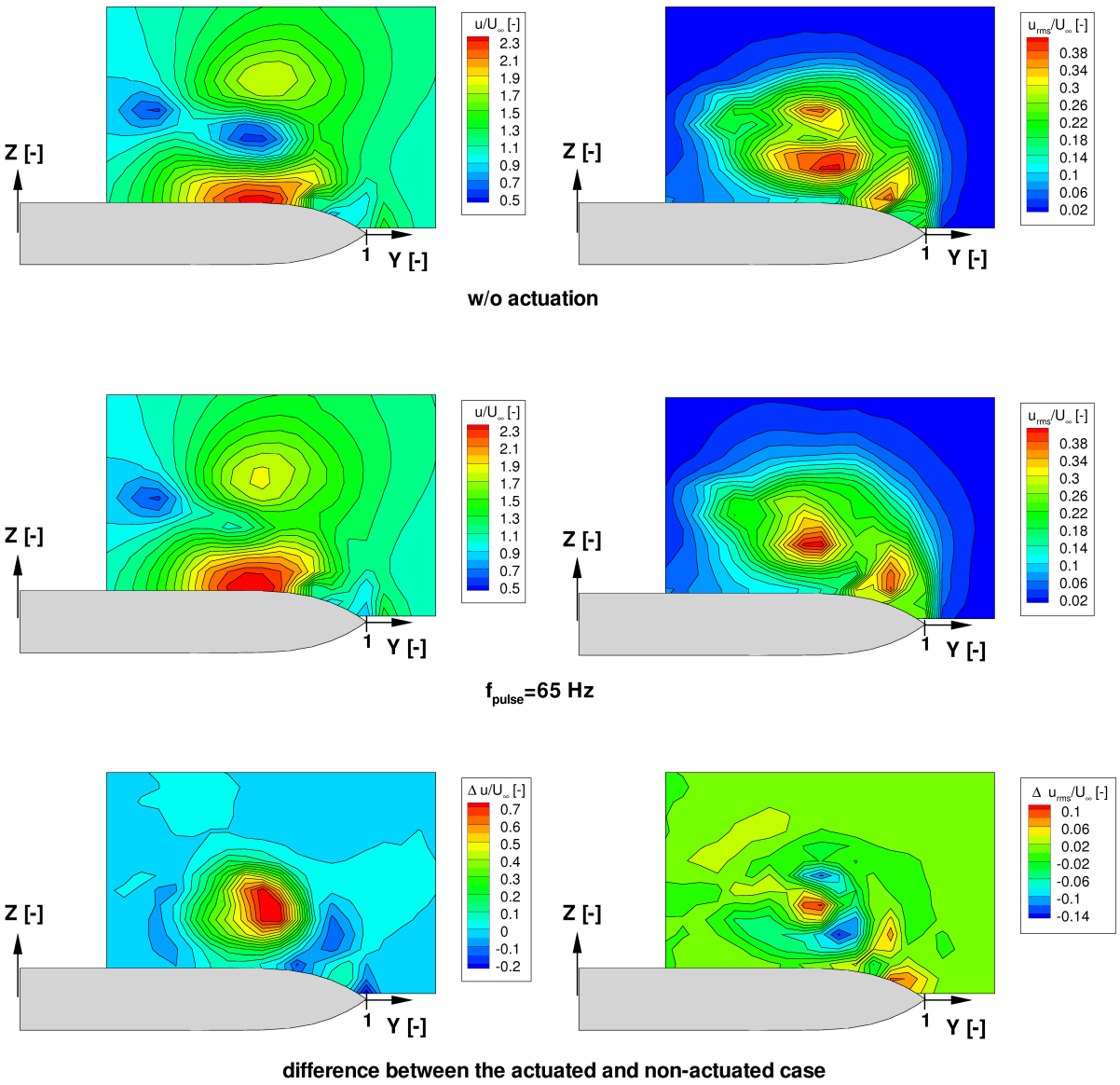

Figure C.1.: Mean and turbulent axial velocity fields for the non-actuated and actuated cases at $\alpha = 23°$, $X = 0.4$, $Re_{mac} = 1 \cdot 10^6$ and $M = 0.07$; pulsed blowing at $f_{pulse} = 65\ Hz$ ($F^+ = 2.6$), $DC = 25\%$ and $U_{jet} \approx 50\ m/s$; HWA measurement result

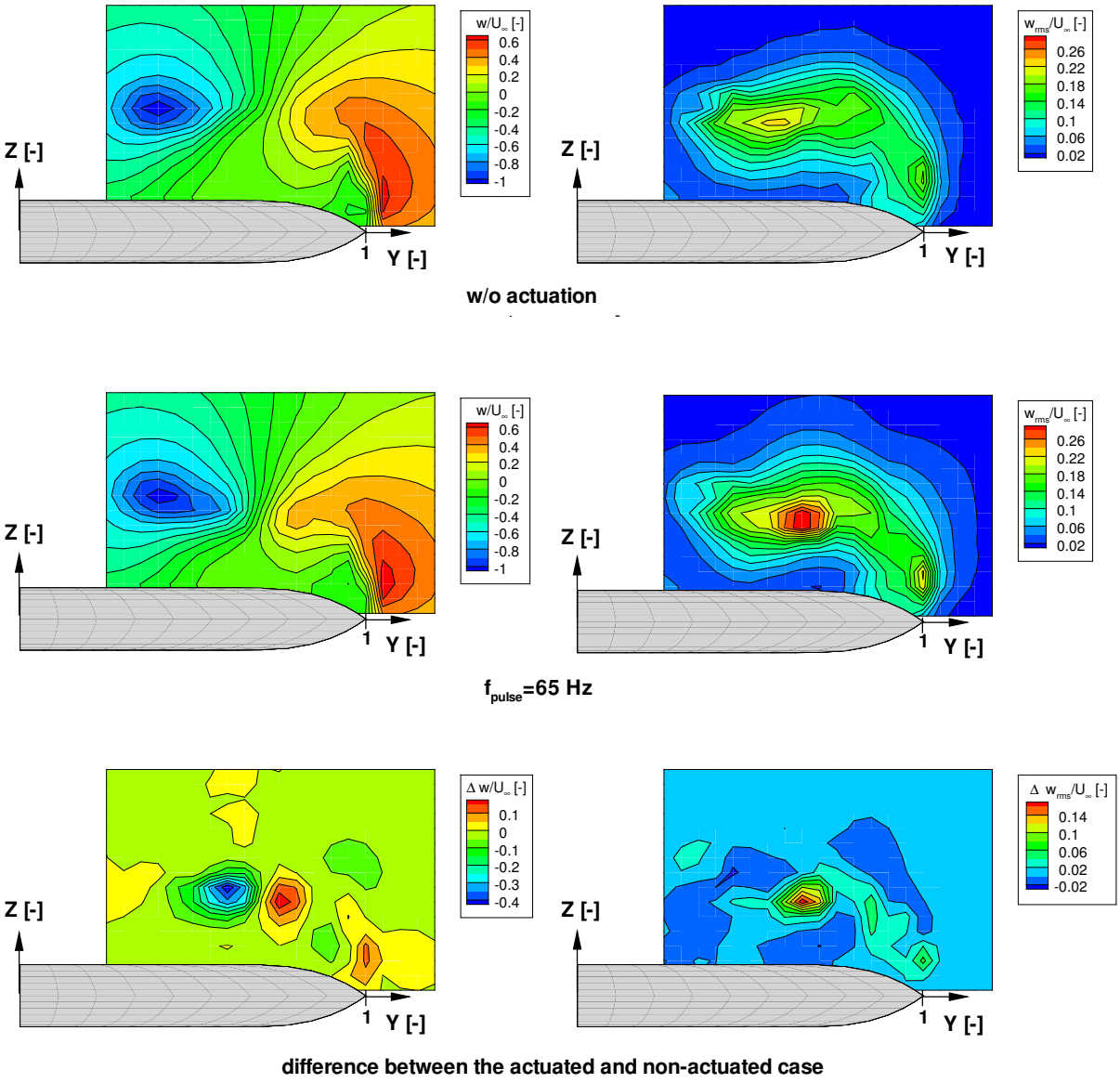

Figure C.2.: Mean and turbulent vertical velocity fields for the actuated and non-actuated cases at $\alpha = 23°$, $X = 0.4$, $Re_{mac} = 1 \cdot 10^6$ and $M = 0.07$; pulsed blowing at $f_{pulse} = 65\ Hz$ ($F^+ = 2.6$), $DC = 25\%$ and $U_{jet} \approx 50\ m/s$; HWA measurement result

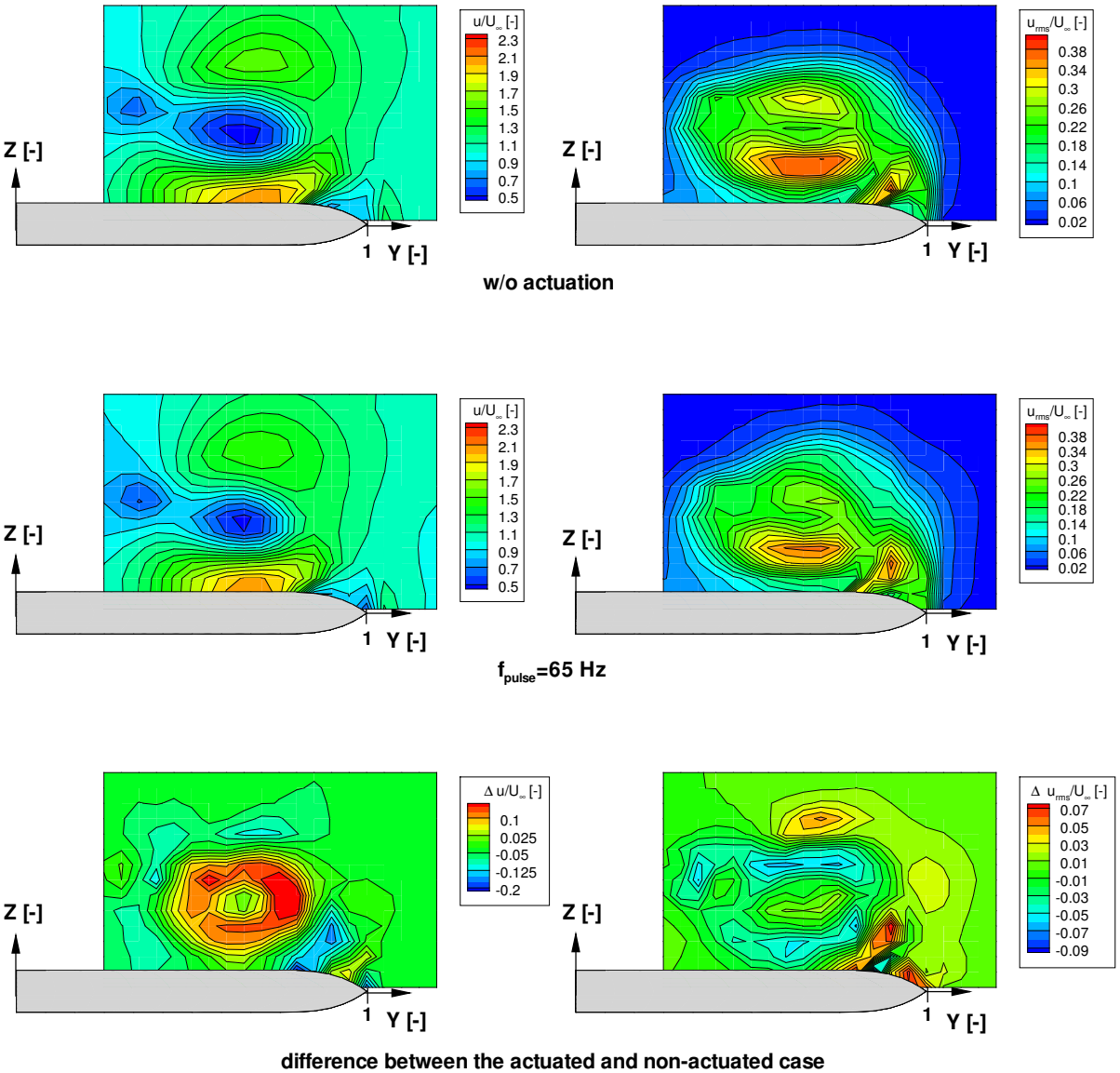

Figure C.3.: Mean and turbulent axial velocity fields for the non-actuated and actuated cases at $\alpha = 23°$, $X = 0.6$, $Re_{mac} = 1 \cdot 10^6$ and $M = 0.07$; pulsed blowing at $f_{pulse} = 65\ Hz$ ($F^+ = 2.6$), $DC = 25\%$ and $U_{jet} \approx 50\ m/s$; HWA measurement result

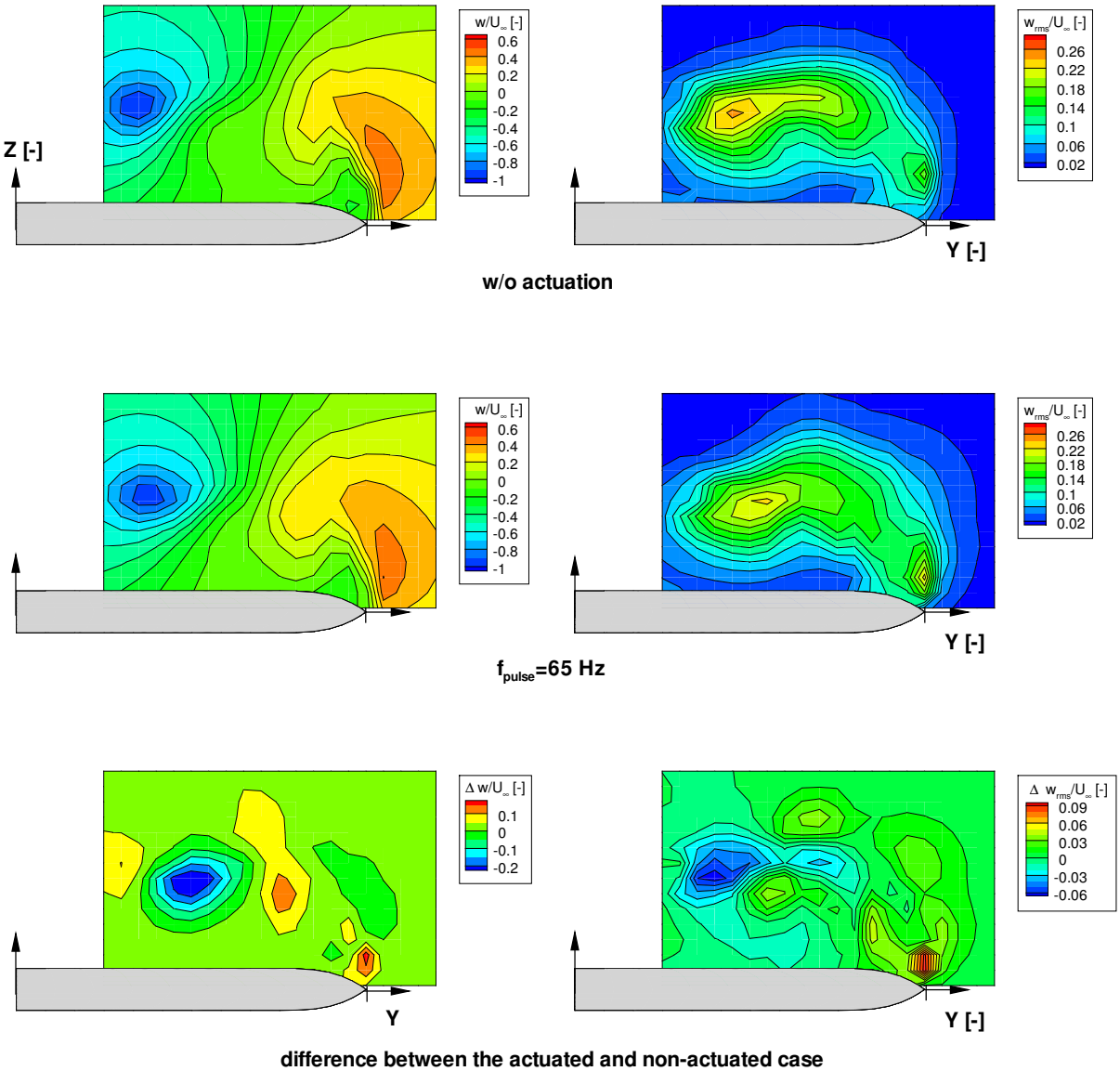

Figure C.4.: Mean and turbulent vertical velocity fields for the non-actuated and actuated cases at $\alpha = 23°$, $X = 0.6$, $Re_{mac} = 1 \cdot 10^6$ and $M = 0.07$; pulsed blowing at $f_{pulse} = 65\ Hz$ ($F^+ = 2.6$), $DC = 25\%$ and $U_{jet} \approx 50\ m/s$; HWA measurement result

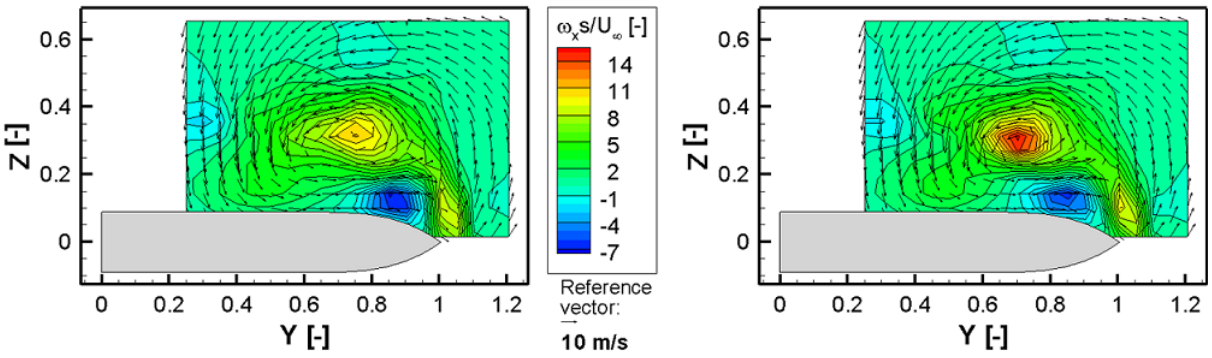

Figure C.5.: Axial vorticity for the non-actuated and actuated cases at $\alpha = 23°$, $X = 0.4$, $Re_{mac} = 1 \cdot 10^6$ and $M = 0.07$; pulsed blowing at $f_{pulse} = 65\ Hz$ ($F^+ = 2.6$), $DC = 25\%$ and $U_{jet} \approx 50\ m/s$; HWA measurement result

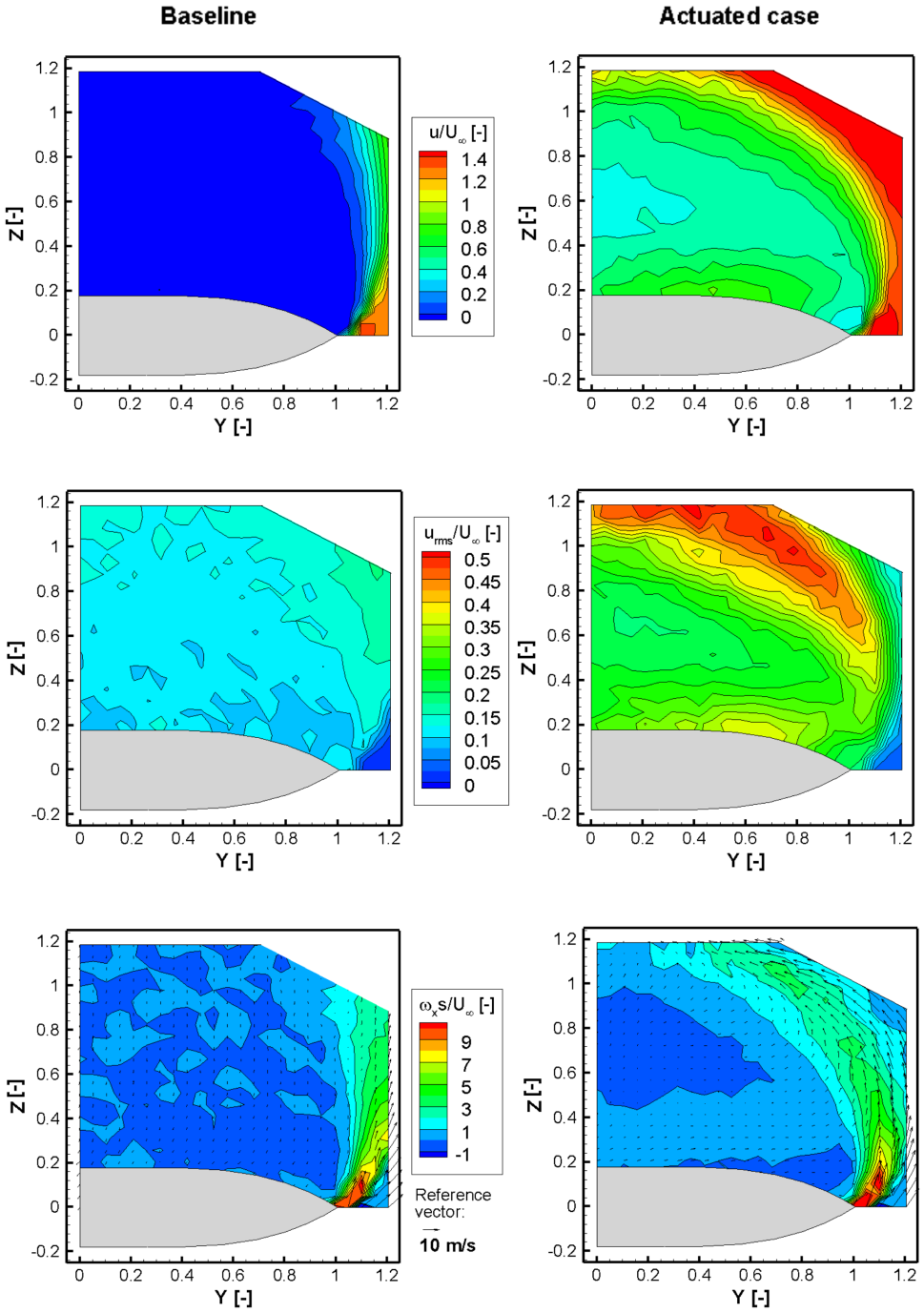

Figure C.6.: Mean and turbulent vertical velocity fields and axial vorticity for the non-actuated and actuated cases at $\alpha = 45°$, $X = 0.4$, $Re_{mac} = 1 \cdot 10^6$ and $M = 0.07$; pulsed blowing at $f_{pulse} = 12\ Hz$ ($F^+ = 1.0$) and $U_{jet} \approx 55\ m/s$; HWA measurement result

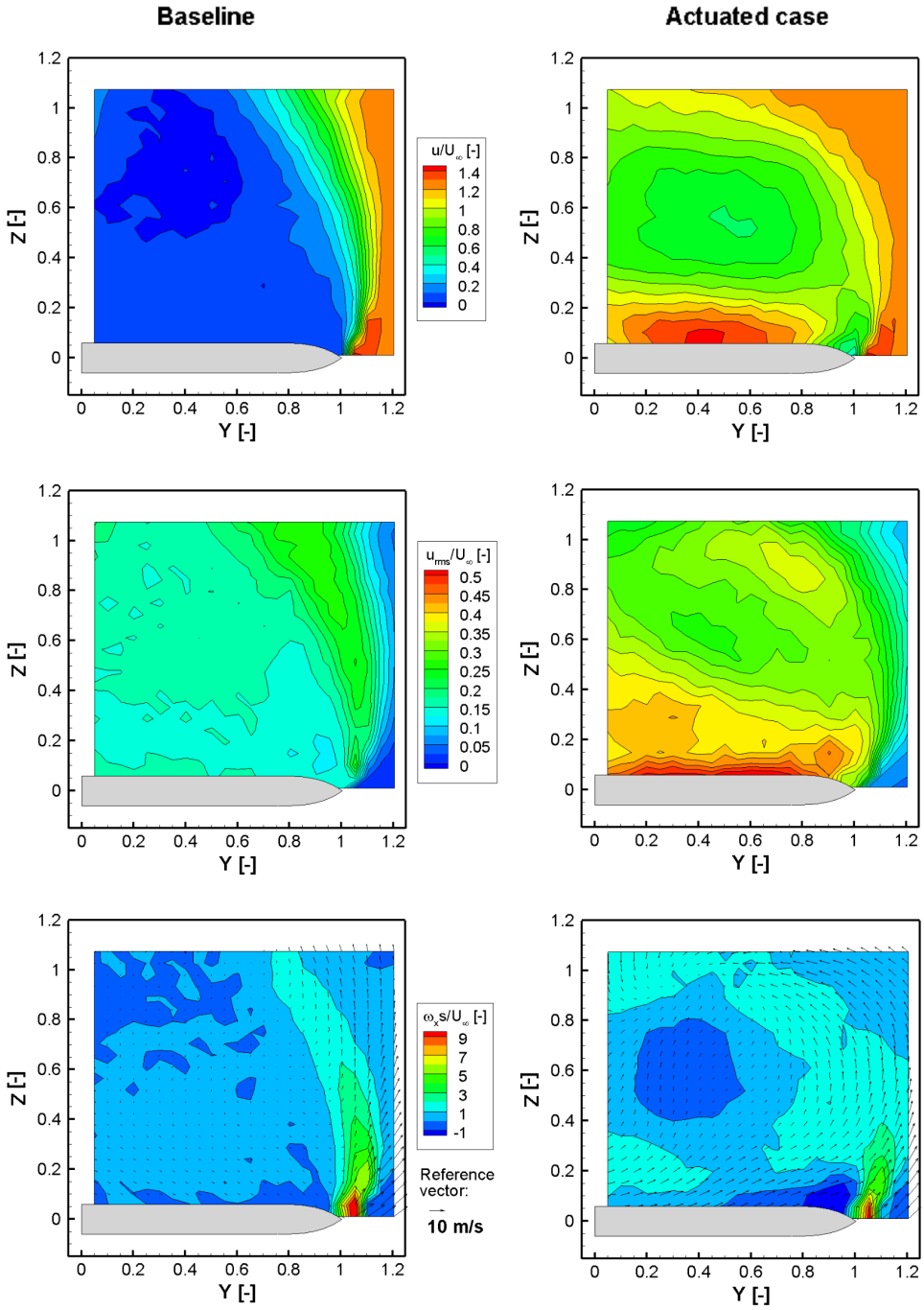

Figure C.7.: Mean and turbulent vertical velocity fields and axial vorticity for the non-actuated and actuated cases at $\alpha = 45°$, $X = 0.6$, $Re_{mac} = 1 \cdot 10^6$ and $M = 0.07$; pulsed blowing at $f_{pulse} = 12\ Hz$ ($F^+ = 1.0$) and $U_{jet} \approx 55\ m/s$; HWA measurement result